INTRAMOLECULAR INTERACTIONS

IN

RHODIUM MONOXIDE AND HALOGEN AZIDES

by

Roy Henry Jensen
B.Sc., University of Victoria, 1995
M.Sc., University of Denver, 1999

A dissertation submitted in partial fulfillment of the requirement for the degree of

DOCTOR OF PHILOSOPHY

in the Department of Chemistry.

We accept this dissertation as conforming to the required standard.

Dr. Walter Balfour, Supervisor
Department of Chemistry, University of Victoria

Dr. Terry Gough, Committee Member
Department of Chemistry, University of Victoria

Dr. Alexandre Brolo, Committee Member
Department of Chemistry, University of Victoria

Dr. Jeremy Tatum, Committee Member
Department of Physics and Astronomy, University of Victoria

Dr. David Harrington, Committee Member
Department of Chemistry, University of Victoria

Dr. Michael Gerry, External Examiner
Department of Chemistry, University of British Columbia

University of Victoria

ABSTRACT

Supervisor: Dr. Walter Balfour

Part A. Vibronic transitions of rhodium monoxide ($Rh^{16}O$ and $Rh^{18}O$) were observed in the 380 to 700 nm region. Laser-induced fluorescence identified two $^2\Pi_r - X^4\Sigma^-$ progressions with origins at {15 667, 15 976} and {15 874, 16 167} cm^{-1}. These progressions were labeled [15.8] $^2\Pi - X^4\Sigma^-$ and [16.0] $^2\Pi - X^4\Sigma^-$, respectively. Vibrational parameters were determined for the ground and excited states; the ground state parameters are $\omega_e = 805.4 \pm 0.6$ cm^{-1}, $\omega_e x_e = 4.5 \pm 0.1$ cm^{-1}, and $D_e = 35\,800 \pm 800$ cm^{-1}. Evidence was found for low-lying electronic states at 3 747, 5 980 and 6 475 cm^{-1}. Lifetime measurements are consistent with the spin-forbidden nature of the transition: $^2\Pi - {}^4\Sigma^-$.

Part B. Density functional and configuration interaction calculations on the lowest singlet and triplet potential energy surfaces of hydrogen, fluorine, and chlorine azide for the reactions $XN_3(\tilde{X}\,^1A') \longrightarrow NX(X^3\Sigma; a^1\Delta) + N_2(X^1\Sigma_g^+)$ and $XN_3 \longrightarrow X(X^2S; X^2P_{3/2}) + N_3(X^2\Pi_g)$ (X = H, F, Cl) show that the lowest energy dissociation pathway proceeds exothermically to $NX(a) + N_2$. This surface is crossed on the bound singlet region by a dissociative triplet surface. Unimolecular decomposition rates for each pathway and the branching ratio support the experimental observations: HN_3 dissociates to ground state products while FN_3 and ClN_3 produce significant amounts of electronically excited NX.

Dr. Walter Balfour, Supervisor
Department of Chemistry, University of Victoria

Dr. Terry Gough, Committee Member
Department of Chemistry, University of Victoria

Dr. Alexandre Brolo, Committee Member
Department of Chemistry, University of Victoria

Dr. Jeremy Tatum, Committee Member
Department of Physics and Astronomy, University of Victoria

Dr. David Harrington, Committee Member
Department of Chemistry, University of Victoria

Dr. Michael Gerry, External Examiner
Department of Chemistry, University of British Columbia

INTRAMOLECULAR INTERACTIONS

IN

RHODIUM MONOXIDE AND HALOGEN AZIDES

TABLE OF CONTENTS

A CD-ROM accompanies the hard-cover copies of this dissertation. The CD contains the spectroscopic data, ab initio calculations, analysis, schematics, presentations, etc., and this dissertation. Installation disks for software not commonly available are also included.

LIST OF TABLES

Part A: Vibronic Analysis of Rhodium Monoxide

Part B: Thermal Dissociation of Halogen Azides

LIST OF FIGURES

Part A: Vibronic Analysis of Rhodium Monoxide

Part B: Thermal Dissociation of Halogen Azides

The only limits in life
are the limits of the mind.

VIBRONIC ANALYSIS OF RHODIUM MONOXIDE

1. INTRODUCTION

In chemical compounds, bonding is envisioned as the overlap of atomic orbitals to form molecular orbitals, into which electrons arrange themselves to minimize the total energy of the system. If the resulting energy is lower than the summed energy of the isolated atoms, a *bond* forms and the system is stable.* The nature of chemical bonding has been the subject of extensive study — all of chemistry, in fact. Diatomic compounds provide the simplest system in which to probe the interaction of atoms. From a detailed understanding of diatomic interactions, we gain the tools necessary to understand bonding and reactions in larger systems: combustion, catalysis, polymerization, protein folding, and biological replication are but a few broad areas of chemical interest.

Multiple techniques are available to probe intramolecular interactions. Spectroscopy — the interaction of a molecule with electromagnetic radiation — has proved to be the most sensitive and the most versatile. Because of each compound's unique spectroscopic signature, spectroscopy has been used to identify and characterize both known and unknown species. The varying energy across the electromagnetic spectrum probes different intramolecular processes. The valence electrons — those responsible for bonding — are probed by infrared (IR), visible, and ultraviolet (UV) radiation. IR radiation probes rovibrational levels while visible and UV (UV/Vis) radiation probes rovibronic levels. Emission spectroscopy is a more sensitive technique, more selective, and provides more information on the system than absorption spectroscopy.

In addition to providing information on intramolecular interactions, knowledge of known systems has allowed scientists to identify them in other environments. Scientists have been able to identify many features in the solar spectrum. Solar absorption lines have been assigned to over 60 elements and dozens of molecules and molecular ions. For example, H_2, OH, C_2, CN, CO, MgH, and SiC have been observed in the photosphere and many others — HF, HCl, H_2O, FeH, CrH, AlCl, MgCN,[1] and MgNC[2] — in cooler sunspots.[3] Their presence in such environments attests to the strong intramolecular bonding in these

---

* Not strictly valid for polyatomics, where metastable compounds can form.

compounds. Notably, many of these species involve bonds to transition metals. Many absorption features still elude assignment, making future spectroscopic studies of small molecules relevant to the understanding of solar and astrophysical processes. Back on Earth, our atmosphere is predominantly composed of small molecules exposed to solar radiation. Solar photolysis plays an integral part in the chemical composition of the atmosphere at all levels. Apart from life itself, solar irradiation is responsible for ground level smog, stratospheric ozone formation and depletion, and the ionosphere, to name a few. Spectroscopic techniques have been developed to simultaneously determine the local, gradient, and total column concentration of analytes in the atmosphere[4] and even a non-invasive method of measuring the combustion efficiency of an automobile engine in real time.[5]

Our laboratory has spectroscopically characterized many first- and second-row transition metal containing compounds. Since 1990, this has included $TiCl^+$,[6] VN,[7] CrN,[8] MnH,[9] FeH,[10] FeC,[11] YH,[12] YC,[13] YNH,[14] YO,[15] InO,[16] InO^+,[17] InCl and $InCl^+$,[18] and ReN.[19] We recently chose to investigate rhodium compounds since they have received little attention from the spectroscopic community but have become very important in industry. Rhodium-containing compounds are known to catalyze polymerization reactions, nitric acid synthesis, hydrocarbon reformulation, ethanol production, and NO_x conversion in automobile catalytic converters, to name a few.[20] RhH,[21] RhC,[22] and RhN[23] have been studied and characterized in this laboratory. RhO is the subject of this dissertation and spectra of RhF and RhS have been collected.

Rhodium monoxide (RhO) is one of the least well characterized of the transition metal monoxides. Originally observed in 1968 by Lagerqvist and Scullman, the high-temperature emission spectrum was too congested to analyze.[24] In our experiments, a low-temperature emission spectrum was obtained using a supersonically cooled RhO generated in a $Rh/O_2/He$ plasma. A complex array of vibronic bands in the 380 to 700 nm region was recorded by laser-induced fluorescence (LIF). Except for highly congested band centers, these bands were rotationally resolved. Isotopic substitution experiments identified four bands between 615 and 640 nm with near-zero isotopic shift. These bands are proposed to be $v' = 0 \rightarrow v'' = 0$ (0–0) transitions and rotational analysis in our laboratory has identified band origins for four $^2\Pi - X^4\Sigma^-$ vibronic progressions. The progressions are labeled the

[15.8] $^2\Pi_r - X^4\Sigma^-$ and [16.0] $^2\Pi_r - X^4\Sigma^-$ with origins at {15 667, 15 976} and {15 874, 16 167} cm^{-1}, respectively.[25] This dissertation focuses on the vibrational progressions from these origins. $^{16}O/^{18}O$ isotopic substitution, laser-induced fluorescence spectroscopy, dispersed fluorescence spectroscopy, and excited state lifetime measurements were made to characterize these bands and obtain information on the electronic states involved.

Previously, Citra and Andrews examined the infrared absorption spectra of laser-ablated rhodium atoms co-deposited with oxygen in argon at 7 K and assigned vibrational features at 799.0 and 759.8 cm^{-1} to $\mathrm{Rh}^{16}\mathrm{O}$ and $\mathrm{Rh}^{18}\mathrm{O}$, respectively.[26] Chen and Armentrout used thermodynamic data to estimate the Rh–O ground state bond dissociation energy, D_0, at 33 800 cm^{-1}.[27] Anion photoelectron spectroscopy identified the ground state and electronic energy levels at ≈ 1 600, 3 800, 5 700 and 8 100 cm^{-1}.[28] These electronic states were assigned based on theoretical arguments as $X^4\Sigma^-_{3/2}$, $X^4\Sigma^-_{1/2}$, $A^2\Sigma^-$, $B^2\Pi_{3/2}$, and $B^2\Pi_{1/2}$. The vibrational intervals of the ground and $^2\Pi_{3/2}$ states were estimated at 730 ± 80 cm^{-1} and 800 ± 90 cm^{-1}, respectively. The present work improves upon the precision of these assignments and, in some cases, suggests alternate assignments.

Theoretical analysis of transition metal containing complexes is difficult owing to the high density of low-lying electronic states and approximate consideration of electron correlation, relativity, spin-orbit coupling, spin-spin coupling, etc.[29] Small changes in basis set or computational method often have large effects on the resulting ordering of states because of the non-linear nature of the calculations. Additionally, multiple unpaired electrons, degenerate levels, and quantum mechanical approximations necessary to make the calculations tractable often lead to inaccuracies. Calculations on FeH[30] and RhN[31] exemplify the problems. Nevertheless, ab initio calculations often provide qualitative information useful in understanding molecular spectra. Several groups predict the ground state of RhO to be $^4\Sigma^-$.[26,32,33]

It is important to note that the demands of ab initio calculations on diatomic molecules are considerably higher than polyatomic molecules: the ability to obtain vibronically accurate potential energy surfaces for even a triatomic molecule is currently impossible, yet expected for diatomics.

2. QUANTUM MECHANICS OF VIBRONIC TRANSITIONS[*]

As the smallest molecular entity, diatomic compounds have received the most attention from both a theoretical and experimental perspective. From this history, several mathematical models for diatomic molecules have evolved.

Apart from the acceptance of the postulates of quantum mechanics and the separability of the wavefunction into space and time components, one underlying assumption is regularly made in quantum mechanical studies: the Born-Oppenheimer approximation.[40] This approximation supposes that the large mass difference between electrons and nuclei allows for the separation of the motions of the electrons and nuclei. The smallest ratio is for hydrogen where the mass ratio is 1:1 836. Thus, classically, electrons move at least 43 times faster than the nucleus ($\sqrt{1836}$), allowing the electrons to find their optimum electronic configuration in the potential generated by near-stationary nuclei. In a wave-mechanics perspective, electrons are delocalized and nuclei do not oscillate. In this perspective, the Born-Oppenheimer approximation results from the different rate at which the electrons and nuclei react to an external force on the system. The electronic redistribution is complete before the nuclei begin to react to the force and 'instantly' redistribute for every nuclear configuration. This separates the total wavefunction, Ψ, into electronic and nuclear terms: Ψ_{elec} and Ψ_{nuc}. These terms can be separated further. Moving to the center-of-mass reference frame separates the translational wavefunction, ψ_{t}, of Ψ_{nuc} from the remaining terms. In the absence of an external field, the translating molecule can be considered as a free particle and has non-discrete (continuous) energy levels. The radial and angular portions of Ψ_{nuc} are separable into vibrational and rotational wavefunctions, ψ_{v} and ψ_{r}, respectively.[†] Nuclear spin (ψ_{I}) and electron spin (ψ_{s}) appear as a result of relativistic quantum mechanics and have no classical counterpart. What remains is the electronic wavefunction, ψ_{e}. The final separated wavefunction takes the form

---

[*] References 34 to 39 were used to prepare this Chapter; individual citations are omitted. Other sources are cited as required.

[†] For completeness, equations include rotational term(s).

$$\Psi = \Psi_{\text{elec}}\,\Psi_{\text{nuc}} \qquad \begin{aligned} \Psi_{\text{elec}} &= \psi_{\text{e}}\,\psi_{\text{s}} \\ \Psi_{\text{nuc}} &= \psi_{\text{t}}\,\psi_{\text{r}}\,\psi_{\text{v}}\,\psi_{\text{I}} \end{aligned} \tag{1}$$

For molecules without a center of inversion, the nuclear spin weighting is the same for each energy level[*] — ψ_{I} will not be discussed further. Relativistic quantum mechanics requires that the total wavefunction, Ψ, be symmetric with respect to exchange of any two bosons and antisymmetric with respect to exchange of any two fermions (electrons).[41] The vibrational wavefunction alternates even/odd symmetry with increasing vibrational quantum number, v.

For an isolated molecule, conservation laws demand that the total energy and total angular momentum remain unchanged. The distribution of the total energy into kinetic and potential components can vary (as can the total angular momentum). Hamiltonian mathematics is used to evaluate this energy distribution problem. A potential field exists within every molecule by virtue of the charge on and position of the nuclei and electrons. Equation (2) shows the Hamiltonian, $\hat{\mathcal{H}}$, for a multinuclear, multielectron system that contains kinetic, $\hat{T}$, and potential, $\hat{V}$, energy operators for the electrons and nuclei.[†] Other terms can be added to treat other interactions, such as spin-orbit coupling, spin-spin coupling, and interactions with external fields.

$$\begin{aligned} \hat{\mathcal{H}} &= \hat{T}_e + \hat{T}_N + \hat{V}_{eN} + \hat{V}_{ee} + \hat{V}_{NN} \\ &= -\frac{\hbar^2}{2m_{\text{e}}}\sum_{\mu}\nabla_{\mu}^2 - \frac{\hbar^2}{2}\sum_{A}\frac{\nabla_A^2}{m_A} - \sum_{\mu}\sum_{A}\frac{Ze^2}{4\pi\varepsilon_0\, r_{\mu A}} + \sum_{\mu}\sum_{\nu>\mu}\frac{e^2}{4\pi\varepsilon_0\, r_{\mu\nu}} + \sum_{A}\sum_{A>B}\frac{Z_A Z_B e^2}{4\pi\varepsilon_0\, r_{AB}} \end{aligned} \tag{2}$$

The energy of the system is determined by solving the Schrödinger equation, (3).

$$\hat{\mathcal{H}}\Psi = E\Psi \tag{3}$$

---

[*] The number of nuclear spin states plays an important role in the spectroscopic study of molecules possessing a center of inversion. The nuclei are now indistinguishable and ψ_{I} must be considered. The intensity of rovibronic transitions depend on the number of nuclear symmetric, $(I + 1)(2I + 1)$, and antisymmetric, $I(2I + 1)$, states and the number that are populated: all if the nuclei are fermions and one [symmetric state] if they are bosons.

[†] Lowercase variables refer to electrons and uppercase variables refer to nuclei.

For fixed nuclear coordinates, the Born-Oppenheimer approximation simplifies (2) to the electronic Hamiltonian

$$\hat{\mathcal{H}}_{\text{elec}} = -\frac{\hbar^2}{2m_{\text{e}}}\sum_{\mu}\nabla_{\mu}^2 - \sum_{\mu}\sum_{A}\frac{Ze^2}{4\pi\varepsilon_0 r_{\mu A}} + \sum_{\mu}\sum_{\nu>\mu}\frac{e^2}{4\pi\varepsilon_0 r_{\mu\nu}} \tag{4}$$

Solving the Schrödinger equation using the electronic Hamiltonian provides the electronic energy of the system at that nuclear configuration. The total energy is obtained by including the Hamiltonian for nuclear potential energy (5), which is a constant under the Born-Oppenheimer approximation. The total energy defines a classical 'turning point' — the location where the kinetic energy is zero, wholly in its potential component. Repeating the calculation while iterating the nuclear coordinates generates a *potential energy surface* (PES), $V(\tau)$.

$$\hat{\mathcal{H}}_{\hat{V}_{\text{NN}}} = \sum_{A}\sum_{A>B}\frac{Z_A Z_B e^2}{4\pi\varepsilon_0 r_{AB}} \tag{5}$$

Solution of the Schrödinger equation using the nuclear kinetic Hamiltonian, (6), in the potential $V(\tau)$ provides the rotational and vibrational energy levels of the system.

$$\hat{\mathcal{H}}_{\hat{T}_{\text{N}}} = -\frac{\hbar^2}{2}\sum_{A}\frac{\nabla_A^2}{m_A} + V(\tau) \tag{6}$$

Potential energy curves

For a diatomic molecule, a one-dimensional 'surface' or curve (PEC) is generated. Experimentally and computationally, the PEC adopts the profile shown in Figure 2.1. At short internuclear distances, internuclear repulsion dominates and forces the nuclei apart. At long distances, there are no internuclear interactions and the energy is the simple sum of the energy of the isolated atoms. At intermediate distances, dynamic electron-electron interactions serve to lower the total energy, resulting in a molecular bond.

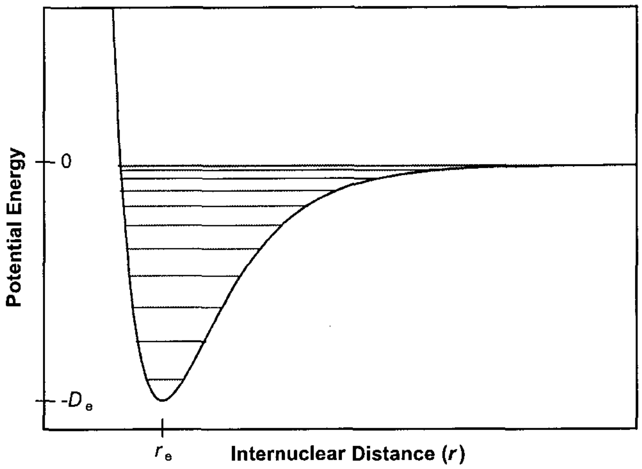

Figure 2.1 Typical diatomic potential energy curve, $V(r)$, and superimposed vibrational levels.

Several mathematical formulae have been used to approximate PECs. Some functions, when sub stituted into (6), return analytical solutions for the rotational and vibrational energy levels of the system.

A *Taylor series* expansion of the potential energy, $V(r)$, about r_e leads to

$$V(r) = V(r_e) + (r - r_e)V'(r_e) + \frac{(r - r_e)^2}{2!}V''(r_e) + \frac{(r - r_e)^3}{3!}V'''(r_e) + \dots \quad (7)$$

The second term is zero. Setting $V(\infty) = 0$ gives $V(r_e) = -D_e$, the dissociation energy from the bottom of the PES; this is often called the *Dunham potential* function:

$$V^{\mathrm{Dun}}(r) = -D_e + \frac{k_2}{2!}(r - r_e)^2 + \frac{k_3}{3!}(r - r_e)^3 + \frac{k_4}{4!}(r - r_e)^4 + \dots \quad (8)$$

where k_i are the i^{th} derivatives of the potential energy evaluated at r_e.

Although accurate if taken to infinite order,[*] the Dunham equation cannot be solved analytically when substituted into (6). Approximate solutions were derived by Dunham and form a basis for interpreting high-resolution spectra. The expression for the rotational and vibrational energy is given by

$$E^{\mathrm{Dun}}(v,J)=\sum_l\sum_m Y_{lm}(v+\tfrac{1}{2})^l[J(J+1)]^m \tag{9}$$

Truncating (8) at the second term results in a parabola centered about r_e, which is the *harmonic oscillator* approximation.

$$V^{\mathrm{HO}}(r)=-D_e+k\frac{(r-r_e)^2}{2!} \tag{10}$$

Solving the Schrödinger equation for the harmonic oscillator results in equally spaced energy levels with spacing ω_e, in cm^{-1}. ω_e is related to k via the reduced mass,[†] μ.

$$G^{\mathrm{HO}}(v)=\omega_e(v+\tfrac{1}{2}) \tag{11}$$

$$\omega_e=\frac{1}{2\pi c}\sqrt{\frac{k}{\mu}} \tag{12}$$

The harmonic approximation is, at best, qualitatively correct near r_e and not suitable for analyzing vibrational progressions. It fails to predict the highly repulsive nature of the PEC at short internuclear separation, fails to account for dissociation at large internuclear separation, and fails to account for the decreasing vibrational energy level spacing and finite number of vibrational levels.

The *Morse function*, (13), is a widely used analytical function that accounts for several failings of the harmonic oscillator potential.[42] The Morse function has three adjustable parameters: a harmonic vibrational constant, ω_e, anharmonic vibrational constant, $\omega_e x_e$,

---

[*] Assuming no interaction between electronic states.

[†] The reduced mass is the effective mass when evaluating intramolecular motion.

and dissociation energy, D_e. These variables are related through (14) and (15), resulting in two independent variables.

$$V^{\mathrm{Morse}}(r) = D_\mathrm{e}\left[1 - \mathrm{e}^{-\beta(r-r_\mathrm{e})}\right]^2 \tag{13}$$

$$\beta = \omega_\mathrm{e}\sqrt{\frac{\pi c \mu}{\hbar D_\mathrm{e}}} \tag{14}$$

$$D_\mathrm{e} = \frac{\omega_\mathrm{e}^2}{4\omega_\mathrm{e}x_\mathrm{e}} \tag{15}$$

If all three parameters have been experimentally determined, the system is overdetermined in this theory. Comparison of the theoretical and experimentally derived parameters can be informative as to the reasonableness of the Morse function. For example, a comparison of $\omega_e x_e$ provides information on the goodness-of-fit in the anharmonic region — a region of spectroscopic interest.

Solving the Schrödinger equation for the Morse potential results in an expression, (16), that accounts for the decreasing spacing between energy levels with increasing υ and the finite number of vibrational energy levels.

$$G^{\mathrm{Morse}}(\upsilon) = \omega_\mathrm{e}(\upsilon + \tfrac{1}{2}) - \omega_\mathrm{e}x_\mathrm{e}(\upsilon + \tfrac{1}{2})^2 \tag{16}$$

This energy expression becomes increasingly inaccurate as the dissociation energy is approached. Extensions of the Morse potential have been developed but have not found general acceptance.

It is unrealistic to believe that a classical function with few variables could represent a quantum mechanical system to infinite accuracy. All of the analytical potentials described above ‘work’ for the system of interest if the intramolecular forces they consider dominate and all other forces are negligible. All become increasingly inaccurate with increasing υ and as the desired accuracy increases.

Alternatively, a numerical potential can be constructed from spectroscopically determined rotational and vibrational constants.[43,44] One implementation is the Rydberg-Klein-Rees

(RKR) method, which determines the classical turning points of the PEC from the spectroscopic data. The resulting PEC is spectroscopically accurate for determining energy level positions and transition intensities. Further, this method intrinsically takes into account interactions between electronic states that perturb the rovibrational levels.

Energy levels

Within the assumption that the wavefunction is separable, (1), there exist expressions for the energy states of the translational, rotational, vibrational, and electronic wavefunctions. Despite this separation, rotational constants do depend on the vibrational and electronic state in which they are found and vibrational constants do depend on their electronic state. Under the assumption of separability, there is no intramolecular conversion from one form to another without the influence of an outside force, such as collisions or photons.

The closeness of the translational energy levels means that a continuum of speeds is observed, not discrete levels. The distribution depends on the experimental conditions.

The expression for the rotational energy levels within a given vibrational state is given by

$$F_\upsilon(J) = B_\upsilon J(J+1) - D_\upsilon J^2(J+1)^2 + H_\upsilon J^3(J+1)^3 + \ldots \tag{17}$$

where J is the rotational quantum number and B_υ, D_υ, etc., are rotational constants for a given vibrational level. In practice, experimental uncertainty and a limited number of observable rotational levels often prevents statistical determination of values beyond D_υ, sometimes only at B_υ. Analytical expressions for the rotational constants can be obtained for some of the model potential energy expressions given above.

The general expression, compared with (11) and (16), for vibrational energy levels within a given electronic state is given by

$$G(\upsilon) = \omega_\mathrm{e}(\upsilon + \tfrac{1}{2}) - \omega_\mathrm{e}x_\mathrm{e}(\upsilon + \tfrac{1}{2})^2 + \omega_\mathrm{e}y_\mathrm{e}(\upsilon + \tfrac{1}{2})^3 + \ldots \tag{18}$$

where $\omega_\mathrm{e}y_\mathrm{e}$, etc., are additional anharmonic vibrational constants. As with rotational constants, statistical determination of values beyond $\omega_\mathrm{e}x_\mathrm{e}$ is infrequent. Analytical expressions for the vibrational constants can be obtained for some of the model potential energy expressions given above.

The electronic energy of the ground state relative to atoms at infinite separation is given by $-D_\mathrm{e}$. Alternatively, the minimum of the ground state PEC can be defined as zero, $T_\mathrm{e} = 0$, and the minimum energy of other electronic states then made relative to the ground state. The latter convention is adopted herein.

The total energy of a given state is the summation of the rotational, vibrational, and electronic components.

$$E(\upsilon,J) = F_\upsilon(J) + G(\upsilon) + T_\mathrm{e} \tag{19}$$

Vibrational transitions

With truncation after the second term, the vibrational energy level spacing is given by

$$\begin{aligned}\Delta G &= G(\upsilon) - G(\upsilon-1)\\ &= \left[\omega_\mathrm{e}(\upsilon+½) - \omega_\mathrm{e}x_\mathrm{e}(\upsilon+½)^2\right] - \left[\omega_\mathrm{e}(\upsilon-½) - \omega_\mathrm{e}x_\mathrm{e}(\upsilon-½)^2\right]\\ &= \omega_\mathrm{e} - 2\upsilon\,\omega_\mathrm{e}x_\mathrm{e}\end{aligned} \tag{20}$$

or, commonly referred to as $\Delta G_{\upsilon+½}$,

$$\Delta G_{\upsilon+½} = G(\upsilon+1) - G(\upsilon) = \omega_\mathrm{e} - 2\,\omega_\mathrm{e}x_\mathrm{e}(\upsilon+1) \tag{21}$$

Figure 2.1 indicates that there are a finite number of bound vibrational levels. The dissociation energy, D_e, is reached when the vibrational spacing becomes zero.* The number of bound vibrational levels, $v_{\max}$, can be derived by setting $\mathrm{d}G/\mathrm{d}v = 0$, resulting in

$$v_{\max} = \frac{\omega_e}{2\,\omega_e x_e} - \frac{1}{2} \tag{22}$$

D_e is determined as the energy of the $v_{\max}$ level:

$$\begin{aligned} D_e = G(v_{\max}) &= \omega_e\left(\frac{\omega_e}{2\,\omega_e x_e}\right) - \omega_e x_e\left(\frac{\omega_e}{2\,\omega_e x_e}\right)^2 \\ &= \frac{\omega_e^2}{4\,\omega_e x_e} \end{aligned} \tag{23}$$

Birge and Sponer developed a graphical method for calculating D_e from $\Delta G_{v+½}$ by plotting $\Delta G_{v+½}$ versus $(v+½)$. The user is able to extrapolate to $\Delta G_{v+½} = 0$ and estimate $v_{\max}$ and D_e. This method is commonly referred to as a linear Birge-Sponer extrapolation.[45] Non-linear behavior at high v is frequently observed with this method, which often results in an overestimate of D_e. If non-linear behavior is evident, non-linear methods can be used to more accurately estimate $v_{\max}$ and D_e.[46]

* An alternate, ***incorrect***, determination of D_e found in some texts involves assuming D_e is reached when the vibrational spacing becomes zero. I.e., (20) is set to zero, giving the number of bound vibrational levels, $v_{\max} = \omega_e/(2\,\omega_e x_e)$. Substitution of $v_{\max}$ into (18) returns

$$\begin{aligned} D_e = G(v_{\max}) &= \omega_e\left(\frac{\omega_e}{2\,\omega_e x_e} + ½\right) - \omega_e x_e\left(\frac{\omega_e}{2\,\omega_e x_e} + ½\right)^2 \\ &= \frac{\omega_e^2}{4\,\omega_e x_e} - \frac{\omega_e x_e}{4} \end{aligned}$$

which differs from (23) by $\omega_e x_e/4$. Although the difference is small, the flaw in the logic is the assumption that there is a vibrational energy level at D_e.

Some texts state that D_e is calculated from

$$D_e = \sum_{v=0}^{v=v_{\max}} \Delta G_{v+½}$$

which returns the same value in error by $\omega_e x_e/4$, for the same reason.

Effect of isotope substitution on vibrational energy levels

A change in the mass of one or both nuclei, through the addition or removal of a neutron, does not affect the potential field in which the electrons move.* Thus, the potential energy diagram of a species is independent of the isotopic mass of the nuclei. However, the energy required to move the nuclei within this potential well *is* dependent on their mass. The harmonic energy, ω_e in (11), is dependent on its isotopic mass through the reduced mass, μ. By changing one or more isotopic masses, we find that ω_e changes by a factor ρ, the isotopic ratio.

$$\rho = \frac{\omega_e^i}{\omega_e} = \sqrt{\frac{\mu}{\mu^i}} \qquad \omega_e^i = \rho\,\omega_e \qquad (24)$$

Noting that D_e is independent of the isotopic mass, we find a relationship between ω_e and $\omega_e x_e$ through Equations (23) and (24).

$$D_e = \frac{\omega_e^2}{4\,\omega_e x_e} = \frac{\omega_e^{i\,2}}{4\,\omega_e x_e^i} \qquad \omega_e x_e^i = \rho^2\,\omega_e x_e \qquad (25)$$

The trend shown in (24) and (25) extends to higher order vibrational anharmonic terms as well.[48] Substitution into (18) leads to the following expression for estimating the position of isotopically substituted vibronic transitions. The change in the transition energy for vibrational and vibronic transitions, calculated in (27) and (29), is useful for identifying the composition of a compound and assigning v to the progression.

$$G^i(v) = \rho\,\omega_e\,(v + \tfrac{1}{2}) - \rho^2\,\omega_e x_e\,(v + \tfrac{1}{2})^2 + \rho^3\,\omega_e y_e\,(v + \tfrac{1}{2})^3 + \ldots \qquad (26)$$

---

* An electronic isotope effect does exist when the ψ_e and ψ_v are not separable (breakdown of the Born-Oppenheimer approximation). This is most pronounced for bonds to hydrogen, where the electronic shift of the zero point energy (zpe) is up to 20 cm^{-1}. Coupling of ψ_e and ψ_v is not linear, and an electronic isotope effect is not observed for bonds not involving hydrogen, which is the case herein.[47]

$$\begin{aligned}\Delta G^{\text{iso}}(\upsilon) &= G(\upsilon) - G^{i}(\upsilon)\\ &= \left[\omega_{\text{e}}\left(\upsilon+\tfrac{1}{2}\right) - \omega_{\text{e}}x_{\text{e}}\left(\upsilon+\tfrac{1}{2}\right)^{2}\right] - \left[\rho\,\omega_{\text{e}}\left(\upsilon+\tfrac{1}{2}\right) - \rho^{2}\,\omega_{\text{e}}x_{\text{e}}\left(\upsilon+\tfrac{1}{2}\right)^{2}\right]\\ &= (1-\rho)\omega_{\text{e}}\left(\upsilon+\tfrac{1}{2}\right) - \left(1-\rho^{2}\right)\omega_{\text{e}}x_{\text{e}}\left(\upsilon+\tfrac{1}{2}\right)^{2}\end{aligned} \qquad (27)$$

Vibronic transitions

Transitions between electronic states can readily be addressed as an extension of the discussion of **Vibrational transitions** by the addition of T_{e} to the formulae. Each bound electronic state has a vibrational progression determined by the geometry of the PES.* Because the vibrational and rotational constants are state dependent: one convention is to ascribe a double-prime (") to constants of the lower electronic state and a prime (') to constants of the upper electronic state.

From (19), the vibronic transition energy can be expressed as

$$\begin{aligned}\Delta E &= E'(\upsilon,J=0) - E''(\upsilon,J=0)\\ &= \left[G'(\upsilon)+T_{e}'\right] - \left[G''(\upsilon)+T_{e}''\right]\end{aligned} \qquad (28)$$

There is no restriction on the change in vibrational quantum number during electronic transitions. The effect of isotopic substitution on a vibronic transition, assuming no electronic isotope effect,† becomes

$$\begin{aligned}\Delta E^{\text{iso}} &= \left[\left(T_{\text{e}}'+G'(\upsilon)\right) - \left(T_{\text{e}}''+G''(\upsilon)\right)\right] - \left[\left(T_{\text{e}}'^{i}+G'^{i}(\upsilon)\right) - \left(T_{\text{e}}''^{i}+G''^{i}(\upsilon)\right)\right]\\ &= \left(T_{\text{e}}'-T_{\text{e}}'^{i}\right) - \left(T_{\text{e}}''-T_{\text{e}}''^{i}\right) + \Delta G'^{\text{iso}}(\upsilon) - \Delta G''^{\text{iso}}(\upsilon)\\ &= 0-0+\left[(1-\rho)\omega_{\text{e}}'\left(\upsilon'+\tfrac{1}{2}\right) - \left(1-\rho^{2}\right)\omega_{\text{e}}x_{\text{e}}'\left(\upsilon'+\tfrac{1}{2}\right)^{2}\right]\\ &\quad -\left[(1-\rho)\omega_{\text{e}}''\left(\upsilon''+\tfrac{1}{2}\right) - \left(1-\rho^{2}\right)\omega_{\text{e}}x_{\text{e}}''\left(\upsilon''+\tfrac{1}{2}\right)^{2}\right]\\ &= (1-\rho)\left[\omega_{\text{e}}'\left(\upsilon'+\tfrac{1}{2}\right) - \omega_{\text{e}}''\left(\upsilon''+\tfrac{1}{2}\right)\right] - \left(1-\rho^{2}\right)\left[\omega_{\text{e}}x_{\text{e}}'\left(\upsilon'+\tfrac{1}{2}\right)^{2} - \omega_{\text{e}}x_{\text{e}}''\left(\upsilon''+\tfrac{1}{2}\right)^{2}\right]\end{aligned} \qquad (29)$$

---

* And each vibrational level has a rotational progression.

† See the footnote on page 13.

For the v'–0 transitions, (29) reduces to

$$\begin{aligned}
\Delta E^{\mathrm{iso}}(v-0) &= (1-\rho)\left[\omega_{\mathrm{e}}'(v'+\tfrac{1}{2})-\frac{1}{2}\omega_{\mathrm{e}}''\right]-(1-\rho^2)\left[\omega_{\mathrm{e}}x_{\mathrm{e}}'(v'+\tfrac{1}{2})^2-\frac{1}{4}\omega_{\mathrm{e}}x_{\mathrm{e}}''\right]\\
\Delta E^{\mathrm{iso}}(3-0) &= (1-\rho)\left(\frac{7}{2}\omega_{\mathrm{e}}'-\frac{1}{2}\omega_{\mathrm{e}}''\right)-(1-\rho^2)\left(\frac{49}{4}\omega_{\mathrm{e}}x_{\mathrm{e}}'-\frac{1}{4}\omega_{\mathrm{e}}x_{\mathrm{e}}''\right)\\
\Delta E^{\mathrm{iso}}(2-0) &= (1-\rho)\left(\frac{5}{2}\omega_{\mathrm{e}}'-\frac{1}{2}\omega_{\mathrm{e}}''\right)-(1-\rho^2)\left(\frac{25}{4}\omega_{\mathrm{e}}x_{\mathrm{e}}'-\frac{1}{4}\omega_{\mathrm{e}}x_{\mathrm{e}}''\right)\\
\Delta E^{\mathrm{iso}}(1-0) &= (1-\rho)\left(\frac{3}{2}\omega_{\mathrm{e}}'-\frac{1}{2}\omega_{\mathrm{e}}''\right)-(1-\rho^2)\left(\frac{9}{4}\omega_{\mathrm{e}}x_{\mathrm{e}}'-\frac{1}{4}\omega_{\mathrm{e}}x_{\mathrm{e}}''\right)\\
\Delta E^{\mathrm{iso}}(0-0) &= (1-\rho)\left(\frac{1}{2}\omega_{\mathrm{e}}'-\frac{1}{2}\omega_{\mathrm{e}}''\right)-(1-\rho^2)\left(\frac{1}{4}\omega_{\mathrm{e}}x_{\mathrm{e}}'-\frac{1}{4}\omega_{\mathrm{e}}x_{\mathrm{e}}''\right)
\end{aligned} \tag{30}$$

From (30), it is apparent that the magnitude of the shift depends on the isotopic ratio, (24), and on the differences in vibrational quanta and the difference between $\{\omega_{\mathrm{e}}'', \omega_{\mathrm{e}}'\}$ and $\{\omega_{\mathrm{e}}x_{\mathrm{e}}'', \omega_{\mathrm{e}}x_{\mathrm{e}}'\}$. In the absence of a large difference in these parameters, there is no shift in the 0–0 transition but an increasing shift with increasing Δv.

Electronic transitions

The interaction of a system with electromagnetic radiation, $\mathscr{E}$, can be treated as a perturbation on the system if the radiation is weak. $\hat{\mathscr{H}}'$ moderates the interaction of the external electric ($\boldsymbol{E}_0$) or magnetic ($\boldsymbol{B}_0$) field and the respective moments, $\boldsymbol{\mu}$,* within the molecule.

$$\hat{\mathscr{H}}' = \mathscr{E}\boldsymbol{\mu} \tag{31}$$

The *transition moment*, *M*, between initial state *m* and final state *n* is defined as

$$\boldsymbol{M}_{nm} = \int \Psi_n^* \boldsymbol{\mu} \Psi_m \,\mathrm{d}\tau = \langle \Psi_n | \boldsymbol{\mu} | \Psi_m \rangle \tag{32}$$

---

* μ represent moments in general and the dipole moment.

and the *line strength*, *S*, as the square of the transition moment.

$$S_{nm} = |\boldsymbol{M}_{nm}|^2 = |\langle \Psi_n | \boldsymbol{\mu} | \Psi_m \rangle|^2 \tag{33}$$

Electric moments

Molecules contain a separation of charge by virtue of the spatial location of the electrons and nuclei. An electrical potential, $V(\tau)$, is established within the molecule. The potential can be expanded as

$$\begin{aligned} V(\tau) &= V_0 + \sum_i \tau_i \left.\frac{\partial V}{\partial \tau_i}\right|_0 + \sum_i \sum_j \frac{\tau_i \tau_j}{2!} \left.\frac{\partial^2 V}{\partial \tau_i \partial \tau_j}\right|_0 + \dots \\ &= V_0 + V'_x x + V'_y y + V'_z z + \frac{V''_{xx} x^2}{2!} + \frac{V''_{xy} xy}{2!} + \dots \end{aligned} \tag{34}$$

With the classical potential energy of the distribution given by,

$$E = \sum_i q_i V(x_i, y_i, z_i) \tag{35}$$

A transition between states occurs when there is a resonance between an intramolecular process of energy E and an external electromagnetic field of energy $\boldsymbol{E}_0$. Substitution of (34) into (35) gives

$$E = V_0 \sum_i q_i + V'_x \sum_i q_i x_i + V'_y \sum_i q_i y_i + V'_z \sum_i q_i z_i + \frac{V''_{xx}}{2} \sum_i \sum_j q_i x_i^2 + \dots \tag{36}$$

The moments of the charge distribution can be defined from (36) as

$$q = \sum_i q_i \qquad \text{zeroth moment (total charge)} \tag{37}$$

$$\mu = \begin{pmatrix} \mu_x \\ \mu_y \\ \mu_z \end{pmatrix} = \begin{pmatrix} \sum_i q_i x_i \\ \sum_i q_i y_i \\ \sum_i q_i z_i \end{pmatrix} \qquad \text{first moment (dipole)} \tag{38}$$

$$\boldsymbol{Q} = \begin{pmatrix} Q_{xx} & Q_{xy} & Q_{xz} \\ Q_{yx} & Q_{yy} & Q_{yz} \\ Q_{zx} & Q_{zy} & Q_{zz} \end{pmatrix} \qquad Q_{mn} = \sum_i \sum_j q_i\, q_j\, m_i\, n_j \quad \text{second moment (quadrupole)} \tag{39}$$

In general, the line strength of each successive moment decreases. However, some situations exist where a given moment has zero magnitude because of symmetry: D_{nh}, T_d, O_h, I_h.

In the Born-Oppenheimer approximation, each moment can be divided into electronic and nuclear components. For the dipole moment,

$$\mu = \mu_{\text{elec}} + \mu_{\text{nuc}} \tag{40}$$

Electric dipole transitions

Application of (1) and (40) to (32) and returning to conventional spectroscopic notation results in

$$\begin{aligned} \boldsymbol{M}_{nm} &= \left\langle \Psi'_{\text{elec}}\, \Psi'_{\text{nuc}} \middle| \boldsymbol{\mu}_{\text{elec}} + \boldsymbol{\mu}_{\text{nuc}} \middle| \Psi''_{\text{elec}}\, \Psi''_{\text{nuc}} \right\rangle \\ &= \left\langle \Psi'_{\text{elec}} \middle| \boldsymbol{\mu}_{\text{elec}} \middle| \Psi''_{\text{elec}} \right\rangle \left\langle \Psi'_{\text{nuc}} \middle| \Psi''_{\text{nuc}} \right\rangle + \left\langle \Psi'_{\text{elec}} \middle| \Psi''_{\text{elec}} \right\rangle \left\langle \Psi'_{\text{nuc}} \middle| \boldsymbol{\mu}_{\text{nuc}} \middle| \Psi''_{\text{nuc}} \right\rangle \end{aligned} \tag{41}$$

Orthogonality of wavefunctions makes the first term zero when considering transitions within a single electronic state and the second term zero when considering transitions between different electronic states. This is the basis for UV/visible (rovibronic) and infrared (rotational and rovibrational) transitions, respectively.

Expansion of $\boldsymbol{M}_{nm}$ for vibronic transitions results in

$$\begin{aligned} \boldsymbol{M}_{nm} &= \left\langle \psi'_{\text{e}}\, \psi'_{\text{s}} \middle| \boldsymbol{\mu}_{\text{elec}} \middle| \psi''_{\text{e}}\, \psi''_{\text{s}} \right\rangle \left\langle \psi'_{\text{t}}\, \psi'_{\text{r}}\, \psi'_{\text{v}}\, \psi'_{\text{I}} \middle| \psi''_{\text{t}}\, \psi''_{\text{r}}\, \psi''_{\text{v}}\, \psi''_{\text{I}} \right\rangle \\ &= \left\langle \psi'_{\text{e}} \middle| \boldsymbol{\mu}_{\text{elec}} \middle| \psi''_{\text{e}} \right\rangle \left\langle \psi'_{\text{s}} \middle| \psi''_{\text{s}} \right\rangle \left\langle \psi'_{\text{t}} \middle| \psi''_{\text{t}} \right\rangle \left\langle \psi'_{\text{r}} \middle| \psi''_{\text{r}} \right\rangle \left\langle \psi'_{\text{v}} \middle| \psi''_{\text{v}} \right\rangle \left\langle \psi'_{\text{I}} \middle| \psi''_{\text{I}} \right\rangle \end{aligned} \tag{42}$$

The translational, rotational, and nuclear overlap integrals are independent of the PESs and integrate to unity. The resulting line strength, from (33), is

$$S_{nm} = \left|\langle \psi'_{\mathrm{e}} | \mu_{\mathrm{elec}} | \psi''_{\mathrm{e}} \rangle\right|^2 \left|\langle \psi'_{\mathrm{s}} | \psi''_{\mathrm{s}} \rangle\right|^2 \left|\langle \psi'_{\mathrm{v}} | \psi''_{\mathrm{v}} \rangle\right|^2 \tag{43}$$

The first term is the electronic transition dipole moment operator, M_{e}. M_{e} is dependent on the atomic coordinates of the nuclei; however, M_{e} changes slowly and is assumed to be constant in the region bounding Ψ''. Failure of this assumption leads to a breakdown of the Born-Oppenheimer approximation since $\psi_{\mathrm{e}}\psi_{\mathrm{v}}$ are no longer separable.

The spin overlap integral is unity if the spin is unchanged and zero if the spin changes during the transition. This is valid only if the total spin quantum number, S, commutes with the Hamiltonian (i.e., it is a good quantum number). Inclusion of additional terms, such as spin-orbit coupling, results in S not commuting with $\hat{\mathscr{H}}$, and transitions with $\Delta S \neq 0$ occurring. This is the case with the RhO transitions in question: $^2\Pi - {}^4\Sigma^-$.

The vibrational overlap integral is non-zero since the vibrational wavefunctions belong to different PESs. Their overlap is highly dependent on the shape of the PES and the specific vibrational quantum numbers involved in the transition, ranging from zero to unity for varying combinations. $\left|\langle \psi'_{\mathrm{v}} | \psi''_{\mathrm{v}} \rangle\right|^2$ is known as the *Franck-Condon factor*, and is a dominant factor in (43).

Excited state lifetimes

The lifetime, τ, of an excited state provides information about the nature of the state and on competing relaxation processes. Lifetime measurements, used in conjunction with methods that probe individual state-to-state processes, provide complementary information to validate vibronic assignments.

Spontaneous emission is a unimolecular process. The intensity, I, follows a single-exponential profile.

$$I(t) = I_0 \mathrm{e}^{\frac{-t}{\tau}} \tag{44}$$

where I_0 is the emission intensity at $t = 0$ and τ is the lifetime of the excited state. If multiple processes are occurring on approximately the same timescale (similar lifetimes), the intensity will be the product of multiple unimolecular processes.

$$I(t) = I_0 \prod_i \mathrm{e}^{\frac{-t}{\tau_i}} \tag{45}$$

Such processes include emission to multiple states, predissociation, and internal conversion. The observed lifetime would be

$$\frac{1}{\tau_{\text{obs}}} = \frac{1}{\tau_a} + \frac{1}{\tau_b} + \ldots \tag{46}$$

The radiative lifetime, τ_{nm}, line strength, S_{nm}, and Einstein spontaneous emission coefficient (A coefficient), A_{nm}, are related through (47) for electric dipole transitions (see Reference 49 for a broader discussion on this topic).

$$\frac{1}{\tau_{nm}} = A_{nm} = \frac{16\pi^3}{3h\varepsilon_0 \lambda_{nm}^3} S_{nm} \tag{47}$$

Lifetime determination

In practice, corrections are made for complications arising from the laser pulse duration and response time of the detection system. The response time approximates a unimolecular process and can be accounted for by adding another term with fixed τ_{detector}. Correction for the laser pulse duration requires that (45) be convoluted by the laser pulse form or the observed signal be deconvoluted accordingly. If the pulse form is assumed to be gaussian, the convolution can be expressed as[50]

$$\begin{aligned} I(t) &= \frac{I_0}{\sqrt{4\pi a}} \int_0^\infty \mathrm{e}^{-\frac{t'}{\tau}} \mathrm{e}^{\frac{-(t-t')^2}{2a^2}} \mathrm{d}t' \\ &= \frac{I_0}{\sqrt{4\pi a}} \mathrm{e}^{\frac{-t}{\tau}} \operatorname{erfc}\left(\frac{2a^2}{\tau} - \frac{t}{a^2}\right) \end{aligned} \tag{48}$$

where a is the standard deviation of the laser pulse and erfc is the complementary error function defined by

$$\mathrm{erfc}(x) = 1 - \mathrm{erf}(x) = \frac{2}{\sqrt{\pi}} \int_x^{\infty} \mathrm{e}^{-\mathrm{x}^2} \mathrm{d}x \qquad (49)$$

3. EXPERIMENTAL SETUP

Laser ablation has become a standard method of rapidly converting detectable quantities of a solid to the gas phase. From metals to proteins, solids have been prepared for analysis, quantification, or further reaction. Fundamental research has adopted this technology to prepare metal clusters and metal compounds. In this laboratory, a Nd:YAG laser vaporized rhodium metal, creating a metal plume into a pulsed molecular beam that contained one or more reactive gases. The reactant gas(es) was activated (dissociated) by the laser and ablated metal. Reaction occurred as the carrier gas transported the metal vapor and reactant gases through a channel. In the channel, the metal vapor thermalized with the gas, to around room temperature, and reacted to form metal clusters and compounds. The carrier gas and reaction mixture further cooled during an unskimmed supersonic expansion into a high vacuum chamber. Translation carried the reaction mixture into the analysis region. A second Nd:YAG laser pumped a tunable dye laser to excite rovibronic transitions in the species present. Emission from the laser-excited compounds was collected, filtered with a monochromator, and detected on a photomultiplier tube (PMT). The signal was digitized on a digital storage oscilloscope and transferred to a computer for storage and post-processing. Figure 3.1 schematically shows the experimental setup used in this laboratory. Each component is detailed below.

Experimental components

Pulsed molecular beam source

The reactant gas mixture was prepared by diluting $^{16}O_2$ (PraxAir, 99.9 %) and/or $^{18}O_2$ (Cambridge Isotope Labs., 98 %) with sufficient helium (PraxAir, 99.9995 %) to prepare an approximately five percent mixture in a ten liter glass bulb. The pressure inside the bulb was initially 1.5 to 2.0 atm. and used until the pressure dropped below 1.0 atm. Teflon tubing carried the gas to the nozzle.

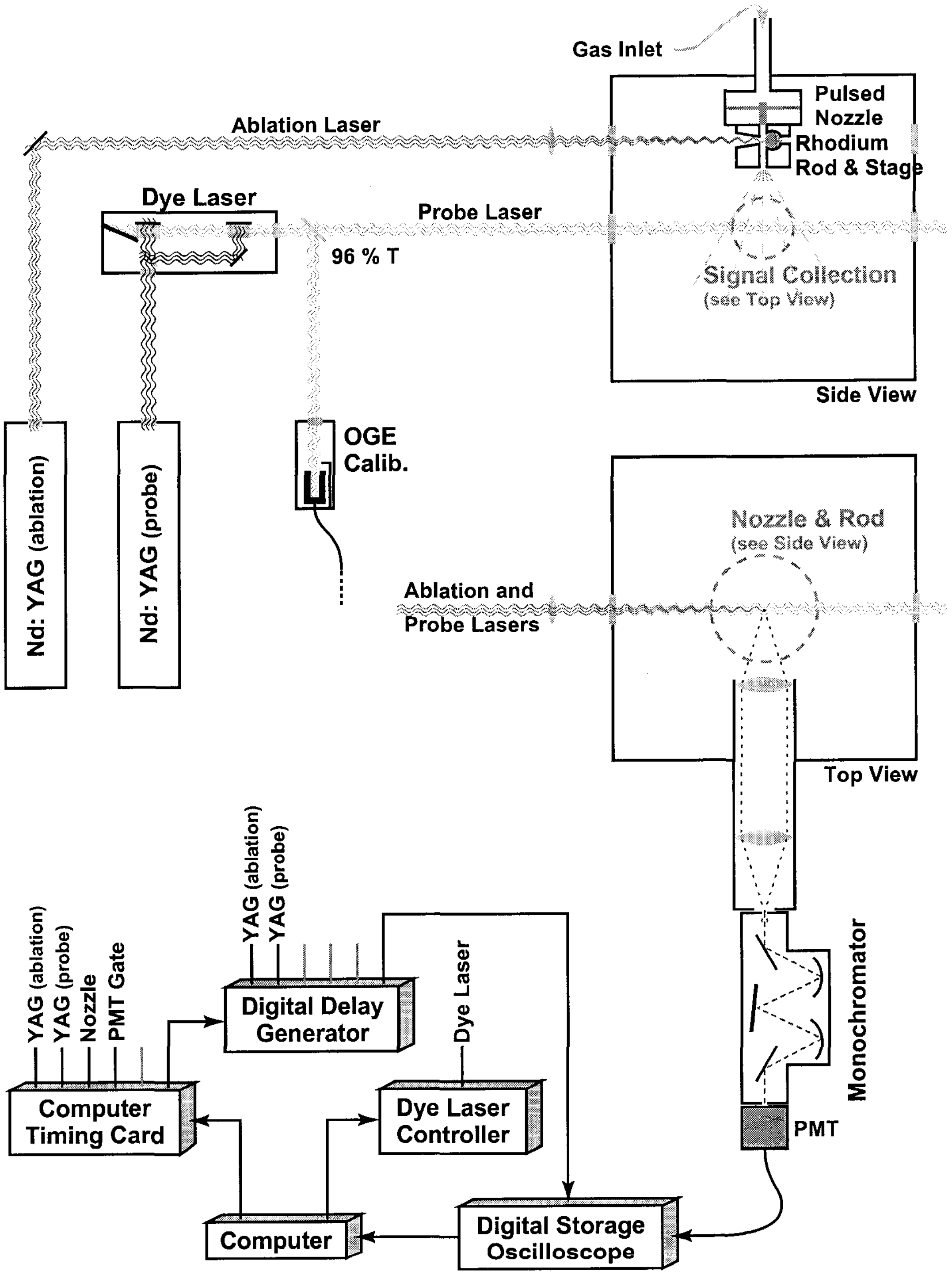

Figure 3.1 Experimental setup for collection of LIF and DF. The optogalvanic calibration experiment is discussed on page 55.

The nozzle follows a standard design by Proch and Trickl.[51] It consisted of a valve stem mounted to the center of a piezoelectric disk (Physik Instrument, P286.20). The gas mixture is contained in the volume surrounding the piezoelectric disk and valve stem. The valve stem covers a 0.5 mm orifice joining the interior of the nozzle and the high vacuum chamber. The piezo crystal was triggered by the computer, which activated a pulsed variable voltage (0 to 1 000 VDC), variable duration (0 to 700 μs), and variable delay (0 to 360 μs) circuit. The valve stem was adjusted to keep the voltage required to lift it below 400 volts, which increased the longevity of the crystal. A trade-off exists between the volume of gas and the background pressure in the vacuum chamber and the load on the diffusion pump. Importantly, more gas does *not* mean greater signal since the amount of metal ablated is the limiting factor. The background pressure controls the degree of cooling during expansion; pumping speed was controlled to obtain spectra at increased temperatures. The pulse duration was nominally 350 μs and optimized by monitoring the LIF signal. The delay was always zero since it could be centrally controlled from the computer. Below the nozzle was mounted the laser ablation assembly.

Laser ablation assembly

Three mutually perpendicular holes allow for the intersection of the reactant gas stream, metal rod, and ablation laser beam (see the Side View of the vacuum chamber in Figure 3.1). Perpendicular to the nozzle orifice was a 2.0 mm channel that directed the expanding gases past the rhodium rod. The channel length beyond the rod was variable, allowing for different residence/reaction times between the gas and metal after ablation. A 17 mm channel was used to generate RhO since it was observed that the yield of RhO depended on the length of the channel beyond the ablation region. The 17 mm channel had generated high yields of RhO during previous experiments in our laboratory. The rotating and translating rhodium rod (5.0 mm diameter × 30.0 mm; 99.9 % purity; Goodfellow) was mounted perpendicular to the gas channel. The rod was 2.5 mm off-axis to allow the gas to pass unimpeded past the rod, and simultaneously rotated and translated by a stepping motor operating at between 15 and 20 Hz. The motor was mounted inside the vacuum chamber. The second harmonic (532 nm) of a Continuum NY61 Nd:YAG was focussed onto the surface of the rod by a convex lens (50 cm focal length). Between 50 and 100 mJ/pulse and a nominal pulse duration of 8 ns ablated the metal rod and created a plasma in the local carrier gas volume. The laser was timed to coincide with approximately the center of the carrier gas volume. The surrounding carrier gas swept the plasma into the reaction channel, allowing for continued reaction and thermalization of the plasma. The products cooled during a supersonic expansion into the high vacuum chamber. Both laser power and timing were optimized for maximum product yield. The optimum laser power was below the maximum of the laser; with maximum power, the plasma did not quench in the reaction channel and was observable in emission immediately after expansion. No spectra could be recorded under these conditions.

The high vacuum chamber consisted of a 30×30×30 cm^3 cubic aluminum housing, pumped by an Edwards Diffstack 160 diffusion pump and an Edwards E2M8 mechanical backing pump. Pressure inside the chamber was monitored with a Granville-Phillips 270006 ion gauge. The background pressure was typically 10^{-6} Torr (1 Torr = 1 mmHg = 1/760 atm.). In operation, the pressure increased by a factor of 10 to 100, depending on the molecular beam volume. The nozzle, optical ports, and collection optics were mounted to other faces of the vacuum chamber as shown in Figure 3.1.

Detection & data collection

A Lumonics YM600 Nd:YAG laser operating at 355 nm pumped a Lumonics HD-300 tunable dye laser (probe laser), which intersected the supersonic molecular beam perpendicularly. This laser was timed to probe the products created in the ablation mixture as they passed through the optical path of the emission detection system. The region from 380 to 700 nm was scanned using a series of laser dyes (Exciton Inc.: Exalite 389, 398, 404, 416, and 428; LD 390; Stilbene 420; Coumarin 440, 450, 460, 480, and 485; Rhodamine 590, 610, and 640; Kiton Red 620; and DCM). Emission was collected perpendicular to both beams by two 5.0 cm diameter × 7.5 cm focal length lenses and imaged onto the entrance of a Jobin-Yvon H20 monochromator. A Hamamatsu R1477 photomultiplier converted the photon intensity to an electrical signal. (See Appendix B for a discussion of the optical setup.)

The signal was digitized with a Tektronics 2440 digital storage oscilloscope and transferred to a personal computer. The computer was equipped with a GPIB board and an

Advantech PCL-830 timer card. In-house software controlled the system timing and data collection. Detailed timing sequences are shown in Figure 3.2 and 3.3. The digitized signal is the emission decay profile (Figure 4.4 on page 47). Software processing allowed for user-selectable region(s) of the decay profile to be extracted and plotted against alternative axes, such as dye laser wavelength, pump laser wavelength, or time. The dye laser wavelength was corrected as described in Appendix C.

Typical instrument settings are given in Appendix D.

Experimental details

Laser-induced fluorescence[*,†]

LIF provides information on rovibrational energy levels of the molecular ground and excited states. LIF records emission as a function of probe laser wavelength. Demtröder[52] and Andrews[53] have summarized some of the standard LIF techniques as well as recent developments. In our experiments, the monochromator usually passed the zeroth order (all emission) but was sometimes set to detect emission to an excited ground state vibrational level to filter overlapping electronic bands (wavelength filtering). With a fully open aperture, the monochromator bandpass was ≈ 100 cm^{-1} in the visible region, sufficiently wide to encompass an entire RhO band. Alternatively, for bands with different excited state lifetimes, different regions of the emission decay could be recorded and mathematically scaled to isolate individual bands (lifetime filtering).[54]

For a given laser dye, a low-resolution scan over the entire dye curve identified the bands in that region. Individual bands were subsequently scanned at higher resolution, typically 0.001 nm, with five to fifteen laser shots averaged per wavelength. Optogalvanic spectroscopy of an iron-neon hollow cathode lamp was used to fine-tune the probe dye laser's internal calibration (see Appendix C).

---

[*] The terms 'laser-induced fluorescence' and 'dispersed fluorescence' are standard in the science and will be used herein, however, the reader should note that the transition in question has been shown to be spin-forbidden in nature, i.e., phosphorescence.

Computer Controlled Timer Board (1 µs resolution)

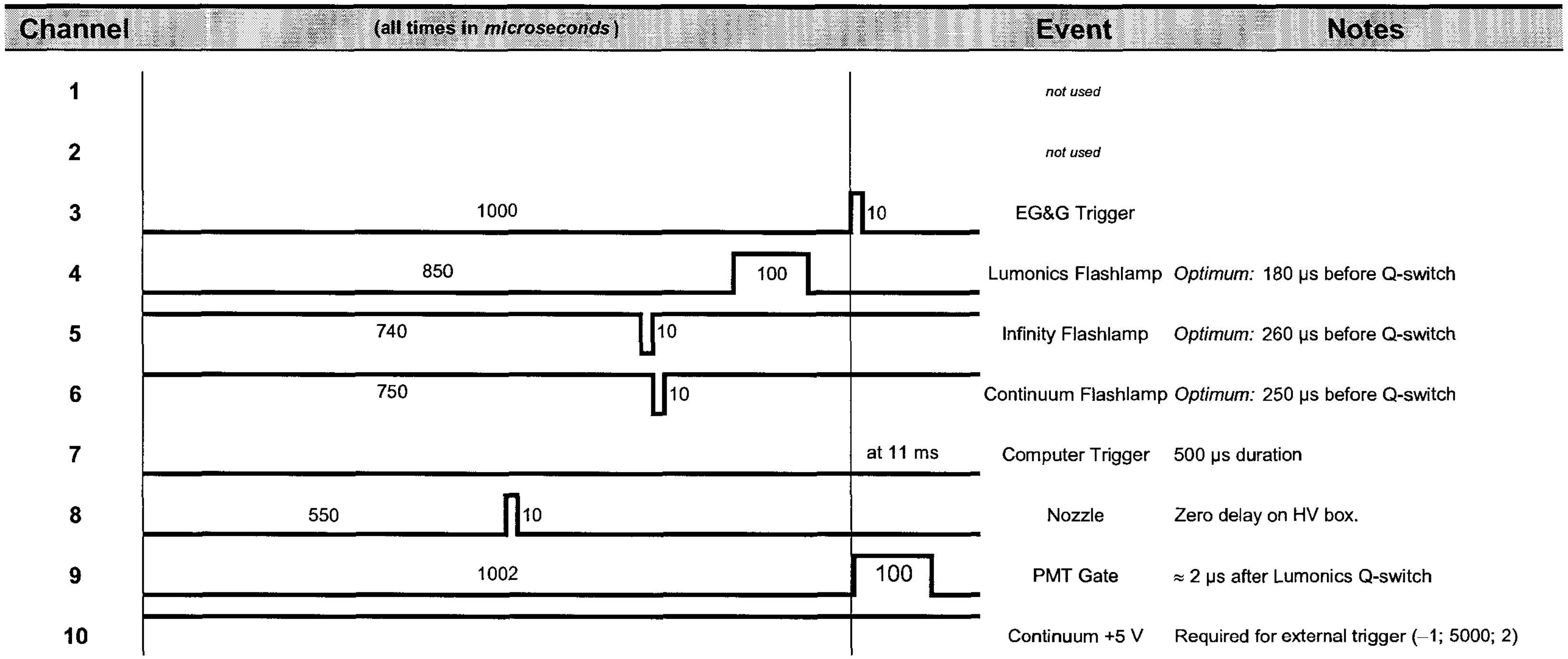

Channel	(all times in *microseconds*)	Event	Notes
1		*not used*	
2		*not used*	
3	1000 10	EG&G Trigger	
4	850 100	Lumonics Flashlamp	*Optimum:* 180 µs before Q-switch
5	740 10	Infinity Flashlamp	*Optimum:* 260 µs before Q-switch
6	750 10	Continuum Flashlamp	*Optimum:* 250 µs before Q-switch
7	at 11 ms	Computer Trigger	500 µs duration
8	550 10	Nozzle	Zero delay on HV box.
9	1002 100	PMT Gate	≈ 2 µs after Lumonics Q-switch
10		Continuum +5 V	Required for external trigger (–1; 5000; 2)

Figure 3.2 Timing signals for the computer timing card. Time zero is the left vertical dashed line with time increasing to the right. The right vertical dashed line corresponds to the rising edge of the timing pulse sent to the digital delay generator (see Figure 3.3). The delay, duration, and pulse direction are indicated. All voltage pulses are 5 V. Some timing signals were not used in the experiments but are included for completeness.

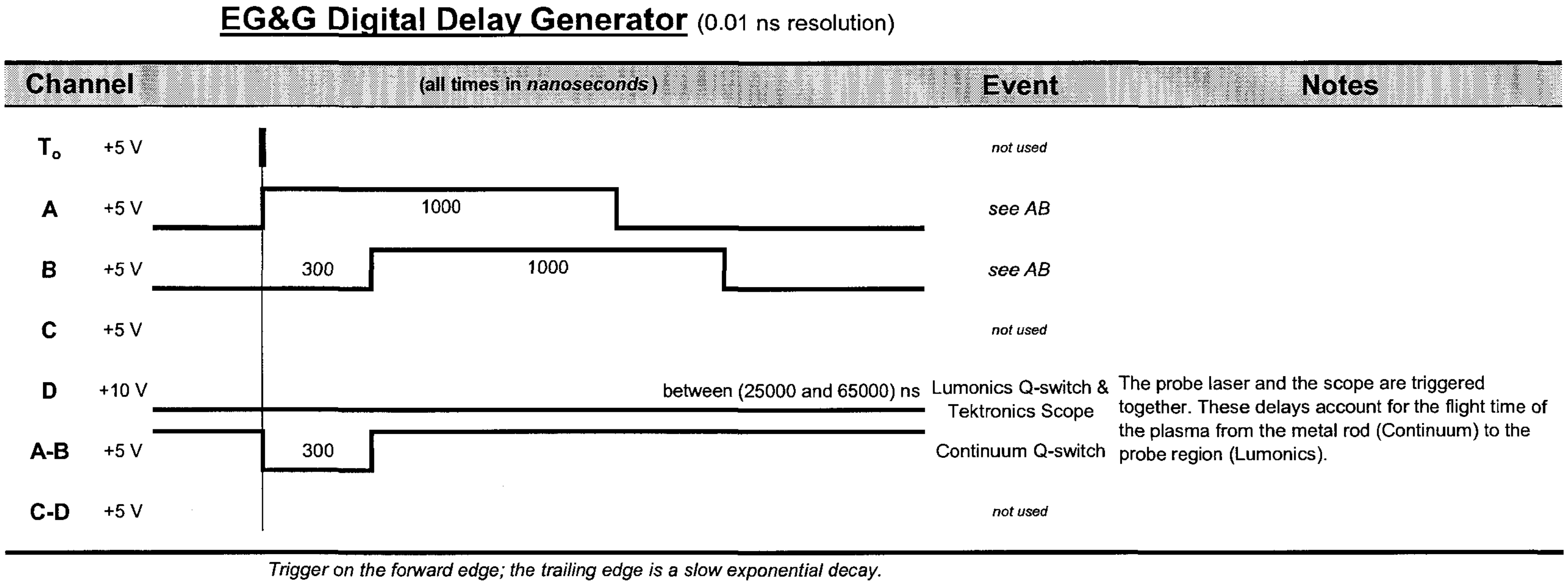

The probe laser and the scope are triggered together. These delays account for the flight time of the plasma from the metal rod (Continuum) to the probe region (Lumonics).

Figure 3.3 Timing signals for the digital delay generator. The left vertical dashed line is time zero supplied by the computer timing card (see Figure 3.2). The delay, duration, magnitude, and pulse direction are indicated.

Dispersed fluorescence*,†

DF provides information on the vibrational levels in the ground state and on other low-lying electronic states. Whereas LIF considers the total emission intensity, DF considers the wavelength(s) at which emission is occurring. The DF intensity depends on the overlap of the vibrational wavefunctions (Franck-Condon factor), (43). In this setup, the probe laser was tuned to a strong rovibronic transition and then the monochromator scanned from above the probe laser wavelength to longer wavelengths. This allows for the detection of hot transitions and provides an internal calibration. A secondary calibration was obtained by allowing the monochromator to scan to sufficiently long wavelengths that second order dispersion was observed. Five to fifteen probe laser shots were averaged per monochromator step. A 0.5 mm aperture yielded a bandpass of ≈ 20 cm^{-1} and was a compromise between signal and resolution. The precision of the band center was ± 2 cm^{-1} and found by fitting the band to a gaussian function, which determined the mass-weighted band center irrespective of the actual profile. We estimate the accuracy of the DF spectral intervals to be ± 15 cm^{-1}.

Excited state lifetimes†

Intensity-decay profiles were obtained by tuning the probe laser to a rovibronic transition and then recording the unaltered decay profile (intensity vs. time). Up to 500 probe laser shots were averaged for each transition. Typically, three to five lifetime measurements were averaged to give a band-averaged lifetime. The precision of a typical profile was ± 5 ns whereas the precision of the band-averaged lifetime was ± 100 ns (taken as the standard deviation of the individual measurements).

[†] LIF, DF, and lifetime experiments were conducted separately. It is possible to design an experiment where all three are recorded simultaneously using a streak camera. Apart from the initial expense (200 000 USD), such a system would allow for rapid data collection and provide more versatility for data processing. Large data-storage capabilities would be required: a single image would represent excitation at a single probe laser wavelength and could be 10 MB; thousands of images would comprise a single band.

4. RESULTS AND DISCUSSION

Laser-induced fluorescence experiments

Laser-induced fluorescence (LIF) on RhO was recorded from 380 to 700 nm and is displayed in Figure 4.1, which is a composite of the survey scans. It is evident that the visible and UV regions are rich with RhO bands of varying profile and intensity. It is easy to envision that these bands, at higher temperatures, would overlap and form an unresolvable array of transitions, as originally recorded in thermal ovens.[24] Isotopic substitution experiments identified the vibrational quantum number involved in each feature in accordance with (29). When the transitions originate from $\upsilon'' = 0$, such as in LIF experiments, (29) simplifies to (30). These isotopic experiments identified four transitions between 615 and 640 nm that had small isotopic shifts and were assigned as 0–0 bands. Rotational analysis identified and labeled these transitions as the origins of the [15.8] $^2\Pi_r - X^4\Sigma^-$ and [16.0] $^2\Pi_r - X^4\Sigma^-$ progressions (*vide supra*).[25] Isotopic substitution directly identified $\upsilon' = 0, 1, 2$ and allowed for extrapolative assignment up to $\upsilon' = 4$ in each of the progressions. The certainty of the assignment decreases for $\upsilon' \geq 3$ because of additional features in the region below 550 nm. In addition, several transitions from $\upsilon'' = 1$ were observed.

Band centers for the transitions between 500 and 650 nm are summarized in Table 4.1. Some transitions below 550 nm and all below 500 nm have not been assigned to the current $^2\Pi$ progressions due to overlapping bands and weak band-intensities. They are likely transitions to other electronic states of RhO. Transitions in other species seem unlikely since no impurity spectra were identified throughout the many studies completed with this rhodium rod.

The signal intensity in Figure 4.1 is a function of the ablation and pump laser powers, dye efficiency, carrier gas mixture, spectral response of the PMT, and Franck-Condon factor. Despite this, it is possible to estimate the relative Franck-Condon overlap from the signal to noise ratio in Figure 4.1. Transitions to $\upsilon' = 0$ and 1 are significantly more intense than transitions to higher vibrational levels. The best overlap is obtained for transitions to $\upsilon' = 1$, indicating that the ground and excited electronic states do not have the same r_e. This supports the rotation analysis,[25] which found r_e as given in Table 4.2.

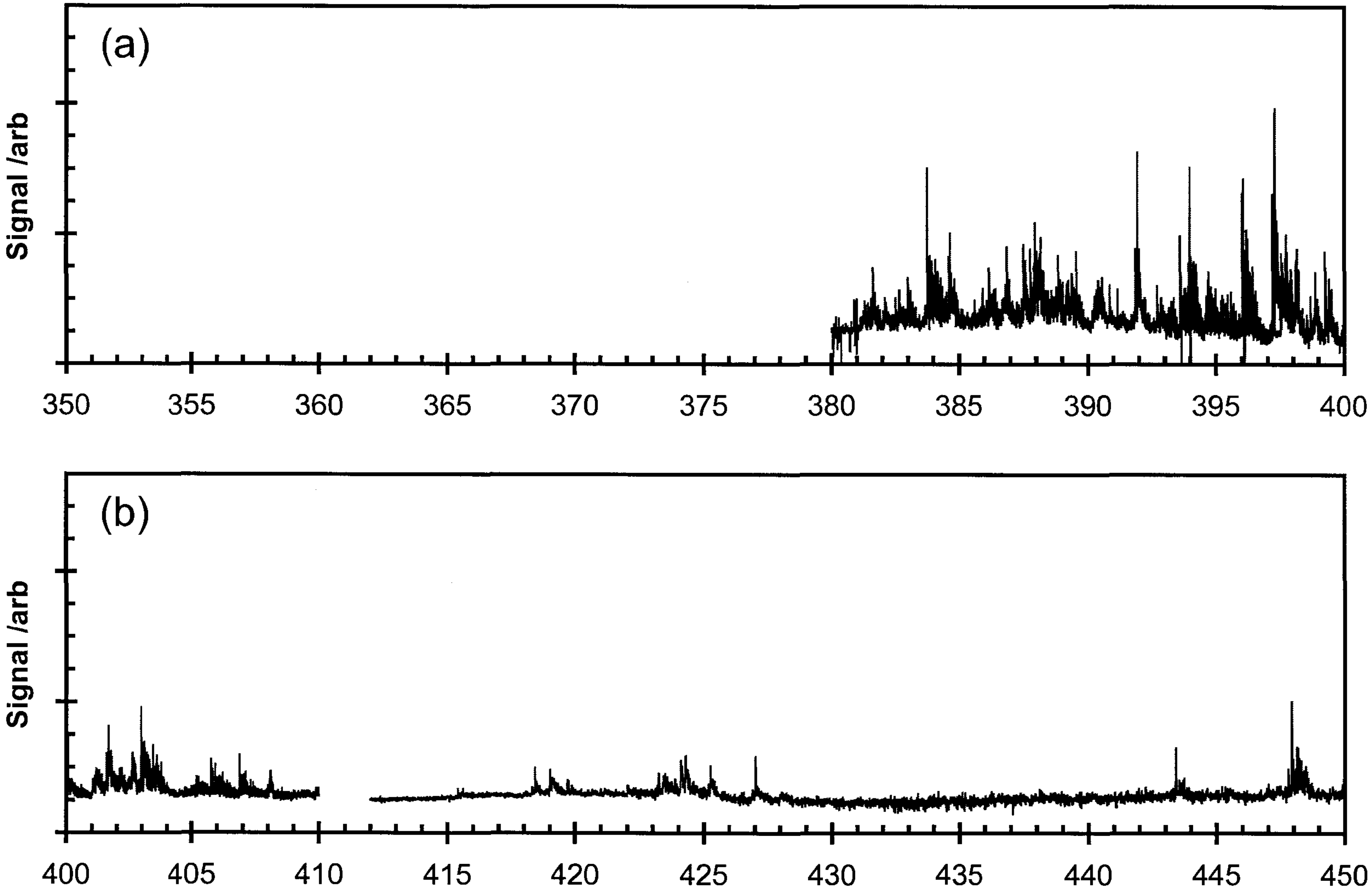
(a)
Signal /arb
350
355
360
365
370
375
380
385
390
395
400
(b)
Signal /arb
400
405
410
415
420
425
430
435
440
445
450

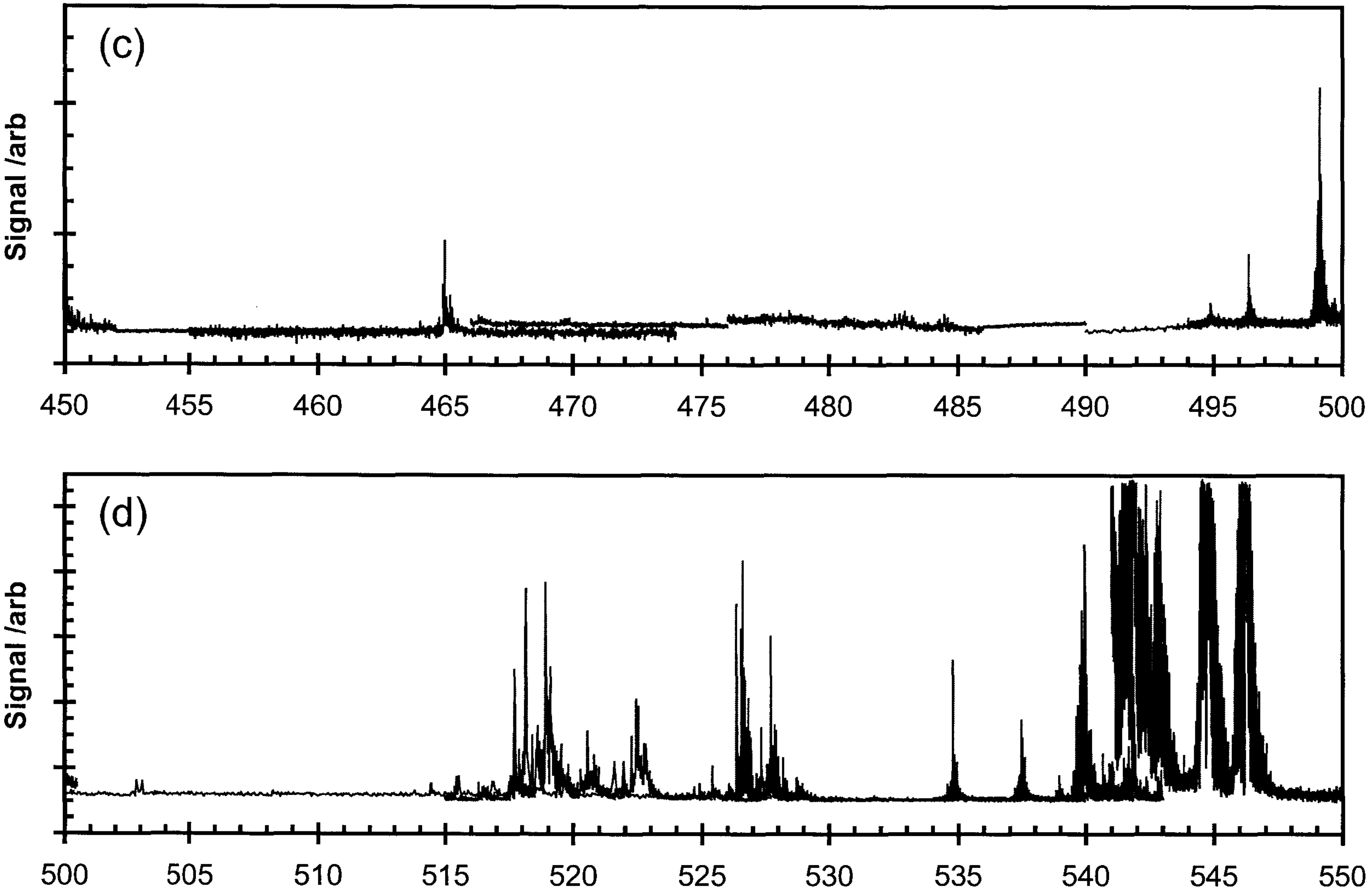
(c)
Signal /arb
450
455
460
465
470
475
480
485
490
495
500
(d)
Signal /arb
500
505
510
515
520
525
530
535
540
545
550

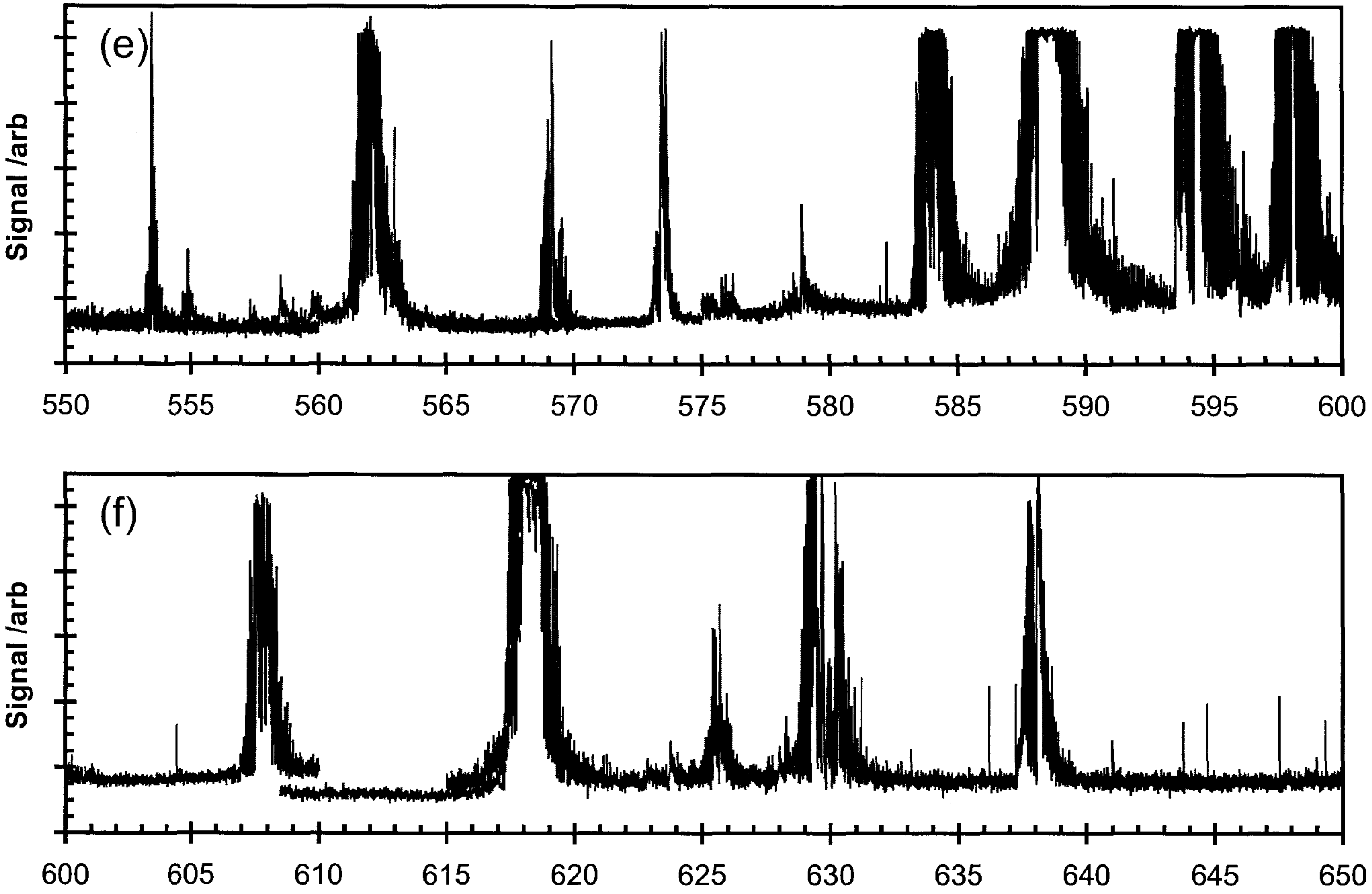
(e)
Signal /arb
550
555
560
565
570
575
580
585
590
595
600
(f)
Signal /arb
600
605
610
615
620
625
630
635
640
645
650

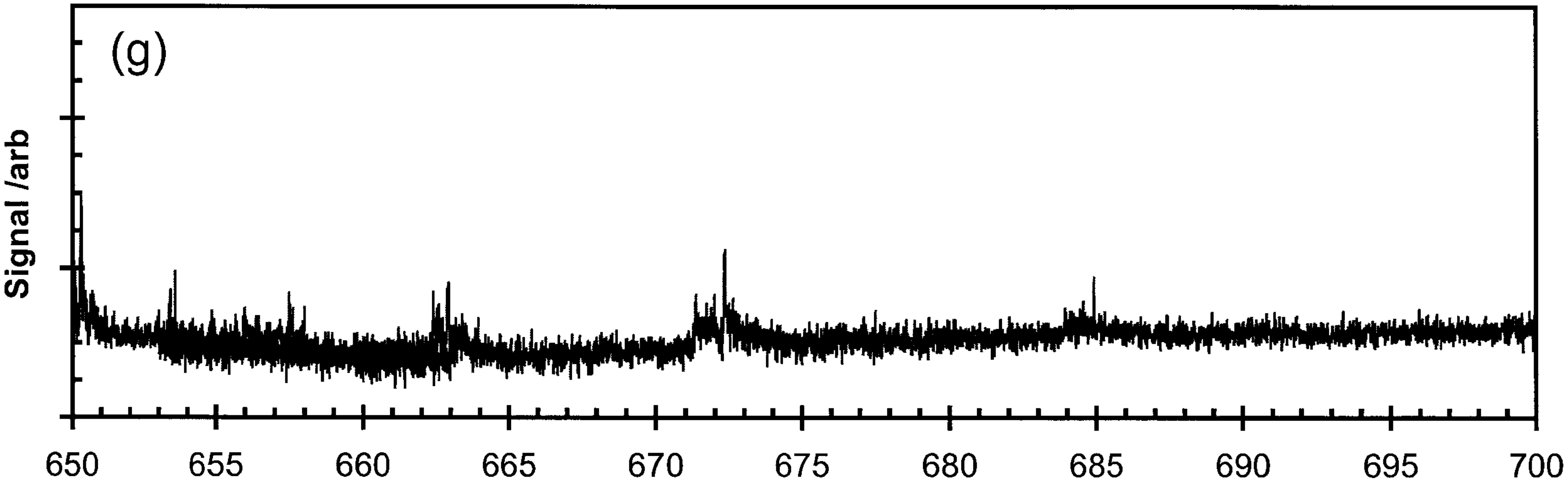

Figure 4.1 LIF spectrum of RhO from 350 to 700 nm in 50 nm sections (a-g). The signal intensity is convoluted by the dye laser power and the detector sensitivity; signal to noise is a better measure of the relative intensity of the transitions. The vertical scale of (a), (b), (c), and (g) are 2× magnified.

Table 4.1 Band centers and assignment of the vibronic transitions in RhO from 500 to 650 nm. All values reported in air.

Rh^{16}O Band Center		Rh^{18}O Band Center		Shift	Assignment
/nm	/cm^{-1}	/nm	/cm^{-1}	/cm^{-1}	
649.9	15 387				[16.0] $^2\Pi_{3/2} - X^4\Sigma^-$ (0,1)
638.2	15 670	638.2	15 670	0	[15.8] $^2\Pi_{1/2} - X^4\Sigma^-$ (0,0)
629.7	15 881	629.7	15 881	0	[16.0] $^2\Pi_{1/2} - X^4\Sigma^-$ (0,0)
625.5	15 987				[15.8] $^2\Pi_{3/2} - X^4\Sigma^-$ (0,0)
618.3	16 174	618.3	16 174	0	[16.0] $^2\Pi_{3/2} - X^4\Sigma^-$ (0,0)
618.0	16 181				[16.0] $^2\Pi_{3/2} - X^4\Sigma^-$ (1,1)
607.9	16 450	608.9	16 423	27	[15.8] $^2\Pi_{1/2} - X^4\Sigma^-$ (1,0)
598.1	16 720	599.4	16 684	36	[16.0] $^2\Pi_{1/2} - X^4\Sigma^-$ (1,0)
594.3	16 827	595.7	16 788	40	[15.8] $^2\Pi_{3/2} - X^4\Sigma^-$ (1,0)
588.7	16 986	590.0	16 948	37	[16.0] $^2\Pi_{3/2} - X^4\Sigma^-$ (1,0)
584.1	17 120	586.1	17 062	58	[15.8] $^2\Pi_{1/2} - X^4\Sigma^-$ (2,0)
578.9	17 274	579.2	17 265	9	[15.8] $^2\Pi_{1/2} - X^4\Sigma^-$ (1,1)
573.5	17 438	575.1	17 389	48	[16.0] $^2\Pi_{1/2} - X^4\Sigma^-$ (2,0)
569.3	17 565	571.6	17 495	71	[15.8] $^2\Pi_{3/2} - X^4\Sigma^-$ (2,0)
561.9	17 797	564.3	17 721	76	[16.0] $^2\Pi_{3/2} - X^4\Sigma^-$ (2,0)
554.7	18 027				
553.3	18 074	555.8	17 993	81	[15.8] $^2\Pi_{1/2} - X^4\Sigma^-$ (3,0)
546.1	18 312				[16.0] $^2\Pi_{1/2} - X^4\Sigma^-$ (3,0)
544.6	18 362				[15.8] $^2\Pi_{3/2} - X^4\Sigma^-$ (3,0)
542.8	18 424				
541.7	18 461				
539.8	18 526				[16.0] $^2\Pi_{3/2} - X^4\Sigma^-$ (3,0)
537.3	18 612				
534.6	18 705				[15.8] $^2\Pi_{1/2} - X^4\Sigma^-$ (4,0)?
526.5	18 992				
524.5	19 067				[16.0] $^2\Pi_{1/2} - X^4\Sigma^-$ (4,0)?
521.8	19 165				[15.8] $^2\Pi_{3/2} - X^4\Sigma^-$ (4,0)?
519.7	19 240				
518.0	19 304				[16.0] $^2\Pi_{3/2} - X^4\Sigma^-$ (4,0)?

Table 4.2 Reported bond lengths for the ground and [15.8] $^2\Pi$ and [16.0] $^2\Pi$ states of RhO. From Reference 25.

State	$X\,^4\Sigma^-$	[15.8] $^2\Pi_{1/2}$	[16.0] $^2\Pi_{1/2}$	[15.8] $^2\Pi_{3/2}$	[16.0] $^2\Pi_{3/2}$
r_e /Å	1.717	1.795	1.784	1.818	1.783

Figure 4.1(f) shows distinct differences in the intensities of the 0–0 transitions. The intensity differences correlate to the relative differences between r_e'' and r_e', further supporting this analysis.

Dispersed fluorescence experiments

Dispersed fluorescence (DF) spectra were obtained for the majority of the $Rh^{16}O$ vibronic levels observed in the LIF experiments. DF provides information on the ground state vibrational progression and on the Franck-Condon overlap between the ground and excited vibrational levels. This information complements LIF experiments, which probe the excited state rovibrational manifold from $\upsilon'' = 0$. In all cases, emission is seen to $\upsilon'' = 0$, i.e., at the probe laser frequency, and to between three and six additional levels in a regular progression. The DF spectra for the four $^2\Pi$ progressions and transitions originating from $\upsilon'' = 1$ (hot transitions) are presented in Figure 4.2 and summarized in Table 4.3.

LIF bands at 598.1(b),[*] 569.3(c), and 625.5(c) are assigned to transitions from $X^4\Sigma^-(\upsilon=0)$. However, these DF spectra also show weak transitions to energies *higher* than the pump laser energy. This indicates that excitation from $X^4\Sigma^-(\upsilon>0)$ is occurring. Given the intensity of these transitions, we believe that the pump laser is simultaneously pumping $\upsilon'' = 0$ and $\upsilon'' = 1$. The displacement of these transitions from the pump laser frequency is, as expected, the same as the displacement of the hot transitions observed in (e). The LIF intensity of the hot transitions discussed above is comparable to those in (e) and much weaker than the transitions from $\upsilon'' = 0$, substantiating this hypothesis.

---

[*] The letter in parentheses identifies the graph in Figure 4.2.

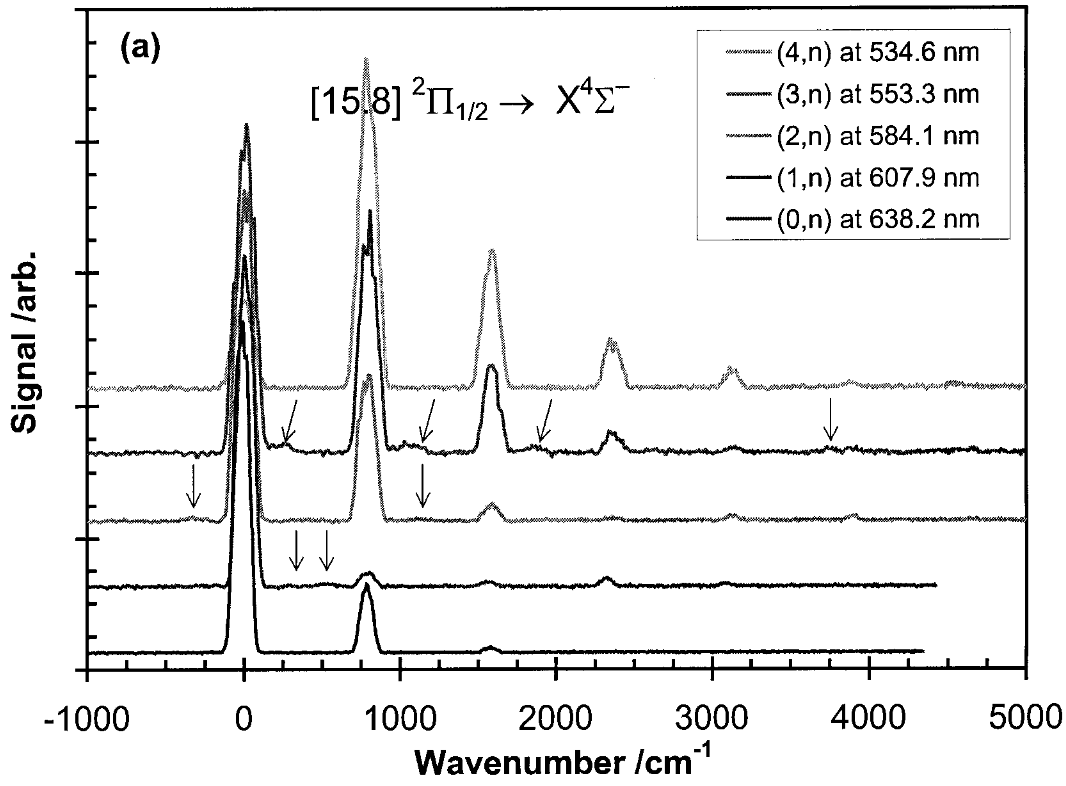
(a)
[15.8] $^2\Pi_{1/2} \rightarrow X^4\Sigma^-$
(4,n) at 534.6 nm
(3,n) at 553.3 nm
(2,n) at 584.1 nm
(1,n) at 607.9 nm
(0,n) at 638.2 nm
Signal /arb.
-1000
0
1000
2000
3000
4000
5000
Wavenumber /cm^{-1}

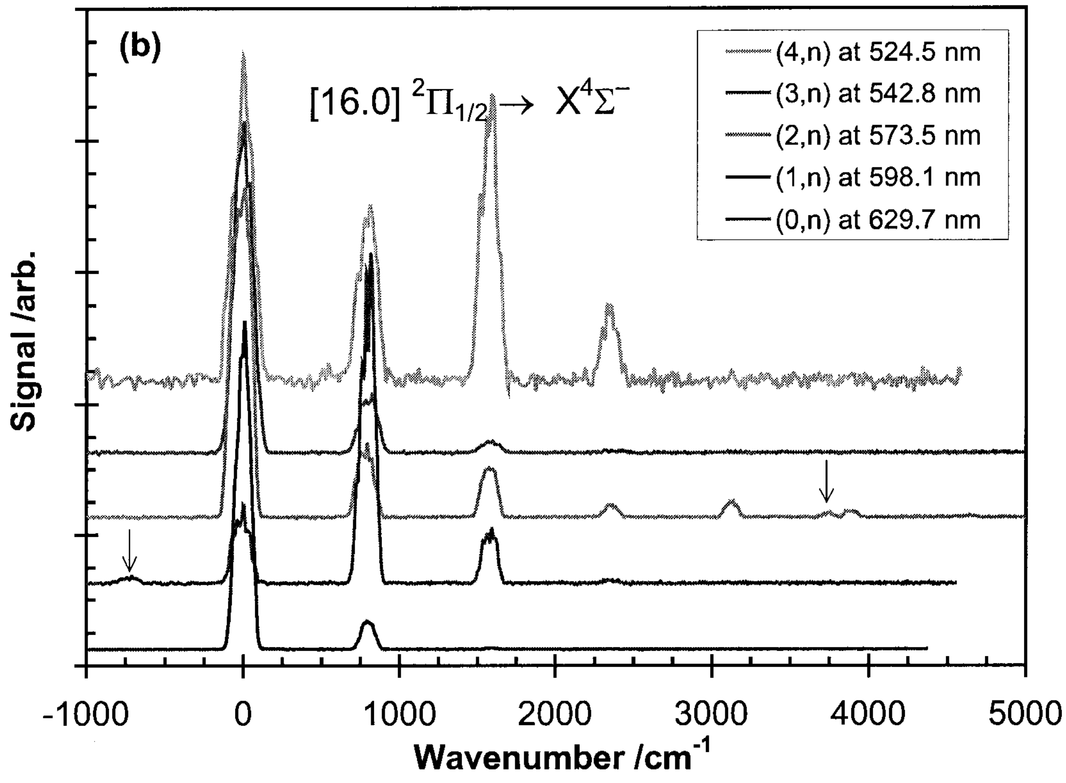
(b)
[16.0] $^2\Pi_{1/2} \rightarrow X^4\Sigma^-$
(4,n) at 524.5 nm
(3,n) at 542.8 nm
(2,n) at 573.5 nm
(1,n) at 598.1 nm
(0,n) at 629.7 nm
Signal /arb.
-1000
0
1000
2000
3000
4000
5000
Wavenumber /cm^{-1}

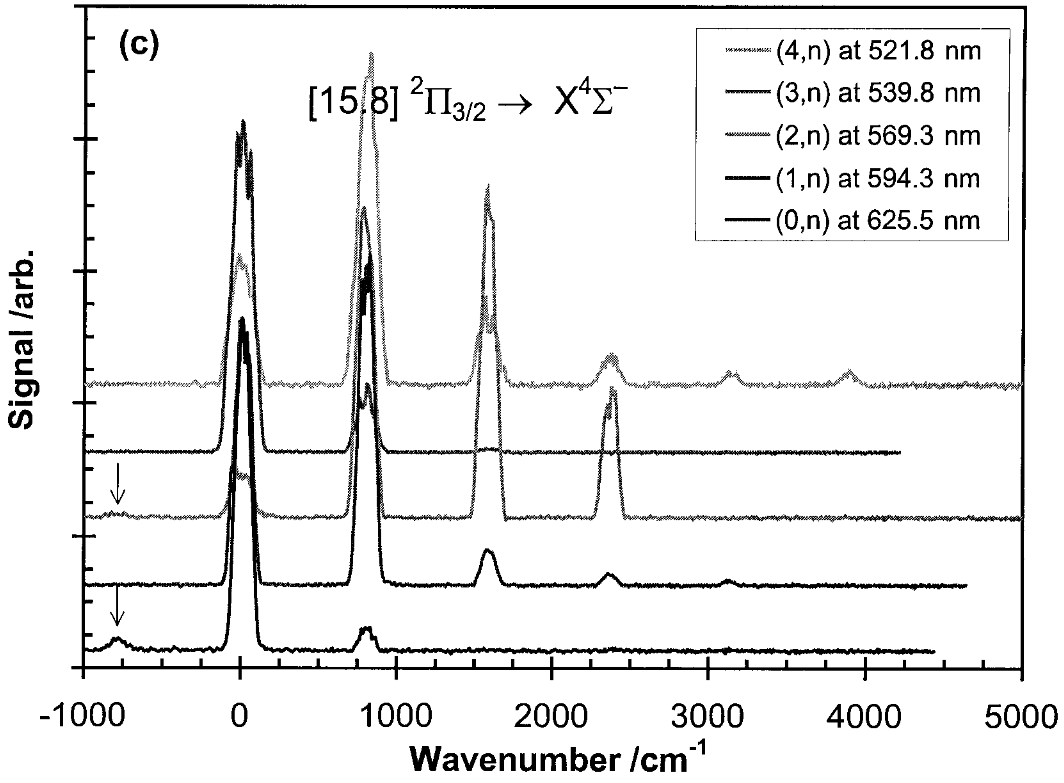
(c)
[15.8] $^2\Pi_{3/2} \rightarrow X^4\Sigma^-$
(4,n) at 521.8 nm
(3,n) at 539.8 nm
(2,n) at 569.3 nm
(1,n) at 594.3 nm
(0,n) at 625.5 nm
Signal /arb.
-1000
0
1000
2000
3000
4000
5000
Wavenumber /cm^{-1}

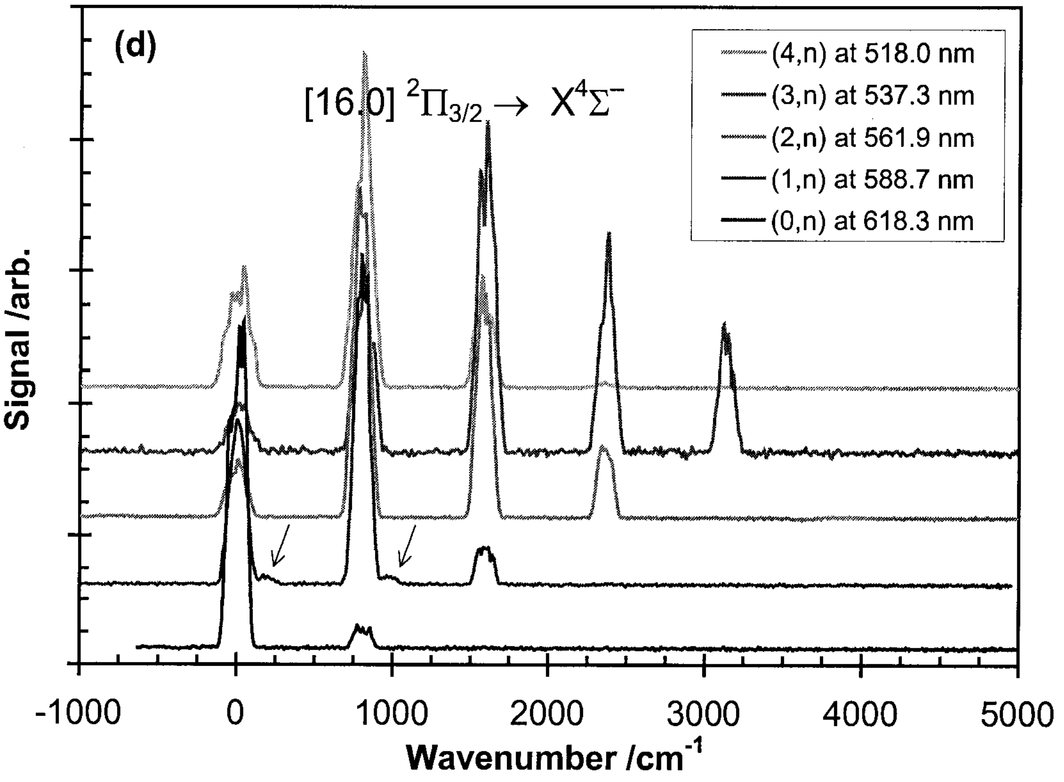
(d)
[16.0] $^2\Pi_{3/2} \rightarrow X^4\Sigma^-$
(4,n) at 518.0 nm
(3,n) at 537.3 nm
(2,n) at 561.9 nm
(1,n) at 588.7 nm
(0,n) at 618.3 nm
Signal /arb.
-1000
0
1000
2000
3000
4000
5000
Wavenumber /cm^{-1}

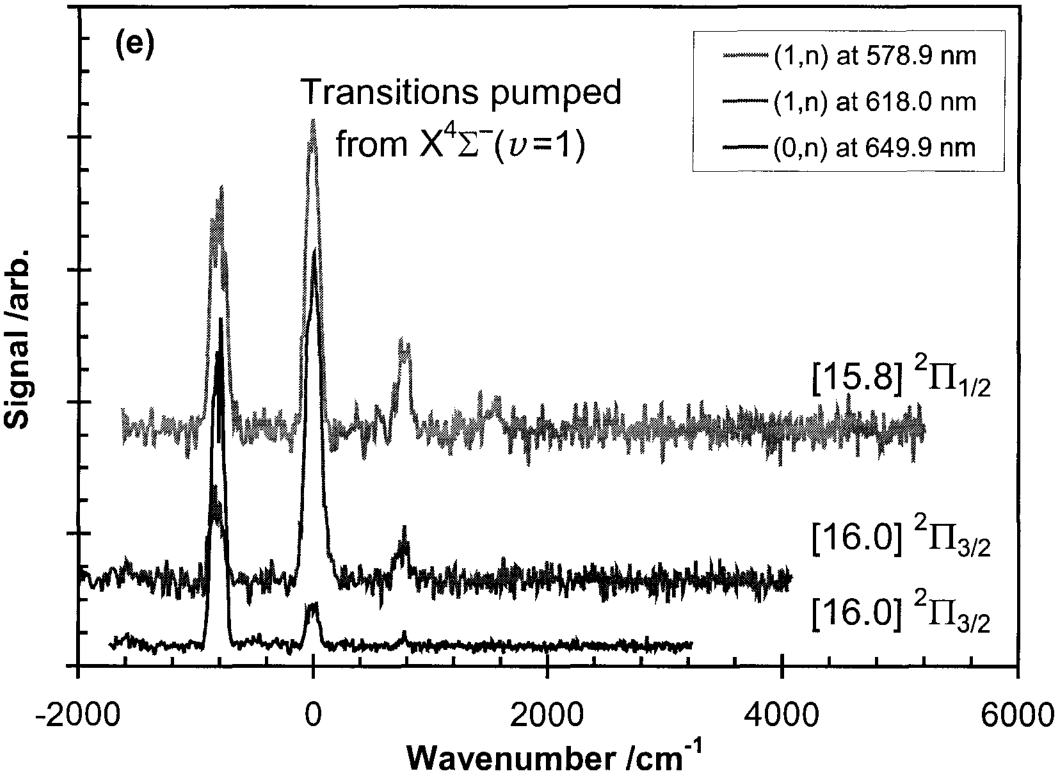

Figure 4.2 DF spectra of the four vibrational progressions $^2\Pi$ – $X^4\Sigma^-(\upsilon=0)$ (a-d) and $^2\Pi$ – $X^4\Sigma^-(\upsilon=1)$ (e). Each spectrum is normalized to the same maximum intensity (the signal/noise ratio gives an indication of the original intensity). The arrows identify reproducible features that are not part of the $X^4\Sigma^-$ progressions (see text).

Table 4.3 DF shifts from the pump laser energy. (a) the average of all the DF transitions assigned to the specified transition; (b) if replicate spectra were recorded at a given excitation laser wavelength, the average is reported; (c) average does not include the band observed in 598.1 nm pumped DF spectrum; (d) transitions from X$^4\Sigma^-$(v=1); (e) coincidental transitions from both X$^4\Sigma^-$(v=0) and X$^4\Sigma^-$(v=1) (the higher energy transition is from v'' = 1); and (f) this transition is not assigned to the $^2\Pi$ progressions investigated herein.

State	v"	Average[a]	Excitation Wavelength /nm and Dispersed Fluorescence Shifts[b] /cm^{-1}								
			649.9	**638.2**	**629.7**	**625.5**	**618.3**	**617.9**	**607.9**	**598.1**	**594.3**
X	c	802	808[d]			793[e]		822[d]		727[e]	
X	0		0	0	0	0	0	0	0	0	0
X	1	795	787	804	800	799	796	766	787	805	794
X	2	1 585		1595					1575	1589	1582
X	3	2 361							2341	2367	2365
X	4	3 131							3115		3126
X	5	3 891									
			588.7	**584.1**	**573.5**	**569.3**	**561.9**	**553.3**	**546.1**	**544.6**	**542.8**
X	c	802				784[e]					
X	0		0	0	0	0	0	0	0	0	0
X	1	795	800	790	793	787	789	791	793	785	794
X	2	1 585	1585	1586	1587	1584	1575	1578	1586	1581	1587
X	3	2 361		2357	2370	2373	2351	2363	2365	2368	
X	4	3 131		3124	3136			3135	3132	3137	
X	5	3 891		3893	3893			3875			
X	6	4 609			4644						
a	0	180	180								
a	1	968	968								

Table 4.3 Continued.

State	*v*"	Average[a]	Excitation Wavelength /nm and Dispersed Fluorescence Shifts[b] /cm^{-1}								
			588.7	**584.1**	**573.5**	**569.3**	**561.9**	**553.3**	**546.1**	**544.6**	**542.8**
b	0	222						222			
b	1	1 051						1051			
b	2	1 853						1853			
c	0	3 747			3746						
			541.7	**539.8**	**538.9[f]**	**537.3**	**534.6**	**526.5**	**524.5**	**521.8**	**518.0**
X	0		0	0	0	0	0	0	0	0	0
X	1	795	798	777	787	795	794	802	798	810	793
X	2	1 585	1585	1583	1589	1577	1583	1577	1578	1639	1586
X	3	2 361	2367	2358	2394	2360	2363	2365	2350	2369	2352
X	4	3 131	3134	3130	3133	3119	3132			3150	
X	5	3 891	3904				3886			3895	
X	6	4 609	4573				4542				
c	0	3 747	3748								
d	0	5 980									5980
d	1	6 475									6475

As with the LIF intensity, the DF band profile is indicative of transitions between states with different equilibrium internuclear distances and/or differently shaped PECs. Both apply to RhO: Table 4.2 shows that r_e differs for the four $^2\Pi$ and the $X^4\Sigma^-$ states and Table 4.4 lists the ω_e and $\omega_e x_e$ values for these states, which are different for the ground and excited states (*vide infra*). However, we were unable to reproduce well the observed intensity profile using the data in Table 4.4. Further analysis with an RKR potential also failed in this regard.[55]

DF spectra pumped at 553.3(a) and 588.7(d) show progressions at energies slightly higher than the main progression: 180 and 222 cm^{-1}, identified by arrows in the respective figure. This suggests that other electronic states exist at these energies above the ground state. However, for two states to exist that close to each other implies that there is very little interaction between them or between them and the ground state. Such a state has not been proposed theoretically or observed experimentally. A cursory evaluation of the high-resolution LIF spectra showed that both excited states have obvious rotational perturbations; however, this does not account for a loss in energy. These features are real and reproducible; however, they defy explanation at this time.

Additional features, identified by arrows in Figure 4.2, are observed at 3 747, 4 542, 5 980, and 6 475 cm^{-1}. Because they were observed together, we tentatively assign the 5 980 and 6 475 cm^{-1} features to a vibrational progression in the same electronic state. Li and Wang found evidence for low-lying states at T_e = 1 600, 3 800, 5 700, and 8 100 ± 100 cm^{-1} in photoelectron experiments.[28] The $X^4\Sigma^-(v=2)$ state at 1 585 cm^{-1} is likely the 1 600 cm^{-1} state. We do observe a state at 3 747 cm^{-1}, which is within the uncertainty of the 3 800 cm^{-1} photoelectron band, but the state at 5 980 cm^{-1} is not within the uncertainty of the 5 700 cm^{-1} band. The state at 4 542 cm^{-1} observed herein has not been previously observed. DF spectra were not recorded to more than 7 000 cm^{-1} beyond the pump laser energy so we are unable to confirm the existence of a state around 8 100 cm^{-1}. The nature of these low-lying states is uncertain; greater resolution than is available in our laboratory is required to characterize them.

Calculation of spectroscopic constants

The LIF band centers from each progression in Table 4.1 were fit to (18), truncated at $\omega_e x_e$, using a non-linear sum-of-squared-differences procedure.* The limited number of vibrational levels, use of band centers rather than band origins, and vibrational perturbations (*vide infra*) precluded a statistically significant determination of $\omega_e y_e$. The weighting of the band centers of $v = 0$, 1, and 2 was double that of $v = 3$ and 4 in consideration of the greater certainty of their assignment. T_e was varied as $\omega_e^2/(4\omega_e x_e)$ during the fitting procedure. Since the $^2\Pi$ states can be formed from the same electronic configuration $(\delta^4\sigma\pi^2)$[56] as the ground state and are the lowest states of this symmetry, they must converge to the same dissociation limit as the ground state. The sum, $T_e' + D_e'$ was fixed at the dissociation energy determined for the ground state (35 800 cm^{-1}; *vide infra*). The method of de Levie[57] was used to estimate the uncertainty of the parameters. The results are summarized in Table 4.4.

Table 4.4 Vibrational parameters for the [15.8] $^2\Pi$ and [16.0] $^2\Pi$ states of RhO. (a) Reference 25.

State	T_e /cm^{-1} this work	T_e /cm^{-1} a	ω_e /cm^{-1}	$\omega_e x_e$ /cm^{-1}	D_e /cm^{-1}
[15.8] $^2\Pi_{1/2}$	15 662 ± 9	15 670	793 ± 10	7.8 ± 2.0	20 200 ± 800
[16.0] $^2\Pi_{1/2}$	15 868	15 881	828	8.6	19 900
[15.8] $^2\Pi_{3/2}$	15 982	15 987	827	8.6	19 800
[16.0] $^2\Pi_{3/2}$	16 161	16 174	830	8.8	19 600

Systematic deviations, which are not accounted for in the uncertainty calculation, exist because of the use of band centers, limitations of the Morse potential, vibrational perturbations, and uncertainty of the high v assignment. The data were of insufficient accuracy to allow for a statistically significant determination of $\omega_e y_e$.

* Microsoft Excel 97 has a built-in routine for optimizing any number of parameters to user-defined constraints. The spreadsheet was set-up to compare the calculated vibrational energy level with the experimental energy level. The difference, weighted, squared, and summed, was minimized by the routine. Dividing by the degrees of freedom gave the standard deviation of the fit. The algorithm is the Generalized Reduced Gradient (GRG2) nonlinear optimization method.

Ground state vibrational parameters were determined from the average DF shift was fit to (18) also truncated at $\omega_e x_e$. All vibrational levels were weighted equally because they could be unambiguously assigned. The vibrational parameters for the ground state were determined to be $\omega_e = 805.4 \pm 0.6$ cm^{-1}, $\omega_e x_e = 4.5 \pm 0.1$ cm^{-1}, and $D_e = 35\,800 \pm 800$ cm^{-1}. These results are in good agreement with a matrix isolation experiment which determined $\Delta G_{½}$ for the ground state to be 799.0 cm^{-1}.[26] $\Delta G_{½}$ based on the spectroscopic constants above is 796.4 cm^{-1}, via (21).

T_e for the four 0–0 transitions was also determined in internally calibrated high-resolution spectroscopic experiments. The values calculated herein are consistently 5 to 12 cm^{-1} lower than those quoted by Heuff *et al.*[25] This is because of a systematic difference between the band center (used in this study) and band origins, and because of limitations of the Morse potential applied to this system.

Systematic deviations from the empirical formula for determining the vibrational energy levels, (18), were observed for $v = 2$, 3, and 4. These deviations are evident in Figure 4.3 and are likely because of vibrational perturbations in the excited state. The perturbing state(s) were not observed spectroscopically. Perturbations *cannot* be handled by fitting to (18) since interactions with other states are not considered. The observed and expected isotopic shift, calculated with (30), is summarized in Table 4.5. The agreement is sufficient to assign the vibrational progressions but some deviations warrant explanation. Deviations are predominantly because of vibrational perturbations, which are not considered in the calculation of ω_e and $\omega_e x_e$, and because of slight differences in the perturba

Table 4.5 Calculated and experimental spectroscopic Rh^{16}O/Rh^{18}O shifts of the $^2\Pi(v'=0,1,2)$ band positions.

Band	Spectroscopic Shift from Rh^{16}O to Rh^{18}O /cm^{-1}					
v' =	0 (calc.)	0 (obs.)	1 (calc.)	1 (obs.)	2 (calc.)	2 (obs.)
[15.8] $^2\Pi_{1/2}$	0	0	38	27	74	58
[16.0] $^2\Pi_{1/2}$	1	0	42	36	81	48
[15.8] $^2\Pi_{3/2}$	1	0	42	40	81	71
[16.0] $^2\Pi_{3/2}$	1	0	40	37	78	76

tional shifts in the isotopomers. With increasing Δv, bands from both Rh^{16}O and Rh^{18}O were not present in the same spectrum and large deviations may be attributable to the mechanical instability of the dye laser in this region.

Chen and Armentrout[27] estimated D_e from thermochemistry to be ≈ 33 800 cm^{-1}, below our value of 35 800 cm^{-1} extrapolated from spectroscopic data. Since extrapolative methods are known to overestimate D_e, these experiments are in agreement.

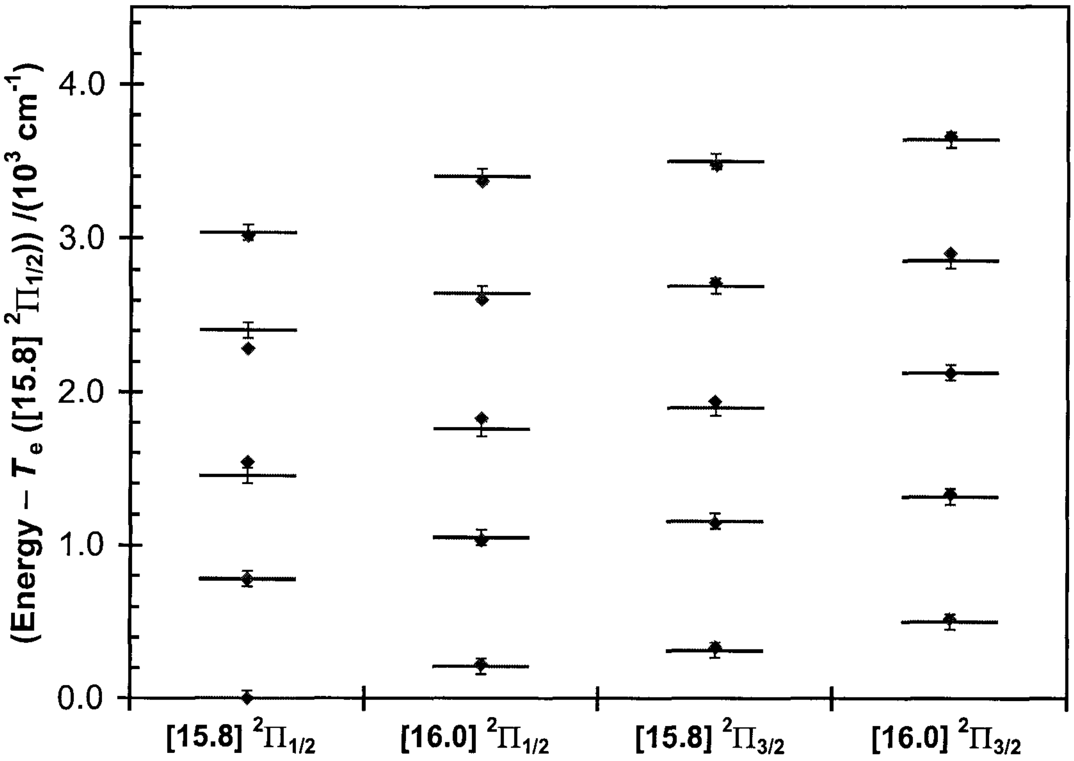

Figure 4.3 Energy level diagram of the observed $^2\Pi$ transitions. Vertical bars cover 50 cm^{-1} (≈ 2 nm). ◆ are the expected band positions based on fitting the observed transitions to $\omega_e(v+½)-\omega_e x_e(v+½)^2$.

Transitions at 578.9, 618.0, and 649.9 nm were found to originate from $v'' = 1$. The ground state vibrational spacing was estimated at 796 cm^{-1} from the data and is in agreement with the value obtained from DF experiments.

Excited state lifetimes

The lifetime of an excited state provides information on the nature of the states involved in the transition. Typical fluorescence lifetimes range from picoseconds to tens of nanoseconds. This is not the case for RhO, which has lifetimes ranging from 450 to 1 700 ns as shown in Table 4.6. A typical decay profile and best-fit single exponential are shown in Figure 4.4.[*] All the decay profiles are well represented by a single exponential function, indicating that either a single unimolecular process is dominant or that all emissions have similar lifetimes. The one to two order-of-magnitude difference between allowed fluorescence lifetimes and those observed for RhO confirms the spectroscopic assignment of a spin-forbidden transition.[25] Spin-orbit coupling from the rhodium atom facilitates this type of transition (phosphorescence).

The lifetimes of the four $\upsilon' = 0$ levels are different but correlate well with observed relative intensities in the LIF spectra. The intensity, difference in equilibrium bond length, and lifetime all point to the same relative Franck-Condon overlap: the 629.7 and 618.3 bands have better overlap with the ground state PEC, while the 625.5 and 638.2 subbands having progressively less overlap. Similar arguments can be made for the $\upsilon' = 1$ and 2 levels.

Table 4.6 Band-averaged lifetimes of the $^2\Pi$ vibronic states taken at three to five unperturbed locations within the band. The uncertainty is ± 100 ns.

λ /nm	state	τ /ns	λ /nm	state	τ /ns
638.2	[15.8] $^2\Pi_{1/2}(v=0)$	1 600	625.5	[15.8] $^2\Pi_{3/2}(v=0)$	1 000
607.9	[15.8] $^2\Pi_{1/2}(v=1)$		594.3	[15.8] $^2\Pi_{3/2}(v=1)$	800
584.1	[15.8] $^2\Pi_{1/2}(v=2)$		569.3	[15.8] $^2\Pi_{3/2}(v=2)$	600
553.3	[15.8] $^2\Pi_{1/2}(v=3)$	1 200			
			618.3	[16.0] $^2\Pi_{3/2}(v=0)$	500
629.7	[16.0] $^2\Pi_{1/2}(v=0)$	900	588.7	[16.0] $^2\Pi_{3/2}(v=1)$	450
598.1	[16.0] $^2\Pi_{1/2}(v=1)$	1 000	561.9	[16.0] $^2\Pi_{3/2}(v=2)$	450
573.5	[16.0] $^2\Pi_{1/2}(v=2)$	1 700			

---

[*] The initial spike is due to the probe laser and was not included in the fit.

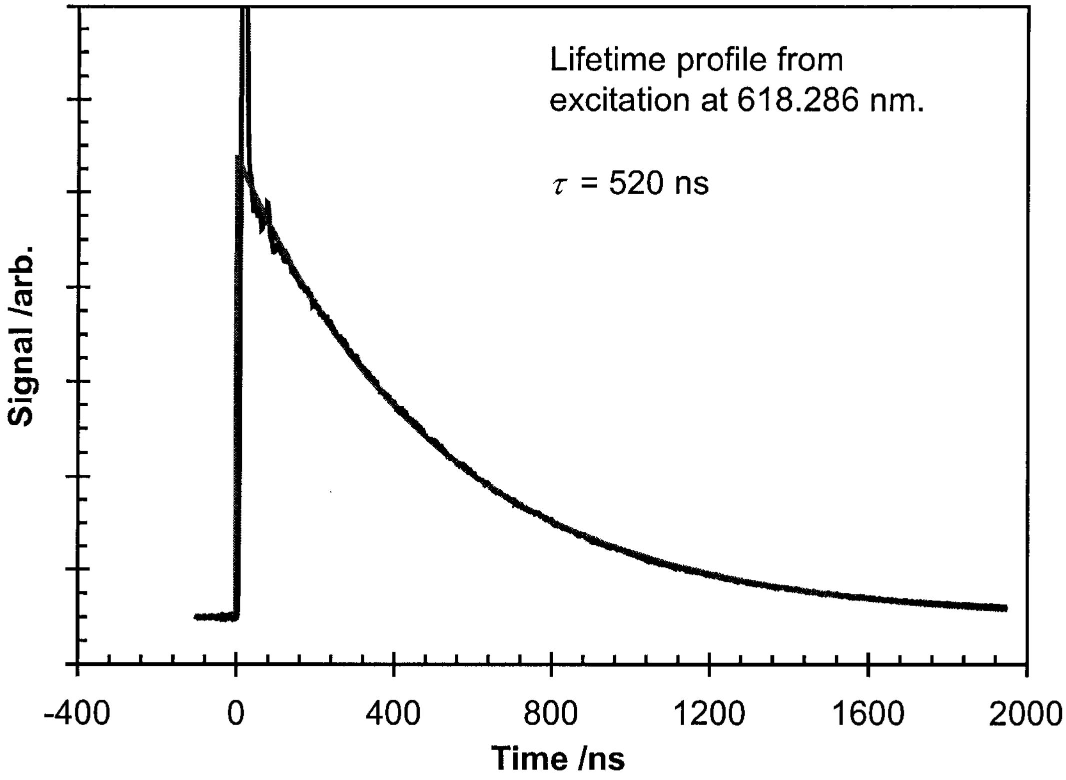

Figure 4.4 Typical lifetime profile (blue) and single-exponential fit (red) for a rovibronic transition of RhO.

Summary

LIF and DF spectroscopy provide complementary information on the electronic states of RhO and were used to characterize the vibrational progressions of the $X^4\Sigma^-$ and four $^2\Pi$ spin-orbit states. This information, coupled with excited state lifetime measurements, produced results that were self-consistent when comparing the bond lengths with the transition intensities and lifetimes. The vibrational parameters for all states are summarized in Table 4.7. Additionally, several low-lying electronic states were observed in DF that either confirm previous observations or have not been previously observed. Progressions originating at 180, 222 and 5 980 cm^{-1} and isolated energy levels at 3 747 and 4 542 cm^{-1} above the ground state correspond to the latter.

Table 4.7 Vibrational parameters for the $X^4\Sigma^-$ and the [15.8] and [16.0] $^2\Pi$ states of RhO. Ground state parameters from DF experiments; excited state parameters from LIF experiments.

State	T_e /cm^{-1}	ω_e /cm^{-1}	$\omega_e x_e$ /cm^{-1}	D_e /cm^{-1}
X $^4\Sigma^-$	0	805.4 ± 0.6	4.5 ± 0.1	35 800 ± 800
[15.8] $^2\Pi_{1/2}$	15 662 ± 9	793 ± 10	7.8 ± 2.0	20 200
[16.0] $^2\Pi_{1/2}$	15 868	828	8.6	19 900
[15.8] $^2\Pi_{3/2}$	15 982	827	8.6	19 800
[16.0] $^2\Pi_{3/2}$	16 161	830	8.8	19 600

The information in Table 4.7 was used to construct depurturbed Morse PECs for the ground and $^2\Pi$ states of RhO. These PECs and the unassigned vibrational levels observed in LIF and DF experiments are shown in Figure 4.5.

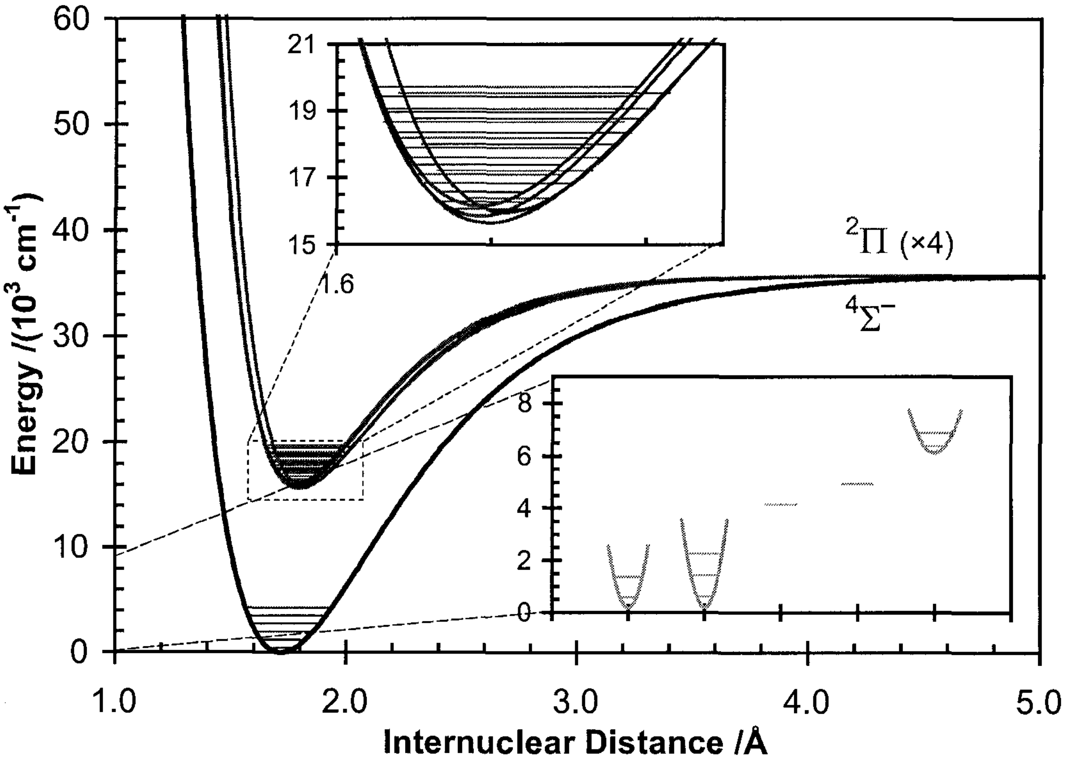

Figure 4.5 Potential curves and observed vibrational energy levels of the ground and $^2\Pi$ states of RhO. Three unassigned progressions and two energy levels are shown in the bottom inset; their absolute positions are uncertain and are separated in the inset for convenience.

5. REFERENCES

1. Kawaguchi, K.; Kagi, E.; Hirano, T.; Tahano, S.; Saito, S. *Astrophys. J.* **1993**, *406*, L39.
2. Ziurys, L. M.; Apponi, A. J.; Guelin, M.; Cernicharo, J. *Astrophys. J.* **1995**, *445*, L47.
3. Grevesse, N.; Sauval, J. *Molecules in the Stellar Environment* Springer-Verlag: New York, *IAU Colloquium No. 146*, **1993**, 197.
4. Werner, C. *Opt. Eng.* **1995**,*34* , 3103. Simonds, M.; Xiao, H. K.; Levine, S. P. *Amer. Ind. Hyg. Assn. J.* **1994**, *55*, 953. Pelon, J. *Onde Elec.* **1992**, *72*, 53.
5. Bishop, G. A.; Stedman, D. H.; Hutton, R. B.; Bohren, L.; Lacey, N. *Environ. Sci. Tech.* **2000**, *34*, 1110. Bishop, G. A.; Stedman, D. H. *Acc. Chem. Res.* **1996**, *29*, 489.
6. Balfour, W. J.; Chandrasekhar, K. S. *J. Mol. Spectrosc.* **1990**, *139*, 245.
7. Balfour, W. J.; Merer, A. J.; Niki, H.; Simard, B.; Hackett, P. A. *J. Chem. Phys.* **1993**, *99*, 3288.
8. Balfour, W. J.; Qian, C. X. W.; Zhou, C. *J. Chem. Phys.* **1997**, *106*, 4383.
9. Balfour, W. J.; Lindgren, B.; Launila, O.; O'Connor, S.; Cusack, E. J. *J. Mol. Spectrosc.* **1992**, *154*, 177.
10. Balfour, W. J.; Klynning, L. *Astrophys. J.* **1994**, *424*, 1049.
11. Balfour, W. J.; Cao, J.; Prasad, C. V. V.; Qian, C. X. W. *J. Chem. Phys.* **1995**, *103*, 4046.
12. Jakubek, Z. J.; Nakhate, S. G.; Simard, B.; Balfour, W. J. *J. Mol. Spectrosc.* **2002**, *211*, 135.
13. Simard, B.; Hackett, P. A.; Balfour, W. J. *Chem. Phys. Lett.* **1994**, *230*, 103.
14. Simard, B.; Jakubek, Z.; Niki, H.; Balfour, W. J. *J. Chem. Phys.* **1999**, *111*, 1483.
15. Simard, B.; James, A. M.; Hackett, P. A.; Balfour, W. J. *J. Mol. Spectrosc.* **1992**, *154*, 455.
16. Balfour, W. J.; Saksena, M. D.; Shetty, B. J.; Brown, J. M.; Barrow, R. F.; Malcolm, I. B.; James, A. M.; Simard, B. *Mol. Phys.* **1996**, *89*, 13.
17. Balfour, W. J.; Saksena, M. D. *J. Mol. Spectrosc.* **1990**, *143*, 392.
18. Balfour, W. J.; Chandrasekhar, K. S.; Saksena, M. D. *J. Mol. Spectrosc.* **1991**, *145*, 458.
19. Balfour, W. J.; Cao, J. Y.; Qian, C. X. W.; Rixon, S. J. *J. Mol. Spectrosc.* **1997**, *183*, 113.
20. The breadth of rhodium's catalytic applications are explored in most General and Inorganic Chemistry textbooks.
21. Balfour, W. J.; Cao, J, Qian, C. X. W. *J. Mol. Spectrosc.* **2000**, *201*, 244.

22. Balfour, W. J.; Fougère, S. G.; Heuff, R. F.; Qian, C. X. W.; Zhou, C. *J. Mol. Spectrosc.* **1999**, *198*, 393.
23. Fougère, S. G.; Balfour, W. J.; Cao, J.; Qian, C. X. W. *J. Mol. Spectrosc.* **2000**, *199*, 18.
24. Scullman, R. *Personal Communication with Dr. Walter Balfour* **1982**.
25. Heuff, R. F.; Balfour, W. J.; Adam, A. G. *J. Mol. Spectrosc.* **2002**, *216*, 136.
26. Citra, A.; Andrews, L. *J. Phys. Chem. A* **1999**, *103*, 4845.
27. Chen, Y.-M.; Armentrout, P. B. *J. Chem. Phys.* **1995**, *103*, 618.
28. Li, X.; Wang, L.-S. *J. Chem. Phys.* **1998**, *109*, 5264.
29. Merer, A. J.; *Ann. Rev. Phys. Chem.* **1989**,*40* , 407.
30. Calculations failed to converge to the ground state of FeH in: Walker, J. H.; Walker, T. E. H.; Kelly, H. P. *J. Chem. Phys.* **1972**,*57* , 2094. Scott, P. R.; Richards, W. G. *J. Chem. Phys.* **1975**,*63* , 1690. Walch, S. P.; Bauschlicher, C. W. *J. Chem. Phys.* **1983**, *78*, 4587.

    The ground state of FeH was correctly identified in: Bauschlicher, C. W.; Langhoff, S. R. *Chem. Phys. Lett.* **1988**,*145* , 205. Langhoff, S. R.; Bauschlicher, C. W. *J. Mol. Spec.* **1990**, *141*, 243.
31. Shim, I.; Mandix, K.; Gingerich, K. A. *J. Mol. Struc. Theochem.* **1997**, *393*, 127.
32. Mains, G. C.; White, J. M. *J. Phys. Chem.* **1991**, *95*, 112.
33. Siegbahn, P. E. M. *Chem. Phys. Lett.* **1993**, *201*, 15.
34. Herzberg, G. *Molecular Spectra and Molecular Structure: Volume I: Spectra of Diatomic Molecules* D. Van Nostrand Company, Inc: Toronto, **1950**.
35. King, G. W. *Spectroscopy and Molecular Structure* Holt, Rinehart and Winston: Toronto, **1964**.
36. Harris, D. C.; Bertolucci, M. D. *Symmetry and Spectroscopy: an Introduction to Vibrational and Electronic Spectroscopy* Dover Publications: New York, **1978**.
37. Steinfeld, J. I. *Molecules and Radiation* MIT Press: Cambridge, 2nd Ed., **1985**.
38. Dykstra, C. E. *Quantum Chemistry & Molecular Spectroscopy* Prentice Hall: New Jersey, **1992**.
39. Bernath, P. F. *Spectra of Atoms and Molecules* Oxford University Press: New York, **1995**.
40. Born, M.; Oppenheimer, R. *Ann . Physik* **1927**, *84*, 457.
41. Landau, L. D.; Lifshitz, E. M. *Relativistic Quantum Mechanics* Pergamon Press: New York, **1977**.
42. Morse, P. M. *Phys. Rev.* **1929**, *34*, 57.
43. Vanderslice, J. T.; Mason, E. A.; Maisch, W. G.; Lippincott, E. R. *J. Mol. Spec.* **1959**, *3*, 17.

44. Le Roy, R. J. *RKR1: A Computer Program Implementing the First-Order RKR Method for Determining Diatom Potential Energy Curves from Spectroscopic Constants* University of Waterloo: Waterloo, ON, **1992**.

45. Birge, R. T.; Sponer, H. *Phys. Rev.* **1926**, *28*, 259.

46. LeRoy, R.J.; Bernstein, R.B. *J. Chem. Phys.* **1970**, *52*, 3869. LeRoy, R.J.; Bernstein, R.B. *J. Mol. Spectrosc.* **1971**, *37*, 109.

47. Bunker, P.R. *J. Mol. Spectrosc.* **1968**, *28*, 422.

48. Dunham, D. L. *Phys. Rev.* **1932**, *41*, 721.

49. Tatum, J. B. *Stellar Atmospheres* (astrowww.phys.uvic.ca/~tatum/stellatm.html) **March 2003**, Ch. 9.

50. Cao, J. *Electronic Structures of Iron Monocarbide (*FeC*) and Rhenium Mononitride (*ReN*)* Ph.D. Dissertation, Department of Physics and Astronomy, University of Victoria, **1997**.

51. Proch, D.; Trickl, T. *Rev. Sci. Instrum.* **1989**, *60*, 713.

52. Demtröder, W. *Laser Spectroscopy* Springer: Berlin, **1982**.

53. Andrews, D. L. (Ed.) *Applied Laser Spectroscopy: Techniques, Instrumentation, and Applications* John Wiley & Sons: New York, **1992**.

54. Fougère, S. G. *The Electronic Structure and Spectroscopy of Rhodium Diatomic Molecules* Ph.D. Dissertation, Department of Chemistry, University of Victoria, **2000**.

55. Jensen, R. H.; Balfour, W. J. *unpublished results*.

56. Jensen, R. H. *Coupling of Orbital and Spin Angular Momentum* MathCad computer program, www.consol.ca (MathCad link), **2002**.

57. de Levie, R. *J. Chem. Ed.* **1999**, *76*, 1594.

APPENDIX A: DEFINITIONS, ACRONYMS, AND ABBREVIATIONS

DF	dispersed fluorescence
compound	a 'molecular entity' as defined by IUPAC
HCL	hollow cathode lamp
IR	electromagnetic radiation in the infrared region
IUPAC	International Union of Pure and Applied Chemistry
LIF	laser-induced fluorescence
molecular entity	Any constitutionally or isotopically distinct atom, molecule, ion, ion pair, radical, radical ion, complex, conformer, etc., identifiable as a separately distinguishable entity.
molecule	a 'molecular entity' as defined by IUPAC
Nd:YAG	neodymium doped yttrium aluminum garnet (used in a solid state laser)
OGE	optogalvanic effect
PEC	potential energy curve
PES	potential energy surface
PMT	photomultiplier tube
rovibrational	a term used to describe a rotationally resolved vibrational transition within a single electronic state
rovibronic	a term used to describe a rotationally resolved electronic transition
species	a 'molecular entity' as defined by IUPAC
system	a collection of one or more 'molecular entities' as defined by IUPAC
UV	electromagnetic radiation in the ultraviolet region
vibronic	a term used to describe a vibrationally resolved electronic transition
Vis	electromagnetic radiation in the visible region

APPENDIX B: COLLECTION OPTICS

The optical collection system in our laboratory was modified early in this project. The original and current configurations are given in Figure B.1. Upon reflection, I question the correctness of this modification.

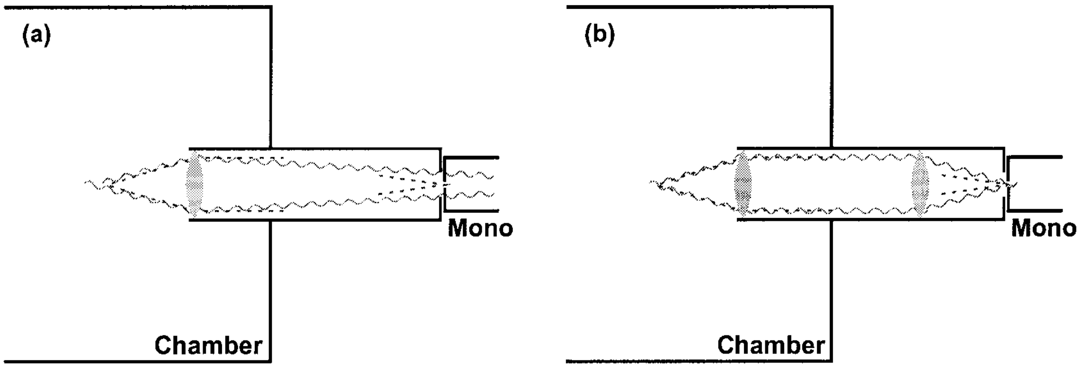

Figure B.1 Original (a) and current (b) optical arrangement. The dashed lines indicate the focal point of the lens or the acceptance angle of the monochromator. The wavy lines indicate the extrema of emission collectable by the lens. (To scale.)

Perusal of the monochromator manual states that its $F_{\#} = 4.2$ ($F_{\#}$ = focal length / diameter). The original configuration had the single lens further from the probe path, resulting in a converging beam (a) into the monochromator. The current configuration has the foci of the lenses on the probe laser path and the monochromator (b). The $F_{\#}$s of the original and current configurations are 7.5 and 1.5 respectively. Clearly, the original configuration did not collect all of the photons; however, the signal that was collected was retained. The current configuration collects all the photons but loses a fraction because of the unchecked divergence ($F_{\#}$ greater than monochromator $F_{\#}$). A further complication is that the lens in the original configuration was further from the probe path, resulting in a smaller solid angle of radiation collected.

Data collected prior to these experiments appear to have a better signal to noise ratio by a factor of two. A different optical system was developed to optimize the signal collection and improve on other aspects of the experimental setup. It is summarized in Figure B.2.

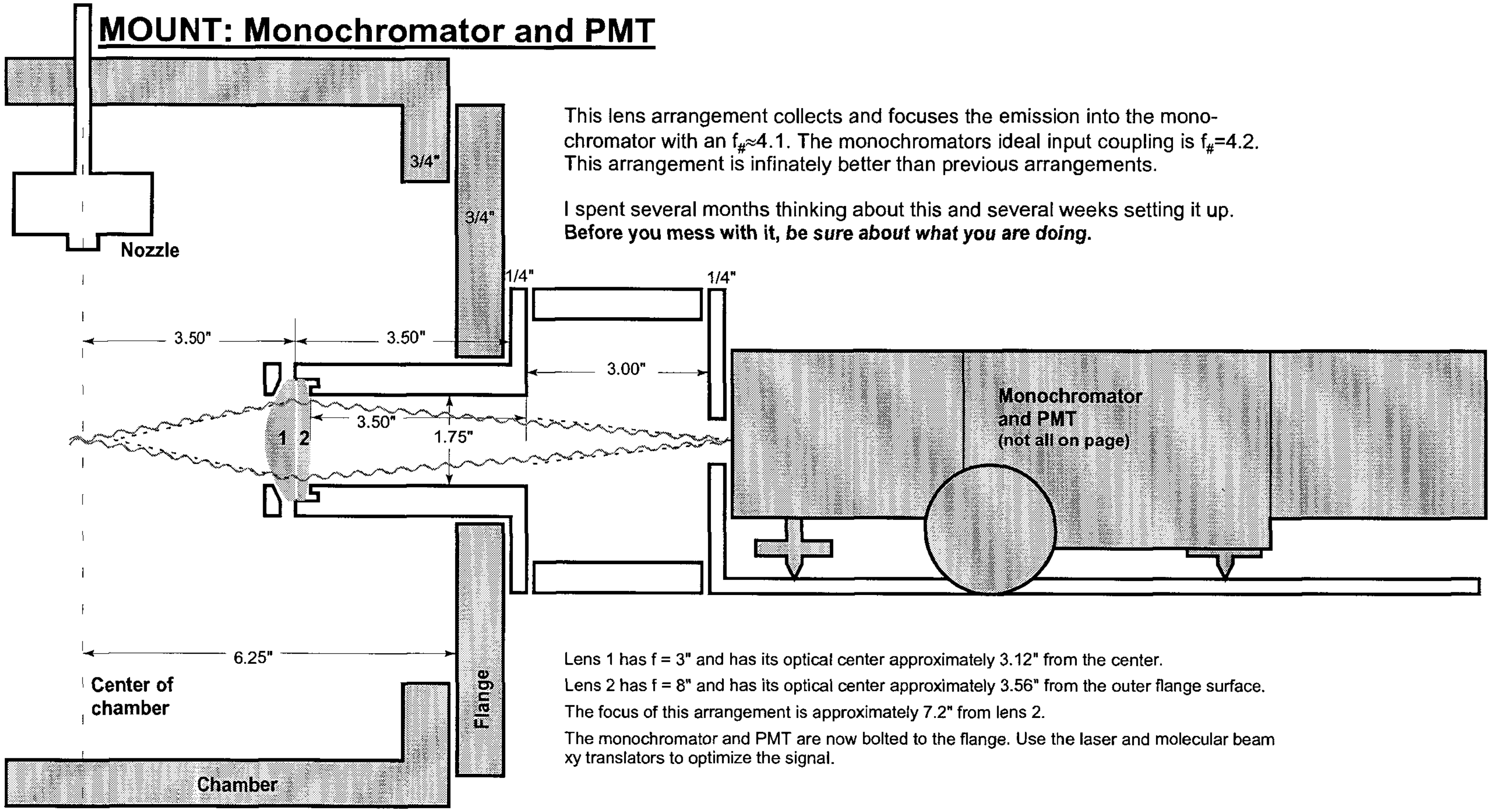

MOUNT: Monochromator and PMT

This lens arrangement collects and focuses the emission into the monochromator with an $f_{\#} \approx 4.1$. The monochromators ideal input coupling is $f_{\#}=4.2$. This arrangement is infinately better than previous arrangements.

I spent several months thinking about this and several weeks setting it up. **Before you mess with it, *be sure about what you are doing.***

Lens 1 has f = 3" and has its optical center approximately 3.12" from the center.

Lens 2 has f = 8" and has its optical center approximately 3.56" from the outer flange surface.

The focus of this arrangement is approximately 7.2" from lens 2.

The monochromator and PMT are now bolted to the flange. Use the laser and molecular beam xy translators to optimize the signal.

Figure B.2 Updated optical arrangement for spectroscopic data collection. Legend same as Figure B.1. (To scale.)

APPENDIX C: DYE LASER CALIBRATION

Previously in our laboratory, questions had been raised about the absolute calibration and linearity of the dye laser. The laser wavelength is based on extrapolating from a single calibration point, at which the position of the mechanical components and the laser output wavelength are known. The calibration is susceptible to changes in the mechanical components of the dye laser, thermal fluctuations, pump laser alignment, and inexperienced operators. Further, there was a suspicion that a discontinuity in the calibration exists somewhere around 500 nm. Experiments were conducted to investigate this phenomenon and to calibrate the dye laser. An iron-neon hollow cathode lamp (HCL; Universal L1788-26NQ) was used in a typical optogalvanic effect (OGE) experiment.[a]

Optogalvanic spectroscopy

In this experiment, laser radiation (or other high intensity monochromatic radiation) is directed into the plasma. Interaction of the radiation with molecules, atoms, or ions in the plasma perturbs the conductivity of the plasma. These perturbations are observed as variations in the energy (current or voltage) needed to maintain the plasma. A HCL serves as an ideal plasma — stable and with a known composition — to calibrate a dye laser. Atomic line energies are known to thousandths of a cm^{-1} and are suitable for calibrating most dye lasers.

HCLs consist of a sealed glass tube containing a metal anode (usually tungsten), a cylindrical cathode made of a known metal(s), and are filled with neon or argon to a pressure between 1 and 5 Torr. A potential difference applied across the electrodes ionizes the gas. The electrons and ions gain sufficient kinetic energy to sputter and ionize the metal atoms from the cathode. Inelastic collisions electronically excite the ions and atoms, leading to a large population of electronically excited species. The shape of the cathode provides for a highly localized plasma.*

---

* The shape of the cathode provides for a linear beam of radiation and ensures that most of the sputtered metal redeposits onto the cathode. These features are important, but secondary for OGE experiments.

Incoming tunable radiation changes the population of the states involved when it becomes resonant with a transition in either the atoms or ions inside the lamp. If the states have different ionization probabilities, the result will be a change in the conductivity of the plasma. This is observed as a change in the potential difference across a constant current power supply. Photoabsorption or photoionization can both change the conductivity.

$$A_i + h\nu \longrightarrow A_j \tag{50}$$

$$A_k + h\nu \longrightarrow A^+ + e^- \tag{51}$$

Reaction (51) directly leads to an increase in the conductivity. Reaction (50) could lead to either an increase or decrease in conductivity, depending on the relative ionization probabilities of A_i and A_j states. In the unlikely event that the ionization probabilities are the same for both states, no optogalvanic signal will be observed. The observed signal is dependent on *both* the transition probability and the difference in ionization probabilities of the two states whereas tabulated atomic line intensity is only dependent on the transition probability.

Experiment & results

The supply from an in-house built constant current power supply was passed through an in-house built voltage probe based on the design by Dovichi *et al.*[b] The electrical circuit is shown in Figure C.1. This circuit measures the time derivative of the voltage. The location of the HCL in the experimental setup is shown in Figure 3.1. A quartz window directed ≈ 4 % of the laser radiation into the HCL. Dovichi suggests that it is better not to irradiate the cathode, but rather to have the laser interact with the plasma just outside the cathode or to use a tubular cathode. We were unable to detect a signal when

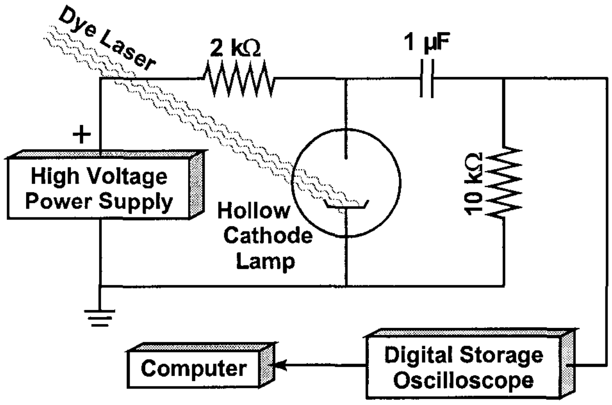

Figure C.1 Electrical circuit for optogalvanic measurements from a hollow cathode lamp.

irradiating outside the cathode and did not encounter any problems when irradiating the cathode. The photon energy was insufficient to directly generate photoelectrons.

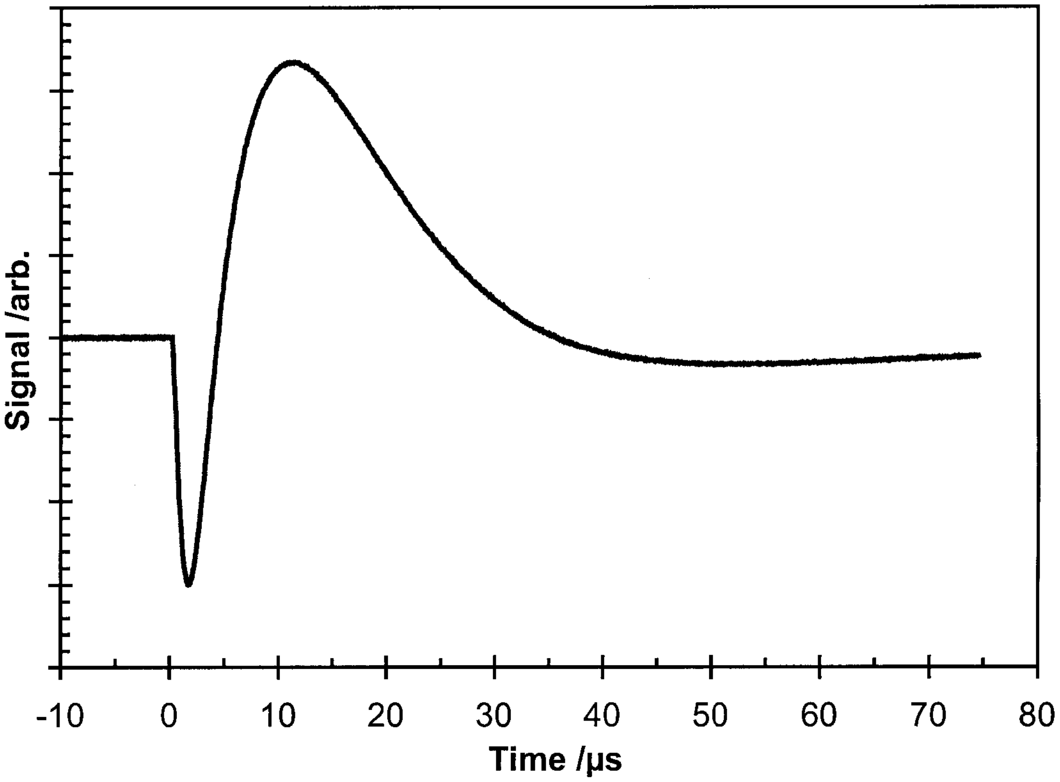

Figure C.2 Typical optogalvanic signal.

A typical OGE signal is shown in Figure C.2. The constant current power sup ply and the OGE circuit control the time profile of the OGE signal. No optimization was undertaken since a strong signal was readily observed with the published circuitry. A portion of the time resolved signal was integrated relative to the background using the same data acquisition system described on page 25. The OGE spectrum was generated by plot ting the integrated signal as a function of dye laser wavelength; the latter stepped at intervals between 0.001 and 0.003 nm. Figure C.3 shows a representative region with assigned and unassigned transitions, including one of several doublet-type features. Each peak was fit with a gaussian function that determined its position and intensity. Using the available laser dyes, we recorded optogalvanic features from 490 nm to 650 nm; these spectra are tabulated in Table C.1 and shown in Figure C.4. The optogalvanic spectrum was compared with the published emission lines from an iron-neon HCL.[c] Consistently, the most intense OGE lines were from neon while few iron lines could be assigned. We speculate that the unassigned lines belong to tungsten (the anode) or impurities in the iron cathode.

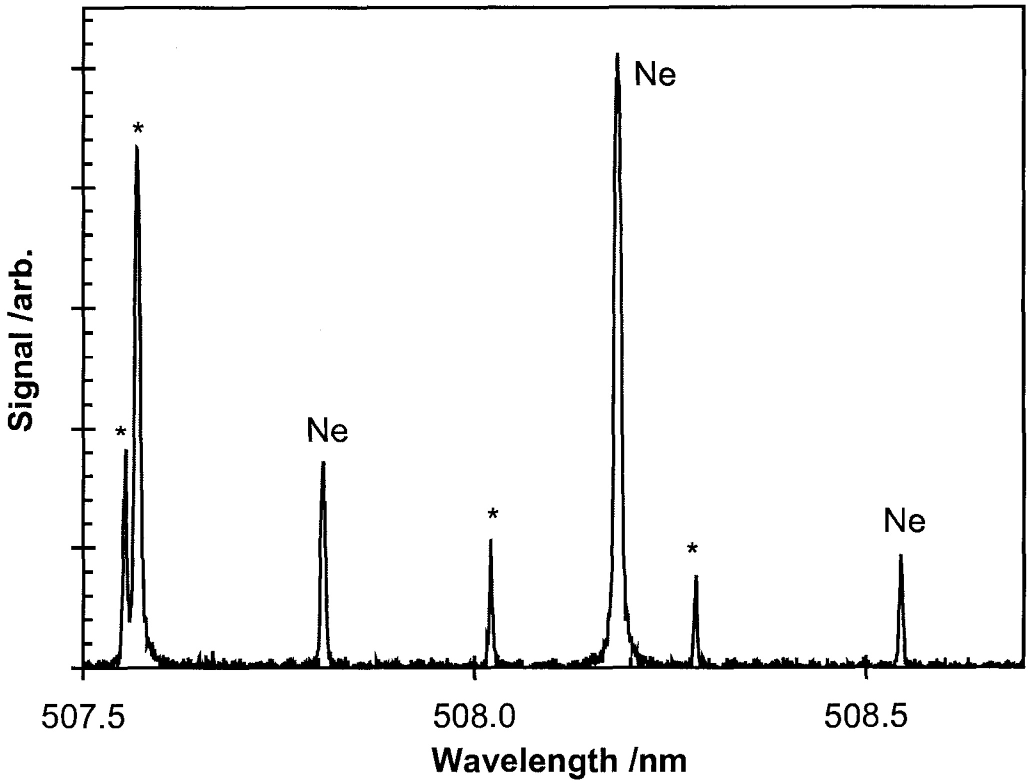

Figure C.3 Typical optogalvanic spectrum. The asterisks indicate unassigned transitions. One of several doublets is shown at 507.57 nm.

The residuals (observed – actual) in Figure C.4 show that there are two distinct progressions. Below 595 nm, there is a constant offset of (0.168 ± 0.014) nm.[*] Above 575 nm, the offset has a slightly sloped function: $-(4.5 \pm 0.5)\cdot 10^{-4}\,\lambda + (0.29 \pm 0.03)$ nm. There is a distinct step of ≈ 0.14 nm that occurs between 575 and 595 nm. Six consecutive scans over the same OGE transitions at 575 nm suggest that this step occurs randomly. In this wavelength region, the reflecting mirror in the dye laser is near the zenith. We suspect

---

[*] Uncertainties calculated in this dissertation represent one standard deviation.

Table C.1 Observed optogalvanic transitions between 490 and 650 nm. Units of a: nanometers, and b: arbitrary.

Assigned OGE Transitions			Duplicate	Unassigned Transitions		Duplicate
observed[a]	intensity[b]	assigned[a]	Difference[a]	observed[a]	intensity[b]	Difference[a]
500.6758	67.0	500.51587		494.0660	29.5	
503.3050	66.7	503.13504		494.6595, 494.6599	51.6	0.0004
503.9387	79.8	503.77512		495.6998, 495.7002	24.5	0.0004
507.5687, 507.5691	84.0	507.42007	0.0004	495.8602, 495.8607	50.2	0.0005
507.8057, 507.8061	35.0	507.62620	0.0004	495.8696, 495.8701	46.4	0.0005
508.1830	102.0	508.03852		497.5010	35.1	
508.5439	18.5	508.33377		497.6244		
511.5427	58.9	511.36724		499.5587, 499.5593		0.0006
511.8262	84.3	511.65030		499.6470, 499.6480	44.7	0.0010
518.8784	132.9	518.86122		499.6565, 499.6580		0.0015
520.5583	72.0	520.38962		499.7791, 499.7809		0.0018
521.2258	52.6	521.05672		499.9032		
522.4050	50.0	522.23517		500.0075	18.7	
528.1557	11.6	528.00853		500.1982	9.7	
529.9844	24.5	529.81891		500.5163		
530.6515	17.8	530.47580		500.6947	37.7	
533.2380	22.5	533.07775		502.4592	32.0	
533.2450, 533.2468	78.0	533.07775	0.0018	503.3207		
534.2749	54.8	534.10233		503.7661	41.3	
534.4898	28.0	534.32834		503.9222	40.6	
535.0814	12.0	534.92038		507.5531, 507.5531	33.0	0.0000
540.0687	98.4	540.05617		508.0207	21.0	
543.3814	31.7	543.36513		508.2826	15.2	
549.6070	16.0	549.44613		511.8777		

Table C.1 Continued.

Assigned OGE Transitions			Duplicate Difference[a]
observed[a]	intensity[b]	assigned[a]	
553.5302	23.0	553.54148	
556.4228	65.9	556.27662	
574.8672	58.0	574.82985	
574.9844	58.0	574.82985	
575.0190	9.6	574.82985	
576.3380	50.8	576.44188	
576.4680, 576.4700	44.2	576.44188	0.0020
576.4740	49.5	576.44188	
576.4757, 576.4774	50.0	576.44188	0.0013
576.4800	47.4	576.44188	
576.5940, 576.6004	48.0	576.44188	0.0024
580.6227	41.2	580.44496	
582.1878, 582.1906	51.6	582.01558	0.0028
585.4124, 585.4130	18.0	585.24878	0.0006
588.3776, 588.3780	78.0	588.18952	0.0004
594.5149	78.3	594.48342	
594.6566	63.4	594.48342	
597.5745	71.0	597.55340	
599.1832	33.5	599.16532	
603.0195	59.7	602.99969	
607.4443	55.0	607.43377	
612.8553	70.9	612.84499	
614.3232	68.9	614.30626	
616.3677	27.7	616.35939	

Unassigned Transitions		Duplicate Difference[a]
observed[a]	intensity[b]	
514.4867	9.7	
514.6555	65.7	
514.6737	43.9	
515.1686	24.0	
515.3564	42.0	
515.6028	32.4	
515.8229	19.2	
516.0459		
519.1466	22.7	
519.3333		
519.3459	28.0	
521.0547		
521.6051	21.4	
532.8094	42.5	
533.4978		
535.5118		
535.6752	27.8	
535.6930		
536.1556, 536.1577	35.3	0.0021
536.1971, 536.1992	26.5	0.0021
556.3903	30.5	
556.4510	21.1	
576.0860, 576.0860	23.2	0.0000
576.0940	14.4	

Table C.1 Continued.

Assigned OGE Transitions			Duplicate Difference[a]	Unassigned Transitions		Duplicate Difference[a]
observed[a]	intensity[b]	assigned[a]		observed[a]	intensity[b]	
618.2173	35.2	618.21460		576.4319, 576.4340	17.4	0.0011
621.7403	77.3	621.72812		576.4380, 576.4380	20.4	0.0000
626.6581	34.0	626.64950		576.4395, 576.4405	20.0	0.0010
630.4865	72.0	630.47890		576.5560, 576.5632	18.7	0.0072
633.4609	49.3	633.44278		580.5867	14.0	
640.2336	70.8	640.22460		591.3938	17.0	
				591.5515		
				597.4827, 597.4828		0.0001
				615.0409	14.2	
				618.2678	27.7	
				638.5184	38.9	

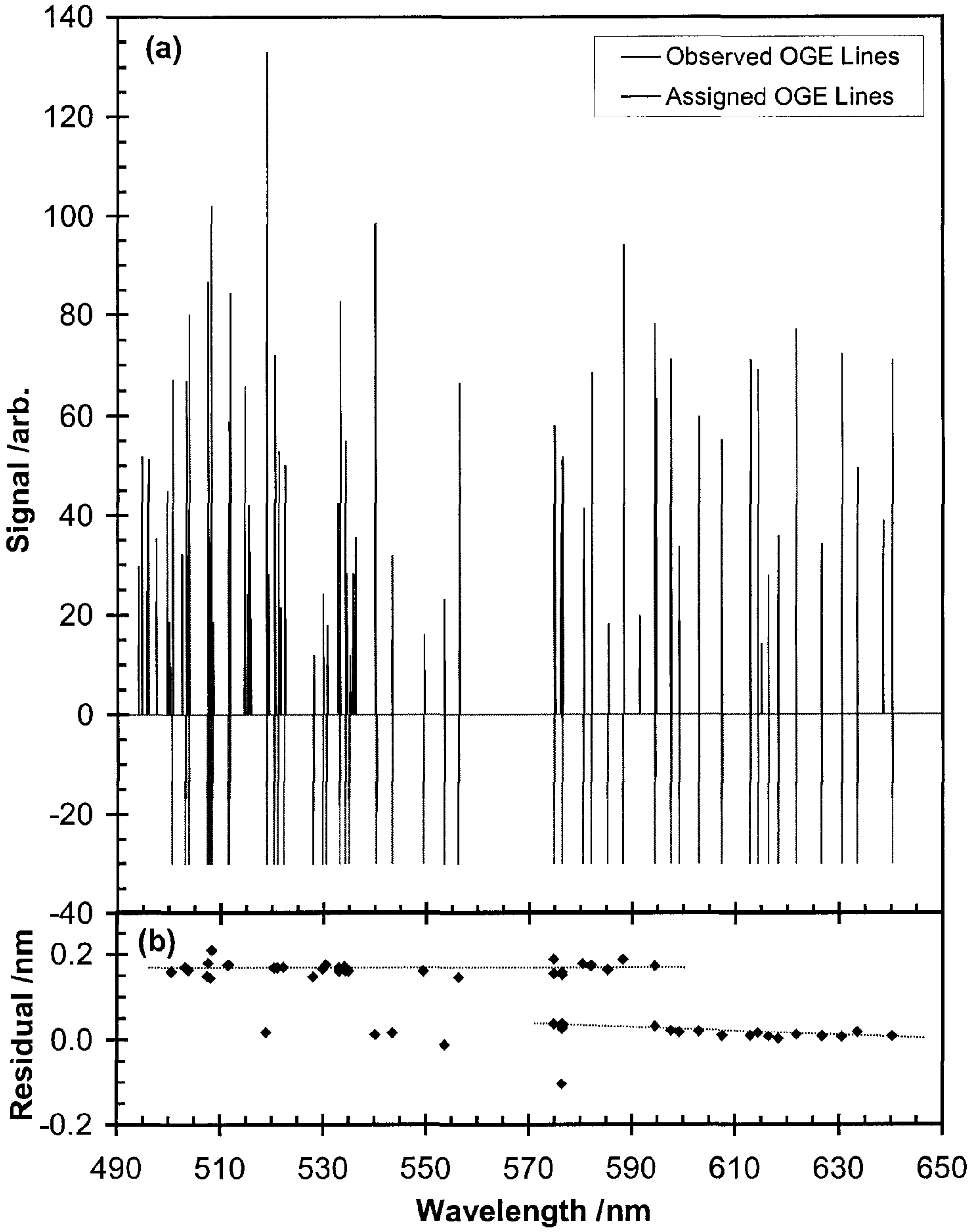

Figure C.4 Results of OGE calibration. In (a), the observed OGE lines and signal intensity are plotted with the mirror presenting the lines that could be assigned to known atomic iron or neon transitions (Reference c). (b) presents the residuals for the calibration and the two trend lines in the residuals (see text).

that the discontinuity is because of a change in the load-bearing position of the worm gear that controls the location of the mirror. For operation, there must be some play between the worm gear and the mirror assembly. Estimating this play at 0.001",[d] the angle change at the location of the worm gear, 3" from center, is 0.02°. This is in good agreement with the angle change corresponding to a 0.14 nm step: 0.015°. In the discontinuity region, friction holds the mirror in position, and the dye laser is susceptible to the slightest vibration. It is also possible that the mirror could 'bounce' between positions. Users need to be aware that an ex situ calibration may not be accurate in this region.

The maximum uncertainty, ± 0.04 nm, is an estimate of the absolute accuracy of any given transition. During the course of this calibration, several peaks were scanned on more than one occasion and often on different days. The precision within a spectrum was observed to be ± 0.0003 nm for a baseline separated peak comprised of more than five data points.* The precision from multiple scans is 0.0012 nm (reported as the mean absolute deviation).

Summary

A discontinuity exists in the dye laser calibration. The exact position of the discontinuity is random between 575 and 595 nm; external calibration is inadequate in this region. Ideally, calibration must be done concurrently with signal collection in all experiments.[a]

---

* A baseline separated peak can be fit with a single gaussian function. The standard deviation represents the range in which another measurement would likely reside at the 68 % confidence level. Independent of where another measurement resides, the mean would shift significantly less. The standard deviation of the mean, s_m, is $s_m = s/\sqrt{n}$.

a. Fougère, S. G. *The Electronic Structure and Spectroscopy of Rhodium Diatomic Molecules* Ph.D. Dissertation, Department of Chemistry, University of Victoria, **2000**.

b. Dovichi, N. J.; Moore, D. S.; Keller, R. A. *Applied Optics* **1982**, *21*, 1468.

c. Crosswhite, H. M. *J. Res. Natl. Inst. Stand.* **1975**, *79A*, 17.

d. Stajduhar, D., machinist, University of Victoria, *Personal Communication* **2002**.

APPENDIX D: TYPICAL INSTRUMENT SETTINGS

Tektronics 2440 Digital Oscilloscope

Setting	Spectroscopy	Mass Spectrometry
Trigger:	positive *(nominally 800 mV)*	positive *(nominally 800 mV)*
Slope:	positive	positive
Mode:	A - Normal; B - Runs After	A - Normal; B - Runs After
Source:	External Trigger 1	External Trigger 1
Coupling:	DC *or* LF Reject	DC *or* LF Reject
Position:	A - 1/8 (128); B - 1/8 (128)	A - 1/8 (128); B - 1/2 (512)
Timebase:	A - 200 ns/div; B - 100 ns/div *(nominally)*	A - 2 μs/div; B - 200 ns/div *(nominally)* 2 μs/div shows masses up to 500 amu

Photomultiplier Tubes

PMT	HV1	HV2	max ΔV
Hamamatsu R1477	-1000	100	1250
Hamamatsu R106UH	This PMT has an external power suppy that provides power and collects signal through a 4 pin connector to the PMT.		1000

Lumonics HyperDye 500

These settings will change if the grating is removed and reinstalled. Read Chapters 4 and 5 for detailed calibration information. Power failures occasionally reset the HD500; these parameters need to be re-entered.

Key	Thumbwheel '0' — Operational Mode		Thumbwheel '1' — Calibration Mode	
	Parameter	Setting	Parameter	Setting
0	Present Position	*<varies>*	Present Position	*<varies>*
1	Start Position	*<varies>*	Home Location Angle	902435
2	End Position	*<varies>*	Angle of Incidence (θ)	867960
3	Increment/Rate	*<varies>*	Grating Groove Density	17997
4	Marker Increment	6.672	Mean Air Pressure	10133
5	Scan Repeats	1	Order of Diffraction	1
6	Scan Delay	0	Harmonic Displayed	2
7	Laser Trigger Frequency	*<varies>*	Backlash	128
8	Number of Pulses	*<varies>*	Loopback	0

Other HD500 Settings

burst/linear burst

Other Settings

Device	
OGE:	have a reflection impinge on the cathode of the HCL.
Nozzle:	HV should be less than 400 V to ensure longevity of the piezo crystal. pressure change should be from $1 \cdot 10^{-5}$ to $4 \cdot 10^{-5}$ Torr
Rod:	rotation rate: 15-20 Hz (no two laser shots in the same location).
Mono:	Not perfectly calibrated. Determine the mirror λ by ①, inserting slits, and ②, varing monochromator to maximize scattered light from probe laser. Currently, $\lambda_{best} \approx (4 \pm 1)$ nm.

THERMAL DISSOCIATION OF HALOGEN AZIDES

1. INTRODUCTION

The azide radical and ion, N_3 and N_3^-, are considered to have the reactivity of a halogen and is often called a pseudohalogen in that context. N_3 has comparable size (space averaged), mass, and electronegativity to chlorine. However, azides are not stable — N_3 is a metastable form of nitrogen — and reacts to produce N_2 exothermically and explosively. Almost all azides are synthesized from sodium azide (NaN_3), which is commercially available and relatively stable. The array of compounds formed follows from its pseudohalogen nature. Known covalent azides include:[1,*] HN_3, $B(N_3)_3$, $Si(N_3)_4$, ONN_3, NCN_3, $\mathit{R}N_3$, $P\mathit{X}_n(N_3)_{3-n}$, $P\mathit{X}_n(N_3)_{5-n}$, $\mathit{X}N_3$, and various ions thereof. N_3N (cf. P_4) was theoretically predicted to have a T_d, D_{2h}, or C_{2v} symmetry,[2,3,4] but a recent experiment has observed N_4 as $2N_2$ units joined by a weak bond in an open-chain configuration.[5] Diazide, $(N_3)_2 \equiv N_6$, has been proposed theoretically but not observed experimentally.[6] Novel azidamines — $HN(N_3)_2$, $N(N_3)_3$, and $N(N_3)_4^+$ — have also been studied theoretically and found to have a bound potential energy minimum and large enthalpies of formation: 820, 1 250, and 2 500 kJ/mol, respectively.[7] However, given the instability of the corresponding halogen amines and high reactivity of N_3,[8] it is questionable whether any high nitrogen density compounds could be sufficiently stabilized for synthesis or use.

Despite limited research into their reactivity and decomposition mechanisms, azide-containing compounds are quite common commercially. For example, approximately 100 g of NaN_3 is used in automobile airbags. An electric charge is used to detonate the airbag on demand. Hydrogen azide (hydrazoic acid; HN_3) is formed through the reaction of acid (organic or inorganic) with NaN_3. HN_3 is often the starting material in the production of other azides. HN_3 reacts with metals to form many compounds: $Cu(N_3)_2$, AgN_3, $Hg(N_3)_2$,[†] and $Pb(N_3)_2$,[†] for example, with varying degrees of stability. The use of azides as 'envi-

---

[*] *A* = anything, *M* = metal, *R* = organic, *X* = halogen, *Y* = p-block. The placeholders are italicized to differentiate *X* from the ground state symbol, X, used in this dissertation, e.g., N*X*(X).

[†] In 1867, Alfred Nobel patented the detonator — the use of one explosive to detonate another — and used mercury (II) azide and/or mercury fulminate to detonate his mixtures of nitroglycerine and diatomaceous earth (powdered silica). Both mercury compounds were so unstable (and toxic) that their use was quickly discontinued, being replaced by lead azide, which remains the detonator of choice in large-bore ammunition. (Primers in small arms are composed of lead styphnate and tetrazene.)

ronmentally safe'[*] rocket fuels has also been proposed.[9] Biologically, azidothymidine (AZT; zidovudine) inhibits reverse transcriptase proteins and was used to treat human immunodeficiency virus (HIV).[10] Additionally, azides can be photoactivated (photodissociated) with red or near-infrared radiation, which penetrates better through tissue, allowing for the localized activation of the drug. Two roles for azides have been proposed: preparing a dendrimer with a photoactive central linkage (azide) and drugs entrained in the voids would allow for localized drug delivery,[11] or the dissociation itself would produce radical fragments that would attack nearby tissue.[†]

Halogen azides, $X\mathrm{N_3}$, are highly unstable and decompose spontaneously and explosively. A novel feature of the decomposition is that the product, $\mathrm{N}X$, has a triplet ground state (isoelectronic with $\mathrm{O_2}$) whereas the parent azide has a singlet ground state. It is thus possible to form $\mathrm{N}X$ in a metastable electronic state, opening the possibility for the electronic energy to be harnessed. In fact, $\mathrm{NCl}(\mathrm{a}^1\Delta)$, a decomposition product of $\mathrm{ClN_3}$, has been shown to efficiently transfer energy to iodine atoms.[12,13] An iodine chemical laser based on this reaction was recently developed.[14,‡] However, little experimental work has been done to understand the reactivity of the halogen azides because of their explosive tendencies. Intuitively, there are three possible decomposition pathways for $X\mathrm{N_3}$:

$$X\mathrm{N_3}(\tilde{\mathrm{X}}\,{}^1\mathrm{A}') \longrightarrow \mathrm{N}X(\mathrm{a}^1\Delta) + \mathrm{N_2}(\mathrm{X}^1\Sigma_g^+) \tag{1}$$

$$\longrightarrow \mathrm{N}X(\mathrm{X}^3\Sigma^-) + \mathrm{N_2}(\mathrm{X}^1\Sigma_g^+) \tag{2}$$

$$\longrightarrow X(\mathrm{X}\,{}^2\mathrm{S};\mathrm{X}\,{}^2\mathrm{P}_{3/2}) + \mathrm{N_3}(\tilde{\mathrm{X}}\,{}^2\Pi_g) \tag{3}$$

For the remainder of this dissertation, X = H, F, and Cl. Reaction (1) proceeds adiabatically along the singlet surface, generating electronically excited $\mathrm{N}X(\mathrm{a})$. The diabatic reaction, (2), is spin-forbidden and produces ground state $\mathrm{N}X(\mathrm{X}^3\Sigma^-)$. The location of the singlet–triplet crossing (intersystem crossing) and coupling between the states determines which reaction dominates during thermal (and explosive) decomposition. Few investiga-

---

[*] Halogen free.

[†] This process is possible and viable, but not likely given the non-selective nature of the treatment.

[‡] The NCl-I laser is an analogue of the chemical-oxygen-iodine-laser (COIL), which is capable of multimegawatt continuous-wave output. Visit www.airbornelaser.com for more information.

tions have probed the location and energy of the singlet–triplet crossing, and these have produced conflicting results (*vide infra*).

HN_3 has received the majority of the experimental and theoretical attention. Most of the previous work has focused on the photochemistry and photodissociation dynamics, which are minimally applicable to this dissertation. Only recently has tunable infrared laser radiation become commonly available. Even so, azides do not appear to be high on the list of target molecules.

Reviews[1,15,16] of the azide literature note that bonding in covalent compounds is closer to the N–N≡N Lewis structure, where the N–N single bond is considerably longer and weaker than the N≡N triple bond and the N_α–N_β–N_γ bond angle is slightly less than 180°.[17] As the ionic character of the A–N_3 bond increases, the N_3 moiety becomes increasingly linear. In the limit of $A^+N_3^-$, the N_3^- product is linear with equal N_α–N_β and N_β–N_γ bond lengths (isovalent with CO_2). ^{14}N nuclear magnetic resonance (nmr) spectroscopy has shown that the N_α, N_β, and N_γ atoms are not equivalent in several covalent azides but become increasing equivalent as the ionic character increases.[18] Figure 1.1 shows the typical Lewis structures of ionic and covalent bonding in azides. It has been proposed that the decomposition pathway of ionic azides proceeds through cleavage of the M–N_3 bond while covalent azides decompose through cleavage of the YN–NN bond,[8] but several counter-examples have been found.[19] It is apparent that the A–N_α and N_α–N_β bond strengths are comparable and, during distortion from equilibrium, the N_β–N_γ bond strength increases at the expense of the other N_α–N_β bond.

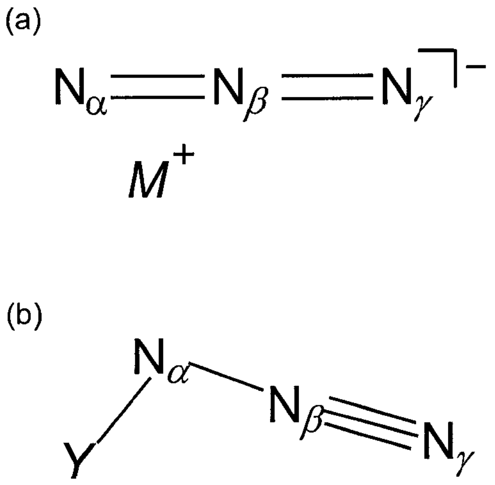

Figure 1.1 Lewis structures for (a) ionic and (b) covalent bonding of azides.

Halogen azides are planar because of a delocalized π orbital over the entire molecule. The trans geometry results from hyperconjugation between the $\sigma_{X\text{-}N_\alpha}$ bond and $\pi^*_{N_\beta\text{-}N_\gamma}$. This strengthens the N_α–N_β bond and weakens the N_β–N_γ bond as shown in Figure 1.2.

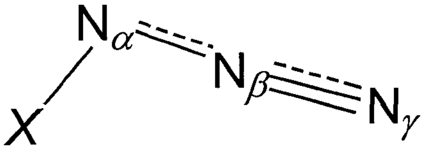

Figure 1.2 Lewis structure of XN_3.

The ground state geometry, vibrational energies, and reaction enthalpies were previously calculated for XN_3 (X = H, F, Cl, Br, I) at the MP2/6-31G(d,p) and MP2/LANL1DZ+P level of theory.[16] The results were found to be in agreement with the limited experimental data available, indicating that the level of theory is sufficient to explain halogen azides in their ground state geometry.

Current understanding of HN_3

Our understanding of the photodissociation dynamics of HN_3 (and HNCO) is evolving both experimentally[20] and theoretically.[21] A summary of the current picture is presented here. Photolysis of HN_3 with $\lambda > 200$ nm probes the $\tilde{A}$ state, which correlates adiabatically with NH(a) and N_2(X). Excess energy is observed to partition into N_2 rotation (approximately 30 % of the available energy) but always in the vibrational ground state. NH had $\langle J \rangle = 6$ and was populated up to $v = 3$ vibrational levels. J and v are the rotational and vibrational quantum numbers, respectively. Ab initio calculations show that the $\tilde{A}$ state potential energy surface (PES) has is different from the ground state: whereas the dihedral angle is at a minimum at 180° in the ground state, there is a double minimum at 120 and 240° in the excited state. The $\angle$HN–N–N is a minimum is at $\approx 172°$ in the ground state and at $\approx 90°$ in the excited state. These result in the dissociation proceeding on a non-planar PES, which induces rotation of N_2 and vibrational excitation of NH. N_2 is found to rotate in the plane of the original molecule (***J***, the angular momentum vector, is perpendicular to the molecular plane *and* to the dissociation coordinate) while a small out-of-place force decouples the NH rotation from the molecular plane, resulting in near-equal populations of the A' and A" (in the C_s point group) Λ-doublets in NH(a), *vide infra.* Dissociation to H + N_3 also occurs. In this case, the H-atom, initially at 108.8° from the N_3 chain, is directed along a 90° dissociation pathway as it recoils. This induces bending of

N_3 ($\upsilon_2 \leq 2$), which is attributed to N_3 being highly displaced from its ground state geometry, $D_{\infty h}$, cf. Figure 1.1(b).

Thermal decomposition of HN_3 proceeds exclusively via Reaction (2) to ground state products because of the relative location of the singlet–triplet crossing and singlet dissociation maximum.[22,23] Being approximately 5 000 cm^{-1} higher in energy, the Boltzmann population available to proceed along the singlet surface is very small compared to that at the singlet–triplet crossing. Even considering the low crossing probability, the population difference ensures that Reaction (2) dominates. Shock tube experiments estimated the singlet–triplet crossing to be at 12 700 ± 600 cm^{-1} and the crossing probability to be between 10^{-3} and 10^{-2},[23,*] based on a comparison of the pre-exponential factor with the expected factor derived from Transition State theory. Computationally, the singlet–triplet transition probability was calculated to be 0.003,[24] within the range proposed above. Vibrational overtone experiments[25,26,27] also determine that (2) has a dissociation barrier of 12 700 cm^{-1} and further predict an enthalpy of reaction of 5 250 cm^{-1}. Reaction (1) is predicted to have a dissociation energy, D_0, of greater than 18 800 cm^{-1}. Vibrationally mediated dissociation dynamics experiments show that both (1) and (2) remain planar during dissociation,[28] which has been explained through the exclusive formation of NH(a) with A' symmetry.[29,30]

The energy of Reaction (3) has been experimentally[31] determined to be 34 600 cm^{-1} and theoretically proposed to be 29 800 cm^{-1},[32] 31 000 ± 200 cm^{-1},[33] and 30 970 ± 50 cm^{-1}.[34] Despite the systematic difference between experiment and theory, this pathway is not thermally accessible compared with (1) and (2). Reaction (2) is thus the lowest energy decomposition pathway but with a sufficiently high barrier that HN_3 is stable and can be stored for long periods without noticeable decomposition.[35]

---

[*] Unless otherwise stated, ab initio calculations reported energy differences without correction for zpe and experimental calculations intrinsically include zpes.

Recently, fully relaxed[*] ab initio calculations have been conducted on HN_3 at the CASSCF/cc-pVDZ level of theory.[32,†] Decomposition along Reaction (1) to NH(a) is found to have a 1 400 cm^{-1} maximum along the dissociation coordinate with a limiting dissociation energy of 16 930 cm^{-1}. The singlet–triplet transition of Reaction (2) was found to be at 14 210 cm^{-1} and ultimately endothermic by 4 700 cm^{-1}. Interestingly, fixed theoretical calculations sometimes calculate the energy of the singlet–triplet crossing to be *lower* than the relaxed calculation above, depending on the level of theory: 12 300 to 13 500 cm^{-1},[30] 15 950 cm^{-1},[24] and 13 830 to 16 890 cm^{-1}.[29] The singlet dissociation energy was found to be 14 170 cm^{-1}.[24] There are obvious differences between the experimental and theoretical estimates of the singlet–triplet crossing and singlet dissociation energy.

Electronic states of HN_3

The electronic configuration of ground state HN_3 is

$$\begin{array}{lll} \text{occupied:} & 1a'^2\ 2a'^2\ 3a'^2\ 4a'^2\ 5a'^2\ 6a'^2\ 1a''^2\ 7a'^2\ 8a'^2\ 9a'^2\ 2a''^2 & A' \\ \text{unoccupied:} & 10a'\ 3a''\ 11a'\ 12a' & \end{array} \tag{4}$$

The 1a' to 3a' molecular orbitals (MOs) correspond to the 1s atomic orbitals (AOs) on nitrogen. The 4a' to 12a' MOs are linear combinations of the 1s orbital of hydrogen and the 2s, $2p_x$, and $2p_y$ (in-plane) orbitals of nitrogen. The 1a" to 3a" MOs are formed from the $2p_z$ (out-of-plane) orbitals on nitrogen.

The electronic configuration of the products, N_2 and NH, are given in (5). Standard notation and notation consistent with the C_s symmetry of HN_3 are given. (the π orbitals are given in square brackets)

---

[*] *Fixed* calculations hold one or more molecular parameter (bond lengths, angles, or dihedrals) constant to decrease the number of optimized variables and increase computational speed. Fixed calculations were common when geometry optimizations were computationally expensive. Even today, molecular parameters far from the center of interest are sometimes held constant in larger molecules (organometallic ligands and proteins, for example).

A *relaxed* calculation optimizes all molecular parameters. The calculations for this dissertation are relaxed unless specified otherwise.

The energies from fixed calculations are inevitably higher than from relaxed calculations.

[†] Ab initio nomenclature is presented in Chapter 2.

$$\begin{array}{lll} \mathrm{N_2}\text{: } 1\sigma^2\, 2\sigma^2\, 3\sigma^2\, 4\sigma^2\, 5\sigma^2\, 1\pi^4 = 1a'^2\, 2a'^2\, 3a'^2\, 4a'^2\, 5a'^2\, [6a'^2\, 1a''^2] & & A' = {}^1\Sigma_g^+ \\ \mathrm{NH}\text{: } 1\sigma^2\, 2\sigma^2\, 3\sigma^2\, 1\pi^2 & = 1a'^2\, 2a'^2\, 3a'^2\, [4a'\, 1a''] & A'' = {}^3\Sigma^- \\ & = 1a'^2\, 2a'^2\, 3a'^2\, [4a'\, 1a''] & A'' = {}^1\Delta \\ & = 1a'^2\, 2a'^2\, 3a'^2\, 2^{-1/2}([4a'^2 - 1a''^2]) & A' = {}^1\Delta \\ & = 1a'^2\, 2a'^2\, 3a'^2\, 2^{-1/2}([4a'^2 + 1a''^2]) & A' = {}^1\Sigma^+ \end{array} \qquad (5)$$

The ${}^1\Delta(A')$ and ${}^1\Sigma^+(A')$ states are linear combinations of two configurations because the individual configurations, $4a'^2$ and $1a''^2$, do not have the same symmetry as the molecular symmetry.[30,36,*]

Coupling between singlet and triplet states involves, predominantly, spin-orbit operator, $\hat{\mathscr{H}}_{\mathrm{SOC}}$, and the spin-spin operator, $\hat{\mathscr{H}}_{\mathrm{SS}}$. Theory to explain coupling between states of different multiplicity in polyatomics is poorly developed. However, the same theory is better developed in diatomics.[37] The diatomic wavefunctions in (5) can be used to approximate the ground state wavefunction of HN_3. The product of the N_2 wavefunction and a linear combination of the ${}^1\Delta$ and ${}^1\Sigma^+$ states result in the A' ground state of HN_3.

$$\Psi\left(\mathrm{HN_3}\left({}^1A'\right)\right) \approx \Psi\left(\mathrm{N_2}(\mathrm{X})\right)\frac{1}{\sqrt{2}}\left[\Psi\left(\mathrm{HN}\left({}^1\Delta\right)\right) + \Psi\left(\mathrm{HN}\left({}^1\Sigma^+\right)\right)\right] \qquad (6)$$

This same conclusion can also be arrived at through symmetry arguments, which further dictate which angular momentum eigenstates should be observed (F_1 and F_3),[30] which are the only states observed.[25]

Because the ground state can be written as a combination of electronic states, it becomes possible to estimate the coupling of the ${}^1A'$ and ${}^3A''$ states of HN_3. Diatomic selection rules for $\hat{\mathscr{H}}_{\mathrm{SOC}}$ ($\Delta\Lambda = 0$ or ± 1) show that spin-orbit coupling between the ${}^1\Delta$ and ${}^3\Sigma^-$ states is zero. $\Psi\left(\mathrm{N_2}(\mathrm{X})\right)$ does not couple through $\hat{\mathscr{H}}_{\mathrm{SOC}}$ because of the spatial separation; therefore $\Psi\left(\mathrm{N_2}(\mathrm{X})\right)$ can be extracted and integrated to unity.

---

[*] Single configuration methods cannot accurately predict the energy of these states. Multi-configurational methods must be used.

$$\begin{aligned}
&\left\langle \Psi\left(\mathrm{HN_3}\left({}^1\mathrm{A}'\right)\right)\middle|\hat{\mathscr{H}}_{\mathrm{SO}}\middle|\Psi\left(\mathrm{HN_3}\left({}^3\mathrm{A}''\right)\right)\right\rangle \\
&\approx \left\langle \Psi(\mathrm{N_2(X)})\frac{1}{\sqrt{2}}\left[\Psi\left({}^1\Delta\right)+\Psi\left({}^1\Sigma^+\right)\right]\middle|\hat{\mathscr{H}}_{\mathrm{SO}}\middle|\Psi(\mathrm{N_2(X)})\Psi\left({}^3\Sigma^-\right)\right\rangle \\
&\approx \frac{1}{\sqrt{2}}\left[\left\langle \Psi\left({}^1\Delta\right)\middle|\hat{\mathscr{H}}_{\mathrm{SO}}\middle|\Psi\left({}^3\Sigma^-\right)\right\rangle+\left\langle \Psi\left({}^1\Sigma^+\right)\middle|\hat{\mathscr{H}}_{\mathrm{SO}}\middle|\Psi\left({}^3\Sigma^-\right)\right\rangle\right] \\
&\approx \frac{1}{\sqrt{2}}\left[\qquad 0 \qquad +\left\langle \Psi\left({}^1\Sigma^+\right)\middle|\hat{\mathscr{H}}_{\mathrm{SO}}\middle|\Psi\left({}^3\Sigma^-\right)\right\rangle\right] \\
&\approx \frac{1}{\sqrt{2}}\left\langle \Psi\left({}^1\Sigma^+\right)\middle|\hat{\mathscr{H}}_{\mathrm{SO}}\middle|\Psi\left({}^3\Sigma^-\right)\right\rangle
\end{aligned} \tag{7}$$

From (7), it is evident that, in the diatomic limit, coupling between the singlet and triplet states in HN_3 exists for the NH($b^1\Sigma^+$) state but not NH($a^1\Delta$). Coupling between $^1\Sigma^+$ and $^3\Sigma^-$ in NH has been estimated at 65 cm^{-1}.[38] Application of (7) predicts a spin-orbit coupling constant of 46 cm^{-1}. Ab initio calculations estimate a coupling constant of 40 cm^{-1},[24] the difference resulting from incomplete consideration of spin-orbit coupling and lack of consideration of spin-spin coupling. The limited agreement herein is because of the many approximations and is, unfortunately, representative of the current 'state-of-the-art' calculations. See **Singlet–triplet coupling** on page 137 for additional examples and discussion.

[H,N,C,O] *analogs of* HN_3

The isomers of [H,N,C,O] are isoelectronic with HN_3 and have received more attention than azides. The ground state geometry of the known isomers is summarized in Table 1.1. All are singlets with a trans-planar geometry. Apart from HNCO, which is stable, HCNO has only been observed in the gas phase and HOCN and HONC in matrix isolation experiments.[39,40] Isomerization was found to occur through NCO ring formation, but whether one concludes the ring is an intermediate or a transition state is dependent on the computational method employed.[41,42,43,44] Notably, energies at the B3LYP/6-31++G(d,p) and QCISD/6-31++G(d,p) levels of theory were within 4 % of the respective 6-311++G(d,p) energies.[45] This suggests that the 6-31++G(d,p) basis set is sufficient to analyze the [H,N,C,O] isomers.

Table 1.1 Isomers, geometries, and relative energies of [H,N,C,O] isomers. All molecules adopt a trans-bent geometry with a dihedral angle of 180°. Bond lengths are in angstroms (± 0.01 Å) and angles in degrees (± 2°). (Uncertainties represent the range of different experimental and theoretical methods.) Methods for (a) B3LYP/6-311G(d,p) (References 41 and 45), (b) QCISD/6-311G(d,p) (Reference 45), and (c) MRD-CI/6-31G(d,p)//UHF/6-31G(d,p) (Reference 44).

Isomer		Geometry	Energy /(kJ/mol)
HNCO	isocyanic acid	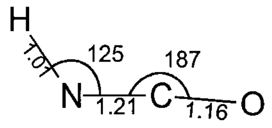	0.0;[a] 0.0;[b] 0.0[c]
HOCN	cyanic acid	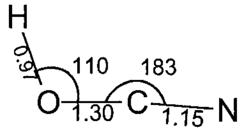	120;[a] 94;[b] 96[c]
HCNO	fulminic acid	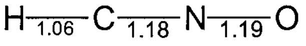	284;[a] 303;[b] 331[c]
HONC	isofulminic acid	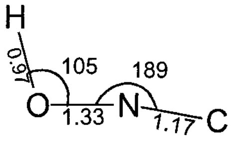	364;[a] 343;[b] 382[c]

HNOC and HCON were either very weakly bound or dissociative (method dependent) to their respective NH + CO and CH + NO products. Experimentally, neither of these species, the NOC radical, nor ion has been observed.[46]

Even though the relative energy of the [H,N,C,O] isomers in Table 1.1 show a strong dependence on the method used, the errors are systematic and cancel when determining relative quantities. The energy differences within a given method (reaction enthalpies, etc.) are within 10 % of experiment.[47]

Several groups have determined the dissociation barrier for the HNCO analog of Reaction (2)[48,49] to be 42 750 ± 30 cm^{-1} and Reaction (3)[49,50,51] to be 38 400 ± 80 cm^{-1}. It is evident that the HN–CO bond is much stronger than the analogous HN–NN bond while the H–NCO bond is comparable to the H–N$_3$ bond strength.

Current understanding of FN_3 and ClN_3

FN_3 is synthesized by the reaction of F_2 with HN_3 or NaN_3.[52,53] Ultraviolet photolysis of FN_3 at 193 nm produced NF(X,a,b) + N_2(X,A,B).[54,*] Even when the fluence is well below that necessary for photobleaching, repeated photolysis of the same system fails to produce emission, indicating that photolysis initiates a chain process that removes the remaining FN_3. Furthermore, FN_3 is observed to decompose to N_2F_2 with a half-life of one hour at 14 °C and 150 Torr.[55] The proposed mechanism assumes the rate-determining step is unimolecular decomposition of FN_3 and imposes a lower limit to the dissociation barrier of 7 700 cm^{-1}.[†] Flow reactor and infrared laser-initiated experiments show that FN_3 undergoes self-sustained thermal decomposition with NF(a) being the only(?; *infra*) electronically excited product. Theoretical work on FN_3 has verified that the ground state is a singlet but estimates the barrier to dissociation via Reaction (1) to be between 2 750 and 5 650 cm^{-1}, again dependent on the level of theory employed, and significantly below the value expected based on the observed lifetime.[56,57,58,59,60,†,‡]

To the best of my knowledge, no experiment has been conducted to look explicitly for NF(X). Emission from NF(a) was observed during thermal decomposition.[61] Concurrent collaborative theoretical work predicted the singlet–triplet crossing to occur beyond the singlet dissociation maximum.[59] Subsequent researchers interpret this to mean that FN_3 dissociates solely to excited state species. It will be shown in this dissertation that the sin-

---

[*] Contrary to convention, N_2(A,B) refers to the two lowest *triplet* states of N_2.

[†] A barrier height of 7 700 cm^{-1} was determined from unimolecular Transition State theory (see **Unimolecular dissociation** on page 141). An alternate approach (steady state kinetics) is taken in Reference 55 that yields a barrier height of 5 080 cm^{-1}. Such a barrier height would result in a kinetic half-life of ten milliseconds, *not* one hour!

[‡] Often, theoretical work is of questionable value. For example, Reference 56 studies FN_3 using a broad array of ab initio methods: MP*n*, QCISD(T), SOICCI, MRCI, CCSD(T), MCSCF, and CASPT2 with basis sets from 6-31G(d) to 6-311G(2df,2pd). Several novel(?) cyclic isomers of FN_3 and transition states between the open and cyclic isomers were identified. However, geometries were optimized with one method and energies calculated with another. This is standard practice for similar methods, but prone to failure for dissimilar ones. The authors further fix the dissociation coordinate such that NF dissociates perpendicular to N_2 in a T-configuration. This is likely a high-order process, but vibrational analysis at the transition state was not reported. In the paper, the authors calculate the singlet–triplet crossing along *their* dissociation coordinate to be 5 000 ± 1 400 cm^{-1}. (Uncertainty is one standard deviation; 16 observations.)

glet–triplet crossing occurs on the bound portion of the potential well and that more experimental work is needed to resolve this issue.

ClN_3 is synthesized by the reaction of NaN_3 with Cl_2.[62] Similar in behavior to FN_3 and illustrative of the instability of halogen azides, photolysis of a 40 mL volume of 0.1 mole % ClN_3 mixture in argon at 300 nm initiates the decomposition of all the ClN_3 in an 11 L bulb.[63] The same experiment on HN_3 did not produce the same result. Photolysis of ClN_3 at 193 and 249 nm was observed to generate NCl(X,b) and N_2(X,A).[64] The authors comment that NCl(a) may have been produced and not observed given its low emission probability. N_2(A) and NCl(b) are observed to have many quanta of vibrational energy. Recent work has shown that, interestingly, photolysis at 193 nm does not initiate chain decomposition while photolysis at 249 nm does.[65,66] A recent study at 203 nm used velocity map imaging to determine the total energies of Reactions (1) and (2) to be 1 690 ± 560 cm^{-1} and -7 500 ± 650 cm^{-1}, respectively, and the NCl(a) branching ratio to be 0.78.[67] If the excited singlet state is dissociative, the branching ratio is a crude estimate of the coupling between the singlet and triplet states.

Thermal dissociation of ClN_3 produces NCl(a) and less than 0.1 % NCl(b) relative to NCl(a).[35,57] The barrier to dissociation was estimated from the ClN_3 decay profile to be 6 370 ± 550 cm^{-1} and the NCl(a) yield at 12 % from modeling the time-resolved reactant profiles. Theoretical work by these authors at the HF/6-31G* level of theory estimates the dissociation barrier of Reaction (1) to be 5 440 cm^{-1} for ClN_3 and 3 840 cm^{-1} for FN_3. As discussed in the footnote on page 75, these values are low given the observed stability of ClN_3. The singlet–triplet crossing was proposed to exist at the maximum of the singlet dissociative surface, permitting only a single pass through the crossing region during dissociation. Other theoretical calculations predict that little NCl(X) is produced during thermal decomposition and that the barrier exists on the dissociative portion of the PES.[35]

Related halogen azides

No studies were found that investigated the decomposition of BrN_3. However, BrN_3 does react differently when exposed to other halogen atoms. Whereas ClN_3 reacts with Cl to produce N_2(A),[68] the reaction of BrN_3 with F, Cl, and Br generates NBr(b).[69,70] The first reaction is consistent with cleavage of the Br–N_3 bond and emission from tertiary reaction of N + N_3 where N is produced from secondary reaction of $2N_3$ radicals.[71] The second reaction is consistent with cleavage of the BrN–NN bond, suggesting that the Br–N_3 bond is the stronger.

Again, no studies investigating the decomposition of IN_3 were found. However, the chemical reactivity of IN_3 has been explored more than other halogen azides.[1] Interestingly and unlike the other halogen azides, solid IN_3 is polymeric, with iodine bridging two N_α atoms to create a zigzag $\text{-}[\text{I–N}_\alpha]\text{-}$ backbone.[72]

In summary, it is evident that the reactivity of ClN_3 is similar to that of FN_3, but significantly different than HN_3, and that there exists much uncertainty as to the location of the singlet–triplet crossing and the branching ratio between N*X*(a) and N*X*(X). This dissertation examines the dissociative PESs in Reactions (1) to (3) for HN_3, FN_3, and ClN_3. Determination of the reaction energy and location of the singlet-triplet crossing will allow for the unimolecular dissociation rate and thermal branching ratio for Reactions (1) to (3) to be calculated. Enthalpies of reaction and formation are also calculated. It must be noted that HN_3 has been studied at higher levels of theory than used herein. Those previous theoretical (and experimental) results are used as a standard by which to compare the results of the methods employed herein. It is assumed that if HN_3 can be reasonably represented, the methods are also valid for FN_3 and ClN_3. The available computational power was insufficient to extend the calculations to include heavier halogens.

2. COMPUTATIONAL CHEMISTRY[*]

In all of quantum mechanics, the only chemical system that can be solved exactly is that of the one-electron atom (H, He^+, Li^{2+}, …). Approximations are made to obtain solutions for all other systems. The type, number, and level of approximation and degree to which they affect the results are system dependent and scale inversely with the size of the system. Quantum mechanical calculations on small systems — H_2 and He — provide results that rival experiment whereas calculations on protein-guest interactions in solution are fraught with uncertainty. And then there is everything else. Various approximations are made to make calculations on larger systems tractable; once defined and validated for a series of molecules, the approximations become a quantum mechanical *method.* For an arbitrary system, one way to determine if a method is reasonable is to compare results obtained with similar systems for which experimental data are available and *assume* that the interactions do not change significantly in the unknown system. This is the approach taken herein.[†]

Apart from the acceptance of the postulates of quantum mechanics, computational chemistry makes several assumptions regarding molecular systems: the wavefunction is assumed to be separable into space and time components, relativistic effects are not considered, and the Born-Oppenheimer approximation is made. The first is reasonable if no time-dependent perturbations exist, such as laser pulses shorter than or of the same timescale as nuclear relaxation. Relativistic effects increase on the order of Z^4, where Z is the atomic number and, while only the core electrons are relativistic, the increased coulombic interaction shrinks the s and p orbitals and expands the d and f orbitals.[‡] Relativistic

---

[*] References 73 to 78 were used to prepare this chapter; individual citations are omitted. Other sources are cited as required.

[†] Alternatively, calculations could be conducted on systems so far removed from physical reality that experimental verification is impossible.

[‡] The radial component of the wavefunction (hydrogenlike) is proportional to $m_e e^{-m_e}$ where m_e is the mass of the electron. As m_e increases relativistically, the radial component tends to zero faster, shrinking the orbital. Core s and p orbitals shrink because of their closeness to the nucleus (s more so than p). Valence s and p orbitals shrink to maintain orthogonality with the respective core orbitals. d and f orbitals expand because of the increased effective nuclear shielding and orthogonality.

effects can be approximately corrected or neglected by ① using relativistically corrected orbitals, ② using the relativistic effective core potential (ECPs), ③ perturbatively correcting for relativistic effects, or ④ ignoring them if relative results are desired. The Born-Oppenheimer (BO) approximation is valid if the nuclear motion is slow compared with the electronic motion. The BO approximation allows the total wavefunction, Ψ, to be separated into electronic and nuclear terms: Ψ_{elec} and Ψ_{nuc}. Computational chemistry solves only for Ψ_{elec}.

Equation (8) gives the Hamiltonian, $\hat{\mathscr{H}}$, for a multinuclear, multielectron system that contains kinetic, $\hat{T}$, and potential, $\hat{V}$, energy operators for the electrons and nuclei.*

$$\begin{aligned}\hat{\mathscr{H}} &= \hat{T}_e + \hat{T}_N + \hat{V}_{eN} + \hat{V}_{ee} + \hat{V}_{NN} \\ &= -\frac{\hbar^2}{2m_{\text{e}}}\sum_{\mu}\nabla^2_{\mu} - \frac{\hbar^2}{2}\sum_{A}\frac{\nabla^2_A}{m_A} - \sum_{\mu}\sum_{A}\frac{Ze^2}{4\pi\varepsilon_0 r_{\mu A}} + \sum_{\mu}\sum_{\nu>\mu}\frac{e^2}{4\pi\varepsilon_0 r_{\mu\nu}} + \sum_{A}\sum_{A>B}\frac{Z_A Z_B e^2}{4\pi\varepsilon_0 r_{AB}}\end{aligned} \tag{8}$$

Other terms can be added to treat other interactions such as spin-orbit coupling,† spin-spin coupling,† and interactions with external fields. Often these are treated perturbatively, as small corrections to (8).

The electronic Hamiltonian reduces to

$$\begin{aligned}\hat{\mathscr{H}}_{\text{elec}} &= \hat{T}_e + \hat{V}_{eN} + \hat{V}_{ee} \\ &= -\frac{1}{2}\sum_{\mu}\nabla^2_{\mu} - \sum_{\mu}\sum_{A}\frac{Z}{r_{\mu A}} + \sum_{\mu}\sum_{\nu>\mu}\frac{1}{r_{\mu\nu}}\end{aligned} \tag{9}$$

where the Hamiltonian has been written in atomic units, where the following constants have a value of unity: $\hbar$, m_{e}, e, a_0, and $4\pi\,\varepsilon_0$. In this system, energy is obtained in hartrees (E_{H}). (1 hartree is equal to $2.195 \cdot 10^5$ cm^{-1} or 2 626 kJ/mol.)

---

* Lowercase variables refer to electrons and uppercase variables refer to nuclei.

† Spin interactions are relativistic in origin.

Wavefunctions, orbitals, and electronic configurations[*]

The electronic wavefunction can be approximated as the sum of n one-electron *spin-orbitals*, (10).[†] Spin-orbitals are the product of a MO (ϕ) and a spin function, $(\alpha\,|\,\beta)$,[‡] operating on a given electron, μ.[§] Two spin-orbitals exist for every MO: $\phi_i(\mu)\alpha(\mu)$ and $\phi_i(\mu)\beta(\mu)$.[**] The square of each spin-orbital, $\varphi^*\varphi\,\mathrm{d}\tau$, is the probability of finding an electron in the volume $\mathrm{d}\tau$ of that orbital. The square of the wavefunction, $\Psi^*\Psi\,\mathrm{d}\tau$, is the probability of finding any electron in the volume $\mathrm{d}\tau$. However, the probability attributed to $\Psi^*\Psi\,\mathrm{d}\tau$ is valid only if the MOs are independent, i.e., there is no correlation between electrons. Integrated over all space, $\langle\Psi|\Psi\rangle$ equals the number of electrons in the system.

$$\Psi_{\text{elec}} = \Psi = \sum_{i=1}^{n} \varphi_i(\mu) \tag{10}$$

The indistinguishability of the electrons requires that exchange of any two electrons must not affect the observable properties of the system. The fermion nature of electrons requires that the wavefunction be antisymmetric with respect to exchange of any two electrons. Thus, the observed probability, $\langle\Psi|\Psi\rangle$, remains unchanged. For the simplest case of two electrons in two spin-orbitals, two possible combinations exist

---

[*] Notation is not consistent between texts. The conventions in Reference 79 are adopted herein and given below.

χ	atomic orbital / basis function	$1, 2, \mu, \nu$	range variables involving electrons
ϕ	molecular orbital	$r, s, \ldots$	range variables for atomic orbitals
ψ, Ψ	molecular wavefunction	$i, j, \ldots$	range variables for molecular orbitals
		$A, B, \ldots$	range variables involving nuclei

[†] The 'elec' subscript on Ψ_{elec} is dropped unless differentiation is necessary.

[‡] $(\alpha\,|\,\beta)$ reads 'alpha or beta spin'.

[§] Spin-orbitals generally refer to molecular orbitals. There is no restriction to that, nor is there a restriction to having molecular orbitals on a single nucleus (core or non-bonding).

[**] For brevity, spin-orbitals are often written in simpler terms or a new function is defined (φ, below). Both are incorporated into this dissertation. The former is used when it is important to distinguish between α and β spin-orbitals. φ is used when the distinction is not critical.

$$\phi_i(\mu) = \phi_i(\mu)\alpha(\mu) \qquad \varphi_{2i}(\mu) = \phi_i(\mu)\alpha(\mu)$$
$$\bar{\phi}_i(\mu) = \phi_i(\mu)\beta(\mu) \qquad \varphi_{2i+1}(\mu) = \phi_i(\mu)\beta(\mu)$$

$$\begin{aligned} \Psi_{12} &= \varphi_i(1)\varphi_j(2) \qquad \text{(electron 1 in orbital } i\text{; electron 2 in orbital } j\text{)} \\ \Psi_{21} &= \varphi_i(2)\varphi_j(1) \qquad \text{(electron 1 in orbital } j\text{; electron 2 in orbital } i\text{)} \end{aligned} \tag{11}$$

The wavefunctions in (11) distinguish between the electrons, and exchange of electrons converts between Ψ_{12} and Ψ_{21} instead of returning the antisymmetric wavefunction. They cannot be used to describe the system. However, the linear combination

$$\begin{aligned} \Psi &= \frac{1}{\sqrt{2}}\left(\varphi_i(1)\varphi_j(2) - \varphi_i(2)\varphi_j(1)\right) \\ &= \frac{1}{\sqrt{2}}\begin{vmatrix} \varphi_i(1) & \varphi_j(1) \\ \varphi_i(2) & \varphi_j(2) \end{vmatrix} \end{aligned} \tag{12}$$

has electrons as a superposition of two configurations (indistinguishable) and satisfies the antisymmetric requirement. Interchanging electrons 1 and 2 results in $\Psi \rightarrow -\Psi$. The determinant in (12) is the simplest *Slater determinant*, (SD).

A Slater determinant is an electronic configuration.

In a Slater determinant, spin-orbitals are arranged in columns and electrons in rows. Only the n occupied spin-orbitals are included in the Slater determinant (see **Configuration interaction** on page 93). Slater determinants ensure that the wavefunction obeys the Pauli exclusion principle (no two electrons in the same spin-orbital) and that the wavefunction is antisymmetric with respect to exchange of any two electrons. This is dictated by the properties of determinants: if any two columns are identical (i.e., two electrons occupying the same spin-orbital), the determinant is zero; interchanging any two rows corresponds to interchanging two electrons and results in the determinant having the opposite sign (i.e., corresponding to the antisymmetric property of the wavefunction). The general form is

$$\Psi^{\mathrm{SD}} = \frac{1}{\sqrt{n!}}\begin{vmatrix} \varphi_1(1) & \varphi_2(1) & \cdots & \varphi_n(1) \\ \varphi_1(2) & \varphi_2(2) & \cdots & \varphi_n(2) \\ \vdots & \vdots & \ddots & \vdots \\ \varphi_1(n) & \varphi_2(n) & \cdots & \varphi_n(n) \end{vmatrix} \tag{13}$$

It is possible to write the Slater determinant with increasing brevity.

$$\begin{aligned}\Psi^{\mathrm{SD}} &= \left|\varphi_1(1)\varphi_2(2)\cdots\varphi_n(n)\right\rangle \\ &= \left|\varphi_1\,\varphi_2\cdots\varphi_n\right\rangle\end{aligned} \tag{14}$$

The first expression in (14) reports the diagonal elements of the determinant in Dirac notation. The second removes the electrons since each orbital is occupied and electrons are indistinguishable. The normalization constant is implied in both.

If an arbitrary function can be expressed as a linear combination of orthonormal functions, the orthonormal functions form a *complete set.* In quantum mechanics, MOs are expressed as a linear combination of AOs, where an infinite number of AOs form a complete set. In practice, only a finite number (k) of AOs are used because of computational limitations. The greater the number, the more 'complete' the set and the better the reproduction of the true MO.

$$\begin{aligned}\phi_i &= \sum_{r=1}^{\infty} c_{ir}\,\chi_r \approx \sum_{r=1}^{k} c_{ir}\,\chi_r \\ \varphi_i &\approx \sum_{r=1}^{2k} c_{ir}\,\chi_r\end{aligned} \tag{15}$$

The optimum coefficients, c_{ir}, of the AOs are determined variationally and subject to the constraint that the resultant MOs remain orthogonal (see Appendix B).

Basis sets

Basis sets are mathematical approximations of AOs.

Consider the hydrogen atom, for which the Schrödinger equation can be solved exactly. The radial component* of the wavefunction has the form

---

* The wavefunction has the form $\Psi = R_n^l(r)Y_l^{m_l}(\theta,\phi)$, where the radial, $R_n^l(r)$, and angular, $Y_l^{m_l}(\theta,\phi)$, components are separable and separately integrate to unity in $\int R^* R\,\mathrm{d}r$ and $\int\int Y^* Y \sin(\theta)\mathrm{d}\theta\,\mathrm{d}\phi$. In this context, ϕ is the angle in the *xy* plane and *not* the atomic orbital, (15).

$$R_{nl}(r) = \sqrt{\frac{(n-l-1)!}{2n(n+l)!^3}} \left(\frac{2Zr}{n}\right)^l L_{n+l}^{2l+1}\left(\frac{2Zr}{n}\right) \mathrm{e}^{\frac{-Zr}{n}} \tag{16}$$

where n and l are the principal and azimuthal quantum numbers and $L_m^{(\alpha)}(x)$ is the generalized Laguerre polynomial. Z is the atomic number ($Z = 1$ for hydrogen). The pre-exponential factor controls the amplitude at short distances from the nucleus and e^{-kr} controls the amplitude at longer distances (k is readily deduced from (16)). The outer edge of the orbital is most important for bonding. The inclusion of Z for heavier nuclei in (16) generates *hydrogenlike orbitals*.

The angular component, $Y_l^{m_l}(\theta, \phi)$, of the wavefunction are a group of functions known as *spherical harmonics*, which have the general form

$$Y_l^{m_l}(\theta,\phi) = \sqrt{\frac{2l+1}{4\pi}\frac{(l-|m_l|)!}{(l+|m_l|)!}}\, P_l^{|m_l|}(\cos(\theta))\, e^{i m_l \phi} \tag{17}$$

where m_l is the projection of l onto the z axis (often simply m) and $P_\nu^\mu(z)$ is the associated Legendre function. Equation (17) is a complex function; linear combinations can be taken to obtain real orbitals.

A simplified version of hydrogenlike orbitals is *Slater orbitals* (SOs), (18). They also have the form $\mathrm{e}^{-\zeta r}$ but do not have the Laguerre function, which is replaced by an empirical function to give the best outer-orbital edge. SOs do not have the same internal profile (nodes) as hydrogenlike orbitals.

$$R_{nl}^{\mathrm{SO}}(r) = \frac{(2\zeta)^{n+1/2}}{\sqrt{(2n)!}}\, r^{n-1}\, \mathrm{e}^{-\zeta r} \tag{18}$$

ζ is the *orbital exponent*, an empirical parameter that best fits the function to a hydrogenlike orbital or experimental data. SOs work well for monatomic systems, but are very inefficient for larger systems since multicenter integrals of (18) are difficult to evaluate. Consequently, SOs are rarely used.

Gaussian-type orbitals (GTOs) are almost exclusively used in place of SOs. The cartesian form is used to avoid working with imaginary numbers and is given by

$$g_{abc}(\alpha) = \left(\frac{2\alpha}{\pi}\right)^{3/4} \sqrt{\frac{(8\alpha)^{a+b+c}\, a!\, b!\, c!}{(2a)!(2b)!(2c)!}}\, x^a\, y^b\, z^c\, \mathrm{e}^{-\alpha r^2} \tag{19}$$

where $\{a, b, c\} \in (0, 1, 2, \ldots)$ and the sum, $a + b + c$, is the angular momentum of the orbital. α in GTOs represents the orbital exponent (not the electron spin), and $r^2 = x^2 + y^2 + z^2$. The $\mathrm{e}^{-\alpha r^2}$ dependence in GTOs is a poor approximation of $\mathrm{e}^{-\zeta r}$, but is analytically integrable. To obtain a better fit, a few gaussians with different α are grouped together to form a contracted gaussian-type function (CGTF), χ,[*] where the GTO is now called a *primitive gaussian* or simply a *primitive*. The *contraction coefficients*, d_{rx}, in (20) are the contribution of each GTO to the basis function and are determined by fitting the basis function to the AO represented as a hydrogenlike orbital, Slater orbital,[†] numerical estimate of the orbital, or fit to experimental data, and ensure the CGTF remains normalized.[‡] Despite the increased number of functions, calculations are faster using CGTFs.

$$\chi_r = \sum_x d_{rx}\, g_x(\alpha) \tag{20}$$

MOs are thus given by

$$\varphi_i = \sum_r c_{ir}\, \chi_r = \sum_r c_{ir} \sum_x d_{rx}\, g_x(\alpha) \tag{21}$$

For example, three GTOs are combined to form a valence 2s orbital of carbon in the 6-31G basis set as shown in (22).

---

[*] The term *basis function* refers to the mathematical function used to represent the atomic orbital. Hydrogenlike, CGTFs, and SOs are basis functions.

[†] A CGTF obtained from fitting to a Slater orbital (SO) is referred to as a *Slater-type orbital* (STO). Some references make no distinction between Slater orbitals, (18), and Slater-type orbitals of the form (20), which causes confusion.

[‡] Some CGTF basis sets are *not* normalized. GAUSSIAN (the ab initio program used in this dissertation) renormalizes them in an early step of the calculations.

$$\chi_{2s}^{\mathrm{C}} = -0.12\left(\frac{2\cdot 7.87}{\pi}\right)^{\frac{3}{4}} e^{-7.87r^2} - 0.16\left(\frac{2\cdot 1.88}{\pi}\right)^{\frac{3}{4}} e^{-1.88r^2} + 1.14\left(\frac{2\cdot 0.54}{\pi}\right)^{\frac{3}{4}} e^{-0.54r^2} \quad (22)$$

The wavefunction* for the hydrogenlike, Slater,[80] and CGTF (6-31G basis set†) orbitals of carbon are plotted in Figure 2.1. The 1s (core) functions are similar for all the orbitals. However, there are notable differences for the valence orbitals. ① The electron density at the nucleus for the s orbitals is very poorly reproduced (the 2s SO fails to have electron density at the nucleus and the CGTFs magnitude is very low at the nucleus). ② SOs and CGTFs fail to reproduce the internal probability and nodal distribution, focussing instead on fitting the outer edge of the orbital, which is the most important in bonding. ③ SOs and CGTFs are not orthogonal. ④ CGTFs also have greater radial extent than hydrogenlike and SOs.

Basis sets contain one or more basis functions for each AO. When one basis function is used, the basis set is a *minimum basis* or single-ζ (zeta). When two, three, or more basis functions are used, the basis set is double-ζ, triple-ζ, etc.

Since the involvement of the core orbitals in bonding is minimal (and often fixed at zero in quantum mechanical calculations), it is not necessary to define these orbitals with the same degree of accuracy as the valence orbitals. Split-valence basis sets apply a single-ζ basis set to the core orbitals and higher-ζ basis sets to the valence orbitals. The notation 6-31G refers to a split-valence basis set where the core orbitals are represented by one basis function of six gaussians while the valence orbitals are represented by two basis functions, one with three gaussians and one with one gaussian. In detail, 6-31G means 6*(core)* - (3 + 1)*(valence)* G*(gaussian functions)*. 6-311G is a triple-ζ split valence basis set. Split valence basis sets are used exclusively in this dissertation.‡

---

* Plotting as $R_n^l(r)Y_l^{m_l}(\theta, \phi)$ for hydrogenlike and SOs and as (20) for CGTFs.

† Available from www.emsl.pnl.gov:2080/forms/basisform.html

‡ Other notations exist; see Reference 81 for more information.

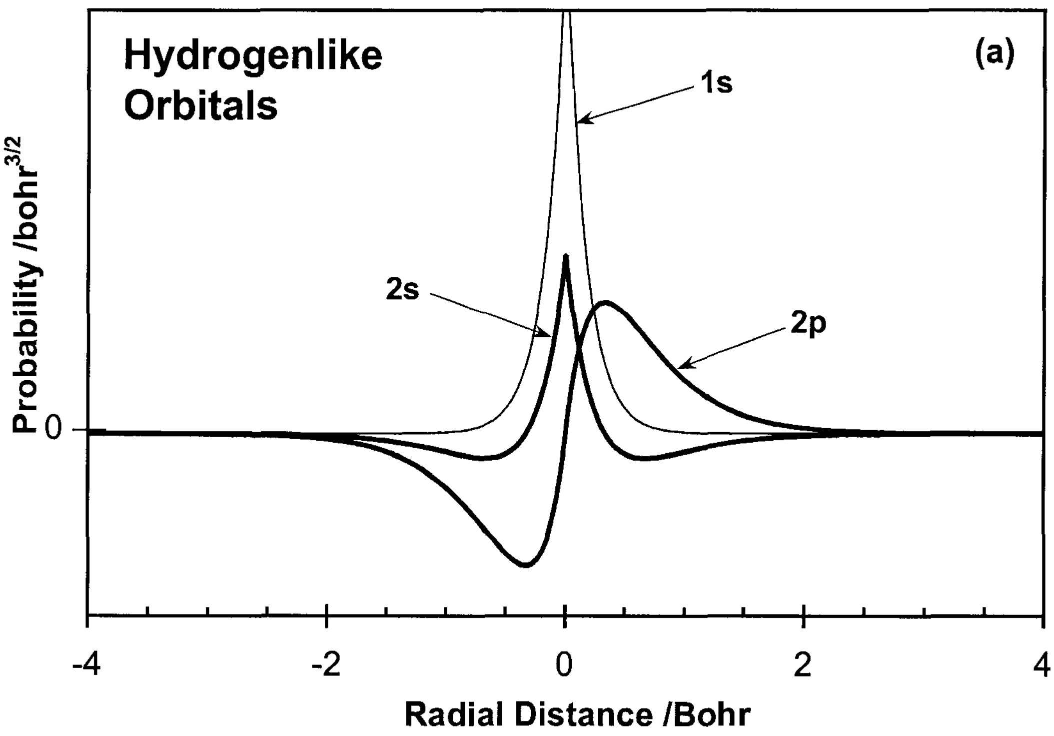
Hydrogenlike
Orbitals
(a)
1s
2s
2p
Probability /bohr$^{3/2}$
0
-4
-2
0
2
4
Radial Distance /Bohr

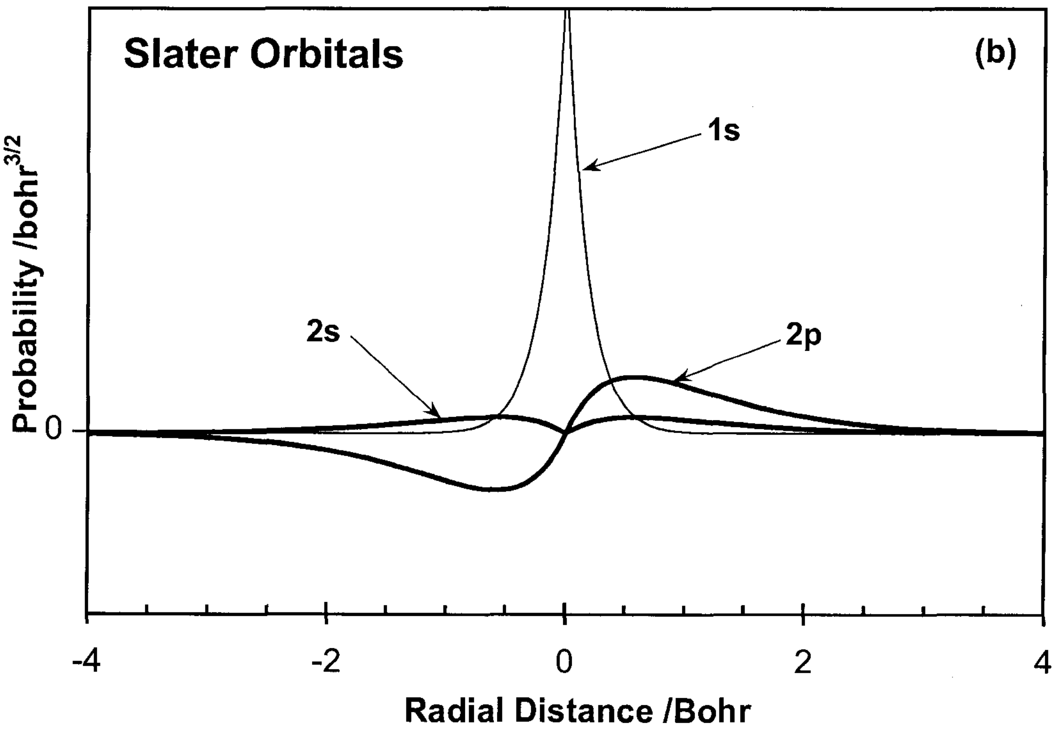
Slater Orbitals
(b)
1s
2s
2p
Probability /bohr$^{3/2}$
0
-4
-2
0
2
4
Radial Distance /Bohr

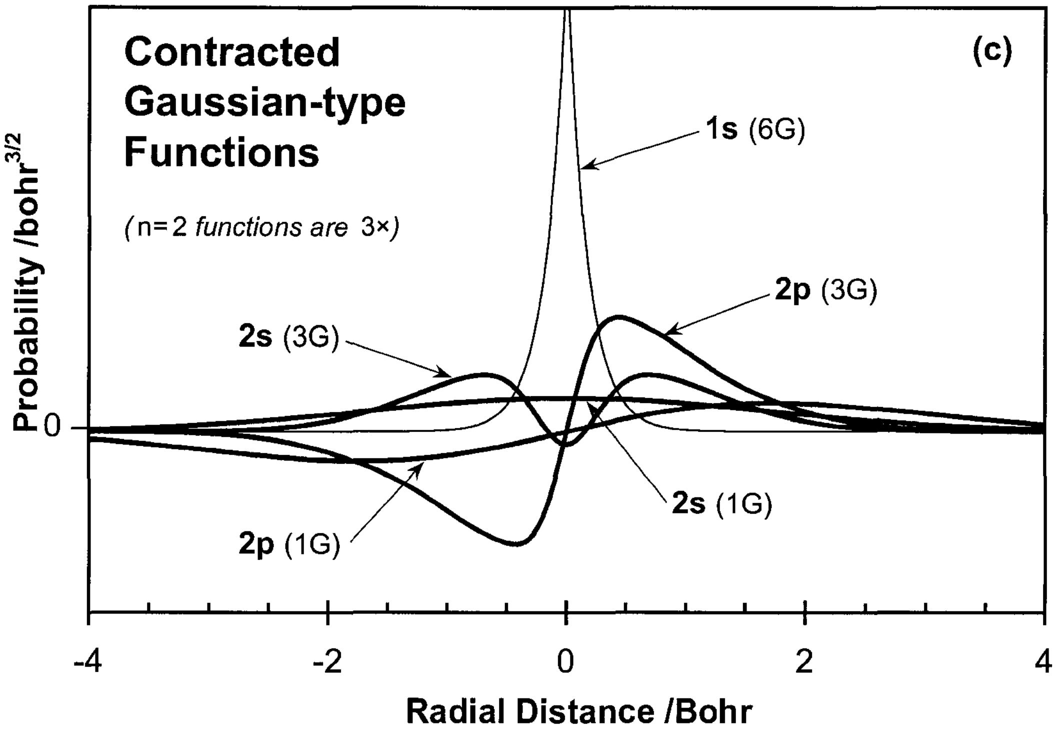

Figure 2.1 Comparison of the (a) hydrogenlike, (b) Slater, and (c) CGTFs atomic orbitals of carbon. Vertical and horizontal scales are the same, however the $n = 2$ functions in (c) are scaled 3×. (1 Bohr = 0.529177 Å)

Linear combinations of basis functions on the same atom allow electrons to be projected into or away from the internuclear region (hybridization). To give molecules more flexibility in forming bonds and in correlating electron motion, *polarization orbitals* can be added to the basis set. Polarization orbitals have higher angular momentum than the valence orbitals. For example, the notation 6-31G(d,p) adds one set of d orbitals (five basis functions) to atoms beyond hydrogen and helium (heavy atoms) and one set of p orbitals (three basis functions) to hydrogen and helium.* (d,p) polarization orbitals are

---

* It is obvious that the CGTFs are not ideal functions to represent atomic orbitals. For this reason, a large number of CGTFs are needed to obtain a reasonable approximation of the atomic orbitals and subsequently of molecular orbitals. Independent of the quality of the individual basis functions, the exact atomic orbital can be determined with a complete set of basis functions.

sometimes abbreviated with asterisks. The notation 6-311G(3df,3pd) adds three sets of d orbitals and one set of f orbitals to heavy atoms, etc.*

The orbitals in anions or electronegative regions of a molecule are larger than those in neutral regions. To address this computationally, *diffuse orbitals* can be added to each atom. Diffuse orbitals have the same angular momentum as the valence orbitals, but their orbital coefficient is smaller, meaning that they decay more slowly and can shift the radial center further from the nucleus. The notation 6-31++G adds one s and one set of p orbitals (four basis functions with small α) to heavy atoms and one s orbital to hydrogen and helium (one basis function with small α). In addition to anions and electronegative regions, diffuse functions are necessary for systems containing hydrogen bonding and Rydberg states.

Computational methods

Hartree-Fock method

The Hartree-Fock (HF) method is central to the vast majority of computational methods. Most calculations in the literature are *post-HF*, meaning that they build on the results of an initial HF calculation. Post-HF methods attempt to correct for the approximations and limitations of the HF method.

The electronic Hamiltonian for a multi-electron system is given in (9) and again in (23). The first two terms depend on only one electron while the last term is a two-electron term. HF theory replaces the n-electron wavefunction with n one-electron spin-orbitals and the multi-electron Hamiltonian operator with the one-electron Fock operator, $\hat{F}$, in (24). In HF theory, the one-electron terms are collected into a *core Hamiltonian*, $\hat{H}_{\mu}^{\text{core}}$, and the two-electron terms become *Coulomb* and *exchange* operators, $\hat{J}_i$ and $\hat{K}_i$, respectively.

---

* Adding one set of polarization orbitals, as in 6-31G(d,p) is analogous to invoking d orbitals in VSEPR theory to explain hybridization. For example, consider a bond to hydrogen along the z-axis. The 1s orbital is symmetric about the hydrogen nucleus. Mixing with a p_z orbital moves the electron density center into and away from the internuclear region.

$$\hat{\mathscr{H}}_{\text{elec}} = \underbrace{-\frac{1}{2}\sum_{\mu}\nabla_{\mu}^{2} - \sum_{\mu}\sum_{A}\frac{Z}{r_{\mu A}}}_{\text{one-electron terms}} + \underbrace{\sum_{\mu}\sum_{\nu>\mu}\frac{1}{r_{\mu\nu}}}_{\text{two-electron term}} \tag{23}$$

$$\hat{F} = \hat{H}_{\mu}^{\text{core}} + \sum_{i}\left(\hat{J}_{i} - \hat{K}_{i}\right) \tag{24}$$

The expressions for the core Hamiltonian, Coulomb, and exchange operators are given in (25). $\hat{H}_{\mu}^{\text{core}}$ calculates the kinetic energy of electron μ and its interaction with the nuclei (one-electron terms). The Coulomb and exchange operators describe electron μ's interaction with other electrons in the system. The Coulomb operator determines the average potential felt by electron μ from the electron in orbital i. The exchange operator arises from the antisymmetric properties of the wavefunction and is the potential involved in exchanging electron μ with the other electrons in the system. The mathematics is explored further in Appendix B.

$$\begin{aligned} \hat{H}_{\mu}^{\text{core}} &= -\frac{1}{2}\nabla_{\mu}^{2} - \sum_{A}\frac{Z_{A}}{r_{\mu A}} \\ \hat{J}_{i}\left|\varphi_{j}(2)\right\rangle &= \left\langle\varphi_{i}(1)\right|\frac{1}{r_{12}}\left|\varphi_{i}(1)\right\rangle\left|\varphi_{j}(2)\right\rangle \\ \hat{K}_{i}\left|\varphi_{j}(2)\right\rangle &= \left\langle\varphi_{i}(1)\right|\frac{1}{r_{12}}\left|\varphi_{j}(1)\right\rangle\left|\varphi_{i}(2)\right\rangle \end{aligned} \tag{25}$$

Each Slater determinant, (13), represents a single electronic configuration of the system. HF theory assumes that the electronic ground state is well-represented by a single Slater determinant. This is not always the case, and some systems require two or more Slater determinants to accurately represent the ground state (*vide infra*). Consideration of the contributions from other electronic configurations will lower the electronic energy by introducing more variational parameters.

The HF ground state wavefunction, Ψ_0, is formed from the first n spin-orbitals, while the remaining $2k - n$ spin-orbitals are unoccupied (*virtual*).

$$\Psi = \frac{1}{\sqrt{n!}} \begin{vmatrix} \varphi_1(1) & \varphi_2(1) & \cdots & \varphi_n(1) \\ \varphi_1(2) & \varphi_2(2) & \cdots & \varphi_n(2) \\ \vdots & \vdots & \ddots & \vdots \\ \varphi_1(n) & \varphi_2(n) & \cdots & \varphi_n(n) \end{vmatrix} \qquad (13)'$$

$$= |\varphi_1(1)\varphi_2(2)\cdots\varphi_n(n)\rangle$$

$$= |\varphi_1\,\varphi_2\cdots\varphi_n\rangle$$

The one-electron equivalent of the Schrödinger equation is the Hartree-Fock equation.

$$\hat{F}|\varphi_i\rangle = \varepsilon_i|\varphi_i\rangle \qquad (26)$$

where each spin MO is a linear combination of the AOs.

$$\varphi_i \approx \sum_{r=1}^{2k} c_{ir}\,\chi_r \qquad (15)'$$

The HF equations are solved variationally. The c_{ir} are varied to obtain the lowest ε_i for each spin-orbital while the orbitals retain their orthonormality. This is explored further in Appendix B.

Thus far, the discussion has considered each spin-orbital to be independent. In reality, two spin-orbitals originate from a single MO (see page 80). These two orbitals should have the same coefficients, c_{ir}, and do if both spin-orbitals of a given MO are either occupied or unoccupied. This leads to a simplified version of HF theory: *restricted Hartree-Fock* (RHF) theory. RHF calculations optimize only half of the Slater determinant because the energy and coefficients are the same for both spin-orbitals, resulting in considerably less computational time. *Unrestricted Hartree-Fock* (UHF) theory optimizes the α and β spin-orbitals separately and is necessary for systems with partially filled orbitals. If a UHF calculation is performed on a system that meets the requirements for RHF theory, the UHF result will be identical to the RHF result but take considerably longer. On systems with unpaired spins, the UHF calculation will find that the energy of the occupied spin-orbital is slightly below that of the corresponding unoccupied spin-orbital. One problem with UHF calculations is that α and β spin-orbitals are no longer orthogonal:

$\langle \phi_i(\mu)\alpha(\mu)|\phi_i(\mu)\beta(\mu)\rangle \neq 0$. Further, the UHF wavefunction is not an eigenfunction of the spin operator, $\hat{S}^2$, i.e., $\hat{S}^2|\Psi\rangle \neq S(S+1)|\Psi\rangle$. Comparison of $\hat{S}^2|\Psi\rangle$ with the expected $S(S+1)|\Psi\rangle$ measures the *spin contamination* in the wavefunction. Methods exist to remove the majority of the spin contamination.

The HF energy is obtained by summing the energies of the occupied orbitals and adding the nuclear energy, V_{NN}. The energy expressions differ for RHF and UHF calculations as shown in (27) and (28). See Appendix B for details.

$$E_{\mathrm{RHF}} = 2\sum_{i=1}^{n/2} H_{ii} + \sum_{i=1}^{n/2}\sum_{j=1}^{n/2}\left(2J_{ij} - K_{ij}\right) + V_{NN} \tag{27}$$

$$E_{\mathrm{UHF}} = \sum_{i=1}^{n} H_{ii} + \frac{1}{2}\sum_{i=1}^{n}\sum_{j=1}^{n}\left(J_{ij} - K_{ij}\right) + V_{NN} \tag{28}$$

H_{ii} is the core Hamiltonian one-electron integral while J_{ij} and K_{ij} are the Coulomb and exchange integrals given by

$$\begin{aligned} H_{ii} &= \langle \varphi_i(\mu)|\hat{H}_\mu^{\mathrm{core}}|\varphi_i(\mu)\rangle \\ J_{ij} &= \langle \varphi_j(2)|\hat{J}_i|\varphi_j(2)\rangle = \langle \varphi_i(1)\varphi_j(2)|\frac{1}{r_{12}}|\varphi_i(1)\varphi_j(2)\rangle \\ K_{ij} &= \langle \varphi_j(2)|\hat{K}_i|\varphi_j(2)\rangle = \langle \varphi_i(1)\varphi_j(2)|\frac{1}{r_{12}}|\varphi_i(2)\varphi_j(1)\rangle \end{aligned} \tag{29}$$

The two-electron integrals in (29) account for *static electron correlation*[*] by the *mean field approximation* (see Appendix B). These integrations determine the correlation between a given electron and the *average* position of the remaining electrons.[†] *Dynamic electron correlation* involves determining the energy in correlating the motion of the

---

[*] Static electron correlation is only considered between electrons of the same spin (Reference 77, p. 52) because of orthogonality.

[†] To understand how this correlation is accounted for, consider ensembles in statistical mechanics: all possible combinations can be obtained by examining one system over infinite time *or* an infinite number of systems frozen in time.

electrons, which tends to keep electrons further apart because of internuclear repulsion. Dynamic electron correlation is indirectly accounted for with post-HF methods, below.

Because the HF method is variational, E_{HF} is always higher than the true energy. Increasing the size of the basis set increases the number of parameters that can be variationally optimized and, consequently, results in lower energies for the species involved.* Calculations at more than one level of theory allow for extrapolation to an 'infinitely' large [complete] basis set. However, even with a complete basis set (CBS) extrapolation, HF theory converges to the Hartree-Fock limit in energy because of its incomplete treatment of electron correlation. The difference in energy between the true non-relativistic energy† and the HF energy is

$$E_{\mathrm{corr}} \equiv E_{\mathrm{true}} - E_{\mathrm{HF}} \qquad (30)$$

E_{corr} amounts to less than 1 % of the total energy, but that is on the order of chemical bond strengths. E_{corr} is therefore relevant when considering chemical processes. Configuration interaction (CI) is a common post-HF method that considers dynamic electron correlation.

---

* Unfortunately, the exact geometry, dipole moment, vibrational frequency, and other features cannot be similarly obtained.

† The 'true' non-relativistic energy is *estimated* from the experimental energy with corrections for relativistic and nuclear motion: $E_{\mathrm{true}} \approx E_{\mathrm{expt}} + E_{\mathrm{rel}} + E_{\mathrm{trans}}$

A second approximation of HF theory is that the wavefunction is expressed as a single Slater determinant, corresponding to a single electronic configuration (*vide supra*). This approximation is either valid or not, depending on the system. HF theory fails if more than one non-equivalent resonance structure can be written.* For example, two non-equivalent resonance structures for ozone are shown in Figure 2.2; the ground state has significant contribution from two electronic configurations (Slater determinants) and is therefore not amenable to solution by HF theory. The resonance structures do not need to be equally probable. Any system with resonance structures that contribute more than 10 % to the ground state wavefunction should not be analyzed with HF theory.

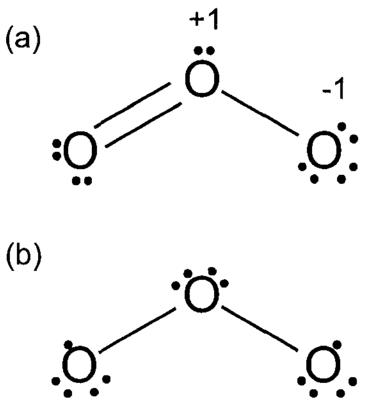

Figure 2.2 Lewis structures and formal charges of ozone.

Configuration interaction

The HF method determines the best single determinant wavefunction for the system. One method to improve on the HF result is to add more determinants and variationally solve for the coefficients, $a_0 + \sum a_i$.

$$\Psi_{\mathrm{CI}} = a_0 \Psi_{\mathrm{HF}} + \sum_{i=1} a_i \Psi_i \tag{31}$$

The configuration interaction (CI) method uses Slater determinants based on excitations from the HF ground state Slater determinant. Each determinant approximates an excited state of the system, and is classified by the number of electrons that are excited: single, double, triple, quadruple, etc. To retain symmetry consistent with the molecular symmetry, linear combinations of two or more Slater determinants may be needed. These symmetry-adapted linear combinations of Slater determinants are called *configurational state*

---

* HF methods can be used on systems with equivalent resonance structures, such as aromatic compounds.

functions (CSFs). The nature of CSFs allows all possible spin states to be formed. However, because spin is not operated on by the Hamiltonian, (8), the spin can be factored out.

$$\hat{\mathscr{H}}\left|(\alpha \mid \beta)\right\rangle = \left|(\alpha \mid \beta)\right\rangle\hat{\mathscr{H}} \tag{32}$$

This results in

$$\left\langle \phi_i(\mu)(\alpha \mid \beta)(\mu)\right|\hat{\mathscr{H}}\left|\phi_j(\mu)(\alpha \mid \beta)(\mu)\right\rangle = \left\langle(\alpha \mid \beta)\right|\left.(\alpha \mid \beta)\right\rangle\left\langle\phi_i(\mu)\right|\hat{\mathscr{H}}\left|\phi_j(\mu)\right\rangle \tag{33}$$

CSFs which differ in the number of spin states become zero. Additionally, CSFs with symmetry different from the ground state also integrate to zero. Neither is included in (31).

configuration state function (CSF) ≡ symmetry adapted Slater determinant

As with HF, CI calculations are basis set dependent, but they are also dependent on the level of excitation. Reaching the HF CBS limit requires increasing the basis set. To account for all the dynamic electron correlation and generate an *exact wavefunction* — a 'full CI' calculation — requires an infinite basis set *and* inclusion of all excitations. *THIS IS IMPOSSIBLE.* The number of possible Slater determinants is a factorial function of the number of total ($2k$) and occupied (n) orbitals in Ψ_{HF}.

$$\#\mathrm{SDs} = \binom{2k}{n} = \frac{(2k)!}{n!(2k-n)!} \tag{34}$$

For $\mathrm{HN_3}$ with a minimal basis (STO-3G, for example), $2k = 30$ and $n = 22$. There are 5 852 925 CSFs assuming each spin-orbital is optimized independently. This calculation is feasible with today's technology, but not informative since it is not near the CBS limit. Calculations using the 3-21+G** basis ($2k = 52$; $n = 38$) generates $1.8 \cdot 10^{12}$ CSFs, the 6-31++G(d,p) basis (94; 38) generates $2.9 \cdot 10^{26}$ CSFs, and the 6-311++G(d,p) basis (118; 52) generates $1.1 \cdot 10^{34}$ CSFs. The 6-311G is triple-ζ and approaches the CBS limit; however, few excitations can be considered given the number of possible spin states. Limiting the CSFs to those that have the same multiplicity and symmetry as Ψ_{HF} reduces the number by approximately an order of magnitude.

To make the calculations tractable, the number of excitations can be limited to singles, CIS, doubles, CID, singles and doubles, CISD, etc. CISD calculations generally recover 80 to 90 % of the dynamic correlation energy with triple-ζ basis sets. In addition to the CSFs removed as a result of spin and symmetry, excitations involving high energy virtual orbitals have little effect on the overall energy and molecular properties and can be excluded to reduce the number of CSFs. The exact non-relativistic CI energy can be determined by extrapolating to an infinite basis analogous to the HF CBS extrapolation.

One problem with CI calculations is that, while full CI is size extensive, truncated CI calculations are not. Consider the minimum basis systems of H_2 and $2H_2$. In H_2, it is possible to generate two singly excited CSFs and one doubly excited CSF. In $2H_2$, it is additionally possible to have single and double excitations to the 2σ orbital of the *other* H_2 molecule. Thus, it is possible to generate eight singly excited CSFs and fourteen doubly excited CSFs (and triply and quadruply excited CSFs). These additional CSFs give greater freedom to the CI calculation and the energy of $2H_2$ is *less* than twice the energy of H_2. It is possible to correct for this by adding quadratic terms to a CI calculation (QCI). The quadratic terms are estimated from the coefficients of the doubly excited coefficients, rather than being explicitly calculated.

Other post-HF methods

For completeness, CC, MCSCF, and MRCI are discussed below.

Coupled cluster (CC) calculations are a type of CI where the Slater determinants are chosen by a cluster operator. CC calculations are variational and size consistent and their results are similar in accuracy to QCI calculations. [CC is believed to be better than QCI.]

Multi-configurational self-consistent field (MCSCF; *complete active space self-consistent field* (CASSCF)) is similar to CI except that both the AO coefficient, c_{ij}, and the CSF coefficient, a_i, are simultaneously variationally optimized. Because of the large number of variables, MCSCF calculations are usually restricted to the region of interest within the larger system, such as the orbitals involved in bond breaking or bond formation — the ‘active space’.

Multi-reference configuration interaction (MRCI) is a CI calculation where excitations are considered from more than one CSF (now called *reference CSFs*). Most often, the reference CSFs are the ground-state wavefunction from an optimized MCSCF calculation (it itself is a linear combination of CSFs).

Density functional theory[*]

The molecular wavefunction considers the location of each of the n electrons in the system and formally scales as n^3 (n^4 with spin). The electron density is a function of real space and has three coordinates, independent of the number of electrons. The impact of this is obvious: the lower order scaling allows larger systems to be explored with the same computational expense. Further, no real information is lost when considering the electron density instead of the wavefunction. The additional information in Ψ is superfluous given the indistinguishability of the electrons. *Both the wavefunction and electron density completely describe the system.* Contrary to conventional ab initio methods, where all electronic configurations contribute to the ground state, a single, unique, electron density describes the ground state in DFT (and a unique electron density describes each excited state).[82] Unfortunately, the mathematical function that describes the electron density is unknown. *If* the exact electron density were known, it would return the true properties of the system, including the energy. Various approximations for the electron density form the different methods of *density functional theory* (DFT).[†] DFT is an ab initio method that variationally optimizes the electron density, $\rho(\tau)$, instead of the wavefunction, Ψ, to determine the minimum energy of the system. The electron density at a given point is the square of the wavefunction, (35).

---

[*] There is no standard notation for DFT as there is for other [more established] ab initio methods. As such, the following terms are used in addition to those in the footnote on page 80.

ρ	electron density	V_{ee}	electron-electron repulsion energy
T_e	electron kinetic energy	V_{eN}	electron-nucleus Coulomb energy

[†] A functional is a function of a function (a meta-function). Whereas $f(x)$ is a function of a scalar, a functional is $F(f)$ (often written $F[f]$). Most of quantum mechanics uses functionals, but it is explicitly noted in density *functional* theory, which has caused problems to the n^{th} degree. In the context of DFT, the density is a function of the spatial coordinates, $\rho(\tau)$, and the energy a functional of the density, $E[\rho(\tau)]$.

$$\rho(\tau_i) = n \int \ldots \int |\Psi(\tau_1 \tau_2 \ldots \tau_n)|^2 \, \mathrm{d}s_j \, \mathrm{d}\tau_k \qquad (35)$$

where $j \in \{1, 2, \ldots, n\}$ and $k \in \{1, 2, \ldots, (\neq i), \ldots, n\}$. $\rho(\tau_i)$ is integrated over all spins, s, and spatial variables, τ, *except* for τ_i.

Pioneering work on applying DFT to chemical systems was done by Hohenberg, Kohn, and Sham.[83] The energy can be written as a functional of the electron density in a form that mirrors the HF method.

$$E[\rho] = T_e[\rho] + V_{eN}[\rho] + V_{ee}[\rho] \qquad (36)$$

The functionals T_e, V_{eN}, and V_{ee} are the kinetic and potential energies of the electron density, analogous to the electronic Hamiltonian, (23). V_{eN} is known exactly within the Born-Oppenheimer approximation but T_e and V_{ee} are not. DFT assumes that the electrons are non-interacting (akin to HF theory). Approximate expressions for T_e and V_{ee} can then be found. Approximate values are given the subscript '*s*'.

$$T_s = \langle \Psi | -\frac{1}{2} \sum_{\mu} \nabla_{\mu}^2 | \Psi \rangle \qquad \text{(approximate)} \qquad (37)$$

$$\begin{aligned} V_{eN} &= \langle \Psi | \sum_{\mu} \sum_{A} \frac{Z}{r_{\mu A}} | \Psi \rangle \\ &= \sum_{A} \int \frac{\rho(r)}{r_{\mu A}} \mathrm{d}r \end{aligned} \qquad \text{(exact)} \qquad (38)$$

$$\begin{aligned} V_s &= \langle \Psi | \frac{1}{r_{12}} | \Psi \rangle \\ &= \frac{1}{2} \iint \frac{\rho(\tau_1)\rho(\tau_2)}{\tau_{12}} \mathrm{d}\tau_1 \, \mathrm{d}\tau_2 \end{aligned} \qquad \text{(approximate)} \qquad (39)$$

The first term in (38) and (39) is written in terms of the wavefunction and the second in terms of the electron density. The second term is derived by multiplying by $|\Psi\rangle\langle\Psi|$ and integrating over all variables except τ_i. This returns $\rho(\tau_i)$, (35), and a single integration variable left to integrate over.

The premise behind the Kohn-Sham approach to DFT is to express all the functions with approximate solutions and group the residuals into a single expression, the *exchange-correlation energy*, E_{xc}.*

The difference between the true and approximate expressions is defined as

$$\Delta T \equiv T_e - T_s \tag{40}$$

$$\Delta V \equiv V_{ee} - V_s \tag{41}$$

And because neither ΔT or ΔV are known [obviously], E_{xc} is defined as their sum.

$$E_{\mathrm{xc}} \equiv \Delta T + \Delta V \tag{42}$$

The energy can therefore be written as

$$E = T_s + V_{eN} + V_s + E_{\mathrm{xc}} \tag{43}$$

or in full form

$$E[\rho] = \langle \Psi | -\frac{1}{2}\sum_{\mu} \nabla_{\mu}^{2} | \Psi \rangle + \sum_{A} \int \frac{\rho(r)}{r_{\mu A}} \mathrm{d}r + \frac{1}{2} \iint \frac{\rho(r_1)\rho(r_2)}{r_{12}} \mathrm{d}r_1 \, \mathrm{d}r_2 + E_{\mathrm{xc}}[\rho] \tag{44}$$

The first three terms contribute most to the energy of the system. The final term, E_{xc}, is small in comparison (assuming the non-interacting electron approximation is reasonable). Different E_{xc} functionals form the different DFT methods commonly available.

The DFT method used herein uses separate expressions for the exchange and correlation functionals. The exchange functional, B3, is Becke's three-parameter equation given by[84,85]

$$E_{\mathrm{x}}^{\mathrm{B3}} = (1 - a_0 - a_{\mathrm{x}}) E_{\mathrm{x}}^{\mathrm{LSDA}} + a_0 \, E_{\mathrm{x}}^{\mathrm{HF}} + a_{\mathrm{x}} \, E_{\mathrm{x}}^{\mathrm{B88}} \tag{45}$$

---

* Although valid and practical, this method makes it nearly impossible to find the 'true' expression for E_{xc} since E_{xc} is the collection of many diverse residuals.

and the correlation functional given by Lee, Yang, and Parr (LYP)[86]

$$E_{\mathrm{c}} = (1 - a_{\mathrm{c}})E_{\mathrm{c}}^{\mathrm{VWN}} + a_{\mathrm{c}}\, E_{\mathrm{c}}^{\mathrm{LYP}} \tag{46}$$

where $E_{\mathrm{x}}^{\mathrm{LSDA}}$, $E_{\mathrm{x}}^{\mathrm{HF}}$, $E_{\mathrm{x}}^{\mathrm{B88}}$, $E_{\mathrm{c}}^{\mathrm{VWN}}$, and $E_{\mathrm{c}}^{\mathrm{LYP}}$ are different functionals for calculating the exchange and correlation energy. LDSA is the local spin density approximation, HF is the Hartree-Fock method, B88 is Becke's 1988 exchange energy functional, VWN is the correlation energy functional by Vosko, Wilk, and Nusair, and LYP is another energy functional by Lee, Yang, and Parr. See References 75 and 76 for more information. The values of a_0, a_{x}, and a_{c} are chosen empirically ($a_0 = 0.20$; $a_{\mathrm{x}} = 0.72$; $a_{\mathrm{c}} = 0.81$) to give good agreement with molecular atomization energies. These empirical parameters result in DFT not being considered 'ab initio' by some. However, given that atomic basis sets are often developed by fitting to atomic ionization energies, the question is that of degree of empiricism. There is no question that DFT with the true exchange-correlation functional is ab initio.

Evaluation of (44) suggests that it has the same form as the HF energy expression. A one-electron Kohn-Sham operator, $\hat{h}$, similar to the Fock operator, can be written, and an eigenvalue equation, (49), generated akin to the HF equation, (26).

$$\hat{H}_{\mu}^{\mathrm{KS}} = -\frac{1}{2}\nabla_{\mu}^{2} - \sum_{A}\frac{Z_A}{r_{\mu A}} \tag{47}$$

$$\hat{h} = \hat{H}_{\mu}^{\mathrm{KS}} + \int\frac{\rho(r_1)}{r_{\mu 1}}\mathrm{d}r_1 + V_{\mathrm{xc}} \tag{48}$$

$$\hat{h}\varphi_i = \varepsilon_i\,\varphi_i \tag{49}$$

Solution of (49) then proceeds analogous to that for HF calculations (see Appendix B).

The use of an approximate expression for E_{xc} introduces unique problems into Kohn-Sham DFT. Importantly, *DFT is solved variationally, but the true energy is not a minimum for the variational calculations because of the empirical parameters discussed above.* CBS extrapolations are thus impossible. It has also been found that E_{xc} poorly describes long-range interactions; consequently, barrier heights (activation energies) and dissociation energies are of lower accuracy than the ground state. Despite these limitations, recent work has shown that electron densities calculated with DFT best reproduce experimental electron momentum spectroscopy measurements of the electron density.[87]

Process calculations

The following methods are applied by GAUSSIAN during the ab initio calculations.

Geometry optimizations

The Born Oppenheimer approximation freezes the nuclear coordinates. However, one goal of quantum chemistry is to determine the lowest energy ground state geometry of a system. The self-consistent field (SCF) method determines the 'best' electronic wavefunction for a given nuclear configuration. Post-SCF processing of the wavefunction provides information on how the energy changes as a function of nuclear configuration: the derivative of the energy with respect to the nuclear coordinates, ∇E, estimates the direction (gradient) and distance (proportional to the magnitude of the gradient) the nuclei should move to further minimize the energy. Since the electronic wavefunction is no longer optimized at the new nuclear coordinates, the process (optimize SCF wavefunction; derivative with respect to nuclear coordinates and motion along gradient) is repeated until the gradient or change in energy is below a threshold. This indicates that the current nuclear position is a *stationary point* on the PES.

The second derivative of the energy with respect to the nuclear coordinates, $\nabla^2 E$, estimates the curvature of the energy with respect to nuclear motion. The matrix of $\nabla^2 E$ is known as the *Hessian.* If one or more second derivatives are negative, the geometry has converged to a saddle point, which is a transition state, not a minimum.

Potential energy surfaces

For every nuclear position, the minimum electronic energy is determined by solving the electronic Schrödinger equation. Energy calculations while systematically varying one or more coordinates generate a potential energy map of the system. These maps are relevant to the fundamental intra- and intermolecular interactions of the system: stability, reaction rates, energy partitioning, etc. The electronic energy is a function of the electronic configuration and different electronic configurations (excited states, states of varying multiplicity) behave differently as functions of nuclear coordinates.

N nuclei exist in $3N$ space. Transformation into a center-of-mass reference frame removes three translational dimensions. Two (linear) or three (non-linear) rotational dimensions act on the whole system and can also be considered separately. This leaves the nuclei in $3N-6$ ($3N-5$ for linear molecules) space. Two nuclei exist in one-dimensional space with the internuclear distance being the independent parameter. However, it is not readily possible to visualize the complete PES for three or more nuclei nor is it computationally possible to calculate it because of the high-dimensional space that must be sampled. In these larger systems, one or two parameters are chosen to be systematically varied.

Vibrational energies

If the energy is known as a function of nuclear coordinates, it is possible to determine its vibrational energy (and frequency). The mass-weighted Hessian provides this information. Diagonalizing the mass-weighted Hessian results in eigenvectors that are the normal vibrational coordinates with eigenvalues that are the corresponding vibrational energies. When the Hessian is not available, the energy associated with movement of each nucleus can be estimated numerically by incrementing each atom in each of the $\{x, y, z\}$ coordinates and completing a single-point calculation. This process is *exceedingly* computationally expensive.

Basis set superposition error

It was discussed above that CI calculations were not size consistent because of the truncated basis set. A similar problem occurs in all calculations because the basis functions of one fragment (atom or molecule) can mix with orbitals on another fragment to artificially lower its energy. This is known as the *basis set superposition error* (BSSE). BSSEs are larger when the fragments are dissimilar with one being well defined by the basis set and the other not. The 'unneeded' orbitals on the well-defined fragment are used to lower the energy of the less well defined fragment. With an infinite basis set, all fragment are equally well defined and there is no BSSE because the basis functions of the other fragment are superfluous.

The BSSE is dependent on the position of the nuclei, and therefore affects all calculations that compare two or more nuclear geometries: bond breakage, molecular dynamics, protein-guest interactions, different configurational isomers, etc. For a species *AB* and its fragments *A* and *B*, the interaction energy is determined from

$$\Delta_{\mathrm{rxn}}E = E_{AB}\{\chi_A + \chi_B\} - E_A\{\chi_A\} - E_B\{\chi_B\} + \Delta_{\mathrm{BSSE}}E \tag{50}$$

where $\{\chi_N\}$ is the basis set of species *N*. A BSSE arises when $\{\chi_A\}$ are extended to *B* and lower its energy. The energy rise in *A* is less than the decrease in *B*: recall that the goal is to find an energy *minimum*.

One method of approximating the BSSE, known as the *counterpoise* method, is to calculate the energy of each fragment within the complex (not at their optimized geometry; denoted by an asterisk in (51)) with their own basis set and also with both basis sets. The second basis set remains centered at the nuclear coordinates of the other fragment, i.e., the nucleus and electrons of one fragment are removed, leaving the orbitals to lower the energy of the remaining fragment. This is repeated for the other fragment(s). For two fragments, the BSSE correction is

$$\Delta_{\mathrm{BSSE}}E = E_A^*\{\chi_A + \chi_B\} + E_B^*\{\chi_A + \chi_B\} - E_A^*\{\chi_A\} - E_B^*\{\chi_B\} \tag{51}$$

Natural population analysis[88]

The SCF procedure generates a set of MOs that are eigenfunctions of the Fock operator (they diagonalize the Fock matrix) and have symmetry in accordance with molecular symmetry. However, this set is not unique and linear combinations of the MOs are equally representative of the system. The SCF MOs are delocalized over the molecule and have fractional electron occupation. It is often convenient to 'localize' MOs akin to the *valence shell electron pair repulsion* (VSEPR) model. There is more than one way to localize the MOs. *Natural population analysis* (NPA) is one commonly used technique and involves diagonalizing the first-order reduced density matrix, which is discussed further in References 73 and 76. NPA reduces the MOs to localized one and two (and sometimes three) center orbitals with integer occupancy — in agreement with our chemical intuition. The resulting orbitals are referred to as *natural atomic orbitals* (NAOs). One-center NAOs are lone electrons (core, radicals, or lone pairs, depending on the occupancy of the other spin-orbital). The remaining NAOs are involved in bonding, forming *natural bonding orbitals* (NBOs). Each NAO contribution to the NBO can be determined, resulting in an estimate of the 'hybridization' of the orbitals.

Methods employed

All species in this dissertation were studied using the GAUSSIAN 98 suite of programs.[89] Hybrid density functional calculations were performed with the Becke's three-parameter exchange functional (B3)[84,85] and the Lee, Yang, and Parr correlation functional (LYP),[86] which together become the common B3LYP method. Configuration interaction calculations used a size-consistent quadratic algorithm with single and double excitations (QCISD).[90] Geometry optimizations were conducted using three basis sets: 3-21+G**, 6-31++G(d,p), and 6-311++G(d,p), and single-point calculations were performed using the 6-311++G(3df,3pd) basis set at the 6-311++G(d,p) optimized geometry. Collectively, ab initio calculations were performed at eight different levels of theory and are referred to as the *standard methods* in this dissertation.

Table 2.1 Ab initio methods (standard methods) used in this dissertation.

Standard Methods	
UB3LYP/3-21+G**	UQCISD/3-21+G**
UB3LYP/6-31++G(d,p)	UQCISD/6-31++G(d,p)
UB3LYP/6-311++G(d,p)	UQCISD/6-311++G(d,p)
UB3LYP/6-311++G(3df,3pd)	UQCISD/6-311++G(3df,3pd)

Each calculation independently optimized all of the alpha and beta spin-orbitals. Spin contamination of the optimized geometries was occasionally 10 % prior to correction but less than 1 % after. Corrections for basis set superposition errors were made using the counterpoise method.[91,92,93] Frequency calculations and natural bond orbital[94] analyses were performed at the ground state geometry and transition states. Relaxed potential energy surfaces (PESs) were calculated for Reactions (1) to (3). The relaxed PES represents the minimum at each step along the reaction coordinate.

Appendix C reviews the procedure for optimizing the geometry using the HF and/or post-HF method.

3. AB INITIO RESULTS AND DISCUSSION

Ab initio calculations on singlet and triplet XN_3 were conducted using the standard methods in Table 2.1. One dimensional relaxed scans of the PES were carried out at the UB3LYP/6-31++G(d,p) and UQCISD/6-31++G(d,p) levels of theory and mapped the molecular geometry as the N_α–N_β and X–N_α bonds were incrementally scanned. The step-size was smaller in regions where the potential changed significantly and near the singlet–triplet crossing. Figure 3.1 illustrates the notation used to identify bond lengths and angles for the azides. The dihedral angle is unambiguous and not shown in Figure 3.1. Calculations were carried out using the standard methods to determine the energy, geometry, and vibrational energies at several *key locations*: the ground state,* singlet–triplet crossing, singlet dissociation maximum, and dissociation products. Previous work on azide systems has shown that the MP2/6-31G* method is sufficient to determine the ground state geometry and vibrational energies in agreement with experiment.[15,16,62]

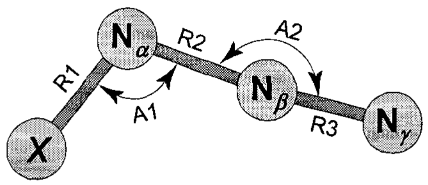

Figure 3.1 Notation used for bond lengths and angles in XN_3.

The concept adopted herein was to mirror calculations using two different computational methods: QCISD and B3LYP. If both gave similar results and results in accordance with the available experimental and theoretical literature (mostly for HN_3), we would have confidence that the results are an accurate representation of the systems under study and therefore could be extended to FN_3 and ClN_3.

Geometries

Potential energy surfaces

Relaxed PES scans of Reactions (1) to (3) are plotted in Figures 3.2 and 3.3. Scales in these Figures are the same for easy comparison. NBO analysis confirmed that the electronic configuration converged to the states indicated in Reactions (1) to (3). The total

---

* 'Ground state' refers to the bound XN_3 species.

energies of each method were offset to make the energy of the ground state geometry zero and converted to cm^{-1}. The inset in each Figure is an expansion of the singlet–triplet crossing region at the UQCISD/6-31++G(d,p) and UQCISD/6-311++G(d,p) levels of theory.

$$X\mathrm{N_3}(\tilde{X}\,^1A') \longrightarrow \mathrm{N}X(a^1\Delta) + \mathrm{N_2}(X^1\Sigma_g^+) \qquad (1)'$$

$$\longrightarrow \mathrm{N}X(X^3\Sigma^-) + \mathrm{N_2}(X^1\Sigma_g^+) \qquad (2)'$$

$$\longrightarrow X(X\,^2S;X\,^2P_{3/2}) + \mathrm{N_3}(\tilde{X}\,^2\Pi_g) \qquad (3)'$$

It is evident that the PES for HN_3 is different from that of FN_3 and ClN_3. The Singlet HN_3 PES is purely dissociative while the PESs of FN_3 and ClN_3 show a pronounced maximum at a N_α–N_β bond length of approximately 1.75 Å. The nature of the maximum is uncertain. In polyatomics, there are many variable nuclear parameters that affect the total energy (there is only one in diatomic systems). In XN_3, the multiple electronic states possible from the isoconfigurational electronic configuration (π^2) is likely a significant factor. The $a^1\Delta$ and $b^1\Sigma^+$ states are equally mixed at the singlet–triplet crossing, and, as the products separate, the mixing is reduced and the states separate in energy. The NF(b–a) and NCl(b–a) energy separation is less than the HN(b–a) separation, which may explain why no maximum in HN_3 was observed. (A small maximum is observed in some ab initio calculations.[29,32]) For all species, the triplet PES is purely dissociative and *the triplet surface crosses the singlet surface on the bound region of the potential.* This is in agreement with published work on HN_3[22,23] but contrary to theoretical calculations on FN_3.[58,61] Details of the calculations on FN_3 are limited (the original work[58] is not available), so I can only speculate that possibly a fixed scan was conducted or too small of a basis set was used. I show below that the 3-21+G** basis set is *insufficient* to describe the geometry and energies of ground state XN_3.

Figure 3.3 presents the PES scan of the X–NNN coordinate. QCISD calculations were not carried out for the entire range because of computational cost. The B3LYP calculation for HN_3 suggests a bond strength of 50 000 cm^{-1} (600 kJ/mol), which is *prima facie* high. (The bond strength of N_2 is 69 000 cm^{-1} (828 kJ/mol).[95]) The H–NNN bond dissociation

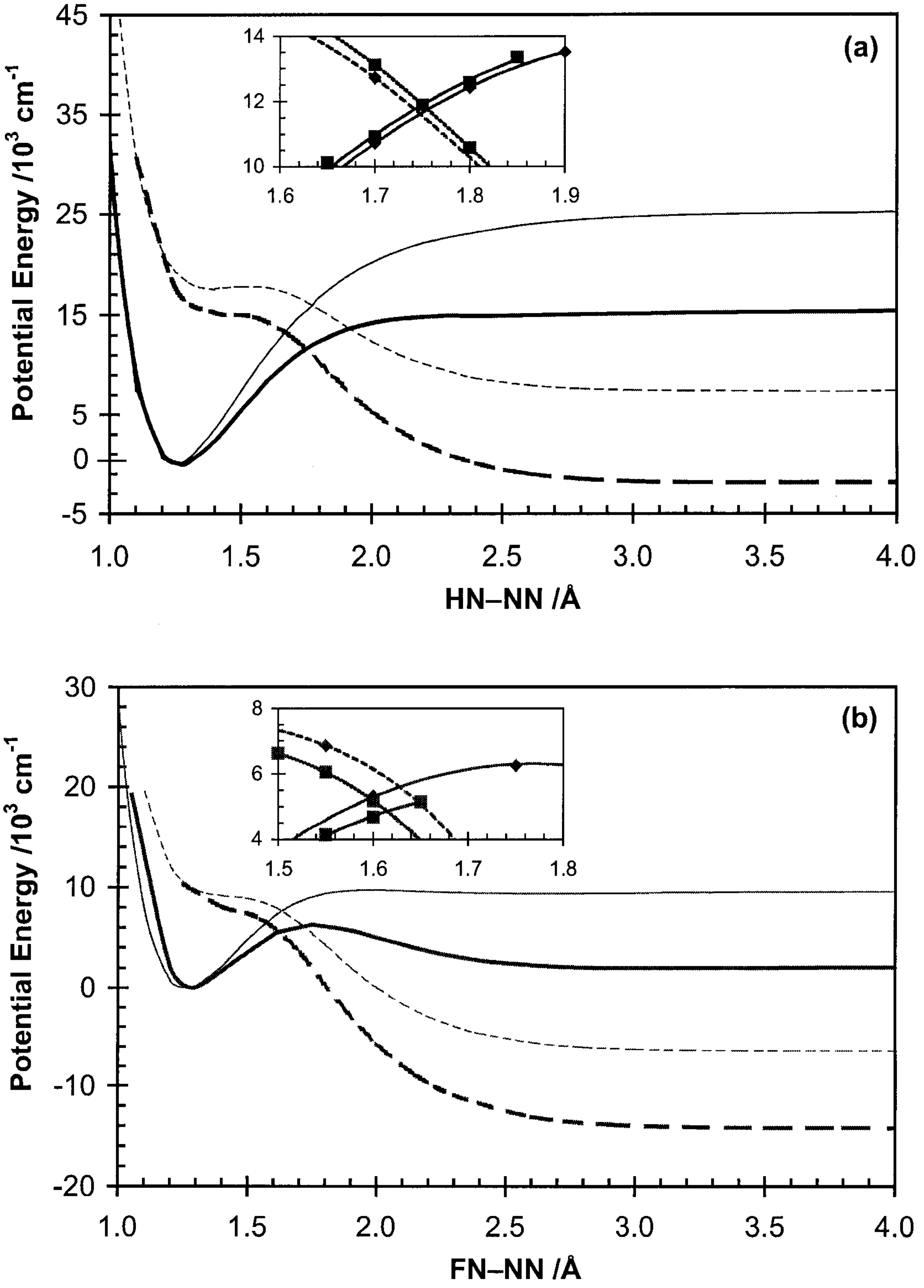
(a)
Potential Energy /10^3 cm^{-1}
45
35
25
15
5
0
-5
1.0
1.5
2.0
2.5
3.0
3.5
4.0
HN–NN /Å
14
12
10
1.6
1.7
1.8
1.9
(b)
Potential Energy /10^3 cm^{-1}
30
20
10
0
-10
-20
1.0
1.5
2.0
2.5
3.0
3.5
4.0
FN–NN /Å
8
6
4
1.5
1.6
1.7
1.8

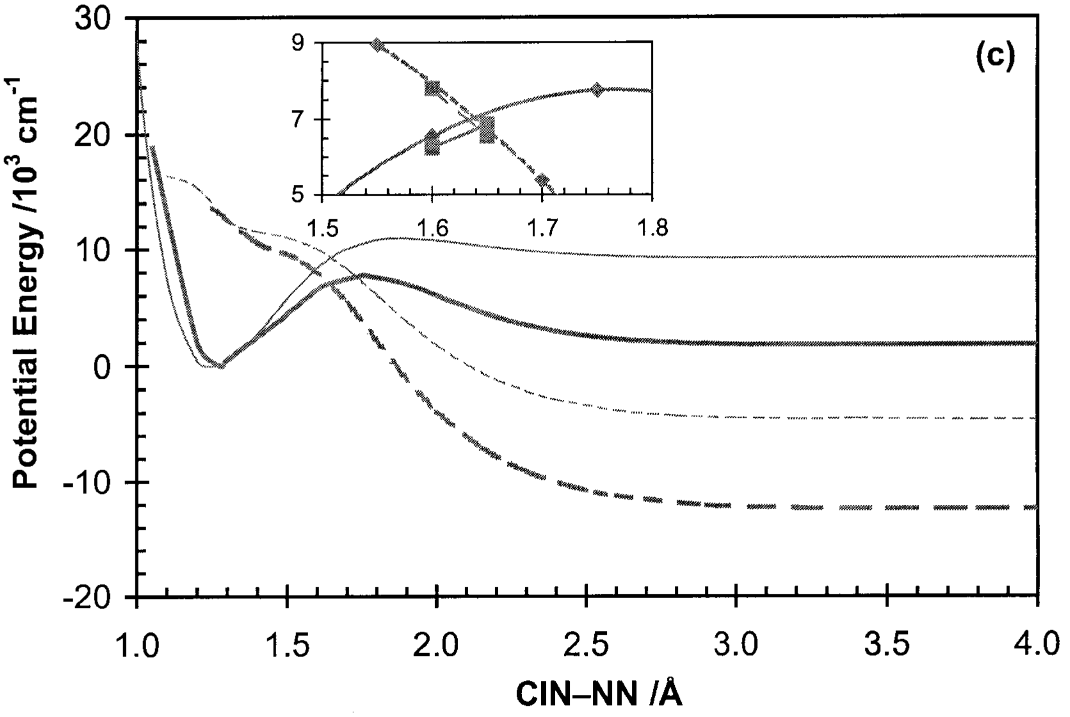

Figure 3.2 Relaxed potential energy curves (PECs) for dissociation of $X\mathrm{N_3}$ along the singlet (solid) and triplet (dashed) XN–NN pathways at the UB3LYP/6-31++G(d,p) (——) and UQCISD/6-31++G(d,p) (——) levels of theory. Inset: magnification of the singlet–triplet crossing region at the UQCISD/6-31++G(d,p) (◆) and UQCISD/6-311++G(d,p) (■) levels of theory. Shading scheme: (a) $\mathrm{HN_3}$; (b) $\mathrm{FN_3}$; (c) $\mathrm{ClN_3}$.

energy has been experimentally measured as 31 000 cm^{-1}, drawing into question the B3LYP calculation (*vide infra*). The QCISD calculations reach a lower dissociation energy for Reaction (3) but this energy is considerably higher than the barrier for Reactions (1) and (2) shown in Figure 3.2. Since the interest of this dissertation is the *thermal* dissociation of azides, no further investigation of Reaction (3) was done.

It is evident in Figures 3.2 and 3.3 that the B3LYP and QICSD energies are in agreement for locations on the PES with the N_α–N_β bond lengths up to and including the ground state geometry. The ground state geometry and vibrational energies between these methods are also in agreement (*vide infra*), indicating that both methods accurately describe ground state $X\mathrm{N_3}$. However, the B3LYP energy becomes consistently higher at N_α–N_β bond

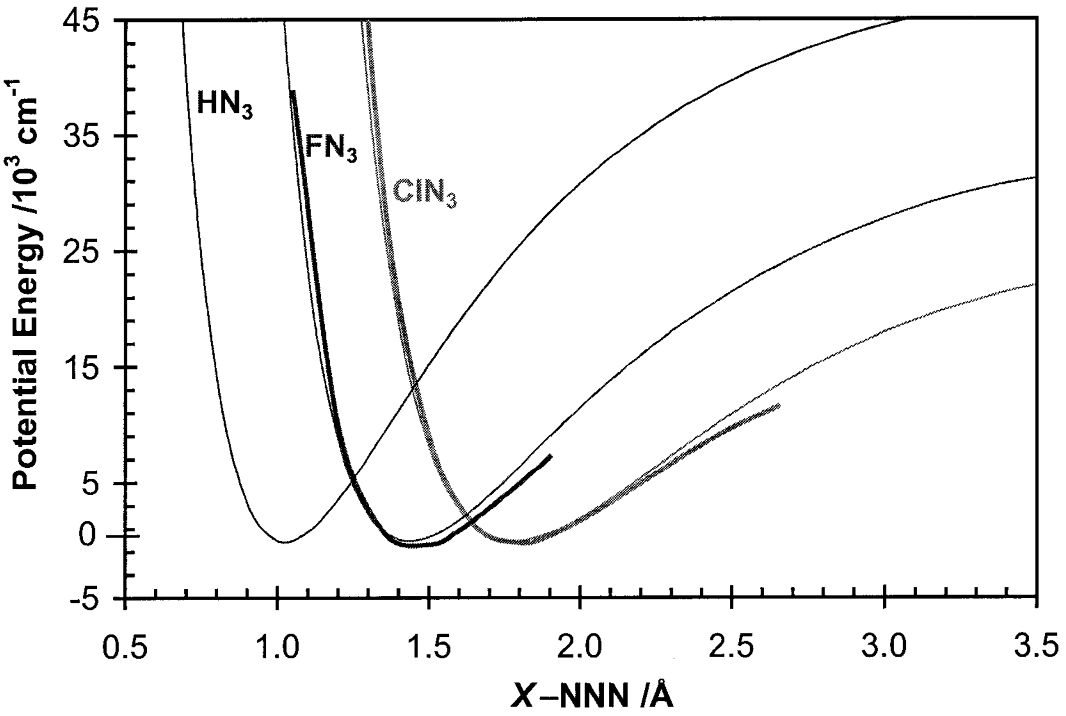

Figure 3.3 Relaxed PECs for dissociation of XN$_3$ along the X–NNN pathway (Reactions (3)) at the UB3LYP/6-31++G(d,p) (——) and UQCISD/6-31++G(d,p) (▬▬) levels of theory. Shading scheme: HN$_3$, FN$_3$, ClN$_3$.

lengths greater than the equilibrium distance. This is not because of a limited basis set, but because of B3LYP itself: DFT is poor at describing the radical nature of complexes, such as seen in transition states.[75,96] Because of the need for accurate PESs, further analysis with B3LYP was not carried out.

Geometries at key locations

These optimized geometries at the key locations are tabulated and compared with experimental values in Tables 3.1 to 3.3. All optimized dihedral angles are between 179.5 and 180.5° and are not reported in the Tables. Calculation of the geometry (and energy) at the singlet–triplet crossing is more complicated because of the different geometries of the singlet and triplet states at the fixed N$_\alpha$–N$_\beta$ bond length. Details of the approach taken to determine these values are given in Appendix D. The energy of the products was deter

Table 3.1 Ab initio and experimental geometry and energy of HN_3 in the ground state, singlet–triplet crossing, and of the dissociation products. Bond lengths in angstroms, bond angles in degrees, and energies in cm^{-1}. (a) Energies are scaled to make the energy of the optimized ground state geometry zero. Zpe corrections are not included. (b) Reference 97. The values in bold are fixed during the optimization.

HN_3	H–N_α	N_α–N_β	N_β–N_γ	H–N_α–N_β	N_α–N_β–N_γ	Energy^a
Optimized singlet ground state						
UB3LYP/3-21+G**	1.020	1.283	1.149	110.0	168.9	0
UB3LYP/6-31++G(d,p)	1.022	1.246	1.139	110.2	171.3	0
UB3LYP/6-311++G(d,p)	1.020	1.241	1.130	110.1	171.0	0
UQCISD/3-21+G**	1.011	1.347	1.152	105.5	168.2	0
UQCISD/6-31++G(d,p)	1.019	1.268	1.143	108.0	171.2	0
UQCISD/6-311++G(d,p)	1.020	1.262	1.133	107.2	170.7	0
Expt.^{b}	1.015	1.243	1.134	108.8	171.3	——
Singlet–triplet crossing						
UQCISD/6-31++G(d,p)	1.036	1.748	1.129	94.6	139.4	12 734
UQCISD/6-311++G(d,p)	1.036	1.750	1.118	94.4	139.5	13 326
Singlet reaction products						
UQCISD/6-31++G(d,p)	1.039	**10.000**	1.115	100.0	160.0	15 458
UQCISD/6-311++G(d,p)	1.039	**10.000**	1.104	100.0	160.0	15 813
Expt.^{b}	1.034	——	1.098	——	——	——
Triplet reaction products						
UQCISD/6-31++G(d,p)	1.042	**10.000**	1.115	100.0	160.0	-1 817
UQCISD/6-311++G(d,p)	1.043	**10.000**	1.104	100.0	160.0	-1 442
Expt.^{b}	1.036	——	1.098	——	——	——

mined by fixing the N_α–N_β bond length at 10 nm; this distance minimizes the interactions of the products, allows for BSSE correction, and avoids any size extensivity problems with the QCISD calculations.

Table 3.2 Ab initio and experimental geometry and energy of FN_3 in the ground state, singlet–triplet crossing, dissociation maximum, and of the dissociation products. Legend same as Table 3.1.

FN_3	F–N_α	N_α–N_β	N_β–N_γ	F–N_α–N_β	N_α–N_β–N_γ	Energy[a]
			Optimized singlet ground state			
UB3LYP/3-21+G**	1.523	1.325	1.147	102.0	172.9	0
UB3LYP/6-31++G(d,p)	1.436	1.265	1.140	104.7	171.1	0
UB3LYP/6-311++G(d,p)	1.432	1.258	1.132	105.2	170.9	0
UQCISD/3-21+G**	1.542	1.470	1.141	98.7	175.7	0
UQCISD/6-31++G(d,p)	1.446	1.286	1.144	103.2	172.4	0
UQCISD/6-311++G(d,p)	1.419	1.284	1.134	104.3	172.1	0
Expt.[b]	1.444	1.253	1.132	103.8	170.9	——
			Singlet–triplet crossing			
UQCISD/6-31++G(d,p)	1.381	1.628	1.143	101.6	134.7	7 426
UQCISD/6-311++G(d,p)	1.353	1.615	1.134	102.3	133.5	6 751
			Singlet dissociation maximum			
UQCISD/6-31++G(d,p)	1.396	1.752	1.117	101.1	170.4	6 260
UQCISD/6-311++G(d,p)	1.370	1.729	1.108	102.2	166.5	5 397
			Singlet reaction products			
UQCISD/6-31++G(d,p)	1.336	**10.000**	1.115	100.5	159.9	2 148
UQCISD/6-311++G(d,p)	1.309	**10.000**	1.104	100.0	160.0	871
Expt.[b]	1.308	——	1.098	——	——	——
			Triplet reaction products			
UQCISD/6-31++G(d,p)	1.350	**10.000**	1.115	100.6	159.9	-14 193
UQCISD/6-311++G(d,p)	1.323	**10.000**	1.104	100.0	159.9	-15 376
Expt.[b]	1.317	——	1.098	——	——	——

The ground state geometry determined using the 3-21+G** basis set is noticeably less accurate than the larger basis sets. The root-mean-square (rms) deviation* between the ab initio and experimental bond lengths is, on average, 5.1× greater for the 3-21+G** basis set, whereas the remaining basis sets have similar rms values and are in agreement with

---

* The root-mean-square of the deviation is identical to the population standard deviation but does not imply a normal distribution.

$$\mathrm{rms} = \sigma = \sqrt{\frac{1}{n}\sum_i (x_i - \mu)^2}$$

Table 3.3 Ab initio and experimental geometry and energy of ClN_3 in the ground state, singlet–triplet crossing, dissociation maximum, and of the dissociation products. Legend same as Table 3.1.

ClN_3	Cl–N$_\alpha$	N$_\alpha$–N$_\beta$	N$_\beta$–N$_\gamma$	Cl–N$_\alpha$–N$_\beta$	N$_\alpha$–N$_\beta$–N$_\gamma$	Energy[a]
			Optimized singlet ground state			
UB3LYP/3-21+G**	1.841	1.305	1.150	108.4	171.6	0
UB3LYP/6-31++G(d,p)	1.783	1.255	1.141	109.6	171.8	0
UB3LYP/6-311++G(d,p)	1.788	1.248	1.132	109.7	172.0	0
UQCISD/3-21+G**	1.861	1.416	1.146	104.6	172.7	0
UQCISD/6-31++G(d,p)	1.769	1.279	1.144	108.8	172.3	0
UQCISD/6-311++G(d,p)	1.765	1.270	1.134	108.8	171.7	0
Expt.[b]	1.745	1.252	1.133	108.4	171.6	——
			Singlet–triplet crossing			
UQCISD/6-31++G(d,p)	1.736	1.638	1.127	105.3	157.5	7 385
UQCISD/6-311++G(d,p)	1.703	1.641	1.128	106.6	135.6	8 655
			Singlet dissociation maximum			
UQCISD/6-31++G(d,p)	1.720	1.755	1.118	106.1	165.3	7 748
UQCISD/6-311++G(d,p)	1.718	1.744	1.108	106.2	164.5	7 634
			Singlet reaction products			
UQCISD/6-31++G(d,p)	1.622	**10.000**	1.115	100.0	160.0	1 892
UQCISD/6-311++G(d,p)	1.616	**10.000**	1.104	107.1	160.4	1 582
Expt.[b]	1.618	——	1.098	——	——	——
			Triplet reaction products			
UQCISD/6-31++G(d,p)	1.658	**10.000**	1.115	100.1	159.9	-12306
UQCISD/6-311++G(d,p)	1.652	**10.000**	1.104	100.0	159.9	-12589
Expt.[b]	1.640	——	1.098	——	——	——

the observed experimental results. It is evident that the 3-21+G** basis set is insufficient to accurately explain these azides. Results supporting this conclusion are given in the **Vibrational analysis** section, below. Ground state geometries calculated using the B3LYP method are of similar accuracy as the QCISD calculations, suggesting that both methods adequately and accurately represent ground state XN_3. Because of the errors with the B3LYP method noted above, the geometries at the singlet–triplet crossing, singlet dissociation maximum, and of the reaction products are only presented for the QCISD calculations using the 6-31++G(d,p) and 6-311++G(d,p) basis sets.

Vibrational analysis

Vibrational analysis was carried out at the key geometries to further validate the method and ensure that the transition states were first order saddle points that led to the correct products. The results are tabulated in Tables 3.4 to 3.6 for XN_3 and in Table 3.7 for the dissociation products.[*] *Zero point energies* (zpes) are scaled by the factors in Table 3.8. Repeated geometry optimizations on the same system resulted in slightly different converged geometries and vibrational energies. An uncertainty in the vibrational energies of ± 10 cm^{-1} can be inferred from these calculations, not considering systematic errors that are discussed below.

The vibrational energies of the ground state geometry are all real while one imaginary energy, the N_α–N_β stretch, was found at the singlet dissociation maximum, indicating a first-order transition state. The energies of the N_β–N_γ stretch and X–N_α stretch approach that of the respective diatomic, while the three bends decrease at the singlet dissociation maximum. In the diatomic limit, the energy of these bends is zero. Although vibrational analysis is only strictly valid for stationary points (minima or saddle points), vibrational

Table 3.4 Ab initio (unscaled) and experimental vibrational energies (in cm^{-1}) of HN_3 in the ground state and at the singlet–triplet crossing. (a) Reference 97. Zpes are scaled by the factors in Table 3.8.

HN_3	N_β–N_γ stretch	N_α–N_β stretch	H–N stretch	in-plane N_3 bend	out-of-plane N_3 bend	in-plane scissor	ZPE
			Optimized singlet ground state				
UB3LYP/3-21+G**	2 053	970	3 495	1 245	535	472	4 444
UB3LYP/6-31++G(d,p)	2 268	1 172	3 491	1 291	590	528	4 511
UB3LYP/6-311++G(d,p)	2 264	1 174	3 488	1 292	591	536	4 522
UQCISD/3-21+G**	1 972	742	3 605	1 251	520	465	4 313
UQCISD/6-31++G(d,p)	2 203	1 114	3 526	1 272	597	536	4 506
UQCISD/6-311++G(d,p)	2 211	1 124	3 492	1 289	594	536	4 512
Expt.[a]	2 140	1 151	3 336	1 264	607	534	4 516

---

[*] The labels in Tables 3.4 to 3.6 identify the atoms with the greatest motion during the vibration.

Table 3.5 Ab initio (unscaled) and experimental vibrational energies (in cm^{-1}) of FN_3 in the ground state, singlet–triplet crossing, and dissociation maximum. (a) Reference 97. Zpes are scaled by the factors in Table 3.8.

FN_3	N_β–N_γ stretch	N_α–N_β stretch	F–N stretch	in-plane N_3 bend	out-of-plane N_3 bend	in-plane scissor	ZPE
			Optimized singlet ground state				
UB3LYP/3-21+G**	1 938	891	829	597	460	206	2 494
UB3LYP/6-31++G(d,p)	2 156	1 149	891	663	491	240	2 700
UB3LYP/6-311++G(d,p)	2 150	1 151	880	667	492	243	2 701
UQCISD/3-21+G**	1 941	831	606	429	280	200	2 161
UQCISD/6-31++G(d,p)	2 099	1 030	880	664	509	255	2 649
UQCISD/6-311++G(d,p)	2 107	1 035	913	678	500	246	2 674
Expt.[a]	2 037	1 090	874	658	504	240	2 702
			Singlet dissociation maximum				
UQCISD/6-31++G(d,p)	2 254	443i	938	491	251	181	2 005
UQCISD/6-311++G(d,p)	2 249	456i	987	499	233	157	2 013

Table 3.6 Ab initio (unscaled) and experimental vibrational energies (in cm^{-1}) of ClN_3 in the ground state, singlet–triplet crossing, and dissociation maximum. (a) Reference 97. Zpes are scaled by the factors in Table 3.8.

ClN_3	N_β–N_γ stretch	N_α–N_β stretch	Cl–N stretch	in-plane N_3 bend	out-of-plane N_3 bend	in-plane scissor	ZPE
			Optimized singlet ground state				
UB3LYP/3-21+G**	1 945	917	472	697	498	198	2 395
UB3LYP/6-31++G(d,p)	2 178	1 197	524	711	517	213	2 579
UB3LYP/6-311++G(d,p)	2 171	1 197	519	701	515	215	2 573
UQCISD/3-21+G**	1 920	699	421	532	477	198	2 141
UQCISD/6-31++G(d,p)	2 127	1 100	544	736	530	222	2 563
UQCISD/6-311++G(d,p)	2 133	1 101	545	732	528	220	2 567
Expt.[a]	2 066	1 134	540	719	522	221	2 601
			Singlet dissociation maximum				
UQCISD/6-31++G(d,p)	2 249	505i	728	414	238	157	1 845
UQCISD/6-311++G(d,p)	2 251	512i	726	411	220	146	1 832

Table 3.7 Ab initio (unscaled) and experimental vibrational energies of singlet and triplet NH, NF, and NCl, and of N_2. (a) Experimental values taken as $\omega_e - 2\,\omega_e x_e$ from Reference 97.

	^{1}NH	^{3}NH	^{1}NF	^{3}NF	^{1}NCl	^{3}NCl	$^1N_2$
UB3LYP/3-21+G**	3289	3245	1066	1026	784	723	2295
UB3LYP/6-31++G(d,p)	3303	3259	1190	1140	883	816	2454
UB3LYP/6-311++G(d,p)	3299	3254	1184	1138	870	803	2445
UQCISD/3-21+G**	3342	3415	964	938	728	669	2204
UQCISD/6-31++G(d,p)	3357	3293	1112	1069	867	800	2369
UQCISD/6-311++G(d,p)	3325	3262	1177	1132	864	798	2370
Expt.[a]	3154	3243	1184	1141	904	827	2351

energies were also calculated at the singlet–triplet crossing and are summarized in Appendix D. They also show only one imaginary energy and the remainder of the vibrational energies are intermediate between the vibrational energies of ground state geometry and the singlet dissociation maximum and dissociation products of XN_3. Further, energies for the singlet and triplet spin-states were comparable. This strongly suggests that only one vibrational mode, the N_α–N_β stretch, maps onto the dissociation coordinate while the remaining vibrational modes remain orthogonal. This is not always the case, but fortuitous for XN_3 in that the vibrational energies calculated at the singlet–triplet crossing can be used in further calculations.

Ab initio vibrational energies assume a harmonic potential and consistently over-estimate the vibrational energy. Vibrational scaling factors can be determined by comparing the ab initio and experimental values for a group of molecules. Given the large vibrational anharmonicity evident in Figure 3.2, scaling factors were calculated by minimizing the rms deviation between the scaled ab initio *harmonic* energies and experimental *fundamental* energies of all species. These

	Scaling Factor[a,b]	Scaling Factor	RMS Deviation
UB3LYP/3-21+G**	——	1.014	103
UB3LYP/6-31++G(d,p)	0.995	0.966	36
UB3LYP/6-311++G(d,p)	0.999	0.968	37
UQCISD/3-21+G**	——	1.008	202
UQCISD/6-31++G(d,p)	0.954	0.975	52
UQCISD/6-311++G(d,p)	——	0.976	41

Table 3.8 Ab initio scaling factors calculated from XN_3 and the dissociation products with the standard methods. (a) Reference 98; (b) see text.

values and the published values[98] are summarized in Table 3.8. Scaling factors were not available for all the standard methods because of the large number of user controllable conditions and continually increasing computational power. Even for those that are available, there were small differences in the calculation and basis set (notably the lack of polarization functions). Differences between the scaling factors calculated herein and those determined from a larger data set exist. The rms deviations are in agreement with the reference rms values.[*] Because of the obvious discrepancies, the scaling factors in Table 3.8 are used in subsequent calculations involving vibrational energies.

It should be noted that scaling factors that reduce the calculated *harmonic* energy to the experimental *fundamental* energy are not exactly the same as those that calculate the experimental zpe.[98,†] The difference is minimal, and the same scaling factor is used for both.

The vibrational energies calculated using the 3-21+G** basis set vary more and differ from those with larger basis sets, which are generally close together in energy. The rms deviation between the scaled ab initio and experimental vibrational energies for the 3-21+G** basis set is, on average, 4.7× larger than the larger basis sets, for both methods. It is evident that the 3-21+G** basis set is insufficient to accurately explain these azides. Consequently, it was not used in further calculations.

---

[*] Ab initio vibrational energies are least well calculated for compounds with multiple bonds, affecting N_2 and several XN_3 modes in this dissertation.

[†] For example, consider the fundamental transition energies of the harmonic oscillator (ab initio) and Morse potentials: ω and ($\omega_e - 2\omega_e x_e$), respectively. Zpes for these models are $\omega/2$ and ($\omega_e/2 - \omega_e x_e/4$). Let the scaling factors, s, be defined as

$$s\,\omega = \omega_e - 2\omega_e x_e \qquad \text{fundamental}$$

$$s'\frac{\omega}{2} = \frac{\omega_e}{2} - \frac{\omega_e x_e}{4} \qquad \text{zero - point energy}$$

It is evident that s and s' are not identical, differing by $1.5\omega_e x_e$.

$$\frac{s}{s'} = \frac{\omega_e - 2\omega_e x_e}{\omega_e - \tfrac{1}{2}\omega_e x_e}$$

Energy partitioning in dissociation products

The PECs in Figure 3.2 show that energy is released during the dissociation of XN_3, moreso for FN_3 and ClN_3. We can estimate how this energy is partitioned into internal modes of the products by observing how the optimized geometry changes along the dissociation coordinate. This investigation is qualitative since only one dimension of the PES has been probed and an impulsive dissociation model is assumed. This model proposes that energy stored as a result of different optimized geometries between the reactants and products is retained in that mode.

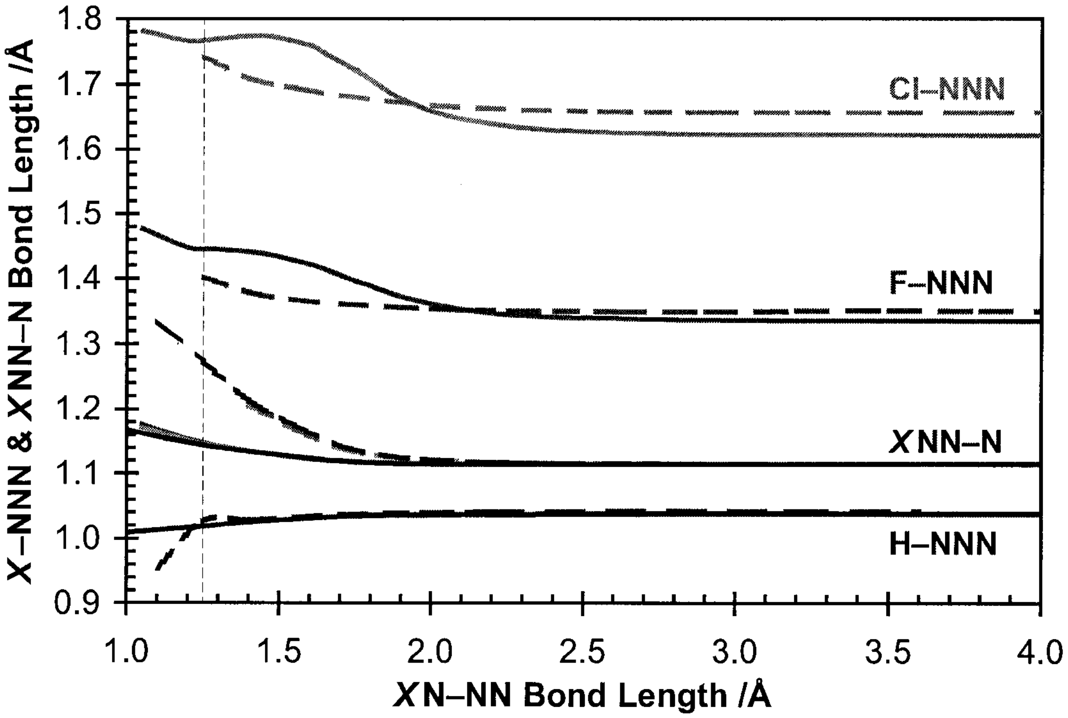

Figure 3.4 Optimized X–N_α and N_β–N_γ bond lengths during XN_3 dissociation along the singlet (solid) and triplet (dashed) XN–NN pathways (Reactions (1) and (2)) at the UQCISD/6-31++G(d,p) (———) levels of theory. Shading scheme: HN_3, FN_3, ClN_3. The vertical dashed line is the approximate equilibrium N_α–N_β bond length.

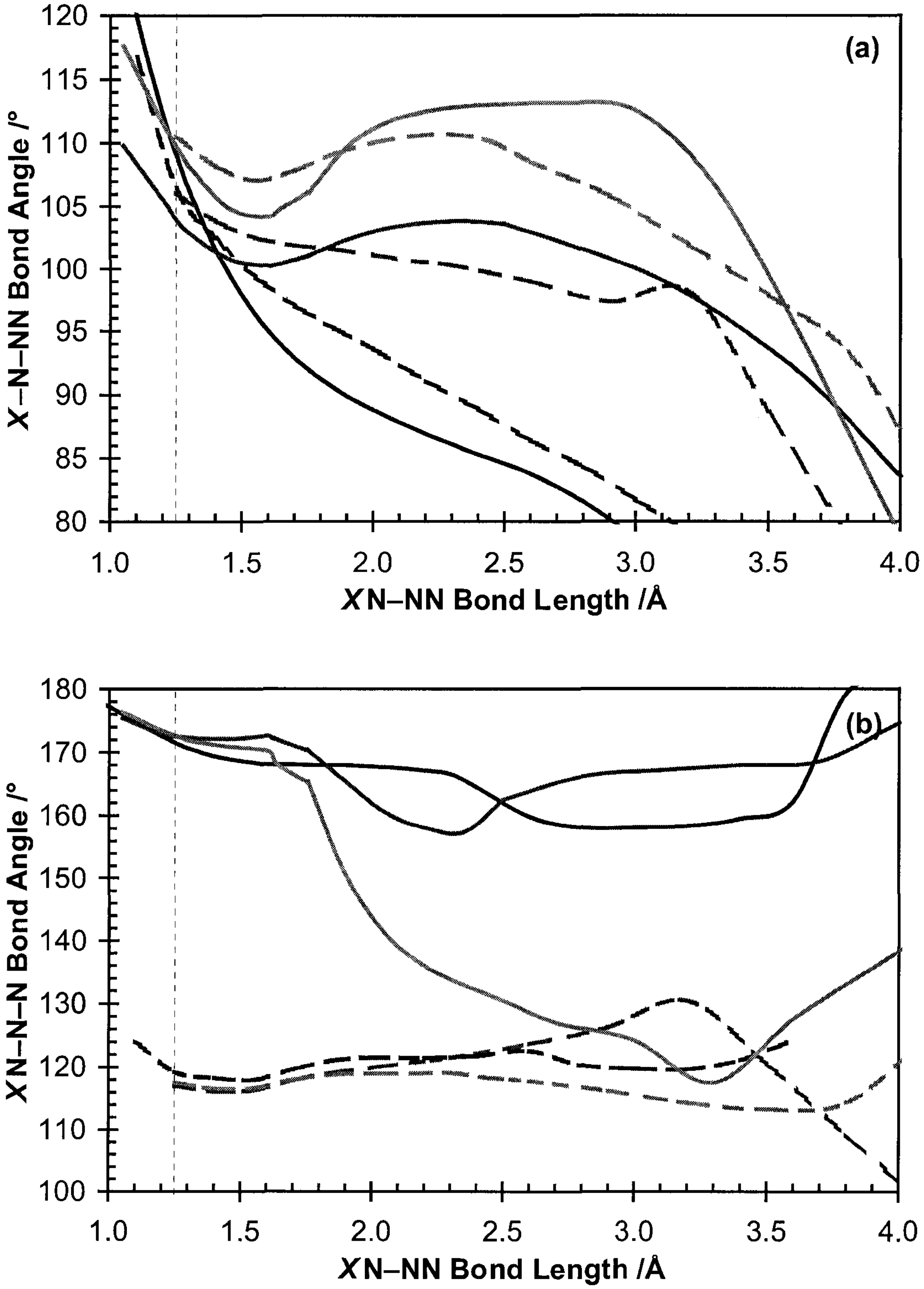

Figure 3.5 Optimized (a) X–N$_\alpha$–N$_\beta$ and (b) N$_\alpha$–N$_\beta$–N$_\gamma$ bond angles during XN$_3$ dissociation along the XN–NN pathway. Legend same as Figure 3.4.

All dissociation pathways, except one, pass through a maximum, suggesting that these pathways should produce products with significant translational energy. The exception is the singlet PES of HN_3, which is purely dissociative and whose products should have little translational energy.

Figures 3.4 and 3.5 map other optimized parameters as a function of the dissociation coordinate: the X–NNN bond length, XNN–N bond length, X–N–NN bond angle, and XN–N–N bond angle from the UQCISD/6-31++G(d,p) PES scans. The near-equilibrium N_α–N_β bond length of 1.25 Å is shown in the Figures for reference. The dihedral angle remained between 179.5 and 180.5° during dissociation and is not shown.

The singlet and triplet NX bond length approaches different limiting values during dissociation, corresponding to NX(a) and NX(X), which are in good agreement with the experimental values in Tables 3.1 to 3.3. The NX bond length *increases* for HN_3 and *decreases* for FN_3 and ClN_3, more so on the singlet PES. The difference of nearly 0.1 Å suggests that NF(a) and NCl(a) are produced with significant vibrational excitation while HN(a) is expected to have less. Reactions that start on the singlet surface and cross to the triplet (at approximately 1.6 Å) should also result in vibrational excitation of the NX product. The N_β-N_γ bond length reaches the same limiting value for all dissociation pathways consistent in that it forms the N_2(X) product in all cases. The difference in the N_β–N_γ bond length between the ground state geometry and the products is small, 0.02 Å, suggesting little vibrational excitation.

Figure 3.5 shows that there is considerable torque applied to the NX product on all PESs. NX dissociates with considerable rotational energy. The dihedral angle is unchanged at 180° during dissociation, so the NX rotation is preferentially aligned with the dissociation coordinate. (The torque vector is perpendicular to the dissociation coordinate and to the molecular plane.) There is little change in the XN–N–N bond angle during dissociation as shown in Figure 3.5, suggesting little rotational excitation of the N_2 product on the singlet PES. The meandering bond angle indicates that the PES is relatively flat, such that a broad range of angles is accessible while still being low enough in energy to meet the convergence criteria of the calculations. *However*, the N_2 product from dissociation that crosses to the triplet PES should be considerably rotationally excited since the equilibrium bond angles are not the same for the singlet and triplet PESs. These results are summarized in Table 3.9.

Table 3.9 Summary of energy partitioning during the dissociation of $X\mathrm{N}_3$.

Species	**Translation**		**N*X* Vibration**		**N*X* Rotation**		**N_2 Vibration**		**N_2 Rotation**	
	sing.	**trip.**	**sing.**	**trip.**	**sing.**	**trip.**	**sing.**	**trip.**	**sing.**	**trip.**
HN_3	no	yes	no	no	yes	yes	no	no	no	yes
FN_3	yes	yes	yes	yes	yes	yes	no	no	no	yes
ClN_3	yes	yes	yes	yes	yes	yes	no	no	no	yes

Product energy distributions were measured in vibrational overtone experiments on HN_3 by monitoring fluorescence of NH($c^1\Pi$–$a^1\Delta$) and NH($A^3\Pi$–$X^3\Sigma^-$) for the singlet and triplet dissociation pathways, respectively.[28] The authors found that dissociation on the singlet surface produced NH(a) with little rotational or vibrational energy but with some translational energy, suggesting a small barrier along the dissociation coordinate. Overtone excitations that provided excess energy resulted in rotational excitation of the products. Dissociation on the triplet surface produces results as predicted in Table 3.9.

4. POST-AB INITIO ANALYSIS AND DISCUSSION

Ab initio calculations are a starting point for detailed analysis of systems. The primary interest of chemistry is to understand and predict the reactivity within chemical systems. This Chapter builds on the results in Chapter 3 to determine the complete basis set energy, energies and enthalpies for multiple reactions on the PESs, the enthalpy of formation of XN_3, and the thermal dissociation rate of XN_3 and branching ratio of $NX(a)$ as a function of temperature.

Complete basis set energy*

Standard methods are available to extrapolate to the energy that would be obtained with a *complete basis set* (CBS). The general idea is to use low levels of theory to determine the geometry and vibrational energies, determine the energy with higher level single-point calculations, and extrapolate the energy to very high correlation levels. The G*x* method uses empirical scaling factors determined much like the vibrational scaling factors in Table 3.8. For example, the G2(MP2) method calculates the vibrational energies with the HF/6-31G(d) level of theory, geometry and vibrational energies at the MP2/6-31G(d) level of theory, single-point calculations with HF/6-311+G(2df,2p), MP2/6-311 +G(2df,2p), and QCISD/6-311G(d,p) levels of theory, and an empirical formula to estimate the energy at the QCISD(T)/6-311+G(3df,2p) level of theory. This returns an energy that has a mean-absolute deviation of 6.3 kJ/mol from the actual QCISD(T)/6-311+G(3df,2p) energy. The CBS-*x* methods are similar in methodology to the G*x* methods.

---

* References 73 to 78 were used to prepare this section; individual citations are omitted. Other sources are cited as required.

A different approach is taken herein. It has been found that the CI energy is approximately linear with the inverse of the number of basis functions, N, used in the calculation.[78]

$$E_N \approx E_\infty + \frac{k}{N} \tag{52}$$

where k is a fitting parameter. The CBS energy is obtained by extrapolating to an infinite number of basis functions. A sample extrapolation is shown in Figure 4.1 and the results of the extrapolation for the key geometries shown in Table 4.1.

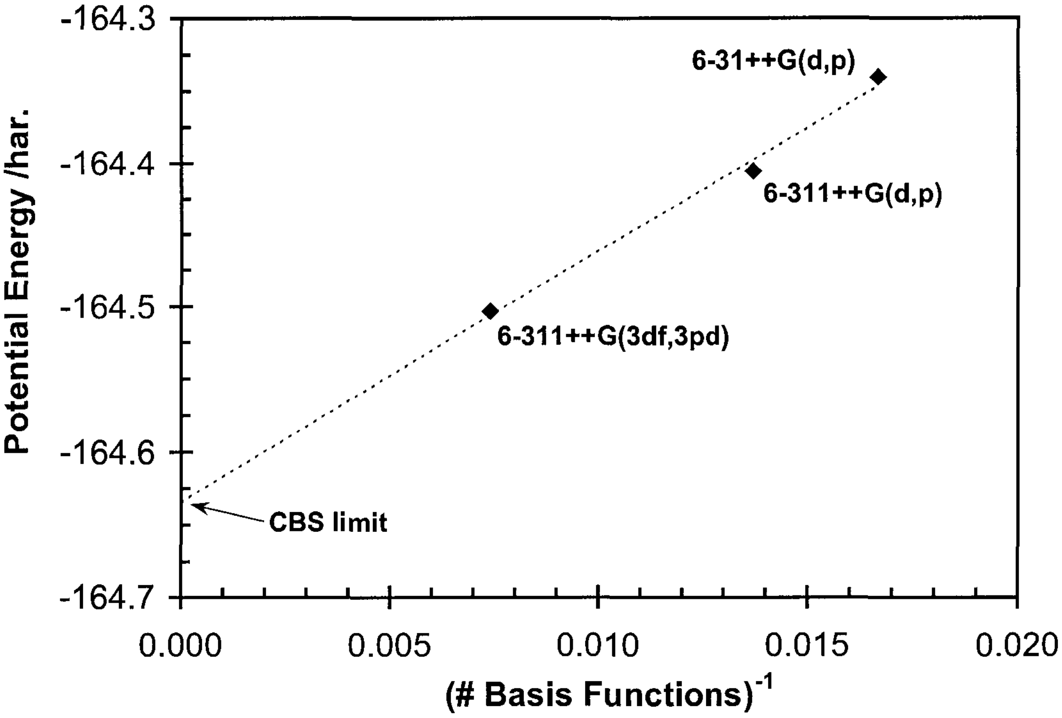

Figure 4.1 Extrapolated CBS energy for ground state HN_3.

Table 4.1 Extrapolated CBS energy of the ground state, singlet–triplet crossing, singlet dissociation maximum, and dissociation products of XN_3 using the QCISD standard methods. Energies in hartrees.

Basis set		Ground State	Singlet–Triplet Crossing	Singlet Dissociation Maximum	Singlet Dissociation Products	Triplet Dissociation Products
label	*N*					
			HN_3			
6-31++G(d,p)	60	-164.3402	-164.2822	——	-164.2698	-164.3485
6-311++G(d,p)	73	-164.4055	-164.3448	——	-164.3334	-164.4121
6-311++G(3df,3pd)	135	-164.5033	-164.4334	——	-164.4180	-164.4932
CBS	∞	-164.6340	-164.5546	——	-164.5369	-164.6093
			FN_3			
6-31++G(d,p)	72	-263.2751	-263.2412	-263.2465	-263.2653	-263.3397
6-311++G(d,p)	88	-263.3911	-263.3604	-263.3665	-263.3871	-263.4612
6-311++G(3df,3pd)	156	-263.5372	-263.4992	-263.5066	-263.5209	-263.5917
CBS	∞	-263.7629	-263.7216	-263.7307	-263.7414	-263.8090
			ClN_3			
6-31++G(d,p)	76	-623.3176	-623.2839	-623.2823	-623.3089	-623.3736
6-311++G(d,p)	96	-623.4123	-623.3729	-623.3776	-623.4051	-623.4697
6-311++G(3df,3pd)	164	-623.5617	-623.5131	-623.5277	-623.5567	-623.6211
CBS	∞	-623.7725	-623.7111	-623.7397	-623.7707	-623.8348

Statistical mechanics[*]

Ab initio calculations determine the minimum energy, *E*, of a system — an absolute value. Quantum mechanics, specifically Heisenberg's uncertainty principle, dictates that it is impossible to exist at this minimum energy where both position and momentum are known exactly. A non-zero ground state vibrational energy results from Planck's quantization of energy and serves to satisfy the uncertainty principle. The sum of all the ground state vibrational energies in a given species is its zpe. The lowest attainable energy is the sum of the ab initio energy and the zpe, which is known as the *internal energy* at 0 K, U_0.[*]

---

[*] References 73 to 78 were used to prepare this section; individual citations are omitted. Other sources are cited as required.

[*] Two conventions exist: one includes the zpe in the electronic partition function while the other includes the zpe in the vibrational partition function. I adopt the former.

$$U_0 = E_{\text{ab initio}} + \sum_i \text{zpe}_i \tag{53}$$

Within a chemical system above 0 K, the total energy is stored in translational, rotational, vibrational, and electronic modes of the system.

$$U_\text{T} = U_0 + U_\text{t} + U_\text{r} + U_\text{v} + U_\text{e} \tag{54}$$

These modes have different energy level spacing and different degeneracy characteristics. The Principle of Equipartition of energy allows for the independent evaluation of each of these modes.

Partition functions

In the limit of more energy levels than entities to fill them,* the Boltzmann distribution determines the probability that a given energy level will be occupied. The Boltzmann probability is given by

$$P(\varepsilon_i) = \frac{g_i \, \mathrm{e}^{\frac{-\varepsilon_i}{k_\text{B} T}}}{\sum_i g_i \, \mathrm{e}^{\frac{-\varepsilon_i}{k_\text{B} T}}} \tag{55}$$

where g_i is the degeneracy of the state with energy ε_i, k_B is Boltzmann's constant ($k_\text{B} = 1.381 \cdot 10^{-23}$ J/K $= 0.6950$ cm^{-1}/K $= 20.85$ GHz/K), and T is the temperature of the system. The normalization function, the denominator in (55), is often referred to as the *partition function*, q, and is of central importance in statistical mechanics. The partition function is the sum of the occupancies of all states within a molecule.

$$q = \sum_i g_i \, \mathrm{e}^{\frac{-\varepsilon_i}{k_\text{B} T}} \tag{56}$$

---

* For fermions (which electrons are), the true distribution is the Fermi-Dirac distribution; for bosons, it is the Bose-Einstein distribution. In the high temperature limit, both of these distributions effectively become the Boltzmann distribution. 'High temperature' is on the order of nanokelvin.

As with separability of the wavefunction and respective energies, the partition function is often assumed to be separable into partition functions of the individual energy modes of the system.[99] The total partition function is the product of the individual partition functions, $q = \prod q_i$.[100]

The *translational partition function*, q_t, is based on the solution to the quantum mechanical 'particle in a box'. The one-dimensional energy level expression is $E_n = \left(n^2 h^2\right)/\left(8 m l^2\right)$. When the translational temperature (E/k_B) is considerably smaller than the temperature of interest (applicable under ambient conditions), the density of states can be approximated as a continuum and the summation changed to an integral. In this limit, q_t becomes

$$\begin{aligned} q_\mathrm{t} &= q_{\mathrm{t},x}\, q_{\mathrm{t},y}\, q_{\mathrm{t},z} \\ &= 3\sum_{n=1}^{\infty} \mathrm{e}^{\frac{-n^2 h^2}{8 m l^2 k_\mathrm{B} T}} = 3\int_0^{\infty} \mathrm{e}^{\frac{-n^2 h^2}{8 m l^2 k_\mathrm{B} T}}\,\mathrm{d}n \\ &= \left(\frac{2\pi m k_\mathrm{B} T}{h^2}\right)^{3/2} V \end{aligned} \tag{57}$$

where m is the particle's mass, n is the translational quantum number, h is Planck's constant, and $V = l^3$ is the volume of the system.

The *rotational partition function*, q_r, for a linear molecule is based on the solution to the quantum mechanical 'rigid rotor' with energy levels given by $E_J = J(J+1)\hbar^2/(2I)$. The rotational temperature is also smaller than ambient temperature, thus q_r becomes

$$\begin{aligned} q_\mathrm{r}^{\mathrm{diatomic}} &= \frac{1}{\sigma}\sum_{J=0}^{\infty}(2J+1)\mathrm{e}^{\frac{-J(J+1)\hbar^2}{2I k_\mathrm{B} T}} = \frac{1}{\sigma}\int_0^{\infty}(2J+1)\mathrm{e}^{\frac{-J(J+1)\hbar^2}{2I k_\mathrm{B} T}}\,\mathrm{d}J \\ &= \frac{2I k_\mathrm{B} T}{\sigma \hbar^2} \end{aligned} \tag{58}$$

where J is the rotational quantum number, I is the moment of inertia of the system (in Hz), and $\hbar = h/(2\pi)$. σ is a symmetry index that accounts for the number of identical geometries that can be obtained through rotation ($\sigma = 1$ for all systems without a rotation axis, such as heteronuclear diatomics and $X\mathrm{N}_3$; $\sigma = 2$ for homonuclear diatomics and water). For a polyatomic system, (58) becomes

$$\begin{aligned} q_\mathrm{r}^\mathrm{poly} &= \frac{\sqrt{\pi}}{\sigma}\left(\frac{2I_a k_\mathrm{B} T}{\hbar^2}\right)^{1/2}\left(\frac{2I_b k_\mathrm{B} T}{\hbar^2}\right)^{1/2}\left(\frac{2I_c k_\mathrm{B} T}{\hbar^2}\right)^{1/2} \\ &= \frac{\sqrt{\pi}}{\sigma}\left(\frac{2k_\mathrm{B} T}{\hbar^2}\right)^{3/2}\sqrt{I_a I_b I_c} \end{aligned} \tag{59}$$

The *vibrational partition function*, q_v, is based on the solution to the quantum mechanical 'harmonic oscillator' with energy levels given by $E_\upsilon = \omega_\mathrm{e}(\upsilon + ½)$. The zpe has previously been taken into account, so the correct energy expression is $E_\upsilon = \omega_\mathrm{e}\,\upsilon$. The vibrational temperature is comparable to or larger than the ambient temperature so q_v must be summed.

$$\begin{aligned} q_\mathrm{v} &= \prod_i q_{\mathrm{v},i} \\ &= \prod_i \sum_{\upsilon=0}^{\infty} \mathrm{e}^{\frac{-\omega_{\mathrm{e},i}\upsilon}{k_\mathrm{B} T}} \\ &= \prod_i \frac{1}{1-\mathrm{e}^{\frac{-\omega_{\mathrm{e},i}}{k_\mathrm{B} T}}} \end{aligned} \tag{60}$$

where $\omega_{\mathrm{e},i}$ is the harmonic vibrational level spacing (in cm^{-1}) of the i^th normal mode and υ is the vibrational quantum number. If taken from zero to infinity, the summation has the closed form solution given by the third expression in (60). However, there are a finite number of vibrational energy levels in each electronic state. If higher order vibrational constants ($\omega_\mathrm{e}x_\mathrm{e}$, etc.) and/or the dissociation limit are known, (60) can be summed explicitly using these energy levels.

The *electronic partition function*, q_e, accounts for the energies of the different electronic configurations. Except for one-electron systems, there is no closed form solution for the electronic energy levels. Additionally, the energy level spacing is also comparable to or larger than the ambient temperature. The partition function is determined by explicitly summing the energy levels.

$$q_{\mathrm{e}} = \sum_{i=0}^{\infty} g_i \, \mathrm{e}^{\frac{-\varepsilon_i}{k_{\mathrm{B}} T}} \tag{61}$$

For a system containing N indistinguishable molecules, the partition function becomes

$$Q = \frac{q^N}{N!} \tag{62}$$

Thermodynamic functions

Once the partition function is known, thermodynamic values can be calculated. Equations for the internal energy (U), Helmholtz free energy (A), enthalpy (H), entropy (S), Gibbs free energy (G), and heat capacity at constant volume (C_V) are given below.[73]

$$U = k_{\mathrm{B}} T^2 \left(\frac{\partial \ln(q)}{\partial T} \right)_V \tag{63}$$

$$A = -k_{\mathrm{B}} T \ln(q) \tag{64}$$

$$H = U + PV = k_{\mathrm{B}} T^2 \left(\frac{\partial \ln(q)}{\partial T} \right)_V + k_{\mathrm{B}} T V \left(\frac{\partial \ln(q)}{\partial V} \right)_T \tag{65}$$

$$S = \frac{U - A}{T} = k_{\mathrm{B}} T \left(\frac{\partial \ln(q)}{\partial T} \right)_V + k_{\mathrm{B}} \ln(q) \tag{66}$$

$$G = H - TS = k_{\mathrm{B}} T V \left(\frac{\partial \ln(q)}{\partial V} \right)_T - k_{\mathrm{B}} T \ln(q) \tag{67}$$

$$C_V = 2 k_{\mathrm{B}} T \left(\frac{\partial \ln(q)}{\partial T} \right)_V + k_{\mathrm{B}} T^2 \left(\frac{\partial^2 \ln(q)}{\partial T^2} \right)_V \tag{68}$$

A thermodynamic expression for pressure was used in (65)

$$P = k_{\mathrm{B}} T \left(\frac{\partial \ln(q)}{\partial V} \right)_T \tag{69}$$

For an ideal gas (which is often assumed computationally and is in GAUSSIAN), Equation (65) simplifies to

$$\begin{aligned} H &= U + PV = U + RT \\ &= k_{\mathrm{B}} T^2 \left(\frac{\partial \ln(q)}{\partial T} \right)_V + RT \end{aligned} \tag{70}$$

where R is a proportionality constant (gas constant). From (70), it is evident that the enthalpy of an ideal gas equals the internal energy of the gas at 0 K.

Conveniently, GAUSSIAN calculates these parameters at 298 K as part of a frequency calculation. Inconvenient is the over-estimate of the vibrational frequencies, which affects the zpe and vibrational partition function.

Gaseous results reported at 1 bar pressure are referred to as the *standard state* and denoted by the symbol $^{\ominus}$. Thus, H°_{298} refers to reactions at 1 bar and 298 K.

Energy of reaction

The current calculations can be compared with experimental photolytic experiments to determine the accuracy of the PES at the bound ground state and of the dissociation products. ΔU_0 was manually calculated for Reactions (71) to (74) using the scaling factors in Table 3.8 and represents the energy between the zpe levels (T_0 in spectroscopy). These are adiabatic energies since the PES scans were relaxed (see Appendix D). Reaction (71) and (72) determine the photon energy required to reach the singlet dissociation maximum and singlet–triplet (S–T) crossing of $X\mathrm{N}_3$. Reaction (73) determines the photon energy required to pump ground-state $X\mathrm{N}_3$ into the lowest triplet state at the equilibrium N_{α}–N_{β} bond length. For this reaction, the triplet zpe was assumed to be the same as the singlet ground state. Reaction (74) determines the photon energy of the NX(a–X) transition. Table 4.2 summarizes these transition energies in cm^{-1} and converted to wavelength in nanometers.

$$XN_3 \longrightarrow [XN_3]^{\ddagger} \tag{71}$$

$$XN_3 \longrightarrow [XN_3]^{S\text{–}T} \tag{72}$$

$$^1XN_3 \longrightarrow {}^3XN_3 \tag{73}$$

$$NX(X^3\Sigma^-) \longrightarrow NX(a^1\Delta) \tag{74}$$

With increasing basis set size, two trends are noted in Table 4.2: constant reaction energies indicating basis set convergence or systematically changing energies toward convergence. Systematically changing energies are observed for HN_3 in Reactions (71) and (72) and for Reaction (72) of ClN_3.[*]

It was noted in the **Introduction** that experimental measurements[23,25] of the energy of the singlet–triplet crossing, (72), in HN_3 gives 12 700 cm^{-1}, while ab initio results range between 12 300 and 16 890 cm^{-1}.[24,29,30,32,†] The majority of the theoretical calculations range from 12 300 to 14 000 cm^{-1}, in reasonable agreement with experiment. The value calculated herein, 16 598 cm^{-1} (with zpe correction), is also in agreement with the ab initio results. The singlet dissociation energy, (71), of HN_3 was determined to be 19 574 cm^{-1}, also in agreement with the experimental[25] estimate of ≥18 800 cm^{-1} and one theoretical[32] calculation of 16 930 cm^{-1}. There is no obvious reasoning to explain the significantly lower calculated[24] value of 14 170 cm^{-1}; however, it should be noted that all values in this particular reference differ significantly from those of other experimental and theoretical works.

---

[*] For all reactions, the CBS limit energy is reported and, where no trend is observed, an uncertainty corresponding to the standard deviation of the values is also reported.

[†] Unless otherwise stated, ab initio calculations reported energy differences without correction for zpe and experimental calculations intrinsically include zpes.

Table 4.2 $\Delta_r U_0$ for Reactions (71) to (74) of XN_3 with the QCISD standard methods. The 6-311++G(3df,3pd) and CBS energies use the zpe from the 6-311++G(d,p) calculation. (a) the singlet zpe was used for the $^3XN_3$; (b) Reference 101; (c) Reference 102; (d) Reference 103.

Reaction:	71	72	73[a]	74
		HN_3 /cm^{-1}		
6-31++G(d,p)	13 742	11 923	16 800	17 306
6-311++G(d,p)	14 080	12 503	——	17 286
6-311++G(3df,3pd)	16 983	14 518	——	16 535
CBS	19 574	16 598	——	15 924
Expt.[b]	——	——	——	12 688
		/nm		
6-31++G(d,p)	728	839	595	578
6-311++G(d,p)	710	800	——	579
6-311++G(3df,3pd)	589	689	——	605
CBS	511	602	——	628
Expt.[b]	——	——	——	788
		FN_3 /cm^{-1}		
6-31++G(d,p)	5 615	6 813	9 750	16 362
6-311++G(d,p)	4 736	6 114	——	16 269
6-311++G(3df,3pd)	6 047	7 686	——	15 546
CBS	6 393	8 417	——	14 853
Expt.[c]	——	——	——	11 435
		/nm		
6-31++G(d,p)	1 781	1 468	1 026	611
6-311++G(d,p)	2 112	1 636	——	615
6-311++G(3df,3pd)	1 654	1 301	——	643
CBS	1 564	1 188	——	673
Expt.[c]	——	——	——	875
		ClN_3 /cm^{-1}		
6-31++G(d,p)	7 030	6 706	13 540	14 230
6-311++G(d,p)	6 899	7 953	——	14 203
6-311++G(3df,3pd)	6 720	9 954	——	14 161
CBS	6 466	12 778	——	14 101
Expt.[c,d]	——	——	——	9 260
		/nm		
6-31++G(d,p)	1 422	1 491	739	703
6-311++G(d,p)	1 449	1 257	——	704
6-311++G(3df,3pd)	1 488	1 005	——	706
CBS	1 547	783	——	709
Expt.[c,d]	——	——	——	1 080

Visible spectra of $X\mathrm{N}_3$ have typically focussed on the UV-Vis region, where strong absorptions exist that are convenient for photolysis.[104] To the best of my knowledge, near-infrared spectra have not been recorded. A CASSCF/TZ+P PES scan on HN_3 estimated Reaction (73) to be 37 310 cm^{-1},[105] significantly higher than the 16 800 cm^{-1} calculated herein. However, the CASSCF calculations held all the parameters fixed, returning the *vertical* excitation energy whereas (73) determines the *adiabatic* excitation energy. A calculation of the vertical excitation energy with the UQCISD/6-11++G(d,p) method produced a vertical excitation energy of 34 600 cm^{-1} (≈ 290 nm) in good agreement with the higher level calculation. The UV-Vis spectrum of HN_3 shows a weak featureless absorption beginning at 320 nm.[106] For FN_3 and ClN_3, vertical excitation energies of 19 700 cm^{-1} (510 nm) and 21 700 cm^{-1} (460 nm), respectively, were calculated with the UQCISD/6-11++G(d,p) method. Experimentally, weak absorptions are also found in FN_3 and ClN_3 at 425 and 330 nm, respectively.[54] The difference between the observed weak absorptions is greater for FN_3 and ClN_3, making their assignment less certain. There does not appear to be any reports of experimental investigations of these species in the visible region.

The calculations herein consistently over-estimate the experimentally known NX(a–X) energy, Reaction (74). The error increases from 26 % in HN_3 to 52 % in ClN_3 for the QCISD/6-31++G(d,p) basis set but decreases with increasing basis set size. (Reference 105 determines a HN(a–X) energy five times the experimental value.)

The agreement between the calculations herein and the previous experimental and theoretical work on HN_3 indicates that the standard methods are sufficient to explain the intramolecular interactions in HN_3 and that the results for FN_3 and ClN_3 should be of comparable accuracy.

Enthalpy of reaction

When a system is acted upon under a constant external pressure, *enthalpy* (*H*), not the internal energy, *U*, measures the energy required to act upon a system. The enthalpy of a reaction, $\Delta_r H^\circ_{298}$, was calculated for Reactions (75) to (78). Reactions (75) and (76) determine the thermal energy required to reach the singlet dissociation maximum and the singlet–triplet crossing location (the dissociation barriers). Reactions (77) and (78) are the net reaction (identical to (1) and (2)).

$$XN_3 \longrightarrow [XN_3]^{\ddagger} \tag{75}$$

$$XN_3 \longrightarrow [XN_3]^{S\text{–}T} \tag{76}$$

$$XN_3 \longrightarrow NX(a^1\Delta) + N_2(X^1\Sigma_g^+) \tag{77}$$

$$XN_3 \longrightarrow NX(X^3\Sigma^-) + N_2(X^1\Sigma_g^+) \tag{78}$$

The results are tabulated in Table 4.3. A trend is again observed in reactions that involve the singlet dissociation products.

As discussed in Appendix D, the adiabatic singlet–triplet crossing energy is higher than shown in Figure 3.2 as a result of the different geometries at the intersection. For HN_3, the singlet–triplet crossing is found to be 3 200 cm^{-1} below the singlet dissociation maximum. However, the crossing for FN_3 is 2 000 cm^{-1} higher and the crossing for ClN_3 is 6 300 cm^{-1} *higher* than the singlet dissociation maximum. These increased barrier heights make the parent molecule more stable and, when compared with previous calculations,[55,56,57,58,59,60] put the results herein closer to the expected minimum barrier height of 7 700 cm^{-1} for FN_3.* This suggests that the discrepancy between calculation and experiment may be partially caused by failing to account for differences in geometries.

Dissociation on the singlet PES, (77), is endothermic, with HN_3 being the most endothermic, requiring 19 880 cm^{-1} of energy. FN_3 is slightly endothermic and ClN_3 nearly thermoneutral when dissociating on the singlet PES: 4 210 cm^{-1} for FN_3 and 41 cm^{-1} for ClN_3. Dissociation on the triplet surface, (78), is endothermic for HN_3 by 3 990 cm^{-1} but significantly exothermic for FN_3 and ClN_3, 10 620 cm^{-1} and 14 030 cm^{-1}, respectively. The $\Delta_r H^{\circ}_{298}$ for HN_3 has been experimentally determined to be 5 250 cm^{-1}.[22]

---

* It was discussed on page 75 that a barrier height of 7 700 cm^{-1} was needed to have a half-life of 30 minutes at 14°C for FN_3.

Table 4.3 $\Delta_r H^\circ_{298}$ for Reactions (75) to (78) of XN$_3$ with the QCISD standard methods. The 6-311++G(3df,3pd) and CBS energies use the zpe from the 6-311++G(d,p) calculation.

Reaction:	**75**	**76**	**77**	**78**
		HN$_3$ /cm^{-1}		
6-31++G(d,p)	14 226	11 973	14 226	-3 050
6-311++G(d,p)	14 385	12 556	14 385	-2 870
6-311++G(3df,3pd)	17 288	14 571	17 288	783
CBS	19 879	16 651	19 879	3 986
		/(kJ/mol)		
6-31++G(d,p)	170	143	170	-36
6-311++G(d,p)	172	150	172	-34
6-311++G(3df,3pd)	207	174	207	9
CBS	238	199	238	48
		FN$_3$ /cm^{-1}		
6-31++G(d,p)	5 695	6 859	1 621	-14 720
6-311++G(d,p)	4 826	6 180	365	-15 881
6-311++G(3df,3pd)	6 137	7 752	3 061	-12 463
CBS	6 483	8 483	4 209	-10 621
		/(kJ/mol)		
6-31++G(d,p)	68	82	19	-176
6-311++G(d,p)	58	74	4	-190
6-311++G(3df,3pd)	73	93	37	-149
CBS	78	101	50	-127
		ClN$_3$ /cm^{-1}		
6-31++G(d,p)	7 118	6 759	1 517	-12 680
6-311++G(d,p)	6 998	8 020	1 217	-12 953
6-311++G(3df,3pd)	6 818	10 021	730	-13 399
CBS	6 564	12 845	41	-14 028
		/(kJ/mol)		
6-31++G(d,p)	85	81	18	-152
6-311++G(d,p)	84	96	15	-155
6-311++G(3df,3pd)	82	120	9	-160
CBS	79	154	0	-168

It has been proposed that the decomposition is autocatalytic with the vibrationally excited products nearly resonant with the vibrational modes of the parent azide.[62,107] Comparison of Tables 3.4 to 3.7 show that vibrational energies of N$_2$ and NX are similar to the vibrational energies of the N_β–N_γ and X–N_α stretches and double the vibrational energy of the

N_α–N_β stretch in XN_3. These near-resonances allow for facile energy transfer and, since the energies are lower in XN_3, the equilibrium lies on the side of XN_3. The large amount of energy released, 127 and 168 kJ/mol for FN_3 and ClN_3 provides sufficient energy to propagate dissociation. This is not the case for HN_3.

The reaction energies, $\Delta_r U_0$, of ClN_3 for Reactions (77) and (78) were found to be 41 and -14 030 cm^{-1}. These values are beyond the quoted uncertainty of a recent experiment that determined these values to be 1 690 ± 560 cm^{-1} and -7 500 ± 650 cm^{-1}, respectively.[67] Despite this discrepancy, these results are in better agreement than a previous theoretical calculation.[108]

Enthalpy of formation

The enthalpy of formation, $\Delta_f H^\circ_{298}$, is a specific reaction where a species is formed from elements in their standard state. $\Delta_f H^\circ_{298}$ is relative since the H°_{298} of elements in their standard state at *standard ambient temperature and pressure* (SATP) are arbitrarily defined to be zero. However, it does provide information on the stability of a species relative to its constituent atoms. A positive $\Delta_f H^\circ_{298}$ indicates that a species would release energy upon dissociation to its elements.

In order to calculate $\Delta_f H^\circ_{298}$ from ab initio data, experimental values must be used to scale the calculated values. The best cancellation of errors is obtained with isodesmic and isogyric reactions.[42,*] Computationally, the species should be small, closed shell, and single reference. For these calculations, the BSSE corrected energy was not used because it cannot be calculated for the isolated species. BSSE corrections should be constant given the large basis sets used and because the species are at their equilibrium geometries.

---

[*] Isodesmic: a chemical reaction that conserves the type and number of chemical bonds.
Isogyric: a chemical reaction that conserves net spin.

For a generic reaction,

$$A + Z \longrightarrow C + D \tag{79}$$

where $\Delta_f H^\circ_{298}(Z)$ is to be calculated and experimental $\Delta_f H^\circ_{298}$ values exist for *A*, *C*, and *D*. The $\Delta_r H^\circ_{298}$ is calculated from

$$\begin{aligned}\Delta_r H^\circ_{298} &= \sum_{\text{products}} \Delta_f H^\circ_{298} - \sum_{\text{reactants}} \Delta_f H^\circ_{298} \\ &= \sum_{\text{products}} H^\circ_{298} - \sum_{\text{reactants}} H^\circ_{298}\end{aligned} \tag{80}$$

for the experimental and ab initio data

$$\Delta_r H^{\circ,\text{expt}}_{298} = \Delta_f H^{\circ,\text{expt}}_{298}(C) + \Delta_f H^{\circ,\text{expt}}_{298}(D) - \Delta_f H^{\circ,\text{expt}}_{298}(A) - \Delta_f H^{\circ,\text{expt}}_{298}(Z) \tag{81}$$

$$\Delta_r H^{\circ,\text{ab initio}}_{298} = H^{\circ,\text{ab initio}}_{298}(C) + H^{\circ,\text{ab initio}}_{298}(D) - H^{\circ,\text{ab initio}}_{298}(A) - H^{\circ,\text{ab initio}}_{298}(Z) \tag{82}$$

In (81), $\Delta_f H^{\circ,\text{expt}}_{298}(Z)$ and consequently $\Delta_r H^{\circ,\text{expt}}_{298}$ are unknown. However $\Delta_r H^{\circ,\text{ab initio}}_{298}$ can be determined from (82). Setting $\Delta_r H^{\circ,\text{ab initio}}_{298} = \Delta_r H^{\circ,\text{expt}}_{298}$ scales the ab initio results. Solving for $\Delta_f H^\circ_{298}(Z)$ gives

$$\Delta_f H^\circ_{298}(Z) = \Delta_f H^{\circ,\text{expt}}_{298}(C) + \Delta_f H^{\circ,\text{expt}}_{298}(D) - \Delta_f H^{\circ,\text{expt}}_{298}(A) - \Delta_r H^{\circ,\text{ab initio}}_{298} \tag{83}$$

Additionally, $\Delta_f H^\circ_{298}(Z)$ can be determined at multiple levels of theory and for multiple reactions. In this dissertation, $\Delta_f H^\circ_{298}(X\text{N}_3)$ was determined for four reactions with the UQCISD/6-31++G(d,p) and UQCISD/6-311++G(d,p) methods. All reactions are isogyric. Reaction (84) directly calculates the negative of the $\Delta_f H^\circ_{298}(X\text{N}_3)$. Reactions (85) and (86) attempt to keep the bonding as similar as possible, i.e., isodesmic.

$$2X\text{N}_3 \longrightarrow 3\text{N}_2 + X_2 \tag{84}$$

$$2X\text{N}_3 + \tfrac{1}{2}\text{O}_2 \longrightarrow 3\text{N}_2 + X_2\text{O} \tag{85}$$

$$2X\text{N}_3 + \text{O}_2 + \text{H}_2 \longrightarrow 3\text{N}_2 + 2\text{HO}X \tag{86}$$

$$X\text{N}_3 + \text{NH}_3 \longrightarrow 2\text{N}_2 + \text{H}_2 + \text{H}X \tag{87}$$

Table 4.4 contains experimental[109] and ab initio $\Delta_f H^\circ_{298}$ results for the species in Reactions (84) to (87) and Table 4.5 summarizes the calculated $\Delta_f H^\circ_{298}(X\mathrm{N}_3)$.

Table 4.4 Experimental $\Delta_f H^\circ_{298}$ and ab initio H°_{298} of the species listed in Reactions (84) to (87) at the QCISD/6-31++G(d,p) and QCISD/6-311 ++G(d,p) levels of theory.

Species	Experimental $\Delta_f H^\circ_{298}$ /(kJ/mol)	Ab initio H°_{298} /har.	
		6-31++G(d,p)	6-311++G(d,p)
H_2	0.00	-1.1654	-1.1662
N_2	0.00	-109.52	-109.55
O_2	0.00	-150.32	-150.36
F_2	0.00	-199.51	-199.57
Cl_2	0.00	-920.34	-920.40
HF	-273.30	-100.44	-100.47
HCl	-92.31	-460.79	-460.82
H_2O	-241.83	-76.41	-76.43
F_2O	24.52	-274.66	-274.74
Cl_2O	87.86	-995.47	-995.55
HOF	-98.32	-175.53	-175.58
HOCl	-74.48	-535.94	-535.99
NH_3	-45.94	-56.528	-56.545
HN_3	—	-164.76	-164.81
FN_3	—	-263.93	-264.00
ClN_3	—	-624.32	-624.39

It is evident that the results are in good agreement for all reactions and both ab initio methods. All $\Delta_f H^\circ_{298}$ are significantly positive and increase from 246 kJ/mol for HN_3 to 350 kJ/mol for ClN_3. This magnitude is indicative of reactive species. However, $\Delta_f H^\circ_{298}$ does not determine stability. The $\Delta_f H^\circ_{298}(\mathrm{HN}_3)$ calculated herein, 246 ± 10 kJ/mol, is in reasonable agreement with the experimental[110] value of 290 kJ/mol and a previous theoretical value of 302 kJ/mol.[1,16,*] An experimental[54] measurement for $\Delta_f H^\circ_{298}(\mathrm{FN}_3)$ of 545 ± 20 kJ/mol is nearly double the value determined herein, 271 ± 12 kJ/mol, and a previous theoretical value of 344 kJ/mol.[1,16] To investigate this anomaly further, I note that an upper limit of $\Delta_f H^\circ_{298}(\mathrm{FN}_3)$ can be obtained from the experimental $\Delta_f H^\circ_{298}(\mathrm{F}+\mathrm{N}_3)$ of

---

[*] Both References use the same method, MP2/6-31G(d,p), and report the same $\Delta_f H^\circ_{298}$.

493 kJ/mol,[95] which draws into question the value of 545 kJ/mol. Subtraction of 240 kJ/mol for the F + N_3 bond energy (extrapolated from Figure 3.3) gives an estimated $\Delta_f H^\circ_{298}(FN_3)$ of 250 kJ/mol, in good agreement with the value calculated herein. The $\Delta_f H^\circ_{298}(ClN_3)$ of 350 ± 9 kJ/mol should be equally accurate and is in agreement with a previous theoretical value of 388 kJ/mol.[1,16]

Table 4.5 $\Delta_f H^\circ_{298}(XN_3)$ for Reactions (84) to (87) at the QCISD/6-31++G(d,p) and QCISD/6-311++G(d,p) levels of theory.

	Rxn.	$\Delta_f H^\circ_{298}$ /(kJ/mol)		
		HN_3	FN_3	ClN_3
6-31++G(d,p)	(85)	251	272	347
	(86)	239	274	350
	(87)	228	253	335
	(88)	243	255	342
6-311++G(d,p)	(85)	260	285	360
	(86)	251	284	358
	(87)	242	265	345
	(88)	253	277	362
Average		246	271	350
Standard Deviation		10	12	9

Singlet–triplet coupling*

Coupling of the singlet and triplet states occurs through coupling of each electron's spin with other angular momenta within the system: orbital, rotation, and the spin of other electrons. Spin-rotation interactions are generally small because of the slower angular velocity of the nuclei; one obvious approximation is to ignore spin-rotation coupling. Spin-orbit and spin-spin coupling are often of the same order of magnitude.[37]

Computationally, incorporation of spin has proved difficult. The majority of the computational effort has been directed at spin-orbit coupling. Unfortunately, extrapolations to multi-electron systems and approximations necessary to make calculations tractable are

---

* Reference 37 was used to prepare this section; individual citations are omitted. Other sources are cited as required.

grosser than those previously described, such as the Hartree-Fock approximation. Spin interactions cannot be treated variationally. The result is 'state-of-the-art' calculations being done on *diatomics* and *triatomics*, both with errors that often exceed 30 %.[111] Some of this error is because of neglect of spin-spin coupling. In polyatomic systems, intersecting surfaces create 'seams', rather than points of intersection, with each position on the seam having unique characteristics.[112]

The generalized (Breit-Pauli) spin-orbit Hamiltonian is given by

$$\hat{\mathscr{H}}_{\text{SOC}} = \frac{\alpha^2}{2}\left\{\sum_{\mu}\sum_{A}\frac{Z_A}{\left|r_{\mu A}\right|^3}\left[r_{\mu A}\times\hat{p}_\mu\right]\cdot\hat{S}_\mu - \sum_{\mu}\sum_{\nu>\mu}\frac{1}{\left|r_{\mu\nu}\right|^3}\left[r_{\mu\nu}\times\hat{p}_\mu\right]\cdot\left[\hat{S}_\mu+2\hat{S}_\nu\right]\right\} \qquad (88)$$

where α is the fine structure constant given by $e^2/(4\pi\varepsilon_0\hbar c)$ or $1/c$ in atomic units, $\hat{p}_\mu$ is the electron momentum operator, and $\hat{S}_\mu$ the electron spin operator. The first term in (88) couples the electron spin with the nuclear spin on each nucleus. The second term couples the electron spin with the spin on the other electrons. Prior to computational algorithms for calculating spin-orbit coupling via (88), $\hat{\mathscr{H}}_{\text{SOC}}$ was often simplified to

$$\hat{\mathscr{H}}_{\text{SOC}} = \sum_i \hat{a}_i\,\mathrm{l}_i\cdot\mathrm{s}_i \qquad (89)$$

with

$$\hat{a}_i\,\mathrm{l}_i = \sum_A \frac{\alpha^2 Z_{\text{eff},A}}{2r_{iA}^3}\mathrm{l}_{iA} \qquad (90)$$

which involves more approximations, notably that spin-orbit interactions between unpaired electrons were ignored and the effective nuclear charge, Z_{eff}, was used.

Of the selection rules* associated with $\hat{\mathscr{H}}_{\text{SOC}}$, those relevant to the current discussion are $\Delta S = 0, \pm 1$. When $\Delta S = 0$, $\Delta\Lambda = 0$ and $\hat{\mathscr{H}}_{\text{SOC}}$ separates open-shell electronic states with $\Lambda > 0$. For example, the diatomic π^1 and π^3 ($^2\Pi$) configuration is separated into $^2\Pi_{1/2}$ and

---

* Presented for the diatomic case.

${}^2\Pi_{3/2}$ states. When $\Delta S = \pm 1$, $\Delta \Lambda$ can be 0 or ±1; the $\Delta\Lambda = \pm\ 1$ case results in $\hat{\mathcal{H}}_{\mathrm{SOC}}$ coupling states of different spin. For example, $\hat{\mathcal{H}}_{\mathrm{SOC}}$ couples the ${}^1\Sigma^+$ and ${}^3\Sigma^-$ states in N*X*, but *not* the ${}^1\Delta$ and ${}^3\Sigma^-$ states because $\Delta\Lambda = 2$.

The spin-spin Hamiltonian is given by

$$\hat{\mathcal{H}}_{\mathrm{SS}} = -\alpha^2 \sum_{\mu} \sum_{\nu>\mu} \frac{1}{\left|r_{\mu\nu}\right|^5} \left[\left(r_{\mu\nu} \cdot \mathrm{s}_\mu\right)\left(r_{\mu\nu} \cdot \mathrm{s}_\nu\right) - \left|r_{\mu\nu}\right|^2 \left(\mathrm{s}_\mu \cdot \mathrm{s}_\nu\right) \right] \tag{91}$$

The selection rules for $\hat{\mathcal{H}}_{\mathrm{SS}}$ are $\Delta S = 0, \pm 1, \pm 2$ and $\Delta\Lambda = 0, \pm 1, \pm 2$. Importantly, $\hat{\mathcal{H}}_{\mathrm{SS}}$ *does* couple the ${}^1\Delta$ and ${}^3\Sigma^-$ states of N*X*.

Simply, it is evident that spin interactions are poorly treated computationally and there is no accurate method of determining the coupling between the singlet and triplet states of $X\mathrm{N}_3$.

Coupling in $X\mathrm{N}_3$

The singlet–triplet transition probability in $X\mathrm{N}_3$ is estimated from the radiative lifetime of the N*X*(a–X) transition, τ_{aX}, through the relationship[113]

$$\frac{1}{\tau_{\mathrm{aX}}} = A_{\mathrm{aX}} = \frac{16\ {}^3}{3h\varepsilon_0\lambda_{\mathrm{aX}}^3} S_{\mathrm{aX}} \tag{92}$$

where A_{aX} is the Einstein spontaneous emission coefficient (A coefficient) and $S_{\mathrm{aX}} = \left|\langle \Psi_{\mathrm{a}} | \boldsymbol{\mu} | \Psi_{\mathrm{X}} \rangle\right|^2$ is the line strength.

The transition probability between states n and m can be determined using the *classical* Landau-Zener expression for diabatic coupling of states.[100,*]

$$P_{nm}^{\mathrm{LZ}} = \mathrm{e}^{\frac{-4\pi V_{nm}^2}{h\nu\left|s_n - s_m\right|}} \tag{93}$$

---

[*] The Landau-Zener expression was originally derived for diatomics.

P_{nm}^{LZ} is the Landau-Zener transition probability between states n and m. V_{nm} is the energy by which each state is shifted and therefore half the total energy separation: $2V_{nm} = S_{nm}$. v is the velocity of the nuclei at the intersection and the s_i are the slopes of the unperturbed PESs.

A comparison of two similar systems, with substitution of (92) into (93), results in the following expression for the transition probability. The nm subscript is dropped, being replaced by {1, 2} to represent the system to which it pertains. λ is converted to energy, T_0.

$$\ln\left(\frac{P_2^{\mathrm{LZ}}}{P_1^{\mathrm{LZ}}}\right) = \left(\frac{A_1}{A_2}\right)\left(\frac{T_{0,1}}{T_{0,2}}\right)^3 \tag{94}$$

Assumptions implicit in (94) are that v_i and $|s_n - s_m|_i$ are the same for both systems. Further, it is assumed that the NX(a–X) coupling is dominant at the singlet–triplet crossing in XN$_3$ and that the Landau-Zener expression is valid.

Recall that the singlet–triplet transition probability of HN$_3$ was experimentally[23] measured to be between 10^{-3} and 10^{-2} and theoretically[24,*] calculated to be 0.003. Equation (94) is used to estimate the transition probability in FN$_3$ and ClN$_3$. The results are shown in Table 4.6. The transition probability estimated for ClN$_3$ from photodissociation experiments,[67] 22 %, is within the range in Table 4.6.

Species	T_0 /cm^{-1} (a)	A_{aX} /s^{-1}	$P_{S\text{–}T}$
NH	12 688	0.08[b]	0.001 0.010
NF	11 435	0.2[c]	0.023 0.081
NCl	9 260	0.69[d]	0.129 0.255

Table 4.6 Intersystem crossing probabilities for XN$_3$. (a) Experimental values; (b) Reference 101; (c) Reference 102; (d) Reference 103.

This approach, although based on diverse and classical expressions, should produce a reasonable estimate of the singlet–triplet transi-

---

[*] The theoretical calculation was based on an approximate singlet–triplet crossing geometry. At the singlet–triplet crossing, the wavefunction is assumed to be an equal mixture of the proto a$^1\Delta$ and b$^1\Sigma^+$ states (see **Electronic states of HN$_3$** on page 71).

tion probability. The use of the limiting diatomic transition probability of N*X* accounts for the single changing factor between systems, namely the change from H → F → Cl, and the relative spin-orbit contribution from the halogen and nitrogen. The range of their atomic contribution to the molecular interactions is evidenced in their spin-orbit constants: H (0.05 cm^{-1}), N (73.3 cm^{-1}), F (269.3 cm^{-1}), and Cl (587.3 cm^{-1}),[37] with N, F, and Cl contributing most to the spin-orbit coupling. The relative nature of (94) approximately cancels contributions from the other atoms since they are constant between systems. The greatest assumptions are that the experimental A and P_{aX} values are correct.

Unimolecular dissociation

Intermolecular collisions result in energy transfer between molecules and randomization of energy within a given molecule. The Boltzmann distribution, (55), for a collection of molecules reflects the probability that a molecule will have energy ε_i. Superimposing the Boltzmann distribution over the PESs in Figure 3.2 indicates that there is some probability of a molecule having a energy above the singlet dissociation and singlet–triplet crossing energy barriers.

A very successful theory for determining the thermal unimolecular dissociation was developed by Rice, Ramsburger, Kassels, and Marcus and is called *RRKM* theory. A more general theory of chemical reactivity, of which RRKM theory is the unimolecular limit, is *Transition State* theory.[100] An underlying assumption of Transition State theory is that an equilibrium exists between the ground and transition state (denoted with a ‡) and that energy redistribution (thermalization) among the available modes is rapid relative to reaction. Rapid thermalization allows for the Boltzmann distribution to be retained despite reaction of those molecules with sufficient energy for reaction. Thermalization occurs in intermolecular collisions and from mixing of vibrational modes, which is aided by anharmonicity of the modes.

The general expression for the unimolecular reaction rate is

$$k_{\mathrm{uni}}(T)=\int_0^\infty\int_0^\infty \frac{k(E_{\mathrm{rot}},E_{\mathrm{vib}})P(E_{\mathrm{rot}})P(E_{\mathrm{vib}})}{1+\frac{k(E_{\mathrm{rot}},E_{\mathrm{vib}})}{\omega}}\,\mathrm{d}E_{\mathrm{rot}}\,\mathrm{d}E_{\mathrm{vib}} \qquad (95)$$

where $k(E_{\mathrm{rot}},E_{\mathrm{vib}})$ is the RRKM rate constant given by (96), $P(E_i)$ the Boltzmann distribution for the respective progression (given by (55)), and ω the collision frequency.

$$k(E_{\mathrm{rot}},E_{\mathrm{vib}})=\frac{G\left(E_{\mathrm{vib}}+E_{\mathrm{vib}}\left(1-I/I^{\ddagger}\right)-E_0\right)}{h\,N(E_{\mathrm{vib}})} \qquad (96)$$

where $G(E)$ is the classical sum of states at the transition state, I the moment of inertia, and $N(E)$ the classical density of states, $N(E)=\mathrm{d}G(E)/\mathrm{d}E$.

In the high-pressure limit, the collision frequency is much greater than the RRKM rate and (95) simplifies to

$$k(T)=P_{\mathrm{rxn}}\frac{k_{\mathrm{B}}T}{h}\frac{q_{\mathrm{r}}^{\ddagger}\,q_{\mathrm{v}}^{\ddagger}}{q_{\mathrm{r}}\,q_{\mathrm{v}}}\mathrm{e}^{\frac{-\Delta E}{k_{\mathrm{B}}T}} \qquad (97)$$

The term P_{rxn} is added to account for the less-than-unity probability of reaction at the singlet–triplet crossing. $P_{\mathrm{rxn}} = 1$ for dissociation on the singlet surface.

Since a critical configuration is required to reach the singlet dissociation maximum, XN$_3$ can exist with energy greater than the singlet dissociation energy and potentially undergo intersystem crossing onto the triplet surface. This is intrinsic in RRKM theory and the assumed Boltzmann distribution.

Equation (97) uses the change in *energy* between the ground state and the transition state rather than enthalpy or free energy. ΔE is independent of temperature and given as $\Delta E = U_0^{\ddagger} - U_0$, cf. (53). The thermal contributions are consolidated into the pre-exponential factor. The majority of systematic errors in the ab initio calculations cancel because of the relative nature of ΔE. Equation (97) was used to determine the unimolecular dissocia tion rate of XN_3 as a function of temperature over the range 250 to 1 000 K. These rates are plotted in Figure 4.2 and unimolecular decomposition lifetimes are plotted in Figure 4.3.

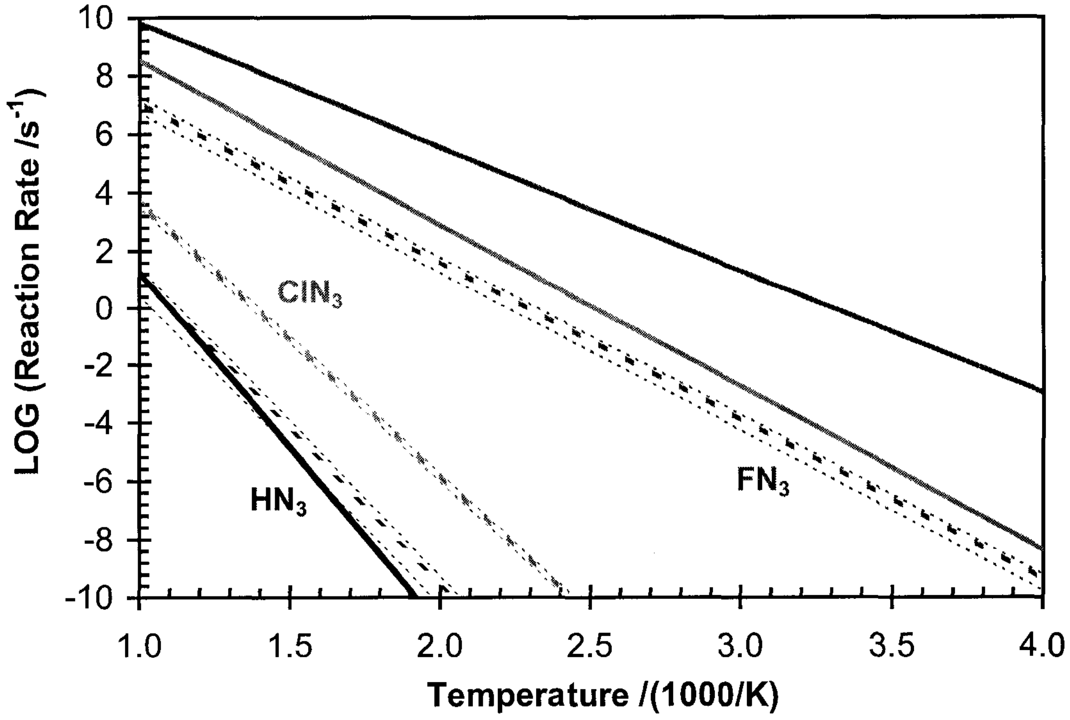

Figure 4.2 Unimolecular dissociation rates of XN_3 for the singlet (solid) and triplet (dashed) XN–NN pathways (Reactions (1) and (2)) at the UQCISD CBS energies. The average (▬▬) and max/min (——) transition probabilities (Table 4.6) are plotted for the triplet pathway. Shading scheme: HN_3, FN_3, ClN_3.

It is evident that the rate of intersystem crossing to the triplet PES is of the same magnitude as dissociation on the singlet PES for HN_3 despite the low singlet–triplet transition probability range given in Table 4.6. For FN_3 and ClN_3, where the singlet dissociation maximum and singlet–triplet crossing are closer in energy, dissociation on the singlet PES is preferred because of its unity efficiency.

The unimolecular dissociation rate changes by more than fifteen orders of magnitude in the temperature range investigated. In reality, the reaction rate loses physical meaning beyond a certain temperature. Intermolecular collisions, which are required for thermalization (a fundamental assumption of Transition State theory), occur at a finite rate, the *collision frequency*.* The *rapid decomposition temperature* is herein defined as the temperature at which the lifetime is less than one microsecond. Rapid decomposition of HN_3 occurs at 1 600 K, of FN_3 at 530 K, and of ClN_3 at 690 K.

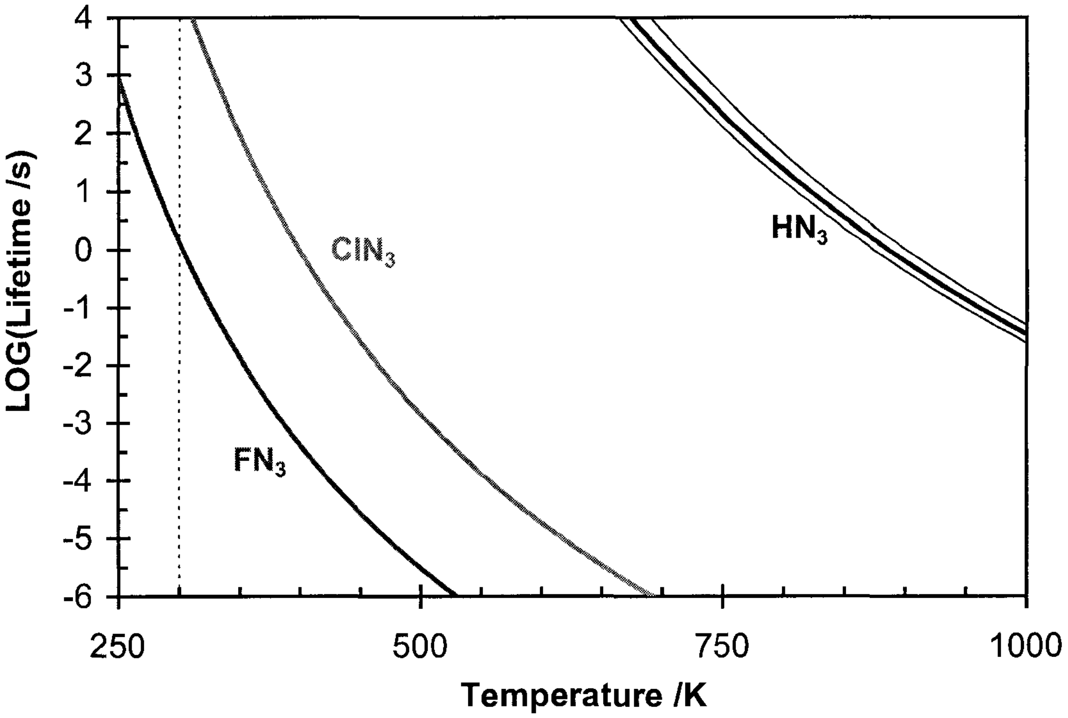

Figure 4.3 Lifetime of XN_3 from the QCISD CBS energies. The vertical dashed line corresponds to 300 K. Legend same as Figure 4.2.

At 300 K, the lifetime of HN_3 is effectively infinite, of FN_3 is 1.3 s, and of ClN_3 is 11 hours. At 14°C, the lifetime of FN_3 is 13 s, significantly lower than the experimentally observed period of 1 800 s, but in better agreement than estimates from other theoretical calculations.[56,57,58,59,60] The values in Figure 4.3 also reproduce the observed stability — HN_3 is significantly more stable than ClN_3, which is more stable than FN_3 — but are likely to be systematically low.

---

* Many parameters affect the collision frequency — temperature, total pressure, velocity (mass), collision cross section — however, they are interrelated and result in an approximately constant value, dependent only on the total pressure: 10 collisions/(μs Torr).

Singlet–triplet branching ratio

The relative yield of N*X*(a) and N*X*(X) is not obvious from Figure 4.2. It is convenient to define the *branching ratio*, $\Phi_a(T)$, to estimate the relative yield of reaction *a* in systems with competing reactions.

The branching ratio of electronically excited N*X*(a) is determined via Equation (98).

$$\Phi_a(T) = \frac{k_a(T)}{\sum_i k_i(T)} \tag{98}$$

When applied to the two state system of $X\mathrm{N}_3$, (98) simplifies to

$$\Phi_{\mathrm{N}X(\mathrm{a})}(T) = \frac{k_{\mathrm{N}X(\mathrm{a})}(T)}{k_{\mathrm{N}X(\mathrm{a})}(T) + k_{\mathrm{N}X(\mathrm{X})}(T)} \tag{99}$$

The lifetime,* τ, for the first-order decomposition of $X\mathrm{N}_3$ is determined from

$$\tau(T) = \frac{1}{\sum_i k_i(T)} = \frac{1}{k_{\mathrm{N}X(\mathrm{a})}(T) + k_{\mathrm{N}X(\mathrm{X})}(T)} \tag{100}$$

Figure 4.4 gives the branching ratio of N*X*(a) and lifetime of $X\mathrm{N}_3$ as a function of temperature up to the temperature of rapid decomposition.

---

* *Lifetime*, τ, is the time taken for 1/e (e = 2.718...) of the species to leave a given state.

Halflife, $t_{½}$, is the time taken for 1/2 of the species to leave a given state.

Lifetime and halflife are related through the expression: $t_{½} = \ln(2)\tau$

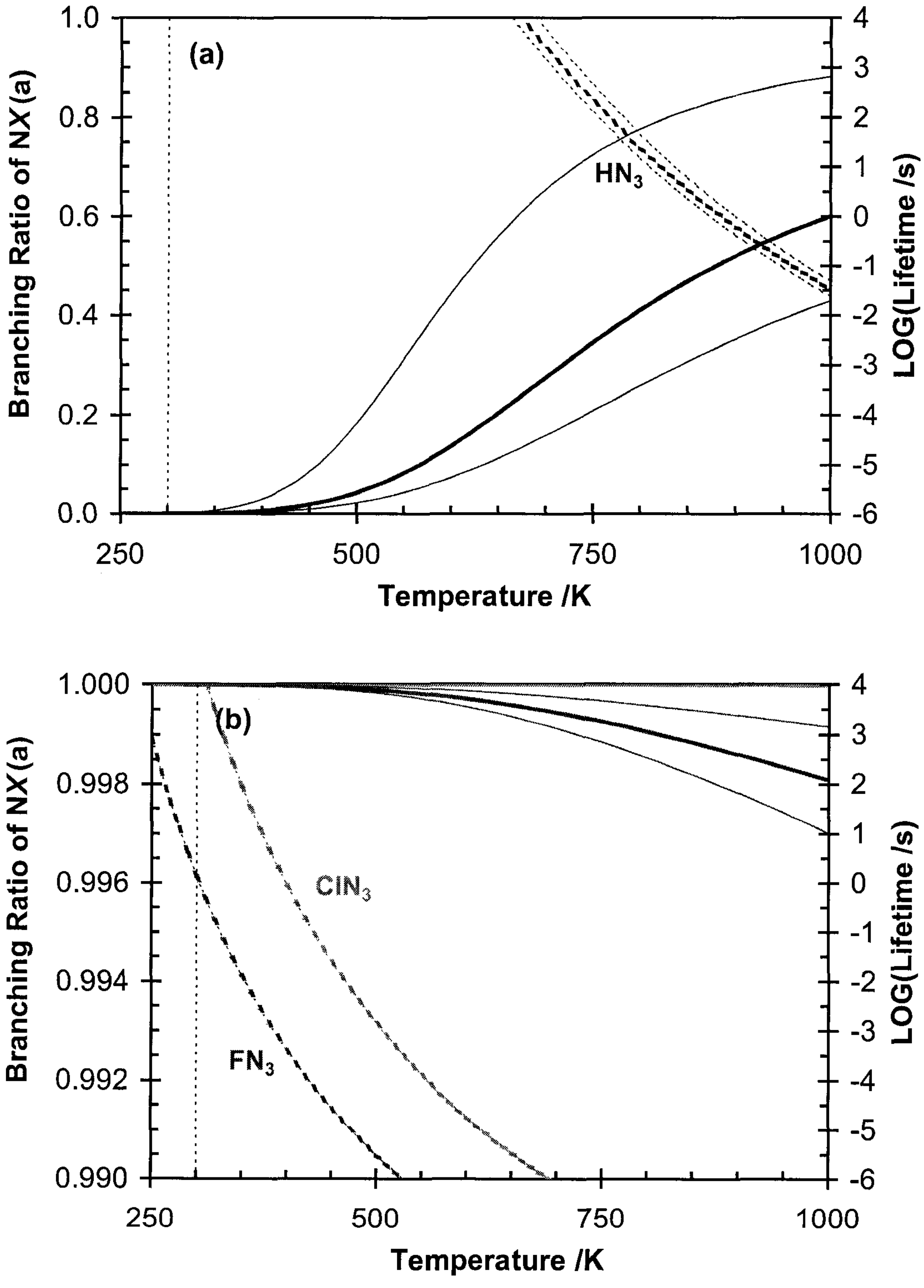

Figure 4.4 Branching ratio (solid) and lifetime (dashed) of (a) NH(a) and (b) NF(a) and NCl(a) of XN_3 based on the QCISD CBS energies. Legend same as Figure 4.2.

It is evident from Figure 4.4 that dissociation of FN_3 and ClN_3 occurs exclusively on the singlet surface, Reaction (1), despite a larger singlet–triplet crossing probability compared with HN_3. The uncertainty associated with the intersystem transition probability is plotted in Figure 4.4, but negligibly affects the lifetime or N*X*(a) branching ratio for FN_3 and ClN_3. This is not the case for HN_3, where the intersystem transition probability has a large affect on the NH(a) branching ratio and lesser affect on the lifetime.

Errors and uncertainty

Several approximations were made in Chapters 3 and 4 that should be discussed.

① The harmonic vibrational energy approximation can be corrected *on average* by applying the scaling factors in Table 3.8. However, any given system may be systematically over- or undercorrected. The azides and their dissociation products are such a system as shown in Tables 3.4 to 3.7. The harmonic vibrational energy levels and rigid rotor approximations also underestimate their respective partition coefficients, (58) to (60). The scaling factors for zpe were not optimized for zpes, but rather for fundamental energies. Despite this, the errors introduced by these approximations are likely to be small in comparison to those below.

② The equation for the complete basis set extrapolation, (52), is an approximation. However, the correlation coefficient of the linear regression was above 0.985, suggesting that the approximations are reasonable. The error introduced by this assumption is unknown, but expected to be small. Systematic errors should largely cancel in the calculation of the energies and enthalpies of reaction

③ The convergence thresholds were set as low as possible while still obtaining convergence in a reasonable number of iterations or, in the case of flat PESs, of converging at all. Convergence thresholds were lower for equilibrium ground state species and products than for the PES scan and geometry optimizations at the singlet–triplet crossing and the singlet dissociation maximum.* A lower convergence threshold means that the geometry must be closer to the 'true' geometry so that the summed PES-derivative forces and displacement vectors are smaller. See, for example, Figure 3.2(b) where there is a noticeable (440 cm^{-1}) step in the QCISD PES near 1.30 Å. However, since all data were taken from geometry optimizations, which had tighter convergence thresholds, the greatest error possible is approximately 200 cm^{-1} (2.5 kJ/mol).

④ The calculation of the singlet–triplet crossing, Appendix D, uses a manual iterative method to determine the geometry of the intersection. One iteration was applied and the resulting energy uncertainty was ± 200 cm^{-1}. Even if this uncertainty was reduced to zero, the method is not variational and would likely *not* find the minimum. Thus, the energy of the optimized geometries in Table D.4 represents a *minimum* barrier energy and the energy at the extrapolated geometry represents a *maximum* barrier energy.

For the FN_3 and ClN_3 systems, the dominant factors in the calculation of Tables 4.2 and 4.3 are the absolute energies calculated from ab initio data, which have uncertainties because of the convergence thresholds (③, *supra*) and limitations in the theoretical methods employed. For HN_3, the transition probabilities in Table 4.6 also contribute to the uncertainty. Fluctuations of ±200 cm^{-1} have little effect on the branching ratio results for FN_3 and ClN_3 — the dominant reaction pathway remains Reaction (1) — but do affect the lifetime. The branching ratio of HN_3 is dramatically affected, ranging from near zero to near unity, but the lifetime is not affected.

---

* In Gaussian, IOP(1/7=10) (corresponding to the 'tight' keyword) and IOP(1/7=60) were used for geometry optimizations. IOP(1/7=300) was used for PES scans.

5. SUMMARY

This investigation mapped the dissociation of HN_3, FN_3, and ClN_3 along the *X*–NNN and *X*N–NN pathways. The *X*N–NN pathway is significantly lower in energy and is therefore the dominant pathway for thermal dissociation. Configuration interaction (QCISD) and density functional (B3LYP) calculations using several basis sets showed consistency between the methods and basis sets for all systems studied and were consistent with the bulk of the available theoretical and experimental literature.

The discrepancy between the theoretical and experimental barrier heights was found to be caused by the failure to account for differences in the geometries of the singlet and triplet species at the singlet–triplet crossing. The results calculated herein, which calculates the barrier height at an average equilibrium geometry, are in much better agreement with experimental results than previous theoretical calculations.

The singlet–triplet crossing was found to occur on the bound portion of the ground state singlet surface. For FN_3 and ClN_3, the singlet–triplet crossing barrier was at energies close to or greater than that of the singlet dissociation maximum. This results in little intersystem crossing for FN_3 and ClN_3. Intersystem crossing is a dominant dissociation pathway for HN_3. Barrier heights were calculated that are in agreement with the experimentally observed stability and predicted to produce $NH(X^3\Sigma^-)$ and $NH(a^1\Delta)$, $NF(a^1\Delta)$, and $NCl(a^1\Delta)$. These results bode well for the use of FN_3 and ClN_3 as chemical energy storage and energy transfer agents. The large amount of energy released, 179 and 155 kJ/mol for FN_3 and ClN_3 provides sufficient energy to propagate dissociation.

The general good agreement between the HN_3 results calculated herein and previous experimental and theoretical work strongly suggests that the results for FN_3 and ClN_3 are of equal accuracy.

6. REFERENCES

1. Tornieporth-Oetting, I. C.; Klapötke, T. M. *Angew. Chem. Int. Ed. Engl.* **1995**, *34*, 511.
2. Bittererova, M.; Ostmark, H.; Brinck, T. *J. Chem. Phys.* **2002**, *116*, 9740. Bittererova, M.; Ostmark, H.; Brinck, T. *Chem. Phys. Lett.* **2001**, *347*, 220. Bittererova, M.; Brinck, T.; Ostmark, H. *Chem. Phys. Lett.* **2001**, *340*, 597.
3. Korin, A. A.; Balkova, A.; Bartlett, R. J.; Boyd, R. J.; Schleyer, P.V. *J. Phys. Chem.* **1996**, *100*, 5702.
4. Glukhovtsev, M. N.; Laiter, S. *J. Phys. Chem.* **1996**, *100*, 1569.
5. Michels, H. H.; Montgomery, J. A.; Christe, K. O; Dixon, D. A. *J. Phys. Chem.* **1995**, *99*, 187.
6. Klapötke, T. M. *J. Mol. Struc.-Theochem.* **2000**, *499*, 99.
7. Cacace, F.; de Petris, G.; Troiani, A. *Science* **2002**, *295*, 480.
8. Piper, L.G.; Krech, R. H.; Taylor, R. L. *J. Chem. Phys.* **1979**, *71,* 2099.
9. *Publication 571-N-2,* Rocketdyne Division of Rockwell International: Canoga Park, CA, **1984**.
10. Menendez-Arias, L. *Trends Pharmacol. Sci.* **2002**, *23*, 381. Erice, A.; Balfour, H. H. *Clin. Infect. Dis.* **1994**, *18*, 149.
11. Fréchet, J. M. J. *1999 Lansdowne Lectures* Department of Chemistry, University of Victoria, **May 1999**.
12. Manke, G. C. II; Setser, D. W. *J. Phys. Chem. A* **1998**, *102*, 7257.
13. Bower, R. D.; Yang, T. T. *J. Opt. Soc. Am. B* **1991**,*8* , 1583.
14. Henshaw, T. L.; Manke, G. C. II; Madden, T. J.; Berman, M. R.; Hager, G. D. *Chem. Phys. Lett.* **2000**, *325*, 537.
15. Klapötke, T. M. *Chem. Ber./Recueil* **1997**, *130*, 443.
16. Otto, M.; Lotz, S. D.; Frenking, G. *Inorg. Chem.* **1992**, *31*, 3647.
17. Lide, D. R., Ed. *CRC Handbook of Chemistry and Physics* 73rd Ed, CRC Press: Boca Raton, FL, **1992**. Alternatively, most general chemistry texts give tables with average single, double, and triple bonds strengths.
18. Geissler, P.; Klapötke, T. M.; Kroth, H. J. *Spectrochim. Acta A* **1995**, *51*, 1075.
19. L'vov, B. V. *Thermochim. Acta* **1997**, *291,* 179.
20. Representative experimental papers from different research groups include: Woods, E.; Berghout, H. L.; Cheatum, C. M.; Crim, F.F. *J. Phys. Chem. A* **2000**,*104* , 10356. Berghout, H. L.; Crim, F. F.; Zyrianov, M.; Reisler, H. *J. Chem. Phys.* **2000**, *112*, 6678. Barnes, R. J.; Sinha, A.; Dagdigian, P. J.; Lambert, H. M. *J. Chem. Phys.* **1999**, *111*, 151. Zyrianov, M.; Sanov, A.; Droz-Georget, T.; Reisler, H. *J. Chem. Phys.* **1999**, *110*, 10774. Zhang, J. S.; Xu, K. S.; Amaral, G. *Chem. Phys. Lett.* **1999**, *299*, 285. Berghout, H. L.; Brown, S. S.; Delgado, R.; Crim, F. F. *J. Chem. Phys.*

1998, *109*, 2257. Sanov, A.; Droz-Georget, T.; Zyrianov, M.; Reisler, H. *J. Chem. Phys.* **1997**, *106*, 7013. Brownsword, R. A.; Hillenkamp, M.; Laurent, T.; Vatsa, R. K.; Volpp, H. R. *J. Chem. Phys.* **1997**, *106*, 4436. Lock, M.; Gericke, K. H.; Comes, F.J. *Chem. Phys.* **1996**, *213*, 385. Brown, S. S.; Berghout, H. L.; Crim, F. F. *J. Chem. Phys.* **1996**, *105*, 8103. Brown, S. S.; Metz, R. B.; Berghout, H. L.; Crim, F. F. *J. Chem. Phys.* **1996**, *105*, 6293. Zhang, J. S; Dulligan, M.; Wittig. C. *J. Phys. Chem.* **1995**, *99*, 7446. Sanov, A.; Droz-Georget, T.; Zyrianov, M.; Reisler, H. *J. Chem. Phys.* **1997**, *106*, 7013. Zyrianov, M.; Droz-Georget, T.; Sanov, A.; Reisler, H. *J. Chem. Phys.* **1996**, *105*, 8111. Hawley, M.; Baronavski, A. P.; Nelson, H. H. *J. Chem. Phys.* **1993**,*99* , 2638. Haas, T.; Gericke, K. H.; Maul, C.; Comes, F. J. *Chem. Phys. Lett.* **1993**, *202*, 108. Bohn, B.; Stuhl, F. *J. Phys. Chem.* **1993**, *97*, 4891. Gericke, K.-H.; Haas, G.; Lock, M.; Theinl, R.; Comes, F. J. *J. Phys. Chem.* **1991**, *95*, 6104. Chu, J.-J.; Marcus, P.; Dagdigian, P. J. *J. Chem. Phys.* **1990**, *93*, 257.

21. Representative theoretical papers from different research groups include: Cook, P. A.; Jimeno, P.; Ashfold, N. R.; Balint-Kurti, G. G.; Dixon, R.N. *Phys. Chem. Chem. Phys.* **2002**, *4*, 1513. Cook, P. A.; Langford, S. R.; Ashfold, N. R. *Phys. Chem. Chem. Phys.* **1998**, *1*, 45. Yarkony, D. R. *Mol. Phys.* **2001**, *99*, 1463. Zhao, L.; Li, Z.H. *Sci. China Ser. B* **2001**, *44*, 31. Fang, W.H. *J. Phys. Chem. A* **2000**, *104*, 4045. Klossika, J. J.; Flothmann, H.; Schinke, R.; Bittererova, M. *Chem. Phys. Lett.* **1999**, *314*, 182. Stevens, J. E.; Cui, Q.; Morokuma, K. *J. Chem. Phys.* **1998**, *108*, 1452. Mebel, A. M.; Luna, A.; Lin, M. C.; Morokuma, K. *J. Chem. Phys.* **1996**, *105*, 6439. Meier, U.; Staemmler, V. *J Phys. Chem.* **1991**, *91*, 6111.
22. Kajimoto, O.; Yamamoto, T.; Fueno, T. *J. Phys. Chem.* **1979**, *83*, 429.
23. Richardson, W. C.; Setser, D. W. *Can. J. Chem.* **1969**,*47* , 2725.
24. Yarkony, D. R. *J. Phys. Chem.* **1990**, *92*, 320.
25. Foy, B. R.; Casassa, M. P.; Stephenson, J. C.; King, D. S. *J. Chem. Phys.* **1988**, *89*, 608.
26. Foy, B. R.; Casassa, M. P.; Stephenson, J. C.; King, D. S. *J. Chem. Phys.* **1990**, *92*, 2782.
27. Foy, B. R.; Casassa, M. P.; Stephenson, J. C.; King, D. S. *J. Chem. Phys.* **1989**, *90*, 7037.
28. Casassa, M. P.; Foy, B. R.; Stephenson, J. C.; King, D. S. *J. Chem. Phys.* **1991**, *94*, 250.
29. Alexander, H. M.; Werner, H.-J.; Hemmer, T.; Knowles, P. J. *J. Chem. Phys.* **1990**, *93*, 3307.
30. Alexander, H. M.; Werner, H.-J.; Dagdigian, P. J. *J. Chem. Phys.* **1988**, *89*, 1388.
31. Gericke, K.-H.; Haas, G.; Lock, M.; Theinl, R.; Comes, F. J. *Chem. Phys. Lett.* **1991**, *186*, 427.
32. Fang, W.H. *J. Phys. Chem. A* **2000**, *104*, 4045.
33. Zhang, J. S.; Xu, K. S.; Amaral, G. *Chem. Phys. Lett.* **1999**, *299*, 285.
34. Cook, P. A.; Langford, S. R.; Ashfold, N. R. *Phys. Chem. Chem. Phys.* **1998**, *1*, 45.

35. Benard, D. J.; Winker, B. K.; Chowdhury, M. A.; Seder, T. A.; Michels, H. H. *Investigation of Two Potential Visible Wavelength Chemical Laser Schemes Based on Thermal Decomposition of Chlorine Azide*, Rockwell International: Thousand Oaks, CA, **1991(?)**.
36. Meier, U.; Staemmler, V. *J Phys. Chem.* **1991**, *91*, 6111.
37. Lefebvre-Brion, H.; Field, R. W. *Perturbations in the Spectra of Diatomic Molecules*, Academic Press: New York, **1986**.
38. Marian, C. M.; Klotz, R. *Chem. Phys.* **1985**, *95*, 213.
39. Teles, J. H.; Maier, G.; Hess, B. A., Jr.; Schaad, L. J.; Winnewisser, M.; Winnewisser, B. P. *Chem. Ber.* **1989**, *122*, 753.
40. Bondybey, V. E.; English, J. H.; Mathews, C. W.; Contolini, R. J. *J. Molec. Spectrosc.* **1982**, *92*, 431.
41. Mebel, A. M.; Luna, A.; Lin, M.C.; Morokuma, K. *J. Chem. Phys.* **1996**, *105*, 6439.
42. East, A. L. L.; Allen, W. D. *J. Chem. Phys.* **1993**, *99*, 4638.
43. East, A. L. L.; Johnson, C. S.; Allen, W. D. *J. Chem. Phys.* **1992**, *98*, 1299.
44. Yokoyama, K.; Takane, S.; Fueno, T. *Bull. Chem. Soc. Jpn.* **1991**,*64* , 2230.
45. Jensen, R. H., *unpublished results*.
46. Linstrom, P. J.; Mallard, W. G.; Eds., *NIST Chemistry WebBook* (webbook.nist.gov) NIST Standard Reference Database Number 69, **July 2001**, National Institute of Standards and Technology, Gaithersburg, MD.
47. East, A. L. L.; Allen, W. D. *J. Phys. Chem. A* **2000**, *104*, 1362.
48. Sanov, A.; Droz-Georget, T.; Zyrianov, M.; Reisler, H. *J. Chem. Phys.* **1997**, *106*, 7013.
49. Brown, S. S.; Berghout, H. L.; Crim, F. F. *J. Chem. Phys.* **1996**, *105*, 8103.
50. Zyrianov, M.; Sanov, A.; Droz-Georget, T.; Reisler, H. *J. Chem. Phys.* **1999**, *110*, 10774.
51. Zhang, J. S; Dulligan, M.; Wittig. C. *J. Phys. Chem.* **1995**, *99*, 7446.
52. Pankratov, A. W.; Sokolov, O. M.; Savenkova, N. I. *Zh. Neorg. Khim.* **1964**, *9*, 2030.
53. Haller, J. F. *Ph.D. Dissertation*, Cornell University: Ithaca, NY, **1942**.
54. Patel, D.; Pritt, A. T., Jr.; Benard, D. J. *J. Chem. Phys.* **1986**, *90*, 1931.
55. Benard, D. J.; Winker, B. K.; Seder, T. A.; Cohn, R. H. *J. Chem. Phys.* **1989**, *93*, 4790.
56. Chaban, G.; Yarkony, D. R.; Gordon, M. S. *J. Chem. Phys.* **1995**, *103*, 7983.
57. Benard, D. J.; Chowdhury, M. A.; Winker, B. K.; Seder, T. A.; Michels, H. H. *J. Phys. Chem.* **1990**, *94*, 7507.
58. Michels, H. H.; Montgomery, J. A., Jr. *Air Force Avionics Laboratory (AFAL) Report F04611-86-C-0071*, **1988**.

59. Montgomery, J. A., Jr.; Michels, H. H. *Abstr. Pap. Amer. Chem. Soc.* **1988**,*196* , 79-Phys.

60. Michels, H. H.; Montgomery, J. A., Jr. *Abstr. Pap. Amer. Chem. Soc.* **1987**,*194* , 38-Phys.

61. Benard, D. J.; Winker, B. K.; Seder, T. A.; Cohn, R.H. *J. Chem. Phys.* **1989**, *93*, 4790.

62. Jensen, R. H. *Chain Decomposition of Chlorine Azide*, M.Sc. Thesis, University of Denver, **1999**.

63. Piper, L. G.; Krech, R. H.; Taylor, R. L. *J. Photochem.* **1982**, *18,* 125.

64. Coombe, R. D.; Patel, D.; Pritt, A. T. Jr.; Wodarczyk, F. J. *J. Chem. Phys.* **1981**, *75*, 2177.

65. Henshaw, T. L.; Herrera, S. D.; Haggquist, G. W.; Schlie, L. A. *J. Phys. Chem. A* **1997**, *101,* 4048.

66. Ray, A. J.; Coombe, R. D. *J. Phys. Chem.* **1994**, *98*, 8940.

67. Hansen, N.; Wodtke, A. M.; Komissarov, A. V.; Heaven, M. C. *Chem. Phys. Lett.* **2003**, *368*, 568.

68. Clarke, T. C.; Clyne, M. A. A. *Trans. Faraday Soc.* **1970**, *66,* 877.

69. Coombe, R. D.; Lam, C. H. T. *J. Chem. Phys.* **1983**, *79,* 3746.

70. Coombe, R. D. *J. Phys. Chem.* **1987**, *91,* 2287.

71. David, S. J.; Coombe, R. D. *J. Phys. Chem.* **1985**, *89,* 5206.

72. Buzek, P.; Klapötke, T. M.; Schleyer, P.V.; Tornieporth-Oetting, I. C. *Angew. Chem. Int. Ed. Engl.* **1993**, *32*, 295.

73. Jensen, F. *Introduction to Computational Chemistry*, John Wiley & Sons: Toronto, **2001**.

74. Young, D. *Computational Chemistry*, John Wiley & Sons: Toronto, **2001**.

75. Koch, W.; Holthausen, M. C. *A Chemist's Guide to Density Functional Theory*, Wiley VCH: Toronto, **2000**.

76. Levine, I. N. *Quantum Chemistry* 5th Ed., Prentice-Hall: Englewood Cliffs, NJ, **2000**.

77. Szabo, A.; Ostlund, N.S. *Modern Quantum Chemistry*, Dover: New York, **1996**.

78. Foresman, J. B.; Frisch, Æ. *Exploring Chemistry with Electronic Structure Methods*, 2nd Ed., Gaussian, Inc.: Pittsburgh, **1996**.

79. Mills, I.; Cvitaš, T.; Homann, K.; Kallay, N.; Kuchitsu, K. *Quantities, Units and Symbols in Physical Chemistry*, 2nd Ed., Blackwell Scientific Publications: London, **1993**.

80. McQuarrie, D. A.; Simon, J. D. *Physical Chemistry: a Molecular Approach* University Science Books: Sausalito, CA, **1997**.

81. Frisch, M. J.; Frisch, Æ. *Gaussian 98 User's Reference*, 2nd Ed., Gaussian, Inc.: Pittsburgh, **1999**.

82. Hohenberg, P. C.; Kohn, W.; Sham, L. J. *Adv. Quantum Chem.* **1990**, *21*, 7.

83. Kohn, W.; Sham, L. J. *Phys. Rev.* **1965**, *140*, A1133.

84. Becke, A. D. *J. Chem. Phys.* **1993**, *98*, 5648.

85. Becke, A. D. *Phys. Rev. A* **1988**, *38*, 3098.

86. Lee, C.; Yang, W.; Parr, R. G. *Phys. Rev. B* **1988**, *37*, 785.

87. Wolfe, S.; Shi, Z.; Brion, C. E.; Rolke, J.; Zheng, Y.; Cooper, G.; Chong, D. P.; Hu, C. Y. *Can. J. Chem.* **2002**, *80*, 222.

88. Reed, A. E.; Curtiss, L. A.; Weinhold, F. *Chem. Rev.* **1988**,*88* , 899.

89. Frisch, M. J.; Trucks, G. W.; Schlegel, H. B.; Scuseria, G. E.; Robb, M. A.; Cheeseman, J. R.; Zakrzewski, V. G.; Montgomery, J. A. Jr.; Stratmann, R. E.; Burant, J. C.; Dapprich, S.; Millam, J. M.; Daniels, A. D.; Kudin, K. N.; Strain, M. C.; Farkas, O.; Tomasi, J.; Barone, V.; Cossi, M.; Cammi, R.; Mennucci, B.; Pomelli, C.; Adamo, C.; Clifford, S.; Ochterski, J.; Petersson, G. A.; Ayala, P. Y.; Cui, Q.; Morokuma, K.; Salvador, P.; Dannenberg, J. J.; Malick, D. K.; Rabuck, A. D.; Raghavachari, K.; Foresman, J. B.; Cioslowski, J.; Ortiz, J. V.; Baboul, A. G.; Stefanov, B. B.; Liu, G.; Liashenko, A.; Piskorz, P.; Komaromi, I.; Gomperts, R.; Martin, R. L.; Fox, D. J.; Keith, T.; Al-Laham, M. A.; Peng, C. Y.; Nanayakkara, A.; Challacombe, M.; Gill, P. M. W.; Johnson, B.; Chen, W.; Wong, M. W.; Andres, J. L.; Gonzalez, C.; Head-Gordon, M.; Replogle, E. S.; Pople, J. A. *Gaussian 98 Revision A.11* Gaussian, Inc.: Pittsburgh, **2001**.

90. Pople, J. A.; Head-Gordon, M.; Raghavachari, K. *J. Chem. Phys.* **1987**,*87* , 5968.

91. van Duijneveldt, F. B.; van Duijneveldt-van de Rijdt, J. G. C. M.; van Lenthe, J. H. *Chem. Rev.* **1994**, *94*, 1873.

92. Simon, S.; Duran, M.; Dannenberg, J. J. *J. Chem. Phys.* **1996**, *105*, 11024.

93. van Mourik, T.; Wilson, A. K.; Peterson, K. A.; Woon, D. E.; Dunning, T. H. Jr. *Adv. Quant. Chem.* **1999**, *31*, 105.

94. Glendening, E. D.; Reed, A. E.; Carpenter, J. E.; Weinhold, F. *NBO Version 3.1 Program Manual* Theoretical Chemistry Institute and Department of Chemistry, University of Wisconsin: Madison, WI.

95. Linstrom, P. J.; Mallard, W. G.; Eds., *NIST Chemistry WebBook* (webbook.nist.gov) NIST Standard Reference Database Number 69, **February 2003**, National Institute of Standards and Technology, Gaithersburg, MD.

96. Boyd, R. *Recent applications of density functional theory calculations to biomolecules*, chemistry seminar, University of Victoria, November 2002.

97. Otto, M.; Lotz, S. D.; Frenking, G. *Inorg. Chem.* **1992**, *31*, 3647, and references cited therein.

98. Scott, A. P.; Radom, L. *J. Phys. Chem.* **1996**, *100*, 16502.

99. Tatum, J. B. *Publications of the Dominion Astrophysical Observatory* Queen's Printers: Ottawa, **1966**, *XIII*, 1.

100. Steinfeld, J. I.; Francisco, J. S.; Hase, W. L. *Chemical Kinetics and Dynamics* Prentice Hall: Englewood Cliffs, NJ, **1989**.

101. Rinnenthal, J. L.; Gericke, K.-H. *J. Mol. Spectrosc.* **1999**, *198*, 115.

102. Coombe, R. D.; Van Benthem, M. H. *J. Chem. Phys.* **1984**, *81*, 2984.

103. Yarkony, D. R. *J. Chem. Phys.* **1987**, *86*, 1642.

104. HN_3: Chu, J.-J.; Marcus, P.; Dagdigian, P. J. *J. Chem. Phys.* **1990**, *93*, 257.

FN_3: Patel, D.; Pritt, A. T., Jr.; Benard, D. J. *J. Phys. Chem.* **1986**, *90*, 1931.

ClN_3: Jensen, R. H. *Chain Decomposition of Chlorine Azide*, M.Sc. Thesis, University of Denver, **1999**.

105. Meier, U.; Staemmler, V. *J. Phys. Chem.* **1991**, *95*, 6111.

106. Baronavski, A. P; Miller, R. G.; McDonald, J. R. *Chem. Phys.* **1978**, *30*, 119. DeKoven, B. M.; Baronavski, A. P. *Chem. Phys.* **1982**, *86*, 392.

107. Jensen, R. H.; Mann, A.; Coombe, R. D. *J. Phys. Chem. A* **2000**, *104*, 6573.

108. Reference 23 in Hansen, N.; Wodtke, A. M.; Komissarov, A. V.; Heaven, M. C. *Chem. Phys. Lett.* **2003**, *368*, 568.

109. Linstrom, P. J.; Mallard, W. G.; Eds., *NIST Chemistry WebBook* (webbook.nist.gov) NIST Standard Reference Database Number 69, **July 2001**. National Institute of Standards and Technology, Gaithersburg, MD. Chase, M. W. Jr., *NIST-JANAF Thermochemical Tables*, 4th Ed, *J. Phys. Chem. Ref. Data, Monograph 9*, **1998**.

110. Wagman, D. D. *Natl. Bur. Stand. Tech. Note 270-3*, **1968**.

111. See, for example: Czuchaj, E.; Krośnicki, M.; Stoll, H. *Theor. Chem. Acc.* **2001**, *107*, 27. Fedorov, D. G.; Gordon, M. S. *J. Chem. Phys.* **2000**, *112*, 5611. Christiansen, O.; Gauss, J.; Schimmelpfennig, B. *Phys. Chem. Chem. Phys.* **2000**, *2*, 965. Minaev, B. F.; Ågren, H. *J. Molec. Struc. (Theochem)* **1999**, *492*, 53. Havlas, Z.; Michl, J *Collect. Czech. Chem. Commun.* **1998**, *63*, 1485. Wheeler, M. D.; Newman, S. M.; Orr-Ewing, A. J. *J. Chem. Phys.* **1998**, *108*, 6594.

112. Yarkony, D. R. *J. Phys. Chem. A* **2001**, *105*, 6277. Yarkony, D. R. *Mol. Phys.* **2001**, *99*, 1463. Yarkony, D. R. *Acc. Chem. Res.* **1998**, *31*, 511. Yarkony, D. R. *Theor. Chem. Acc.* **1997**, *98*, 197.

113. Steinfeld, J. I. *Molecules and Radiation* MIT Press: Cambridge, 2nd Ed., **1985**.

APPENDIX A: DEFINITIONS, ACRONYMS, AND ABBREVIATIONS

adiabatic	a process in which where no energy transfer is permitted
B3LYP	a density functional method
BO	Born-Oppenheimer
BSSE	basis set superposition error
CASSCF	complete active space self consistent field (synonym: MCSCF)
CASPT2	complete active space with second order energy correction via perturbation theory
CC	coupled cluster
CBS	complete basis set
CGTF	contracted gaussian-type function (basis function)
CI	configuration interaction
CSF	configurational state function
diabatic	a process in which where energy transfer is permitted
DFT	density functional theory
ECP	effective core potential
GTO	gaussian-type orbital
halflife	is the time taken for 1/2 of the species to leave a given state (cf. lifetime)
HF	Hartree-Fock
isc	intersystem crossing (a specific singlet–triplet crossing in this dissertation)
isodesmic	a chemical reaction that conserves the type and number of chemical bonds
isogyric	a chemical reaction that conserves net spin
lifetime	is the time taken for 1/e of the species to leave a given state (cf. halflife)
MAD	mean absolute deviation
MCSCF	multi-configurational self-consistent field (synonym: CASSCF)
MP*n*	Møller-Plesset perturbation theory with n^{th} order energy correction (synonym: MPPT*n*, but not commonly used)
MRCI	multireference configuration interaction
NBO	natural bond orbital

nmr	nuclear magnetic resonance
NO	natural orbital
NPA	natural population analysis
PEC	potential energy curve
PES	potential energy surface
QCI	quadratically-converged configuration interaction
rms	root-mean-square
S–T	singlet–triplet crossing (cf. intersystem crossing)
SATP	standard ambient temperature and pressure
S/D/T	single/double/triple excitations from the reference state; often multiples used as in CIS, CID, or CISD. Values in brackets refer to estimated or non-optimized parameter: QCISD(T).
SCF	self-consistent field
SD	Slater determinant
SO	Slater orbital
SOC	spin-orbit coupling
SOICCI	second-order internally contracted configuration interaction
STO	Slater-type orbital
zpe	zero point energy

Methods

single determinant	a method that uses one Slater determinant to define the wavefunction
single reference	a method that uses one CSF to define the wavefunction (identical with single determinant if the CSF is a single determinant)
multi reference	a method that uses more than one CSF to define the wavefunction

APPENDIX B: THE HARTREE-FOCK EQUATION*

Derivation of the Hartree-Fock equation starts with consideration of the Schrödinger equation.

$$\begin{aligned} &\hat{\mathcal{H}}\left|\Psi\right\rangle = E\left|\Psi\right\rangle \\ &\left\langle\Psi\right|\left[\hat{\mathcal{H}}\left|\Psi\right\rangle = E\left|\Psi\right\rangle\right] \\ &\left\langle\Psi\right|\hat{\mathcal{H}}\left|\Psi\right\rangle = E\left\langle\Psi|\Psi\right\rangle \end{aligned} \tag{101}$$

One- and two-electron components of the electronic energy

Considering the left-hand side (LHS) of (101), substitution for the Hamiltonian operator, (23), allows for the separation of the Hamiltonians into one- and two-electron integrals. These are the core Hamiltonian and correlation terms, respectively.

$$\begin{aligned} \left\langle\Psi\right|\hat{\mathcal{H}}\left|\Psi\right\rangle &= \left\langle\Psi\right| -\frac{1}{2}\sum_{\mu}\nabla_{\mu}^{2} - \sum_{\mu}\sum_{A}\frac{Z}{r_{\mu A}} + \sum_{\mu}\sum_{\nu>\mu}\frac{1}{r_{\mu\nu}}\left|\Psi\right\rangle \\ &= \left\langle\Psi\right|\sum_{\mu}\hat{H}_{\mu}^{\text{core}} + \sum_{\mu}\sum_{\nu>\mu}\frac{1}{r_{\mu\nu}}\left|\Psi\right\rangle \\ &= \left\langle\Psi\right|\sum_{\mu}\hat{H}_{\mu}^{\text{core}}\left|\Psi\right\rangle + \left\langle\Psi\right|\sum_{\mu}\sum_{\nu>\mu}\frac{1}{r_{\mu\nu}}\left|\Psi\right\rangle \end{aligned} \tag{102}$$

In HF theory, $\left|\Psi\right\rangle$ is a single Slater determinant. For a system with two electrons in two spin-orbitals, we generate a 2×2 Slater determinant, (12).

$$\begin{aligned} \Psi &= \frac{1}{\sqrt{2}}\begin{vmatrix} \varphi_i(1) & \varphi_j(1) \\ \varphi_i(2) & \varphi_j(2) \end{vmatrix} \\ &= \frac{1}{\sqrt{2}}\left(\varphi_i(1)\varphi_j(2) - \varphi_i(2)\varphi_j(1)\right) \end{aligned} \tag{12)'$$

---

* There are many paths to the Hartree-Fock equation. A considerable amount of time was spent with References 73 to 77 developing a logical [in my mind] path.

Substitution into (102) gives

$$\langle\Psi|\hat{\mathscr{H}}|\Psi\rangle=\frac{1}{2}\begin{bmatrix}\big\langle(\varphi_i(1)\varphi_j(2)-\varphi_i(2)\varphi_j(1))\big|\sum\limits_{\mu}\hat{H}_{\mu}^{\text{core}}\big|(\varphi_i(1)\varphi_j(2)-\varphi_i(2)\varphi_j(1))\big\rangle+\\ \big\langle(\varphi_i(1)\varphi_j(2)-\varphi_i(2)\varphi_j(1))\big|\sum\limits_{\mu}\sum\limits_{\nu>\mu}\frac{1}{r_{\mu\nu}}\big|(\varphi_i(1)\varphi_j(2)-\varphi_i(2)\varphi_j(1))\big\rangle\end{bmatrix}\tag{103}$$

Probing only the core Hamiltonian function, we expand the summation and collect like terms.

$$\begin{aligned}
&\langle\Psi|\sum_{\mu}\hat{H}_{\mu}^{\text{core}}|\Psi\rangle\\
&=\frac{1}{2}\big\langle(\varphi_i(1)\varphi_j(2)-\varphi_i(2)\varphi_j(1))\big|\hat{H}_1^{\text{core}}+\hat{H}_2^{\text{core}}\big|(\varphi_i(1)\varphi_j(2)-\varphi_i(2)\varphi_j(1))\big\rangle\\
&=\frac{1}{2}\begin{bmatrix}\big\langle(\varphi_i(1)\varphi_j(2)-\varphi_i(2)\varphi_j(1))\big|\hat{H}_1^{\text{core}}\big|(\varphi_i(1)\varphi_j(2)-\varphi_i(2)\varphi_j(1))\big\rangle\\ +\big\langle(\varphi_i(1)\varphi_j(2)-\varphi_i(2)\varphi_j(1))\big|\hat{H}_2^{\text{core}}\big|(\varphi_i(1)\varphi_j(2)-\varphi_i(2)\varphi_j(1))\big\rangle\end{bmatrix}\\
&=\frac{1}{2}\begin{bmatrix}\langle\varphi_j(2)|\varphi_j(2)\rangle\langle\varphi_i(1)|\hat{H}_1^{\text{core}}|\varphi_i(1)\rangle-\langle\varphi_i(2)|\varphi_j(2)\rangle\langle\varphi_j(1)|\hat{H}_1^{\text{core}}|\varphi_i(1)\rangle\\ -\langle\varphi_j(2)|\varphi_i(2)\rangle\langle\varphi_i(1)|\hat{H}_1^{\text{core}}|\varphi_j(1)\rangle+\langle\varphi_i(2)|\varphi_i(2)\rangle\langle\varphi_j(1)|\hat{H}_1^{\text{core}}|\varphi_j(1)\rangle\\ +\langle\varphi_i(1)|\varphi_i(1)\rangle\langle\varphi_j(2)|\hat{H}_2^{\text{core}}|\varphi_j(2)\rangle-\langle\varphi_i(1)|\varphi_j(1)\rangle\langle\varphi_j(2)|\hat{H}_2^{\text{core}}|\varphi_i(2)\rangle\\ -\langle\varphi_j(1)|\varphi_i(1)\rangle\langle\varphi_i(2)|\hat{H}_2^{\text{core}}|\varphi_j(2)\rangle+\langle\varphi_j(1)|\varphi_j(1)\rangle\langle\varphi_i(2)|\hat{H}_2^{\text{core}}|\varphi_i(2)\rangle\end{bmatrix}
\end{aligned}\tag{104}$$

Orthogonality of the spin-orbitals simplifies (104) to

$$\begin{aligned}
&\langle\Psi|\sum_{\mu}\hat{H}_{\mu}^{\text{core}}|\Psi\rangle\\
&=\frac{1}{2}\begin{bmatrix}\langle\varphi_i(1)|\hat{H}_1^{\text{core}}|\varphi_i(1)\rangle+\langle\varphi_j(1)|\hat{H}_1^{\text{core}}|\varphi_j(1)\rangle+\\ \langle\varphi_j(2)|\hat{H}_2^{\text{core}}|\varphi_j(2)\rangle+\langle\varphi_i(2)|\hat{H}_2^{\text{core}}|\varphi_i(2)\rangle\end{bmatrix}\\
&=\frac{1}{2}\left[2\langle\varphi_i(1)|\hat{H}_1^{\text{core}}|\varphi_i(1)\rangle+2\langle\varphi_j(1)|\hat{H}_1^{\text{core}}|\varphi_j(1)\rangle\right]\\
&=\frac{1}{2}\left[2\langle\varphi_i(\mu)|\hat{H}_{\mu}^{\text{core}}|\varphi_i(\mu)\rangle+2\langle\varphi_j(\mu)|\hat{H}_{\mu}^{\text{core}}|\varphi_j(\mu)\rangle\right]\\
&=\langle\varphi_i(\mu)|\hat{H}_{\mu}^{\text{core}}|\varphi_i(\mu)\rangle+\langle\varphi_j(\mu)|\hat{H}_{\mu}^{\text{core}}|\varphi_j(\mu)\rangle\\
&=\sum_i h_i
\end{aligned}\tag{105}$$

where $\langle\varphi_i(1)|\hat{H}_1^{\text{core}}|\varphi_i(1)\rangle = \langle\varphi_i(2)|\hat{H}_2^{\text{core}}|\varphi_i(2)\rangle = \langle\varphi_i(\mu)|\hat{H}_\mu^{\text{core}}|\varphi_i(\mu)\rangle$ as a result of the indistinguishability of the electrons. h_i is defined to be $\langle\varphi_i(\mu)|\hat{H}_\mu^{\text{core}}|\varphi_i(\mu)\rangle$. (105) shows that the one-electron energy in an n-electron system is the simple sum of the n one-electron contributions.

Coulomb and exchange operators

The correlation term* is evaluated the same way, yielding

$$\begin{aligned}
&\langle\Psi|\sum_{\mu}\sum_{\nu>\mu}\frac{1}{r_{\mu\nu}}|\Psi\rangle \\
&=\frac{1}{2}\langle(\varphi_i(1)\varphi_j(2)-\varphi_i(2)\varphi_j(1))|\frac{1}{r_{12}}|(\varphi_i(1)\varphi_j(2)-\varphi_i(2)\varphi_j(1))\rangle \\
&=\frac{1}{2}\begin{bmatrix}\langle\varphi_i(1)\varphi_j(2)|\frac{1}{r_{12}}|\varphi_i(1)\varphi_j(2)\rangle-\langle\varphi_i(1)\varphi_j(2)|\frac{1}{r_{12}}|\varphi_i(2)\varphi_j(1)\rangle \\ -\langle\varphi_i(2)\varphi_j(1)|\frac{1}{r_{12}}|\varphi_i(1)\varphi_j(2)\rangle+\langle\varphi_i(2)\varphi_j(1)|\frac{1}{r_{12}}|\varphi_i(2)\varphi_j(1)\rangle\end{bmatrix} \\
&=\langle\varphi_i(1)\varphi_j(2)|\frac{1}{r_{12}}|\varphi_i(1)\varphi_j(2)\rangle-\langle\varphi_i(1)\varphi_j(2)|\frac{1}{r_{12}}|\varphi_i(2)\varphi_j(1)\rangle
\end{aligned} \tag{106}$$

The last simplification is because of the indistinguishability of the electrons. Two types of integrals exist in (106), the Coulomb and exchange integrals, J_{ij} and K_{ij}.

$$\begin{aligned}
J_{ij}&=\langle\varphi_i(1)\varphi_j(2)|\frac{1}{r_{12}}|\varphi_i(1)\varphi_j(2)\rangle \\
K_{ij}&=\langle\varphi_i(1)\varphi_j(2)|\frac{1}{r_{12}}|\varphi_i(2)\varphi_j(1)\rangle
\end{aligned} \tag{107}$$

The integrals in (107) can alternatively be expressed in terms of the Coulomb, $\hat{J}_i$, and exchange, $\hat{K}_i$, operators.

---

* The $1/r_{ij}$ operation is sometimes referred to as the $\hat{g}$o perator.

$$
\begin{aligned}
\hat{J}_i\left|\varphi_j(2)\right\rangle &= \langle\varphi_i(1)|\frac{1}{r_{12}}|\varphi_i(1)\rangle\left|\varphi_j(2)\right\rangle \\
\hat{K}_i\left|\varphi_j(2)\right\rangle &= \langle\varphi_i(1)|\frac{1}{r_{12}}|\varphi_j(1)\rangle\left|\varphi_i(2)\right\rangle
\end{aligned}
\tag{108}
$$

such that

$$
\begin{aligned}
J_{ij} &= \left\langle\varphi_j(2)\middle|\hat{J}_i\middle|\varphi_j(2)\right\rangle = \left\langle\varphi_i(1)\varphi_j(2)\right|\frac{1}{r_{12}}\left|\varphi_i(1)\varphi_j(2)\right\rangle \\
K_{ij} &= \left\langle\varphi_j(2)\middle|\hat{K}_i\middle|\varphi_j(2)\right\rangle = \left\langle\varphi_i(1)\varphi_j(2)\right|\frac{1}{r_{12}}\left|\varphi_i(2)\varphi_j(1)\right\rangle
\end{aligned}
\tag{109}
$$

For the two-electron system in question, the correlation term in (106) simplifies to

$$
\langle\Psi|\sum_{\mu}\sum_{\nu>\mu}\frac{1}{r_{\mu\nu}}|\Psi\rangle = J_{ij} - K_{ij}
\tag{110}
$$

For a system with more electrons and orbitals,

$$
\langle\Psi|\sum_{\mu}\sum_{\nu>\mu}\frac{1}{r_{\mu\nu}}|\Psi\rangle = \sum_{i}\sum_{j>i}\left(J_{ij} - K_{ij}\right)
\tag{111}
$$

Electronic energy

The HF electronic energy is the sum of the one- and two-electron contributions. This derivation returns the *unrestricted* HF energy since all spin-orbits are considered independently.

$$
\boxed{E_{\mathrm{UHF}} = \sum_i h_i + \sum_i\sum_{j>i}\left(J_{ij} - K_{ij}\right)}
\tag{112}
$$

In the RHF simplification, both spin-orbitals from a single MO are either occupied or unoccupied. The orbital coefficients, c_{ir}, are assumed to be the same and thus, only half the spin-orbitals in the Slater determinant need to be considered. The resulting energy expression is half (112). The true HF energy is obtained by multiplying by two. However, the factor of two does not apply to the exchange energy since that would mean each exchange energy is counted twice (1 ↔ 2 and 2 ↔ 1). The RHF energy expression is thus given in (113).

$$\boxed{E_{\text{RHF}} = 2\sum_{i=1}^{n/2} h_i + \sum_{i=1}^{n/2}\sum_{j=1}^{n/2}\left(2J_{ij} - K_{ij}\right)} \tag{113}$$

(112) sums over the occupied orbitals for both the core Hamiltonian and correlation terms. If we consider a single orbital, we have an expression for the energy of an electron in that orbital, ε_i. The factor of ½ is introduced because the j orbitals cannot be made a function of the i orbitals and are counted twice.*

$$\varepsilon_i = h_i + \frac{1}{2}\sum_j \left(J_{ij} - K_{ij}\right) \tag{114}$$

The Variational theorem

The variational theorem is the fundamental theory on which the vast majority of quantum mechanical calculations are based, including those used in this dissertation. The variational theorem determines the atomic orbital coefficients that minimize the energy of the system and is determined by setting the respective derivative to zero.

$$\frac{\partial E}{\partial c_i} \underset{\text{set}}{\underset{\uparrow}{=}} 0 \tag{115}$$

The optimized c_i could equally return a minimum or maximum energy, but this can be determined with further analysis $\left(\mathrm{d}^2E/\mathrm{d}c_i^2\right)$ or by applying chemical intuition to the result.

The variational theorem is presented in several stages. A system comprising two orbitals is solved in the most general manner. Approximations are introduced as necessary and with reference to their effect on the result. The general formulation is presented as an

---

* $\sum_i\sum_{j>i} f(i,j) \equiv \sum_{i=1}^{n-1}\sum_{j=i+1}^{n} f(i,j) \equiv \frac{1}{2}\sum_i\sum_j f(i,j)$

extension of the simple system. Finally, the implementation of the variational theorem in HF theory is presented.

Variational treatment of a simple system

A spin MO comprising the linear combination of two normalized AOs is given by

$$\varphi = c_1 \chi_1 + c_2 \chi_2 \tag{116}$$

Substitution of (116) into (101) results in

$$E = \frac{\langle \varphi | \hat{\mathscr{H}} | \varphi \rangle}{\langle \varphi | \varphi \rangle} = \frac{\langle c_1 \chi_1 + c_2 \chi_2 | \hat{\mathscr{H}} | c_1 \chi_1 + c_2 \chi_2 \rangle}{\langle c_1 \chi_1 + c_2 \chi_2 | c_1 \chi_1 + c_2 \chi_2 \rangle} \left(= \frac{Num}{Denom} \right) \tag{117}$$

We can simplify the numerator (the Hamiltonian function) as follows

$$\begin{aligned} Num &= \langle c_1 \chi_1 + c_2 \chi_2 | \hat{\mathscr{H}} | c_1 \chi_1 + c_2 \chi_2 \rangle \\ &= \langle c_1 \chi_1 | \hat{\mathscr{H}} | c_1 \chi_1 \rangle + \langle c_1 \chi_1 | \hat{\mathscr{H}} | c_2 \chi_2 \rangle + \langle c_2 \chi_2 | \hat{\mathscr{H}} | c_1 \chi_1 \rangle + \langle c_2 \chi_2 | \hat{\mathscr{H}} | c_2 \chi_2 \rangle \\ &= c_1^* c_1 \langle \chi_1 | \hat{\mathscr{H}} | \chi_1 \rangle + c_1^* c_2 \langle \chi_1 | \hat{\mathscr{H}} | \chi_2 \rangle + c_2^* c_1 \langle \chi_2 | \hat{\mathscr{H}} | \chi_1 \rangle + c_2^* c_2 \langle \chi_2 | \hat{\mathscr{H}} | \chi_2 \rangle \end{aligned} \tag{118}$$

Letting $H_{rs} \equiv \langle \chi_r | \hat{\mathscr{H}} | \chi_s \rangle$ be the Coulomb integral[†] simplifies (118) to

$$Num = c_1^* c_1 H_{11} + c_1^* c_2 H_{12} + c_2^* c_1 H_{21} + c_2^* c_2 H_{22} \tag{119}$$

If we assume that the wavefunction is real, then $H_{ij} = H_{ji}$ because of the hermitian nature of the Hamiltonian, $H_{ij} = H_{ji}^*$. The coefficients are likewise real. (119) then reduces to

$$Num = c_1^2 H_{11} + 2 c_1 c_2 H_{12} + c_2^2 H_{22} \tag{120}$$

[†] Confusion may arise between the Coulomb integral of variational theory, $H_{rs} = \langle \chi_r | \hat{\mathscr{H}} | \chi_s \rangle$, with the Coulomb integral in HF theory, $J_{ij} = \langle \varphi_i(1)\varphi_j(2) | \frac{1}{r_{12}} | \varphi_i(1)\varphi_j(2) \rangle$.

Similarly for the denominator (the overlap function),

$$\begin{aligned} Denom &= \langle c_1\,\chi_1 + c_2\,\chi_2 \,|\, c_1\,\chi_1 + c_2\,\chi_2 \rangle \\ &= \langle c_1\,\chi_1 | c_1\,\chi_1 \rangle + \langle c_1\,\chi_1 | c_2\,\chi_2 \rangle + \langle c_2\,\chi_2 | c_1\,\chi_1 \rangle + \langle c_2\,\chi_2 | c_2\,\chi_2 \rangle \\ &= c_1^*\,c_1 \langle \chi_1 | \chi_1 \rangle + c_1^*\,c_2 \langle \chi_1 | \chi_2 \rangle + c_2^*\,c_1 \langle \chi_2 | \chi_1 \rangle + c_2^*\,c_2 \langle \chi_2 | \chi_2 \rangle \end{aligned} \tag{121}$$

Note that $\langle \varphi | \varphi \rangle \neq 1$ because, although the individual AOs are normalized, the MOs depend on the coefficients. Normalization is completed below.

Let $S_{rs} \equiv \langle \chi_r | \chi_s \rangle$ be the overlap integral of orbitals r and s. Since the AOs are normalized, $S_{rr} = \langle \chi_r | \chi_r \rangle = 1$. Further, it is obvious that $S_{rs} = S_{sr} = S$. Thus, (121) simplifies to

$$Denom = c_1^2 + c_2^2 + 2\,c_1\,c_2\,S \tag{122}$$

Thus, (117) becomes

$$\begin{aligned} E &= \frac{c_1^2 + c_2^2 + 2\,c_1\,c_2\,H_{12}}{c_1^2 + c_2^2 + 2\,c_1\,c_2\,S} \\ E\left(c_1^2 + c_2^2 + 2\,c_1\,c_2\,S\right) &= c_1^2 + c_2^2 + 2\,c_1\,c_2\,H_{12} \end{aligned} \tag{123}$$

We want to minimize the energy by varying the coefficients, c_i. Taking the derivative with respect to c_i results in two equations

$$\begin{aligned} &\frac{\partial}{\partial c_1}\left[E\left(c_1^2 + c_2^2 + 2\,c_1\,c_2\,S\right) = c_1^2 + c_2^2 + 2\,c_1\,c_2\,H_{12}\right] \\ &\qquad \Rightarrow 2\,c_1\,E + 2\,c_2\,S\,E = 2\,c_1\,H_{11} + 2\,c_2\,H_{12} \\ &\qquad \Rightarrow c_1\,E + c_2\,S\,E = c_1\,H_{11} + c_2\,H_{12} \\ &\frac{\partial}{\partial c_2}\left[E\left(c_1^2 + c_2^2 + 2\,c_1\,c_2\,S\right) = c_1^2 + c_2^2 + 2\,c_1\,c_2\,H_{12}\right] \\ &\qquad \Rightarrow c_2\,E + c_1\,S\,E = c_2\,H_{22} + c_1\,H_{12} \end{aligned} \tag{124}$$

which can be rearranged and like terms of c_i collected to give the *secular equations*

$$\begin{aligned}(H_{11}-E)c_1+(H_{12}-ES)c_2&=0\\(H_{21}-ES)c_1+(H_{22}-E)c_2&=0\end{aligned}\tag{125}$$

or, in matrix form,

$$\begin{aligned}&\begin{pmatrix}H_{11}-E & H_{12}-ES_{12}\\ H_{21}-ES_{21} & H_{22}-E\end{pmatrix}\begin{pmatrix}c_1\\c_2\end{pmatrix}=\begin{pmatrix}0\\0\end{pmatrix}\\&(\boldsymbol{H}-E\boldsymbol{S})\boldsymbol{c}=\boldsymbol{0}\end{aligned}\tag{126}$$

Three solutions exist to (126), the trivial solution, $\boldsymbol{c}=\mathbf{0}$, and

$$\begin{pmatrix}H_{11}-E & H_{12}-ES_{12}\\ H_{21}-ES_{21} & H_{22}-E\end{pmatrix}=0\tag{127}$$

The eigenvalues (energies) of (127) can be found by setting the determinant equal to zero.

$$\begin{vmatrix}H_{11}-E & H_{12}-ES\\ H_{21}-ES & H_{22}-E\end{vmatrix}=0\tag{128}$$

Solution of (128) for E results in the quadratic equation

$$(1-S^2)E^2+(2H_{12}S-H_{11}-H_{22})E+(H_{11}H_{22}-H_{12}^2)=0\tag{129}$$

Application of the quadratic equation to (129) results in a complicated expression for the energy. More information can be obtained by limiting the system such that there is symmetry between the AOs in (116).

Variational treatment of a homonuclear diatomic system

A general solution can be found if the system is a homonuclear diatomic or a similarly symmetric system where χ_1 and χ_2 are equivalent. In this case, $H_{11}=H_{22}$. Letting $\alpha=H_{rr}$, $\beta=H_{rs}$ simplifies (128) to

$$\begin{vmatrix} \alpha - E & \beta - ES \\ \beta - ES & \alpha - E \end{vmatrix} = 0 \tag{130}$$

resulting in a quadratic expression which is solvable.

$$\left(1 - S^2\right)E^2 + (2\beta S - 2\alpha)E + \left(\alpha^2 - \beta^2\right) = 0 \tag{131}$$

$$\begin{aligned} E_+ &= \frac{\alpha+\beta}{1+S} = \frac{H_{11}+H_{12}}{1+S} = \frac{\langle \chi_1 | \hat{\mathscr{H}} | \chi_1 \rangle + \langle \chi_1 | \hat{\mathscr{H}} | \chi_2 \rangle}{1 + \langle \chi_1 | \chi_1 \rangle} = \ldots \\ E_- &= \frac{\alpha-\beta}{1-S} \end{aligned} \tag{132}$$

where the second and third expressions of E_+ illustrate the information contained in the simple expression. E_+ and E_- are the energies of the bonding and antibonding MOs within a homonuclear diatomic (or symmetrically equivalent species) considering only two MOs.

The MO coefficients can be determined by substituting the energy expressions, (132), into the secular equations, (125). Together with the normalization expression: $\langle \varphi | \varphi \rangle = c_1^2 + c_2^2 + 2c_1 c_2 S$, (122), it can be shown that

$$\boxed{\begin{array}{ll} E_+ = \dfrac{\alpha+\beta}{1+S} & c_1 = c_2 = \sqrt{\dfrac{1}{2(1+S)}} \\ E_- = \dfrac{\alpha-\beta}{1-S} & c_1 = -c_2 = \sqrt{\dfrac{1}{2(1-S)}} \end{array}} \tag{133}$$

The bonding and antibonding MOs become

$$\boxed{\begin{array}{l} \varphi_+ = \sqrt{\dfrac{1}{2(1+S)}}(\chi_1 + \chi_2) \\ \varphi_- = \sqrt{\dfrac{1}{2(1-S)}}(\chi_1 - \chi_2) \end{array}} \tag{134}$$

Variational treatment of a general system

A general system can be treated analogously to the simple system above. Equation (116) can be written as a summation of $2k$ AOs.

$$\varphi_i \approx \sum_{r=1}^{2k} c_{ir}\,\chi_r \tag{15)'$$

The Coulomb and overlap functions become

$$\begin{aligned}\langle \varphi_i|\hat{\mathscr{H}}|\varphi_j\rangle &= \left\langle \sum_{r=1}^{2k} c_{ir}^{*}\,\chi_r \middle| \hat{\mathscr{H}} \middle| \sum_{s=1}^{2k} c_{js}\,\chi_s \right\rangle \\ &= \sum_{r=1}^{2k}\sum_{s=1}^{2k} c_{ir}^{*}\,c_{js}\langle \chi_r|\hat{\mathscr{H}}|\chi_s\rangle \\ &= \sum_{r=1}^{2k}\sum_{s=1}^{2k} c_{ir}^{*}\,c_{js}\,H_{rs}\end{aligned} \tag{135}$$

$$\begin{aligned}\langle \varphi_i|\varphi_j\rangle &= \left\langle \sum_{r=1}^{2k} c_{ir}^{*}\,\chi_r \middle| \sum_{s=1}^{2k} c_{js}^{*}\,\chi_s \right\rangle \\ &= \sum_{r=1}^{2k}\sum_{s=1}^{2k} c_{ir}^{*}\,c_{js}\langle \chi_r|\chi_s\rangle \\ &= \sum_{r=1}^{2k}\sum_{s=1}^{2k} c_{ir}^{*}\,c_{js}\,S_{rs}\end{aligned} \tag{136}$$

Substituting (135) and (136) into (117), we obtain

$$\begin{aligned}&E\langle \varphi_i|\varphi_j\rangle = \langle \varphi_i|\hat{\mathscr{H}}|\varphi_j\rangle \\ &E\sum_r\sum_s c_{ir}^{*}\,c_{js}\,S_{rs} = \sum_r\sum_s c_{ir}^{*}\,c_{js}\,H_{rs}\end{aligned} \tag{137}$$

Assuming $\{\chi, \varphi, c\} \in \mathscr{R}$, and taking the derivative of (137) with respect to c_i, we obtain a set of $2k$ linear equations that can be expressed as

$$\begin{pmatrix} H_{11}-E & H_{12}-E\,S_{12} & \cdots & H_{1(2k)}-E\,S_{1(2k)} \\ H_{21}-E\,S_{21} & H_{22}-E & \cdots & H_{2(2k)}-E\,S_{2(2k)} \\ \vdots & \vdots & \ddots & \vdots \\ H_{(2k)1}-E\,S_{(2k)1} & H_{(2k)2}-E\,S_{(2k)2} & \cdots & H_{(2k)(2k)}-E \end{pmatrix}\begin{pmatrix} c_1 \\ c_2 \\ \vdots \\ c_{2k} \end{pmatrix}=\begin{pmatrix} 0 \\ 0 \\ 0 \\ 0 \end{pmatrix} \tag{138}$$

or, in matrix notation

$$\begin{gathered} (\boldsymbol{H}-E\,\boldsymbol{S})\boldsymbol{c}=\boldsymbol{0} \\ \boldsymbol{H}\,\boldsymbol{c}=E\,\boldsymbol{S}\,\boldsymbol{c} \end{gathered} \tag{139}$$

and solved analogously to the two-orbital system.

The method of Lagrange multipliers

In many situations, it is not convenient to solve a system in a stepwise manner. The method of Lagrange multipliers introduces constraints and constants (multipliers) so that an extrema (maximum or minimum) in the system can be determined subject to the constraints. This method is illustrated below, where the energy is minimized as a function of the orbital coefficients subject to maintaining the orthonormality of the orbitals.

A Lagrange expression is designed based on the energy of the system, $E=\langle\Psi|\hat{\mathscr{H}}|\Psi\rangle$,

$$L=E-\sum_i\sum_j\lambda_{ij}\left(\langle\varphi_i|\varphi_j\rangle-\delta_{ij}\right) \tag{140}$$

where the second expression constrains the spin orbitals to be orthonormal and λ_{ij} are the Lagrange multipliers. An extrema is obtained by setting the variation of (140) to zero.

$$\delta L=\delta E-\delta\left[\sum_i\sum_j\lambda_{ij}\left(\langle\varphi_i|\varphi_j\rangle-\delta_{ij}\right)\right]\underset{\substack{\uparrow\\ \text{set}}}{=}0 \tag{141}$$

The variation in the energy, δE, is determined as the energy associated with an infinitesimal change in Ψ: $\Psi\rightarrow\Psi+\delta\Psi$.

$$\begin{aligned} E(\Psi+\delta\Psi) &= \langle \Psi+\delta\Psi|\hat{\mathscr{H}}|\Psi+\delta\Psi\rangle \\ &= \langle\Psi|\hat{\mathscr{H}}|\Psi\rangle + \langle\delta\Psi|\hat{\mathscr{H}}|\Psi\rangle + \langle\Psi|\hat{\mathscr{H}}|\delta\Psi\rangle + \langle\delta\Psi|\hat{\mathscr{H}}|\delta\Psi\rangle \\ &= E + \delta\langle\Psi|\hat{\mathscr{H}}|\Psi\rangle + \langle\delta\Psi|\hat{\mathscr{H}}|\delta\Psi\rangle \\ &= E + \delta E + \langle\delta\Psi|\hat{\mathscr{H}}|\delta\Psi\rangle \end{aligned} \tag{142}$$

where δE is the first order variation of the energy. (Higher order terms are ignored.)

$$\delta E = \delta\langle\Psi|\hat{\mathscr{H}}|\Psi\rangle = \langle\delta\Psi|\hat{\mathscr{H}}|\Psi\rangle + \langle\Psi|\hat{\mathscr{H}}|\delta\Psi\rangle \tag{143}$$

An infinitesimal change in φ within the constraint in (140) results in

$$\begin{aligned} \delta\left[\sum_i\sum_j \lambda_{ij}\left(\langle\varphi_i|\varphi_j\rangle - \delta_{ij}\right)\right] &= \sum_i\sum_j \lambda_{ij}\delta\langle\varphi_i|\varphi_j\rangle - \delta\delta_{ij} \\ &= \sum_i\sum_j \lambda_{ij}\left(\langle\delta\varphi_i|\varphi_j\rangle + \langle\varphi_i|\delta\varphi_j\rangle\right) \end{aligned} \tag{144}$$

since the change in a constant, $\delta\delta_{ij}$, is 0.

The complete Lagrange expression, (141), becomes

$$\begin{aligned} \delta L = &\sum_i\sum_j \delta c_i^* c_j \langle\delta\varphi_i|\hat{\mathscr{H}}|\varphi_j\rangle + \sum_i\sum_j \delta c_i c_j^* \langle\varphi_i|\hat{\mathscr{H}}|\delta\varphi_j\rangle \\ &- \sum_i\sum_j \lambda_{ij}\left(\langle\delta\varphi_i|\varphi_j\rangle + \langle\varphi_i|\delta\varphi_j\rangle\right) \end{aligned} \tag{145}$$

The Hartree-Fock equation

Equation (112) determines the total energy from n one-electron spin-orbitals. The goal herein is to determine the orbital coefficients that variationally minimize the energy.

$$E = \sum_i h_i + \sum_i\sum_{j>i}\left(J_{ij} - K_{ij}\right) \tag{112'}$$

Instead of sequentially solving the system in a stepwise manner, the method of Lagrange multipliers introduces constraints and constants (multipliers) so that an extrema (maximum or minimum) in the system can be determined subject to the imposed constraints. In this case, the energy is minimized as a function of the orbital coefficients subject to maintaining the orthonormality of the orbitals.

The variation in the energy is determined from (112)

$$
\begin{aligned}
E &= \sum_i \langle \varphi_i(\mu) | \hat{H}_\mu^{\text{core}} | \varphi_i(\mu) \rangle + \frac{1}{2} \sum_i \sum_j \Big(\langle \varphi_j(\mu) | \hat{J}_i | \varphi_j(\mu) \rangle - \langle \varphi_j(\mu) | \hat{K}_i | \varphi_j(\mu) \rangle \Big) \\
&= \sum_i \langle \varphi_i(\mu) | \hat{H}_\mu^{\text{core}} | \varphi_i(\mu) \rangle + \frac{1}{2} \sum_i \sum_j \Big(\langle \varphi_j(\mu) | \hat{J}_i - \hat{K}_i | \varphi_j(\mu) \rangle \Big)
\end{aligned}
\qquad (146)
$$

or simply

$$
E = \sum_i \langle \varphi_i | \hat{H}_\mu^{\text{core}} | \varphi_i \rangle + \frac{1}{2} \sum_i \sum_j \Big(\langle \varphi_j | \hat{J}_i - \hat{K}_i | \varphi_j \rangle \Big) \qquad (147)
$$

so that the variation is given by

$$
\begin{aligned}
\delta E &= \sum_i \Big(\langle \delta\varphi_i | \hat{H}_\mu^{\text{core}} | \varphi_i \rangle + \langle \varphi_i | \hat{H}_\mu^{\text{core}} | \delta\varphi_i \rangle \Big) \\
&\quad + \frac{1}{2} \sum_i \sum_j \begin{pmatrix} \langle \delta\varphi_i | \hat{J}_j - \hat{K}_j | \varphi_i \rangle + \langle \varphi_i | \hat{J}_j - \hat{K}_j | \delta\varphi_i \rangle \\ + \langle \delta\varphi_j | \hat{J}_i - \hat{K}_i | \varphi_j \rangle + \langle \varphi_j | \hat{J}_i - \hat{K}_i | \delta\varphi_j \rangle \end{pmatrix}
\end{aligned}
\qquad (148)
$$

Because the orbital indices are arbitrary, the first and third terms in the double summation are identical, as are the second and fourth. This simplifies (148) to

$$
\begin{aligned}
\delta E &= \sum_i \Big(\langle \delta\varphi_i | \hat{H}_\mu^{\text{core}} | \varphi_i \rangle + \langle \varphi_i | \hat{H}_\mu^{\text{core}} | \delta\varphi_i \rangle \Big) \\
&\quad + \sum_i \sum_j \Big(\langle \delta\varphi_i | \hat{J}_j - \hat{K}_j | \varphi_i \rangle + \langle \varphi_i | \hat{J}_j - \hat{K}_j | \delta\varphi_i \rangle \Big)
\end{aligned}
\qquad (149)
$$

A one-electron Fock operator,

$$
\boxed{\hat{F} = \hat{H}_\mu^{\text{core}} + \sum_j \big(\hat{J}_j - \hat{K}_j \big)} \qquad (150)
$$

further simplifies (149) to

$$\delta E = \sum_i \left(\langle \delta\varphi_i | \hat{F} | \varphi_i \rangle + \langle \varphi_i | \hat{F} | \delta\varphi_i \rangle \right) \tag{151}$$

The variation of the constraint in (140) results in

$$\begin{aligned} \delta\left[\sum_i \sum_j \lambda_{ij} \left(\langle \varphi_i | \varphi_j \rangle - \delta_{ij} \right) \right] &= \sum_i \sum_j \lambda_{ij} \delta \langle \varphi_i | \varphi_j \rangle - \delta\delta_{ij} \\ &= \sum_i \sum_j \lambda_{ij} \left(\langle \delta\varphi_i | \varphi_j \rangle + \langle \varphi_i | \delta\varphi_j \rangle \right) \end{aligned} \tag{152}$$

The Lagrange function, (141), becomes

$$\begin{aligned} \delta L &= \sum_i \left(\langle \delta\varphi_i | \hat{F} | \varphi_i \rangle + \langle \varphi_i | \hat{F} | \delta\varphi_i \rangle \right) - \sum_i \sum_j \lambda_{ij} \left(\langle \delta\varphi_i | \varphi_j \rangle - \langle \varphi_j | \delta\varphi_i \rangle \right) \\ &= \sum_i \delta\varphi_i^* \left(\hat{F} | \varphi_i \rangle + \sum_j \lambda_{ij} | \varphi_j \rangle \right) + \sum_i \delta\varphi_i \left(\langle \varphi_i | \hat{F} + \sum_j \lambda_{ij} \langle \varphi_j | \right) \underset{\substack{\uparrow \\ \text{set}}}{=} 0 \end{aligned} \tag{153}$$

where the second expression is the complex conjugate of the first. Since δc_i cannot always be zero, the values in brackets must be zero. This returns

$$\hat{F} \varphi_i = \sum_j \lambda_{ij} \varphi_j \tag{154}$$

Diagonalizing the Lagrange multipliers returns a set of orthonormal MOs (φ_i') and a Lagrange matrix with $\lambda_{ij} = 0$ and $\lambda_{ii} = \varepsilon_i$. ε_i are the energy of the MOs. this results in the Hartree-Fock equation:

$$\boxed{\hat{F} \varphi_i' = \varepsilon_i \varphi_i'} \tag{155}$$

Note that the Fock operator is a function of the MOs through the Coulomb and exchange integrals. Thus, (155) must be solved iteratively to obtain a set of self-consistent MOs. This is the well-known *self-consistent field* (SCF) procedure.

APPENDIX C: A TYPICAL POST-HF CALCULATION

The general geometry optimization procedure for a post-HF method is given below.

① An estimate of the geometry is given in the input file.

② The basis functions are prepared as a summation of GTOs.

$$\chi_r = \sum_x d_{rx}\, g_x(\alpha) \qquad (20)'$$

③ An estimate of the AO coefficients, c_{ir}, for each spin-orbital is obtained using a single-point semi-empirical method (MNDO in GAUSSIAN).

$$\varphi_i \approx \sum_r c_{ir}\, \chi_r \qquad (15)'$$

④ c_{ir} are optimized through iterative SCF solution of the HF equation.

$$\hat{F}|\varphi_i\rangle = \varepsilon_i|\varphi_i\rangle \qquad (26)'$$

⑤ c_{ir} are further optimized using a post-HF method.

⑥ The energy of the system is determined.

⑦ The derivative of the energy is determined and the nuclei shifted accordingly.

⑧ Step ④ though ⑦ are repeated until the change in energy is below a set threshold.

⑨ Post-optimization calculations are conducted (NPA, vibrational energies, single-point energy with other methods, etc.)

APPENDIX D: MOLECULAR GEOMETRY AT THE SINGLET–TRIPLET CROSSING

The Hamiltonian used by the standard methods does not contain spin-coupling terms. As a result, there is no interaction between states of different multiplicity and the singlet and triplet PESs cross as shown in Figure 3.2. However, the geometries of the singlet and triplet states at the intersection in Figure 3.2 are not the same as shown in Tables D.1 to D.3. The true intersection is when the energy and geometries are the same. In this Appendix, a location on the PES is found where both the geometry and energy are [approximately] the same for both singlet and triplet states. This was done manually using the procedure below as it is not implemented in GAUSSIAN.

The transition region was scanned and a polynomial fit to both the singlet and triplet states for all QCISD methods. This is shown in the insets in Figure 3.2. It is evident that all methods (including B3LYP, but not shown) localize the diabatic singlet–triplet crossing to the same region — *the bound portion of the potential well* — contradicting earlier work.[35,56,57,58,59,60] It is possible that the earlier work is in error because of constraints placed on the geometry to facilitate calculation.

The optimized geometry of the singlet and triplet states was calculated at the crossover point and is tabulated in Tables D.1 to D.3. The XN–N–N bond angle is the only significantly different molecular parameter between the two spin-states. However, calculating the singlet and triplet energy at the *average* geometry resulted in energies that were up to 1 000 cm^{-1} different. The singlet PES was evidently 'tighter' in the crossing region than the triplet PES. To compensate, the energies for each spin-state were calculated at the optimized geometry of the *other* spin state and the singlet–triplet crossing estimated as the weighted average geometry given by

$$X_{\text{avg}} = X_{\text{sing}} + \frac{\Delta E_{\text{sing}}}{\Delta E_{\text{sing}} + \Delta E_{\text{trip}}}\left(X_{\text{trip}} - X_{\text{sing}}\right) \tag{156}$$

where X_{sing} is the parameter of the singlet optimized geometry and $\Delta E^{*}_{\text{sing}}$ is the energy difference between the triplet single-point energy calculated at the optimized singlet geometry (denoted by an asterisk) and the singlet energy at that geometry: $\Delta E_{sing} = E^{*}_{trip} - E_{sing}$. The energies of both states were determined at the weighted average geometry and are also tabulated in Tables D.1 to D.3. The uncertainty in the energy at the singlet–triplet crossing was reduced to approximately 400 cm^{-1} with this method.

Table D.1 Geometry of HN_3 in the singlet and triplet states at the singlet–triplet crossing and the mean geometry for single-point calculations. The values in bold are fixed during the optimization.

HN_3	$H–N_\alpha$	$N_\alpha–N_\beta$	$N_\beta–N_\gamma$	$H–N_\alpha–N_\beta$	$N_\alpha–N_\beta–N_\gamma$	Energy[a]
			Singlet–triplet crossing (singlet)			
UQCISD/6-31++G(d,p)	1.035	**1.7475**	1.118	92.0	168.0	11 618
UQCISD/6-311++G(d,p)	1.034	**1.7500**	1.107	91.6	167.6	12 054
			Singlet–triplet crossing (triplet)			
UQCISD/6-31++G(d,p)	1.037	**1.7475**	1.136	96.3	120.2	11 414
UQCISD/6-311++G(d,p)	1.037	**1.7500**	1.125	96.2	120.6	11 896
			Singlet–triplet crossing (weighted average)			
UQCISD/6-31++G(d,p)	**1.0361**	**1.7475**	**1.1290**	**94.5990**	**139.3656**	S: 12627 T: 12841
UQCISD/6-311++G(d,p)	**1.0360**	**1.7500**	**1.1176**	**94.3791**	**139.4987**	S: 13343 T: 13308

Vibrational energies were calculated at the singlet–triplet crossing at the optimized singlet and triplet geometries in Tables D.1 to D.3 and summarized in Table D.4. Although only strictly valid at stationary points, this analysis found one imaginary energy and the remainder of the vibrational energies intermediate between the optimized geometry and the singlet dissociation maximum and dissociation products. Vibrational energies for the singlet and triplet states were also comparable.

Inspection of the vibrational displacements of all the atoms shows that one mode, labelled 'N_α–N_β stretch' in the Tables, clearly follows the observed optimized geometries during dissociation, i.e., this vibrational mode maps very strongly onto the dissociation coordinate. This surprising and fortuitous event indicates that the other vibrational modes are orthogonal to the dissociation and therefore reasonably valid at any point during the dissociation.

Table D.2 Geometry of FN_3 in the singlet and triplet states at the singlet–triplet crossing and the mean geometry for single-point calculations. The values in bold are fixed during the optimization.

FN_3	F–N_α	N_α–N_β	N_β–N_γ	F–N_α–N_β	N_α–N_β–N_γ	Energy[a]
			Singlet–triplet crossing (singlet)			
UQCISD/6-31++G(d,p)	1.417	**1.6278**	1.122	100.4	172.0	5 515
UQCISD/6-311++G(d,p)	1.390	**1.6146**	1.112	101.4	170.0	4 948
			Singlet–triplet crossing (triplet)			
UQCISD/6-31++G(d,p)	1.364	**1.6278**	1.153	102.2	117.1	5 335
UQCISD/6-311++G(d,p)	1.336	**1.6146**	1.144	102.7	117.5	4 851
			Singlet–triplet crossing (weighted average)			
UQCISD/6-31++G(d,p)	**1.3809**	**1.6278**	**1.1430**	**101.6014**	**134.6779**	S: 7748 T: 7104
UQCISD/6-311++G(d,p)	**1.3529**	**1.6146**	**1.1343**	**102.3268**	**133.5399**	S: 6893 T: 6608

Table D.3 Geometry of ClN_3 in the singlet and triplet states at the singlet–triplet crossing and the mean geometry for single-point calculations. The values in bold are fixed during the optimization.

ClN_3	Cl–N_α	N_α–N_β	N_β–N_γ	Cl–N_α–N_β	N_α–N_β–N_γ	Energy[a]
			Singlet–triplet crossing (singlet)			
UQCISD/6-31++G(d,p)	1.749	**1.6382**	1.122	104.8	167.9	6 749
UQCISD/6-311++G(d,p)	1.747	**1.6413**	1.111	104.7	168.6	7 113
			Singlet–triplet crossing (triplet)			
UQCISD/6-31++G(d,p)	1.687	**1.6382**	1.149	107.3	117.5	6 883
UQCISD/6-311++G(d,p)	1.680	**1.6413**	1.137	107.6	118.0	6 780
			Singlet–triplet crossing (weighted average)			
UQCISD/6-31++G(d,p)	**1.7363**	**1.6382**	**1.1273**	**105.3042**	**157.5073**	S: 7276 T: 7494
UQCISD/6-311++G(d,p)	**1.7034**	**1.6413**	**1.1279**	**106.6334**	**135.5996**	S: 8802 T: 8508

Vibrational energies are not calculated at the mean geometry since it is assumed that vibrational excitation puts XN_3 in the correct geometry for facile intersystem crossing.

Table D.4 Vibrational energies of the singlet and triplet spin-states of XN$_3$ at the singlet–triplet crossing.

	N_β–N_γ stretch	N_α–N_β stretch	X–N stretch	in-plane N_3 bend	out-of-plane N_3 bend	in-plane scissor	ZPE
$^1HN_3$							
6-31++G(d,p)	2 255	489i	3 384	1 229	362	355	3 696
6-311++G(d,p)	2 263	352i	3 361	1 237	352	348	3 690
$^3HN_3$							
6-31++G(d,p)	2 047	489i	3 346	981	92i	440	3 320
6-311++G(d,p)	2 066	405i	3 316	979	109	438	3 371
$^1FN_3$							
6-31++G(d,p)	2 192	518i	907	565	319	196	2 036
6-311++G(d,p)	2 191	527i	951	571	295	167	2 038
$^3FN_3$							
6-31++G(d,p)	1 907	599i	1 020	541	174	354	1 947
6-311++G(d,p)	1 078	600i	1 078	555	157	354	1 572
$^1ClN_3$							
6-31++G(d,p)	2 194	579i	470	723	315	164	1 884
6-311++G(d,p)	2 203	581i	462	717	288	151	1 865
$^3ClN_3$							
6-31++G(d,p)	1 930	558i	477	774	158	275	1 761
6-311++G(d,p)	1 951	541i	479	774	148	267	1 766

OTHER PUBLISHED WORK

The work described in the body of this dissertation is the principal research I conducted during my tenure as a graduate student at the University of Victoria. Other activities have led to publications not directly related to this dissertation.

Thermal Dissociation of Halogen Azides is in preparation. The abstract is reproduced on page 178.

Laser-induced Fluorescence and Dispersed Fluorescence Spectroscopy, Isotopic Studies, and Lifetime Measurements for Rhodium Monoxide was published in *Chemistry and Physics Letters*, **2003**, *370*, 106. The abstract is reproduced on page 179.

Applied Statistics in Chemistry is a review of statistics for students taking analytical and physical chemistry at the University of Victoria. It is incorporated as an appendix in several laboratory manuals and distributed to students in other laboratory courses. This document is reproduced starting on page 181.

Chemistry 212 Analytical Chemistry Laboratory Manual is used by students taking second year analytical chemistry at the University of Victoria. I co-authored the laboratory manual with Dr. Jane Browning. (This document is not reproduced herein.)

Transition Metal-Chlorine Anions and Cations: Monomers, Clusters, and Periodic Trends was published in *Chemistry and Physics Letters*, **2000**, *331*, 163. The abstract and first page are reproduced on page 195.

Energy Transfer from $N_2(v)$ *to* ClN_3 *and a Kinetic Model for the Chain Decomposition of Chlorine Azide* was published in the *Journal of Physical Chemistry A* **2000**, *104*, 6573. The abstract and first page are reproduced on page 196.

1. THERMAL DISSOCIATION OF HALOGEN AZIDES

Thermal dissociation of halogen azides

Configuration interaction calculations on the lowest singlet and triplet potential energy surfaces of hydrogen, fluorine, and chlorine azide for the thermally accessible reactions $X\mathrm{N_3}(\tilde{\mathrm{X}}\,^1\mathrm{A}') \longrightarrow \mathrm{N}X(\mathrm{X}^3\Sigma;\ \mathrm{a}^1\Delta) + \mathrm{N_2}(\mathrm{X}^1\Sigma_g^+)$ (X = H, F, N) finds that the singlet surface is intersected on the bound singlet region by a dissociative triplet surface. Unimolecular decomposition rates for each pathway and the branching ratio predict that HN_3 dissociates to ground state products while FN_3 and ClN_3 produce predominantly electronically excited NX(a). These results are in agreement with the limited experimental work and in better agreement than previous ab initio calculations. A rationale for the systematic errors in previous ab initio calculations is proposed.

2. LASER-INDUCED FLUORESCENCE AND DISPERSED FLUORESCENCE SPECTROSCOPY, ISOTOPIC STUDIES, AND LIFETIME MEASUREMENTS FOR RHODIUM MONOXIDE

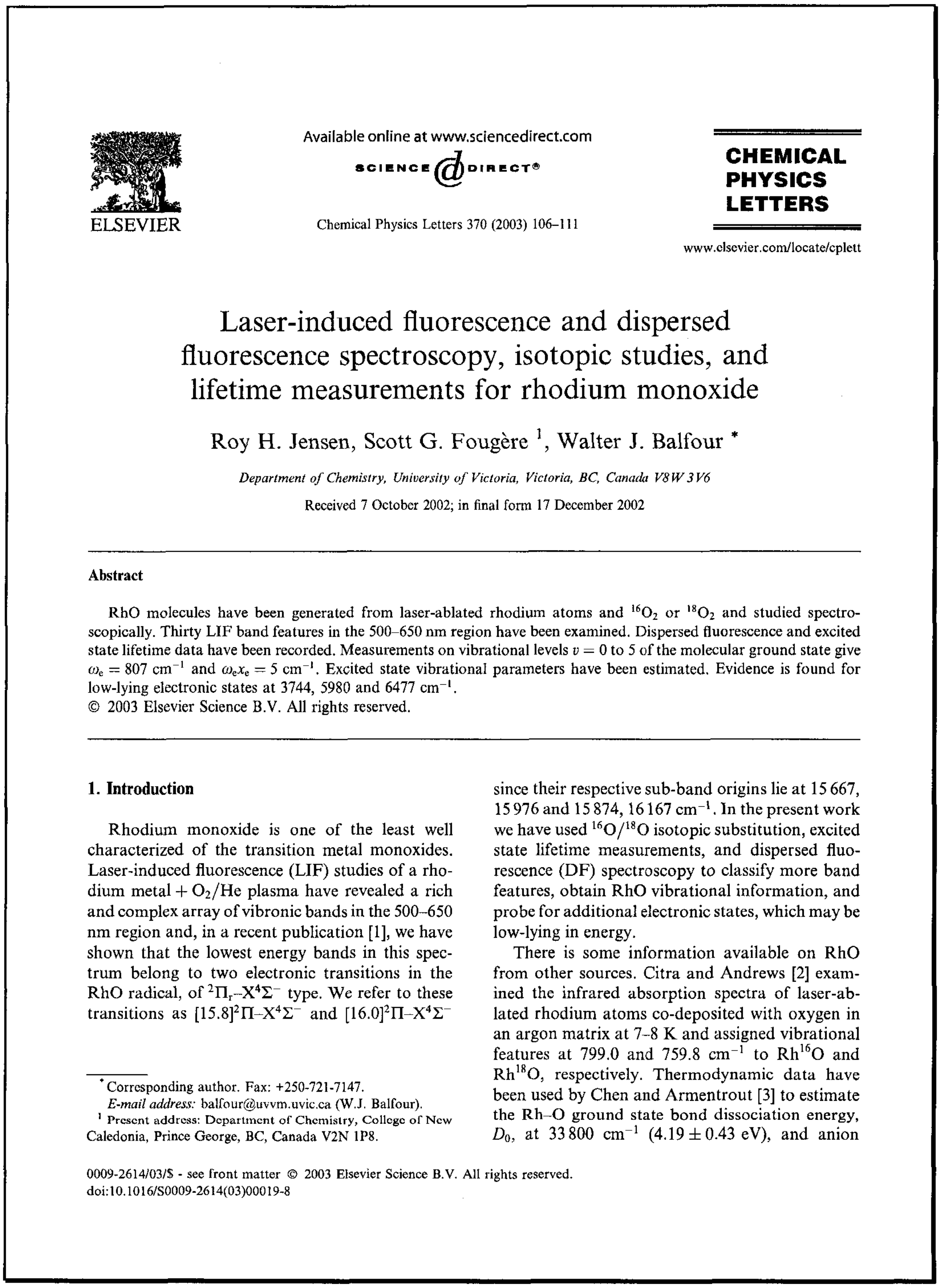

ELSEVIER

Available online at www.sciencedirect.com
SCIENCE DIRECT®

Chemical Physics Letters 370 (2003) 106–111

CHEMICAL PHYSICS LETTERS

www.elsevier.com/locate/cplett

Laser-induced fluorescence and dispersed fluorescence spectroscopy, isotopic studies, and lifetime measurements for rhodium monoxide

Roy H. Jensen, Scott G. Fougère [1], Walter J. Balfour *

Department of Chemistry, University of Victoria, Victoria, BC, Canada V8W 3V6

Received 7 October 2002; in final form 17 December 2002

Abstract

RhO molecules have been generated from laser-ablated rhodium atoms and $^{16}O_2$ or $^{18}O_2$ and studied spectroscopically. Thirty LIF band features in the 500–650 nm region have been examined. Dispersed fluorescence and excited state lifetime data have been recorded. Measurements on vibrational levels $v = 0$ to 5 of the molecular ground state give $\omega_e = 807$ cm^{-1} and $\omega_e x_e = 5$ cm^{-1}. Excited state vibrational parameters have been estimated. Evidence is found for low-lying electronic states at 3744, 5980 and 6477 cm^{-1}.

1. Introduction

Rhodium monoxide is one of the least well characterized of the transition metal monoxides. Laser-induced fluorescence (LIF) studies of a rhodium metal + O_2/He plasma have revealed a rich and complex array of vibronic bands in the 500–650 nm region and, in a recent publication [1], we have shown that the lowest energy bands in this spectrum belong to two electronic transitions in the RhO radical, of $^2\Pi_r$–$X^4\Sigma^-$ type. We refer to these transitions as $[15.8]^2\Pi$–$X^4\Sigma^-$ and $[16.0]^2\Pi$–$X^4\Sigma^-$ since their respective sub-band origins lie at 15 667, 15 976 and 15 874, 16 167 cm^{-1}. In the present work we have used $^{16}O/^{18}O$ isotopic substitution, excited state lifetime measurements, and dispersed fluorescence (DF) spectroscopy to classify more band features, obtain RhO vibrational information, and probe for additional electronic states, which may be low-lying in energy.

There is some information available on RhO from other sources. Citra and Andrews [2] examined the infrared absorption spectra of laser-ablated rhodium atoms co-deposited with oxygen in an argon matrix at 7–8 K and assigned vibrational features at 799.0 and 759.8 cm^{-1} to Rh^{16}O and Rh^{18}O, respectively. Thermodynamic data have been used by Chen and Armentrout [3] to estimate the Rh–O ground state bond dissociation energy, D_0, at 33 800 cm^{-1} (4.19 ± 0.43 eV), and anion

---

* Corresponding author. Fax: +250-721-7147.
E-mail address: balfour@uvvm.uvic.ca (W.J. Balfour).

[1] Present address: Department of Chemistry, College of New Caledonia, Prince George, BC, Canada V2N 1P8.

0009-2614/03/$ - see front matter © 2003 Elsevier Science B.V. All rights reserved.
doi:10.1016/S0009-2614(03)00019-8

Reprinted with permission from Elsevier (see page 180)

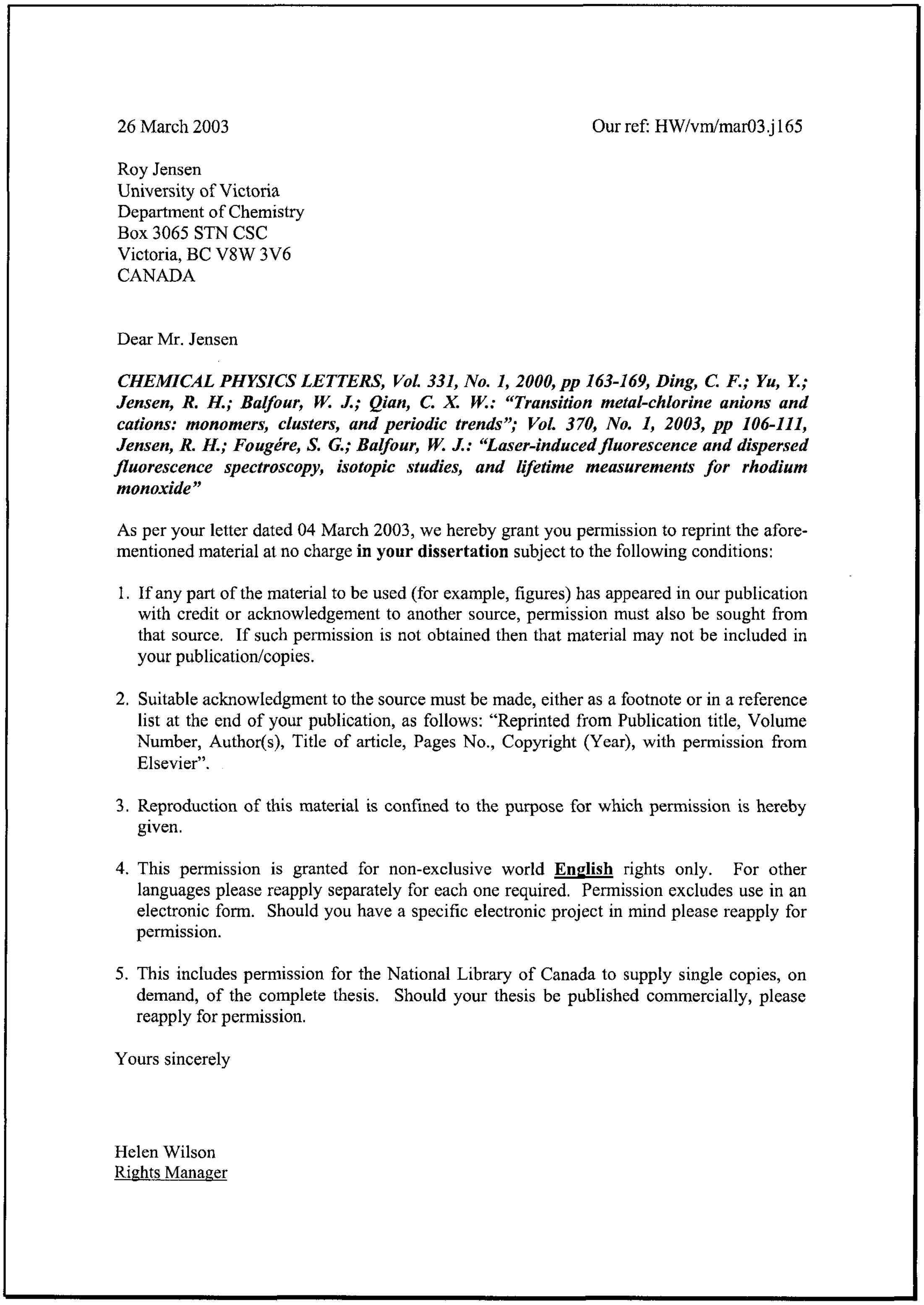

26 March 2003 Our ref: HW/vm/mar03.j165

Roy Jensen
University of Victoria
Department of Chemistry
Box 3065 STN CSC
Victoria, BC V8W 3V6
CANADA

Dear Mr. Jensen

CHEMICAL PHYSICS LETTERS, Vol. 331, No. 1, 2000, pp 163-169, Ding, C. F.; Yu, Y.; Jensen, R. H.; Balfour, W. J.; Qian, C. X. W.: "Transition metal-chlorine anions and cations: monomers, clusters, and periodic trends"; Vol. 370, No. 1, 2003, pp 106-111, Jensen, R. H.; Fougére, S. G.; Balfour, W. J.: "Laser-induced fluorescence and dispersed fluorescence spectroscopy, isotopic studies, and lifetime measurements for rhodium monoxide"

As per your letter dated 04 March 2003, we hereby grant you permission to reprint the aforementioned material at no charge **in your dissertation** subject to the following conditions:

1. If any part of the material to be used (for example, figures) has appeared in our publication with credit or acknowledgement to another source, permission must also be sought from that source. If such permission is not obtained then that material may not be included in your publication/copies.

2. Suitable acknowledgment to the source must be made, either as a footnote or in a reference list at the end of your publication, as follows: "Reprinted from Publication title, Volume Number, Author(s), Title of article, Pages No., Copyright (Year), with permission from Elsevier".

3. Reproduction of this material is confined to the purpose for which permission is hereby given.

4. This permission is granted for non-exclusive world **English** rights only. For other languages please reapply separately for each one required. Permission excludes use in an electronic form. Should you have a specific electronic project in mind please reapply for permission.

5. This includes permission for the National Library of Canada to supply single copies, on demand, of the complete thesis. Should your thesis be published commercially, please reapply for permission.

Yours sincerely

Helen Wilson
Rights Manager

3. APPLIED STATISTICS IN CHEMISTRY

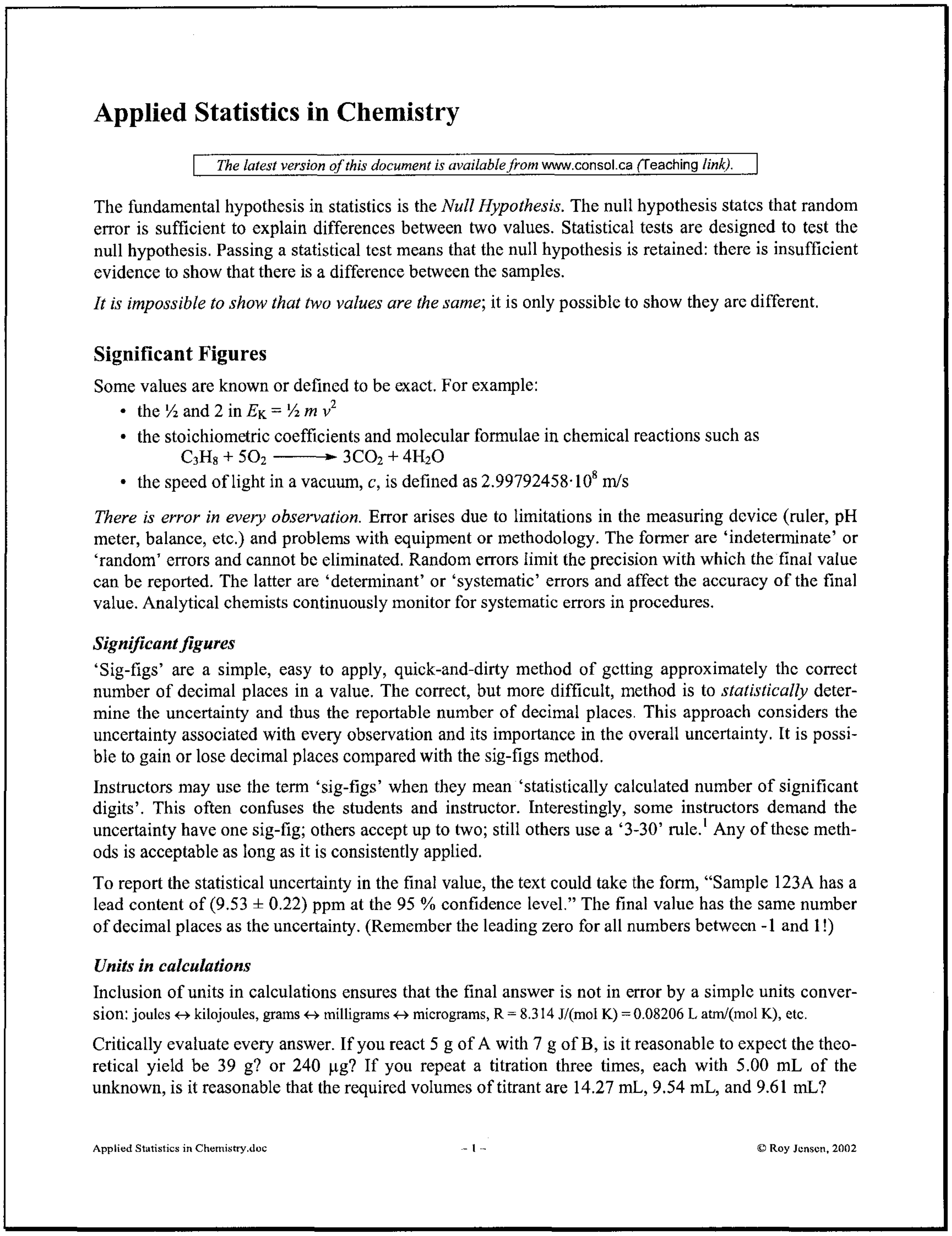

Applied Statistics in Chemistry

The latest version of this document is available from www.consol.ca *(*Teaching *link).*

The fundamental hypothesis in statistics is the *Null Hypothesis*. The null hypothesis states that random error is sufficient to explain differences between two values. Statistical tests are designed to test the null hypothesis. Passing a statistical test means that the null hypothesis is retained: there is insufficient evidence to show that there is a difference between the samples.

It is impossible to show that two values are the same; it is only possible to show they are different.

Significant Figures

Some values are known or defined to be exact. For example:

- the ½ and 2 in $E_\mathrm{K} = \frac{1}{2} m v^2$
- the stoichiometric coefficients and molecular formulae in chemical reactions such as
  $C_3H_8 + 5O_2 \longrightarrow 3CO_2 + 4H_2O$
- the speed of light in a vacuum, *c*, is defined as $2.99792458 \cdot 10^8$ m/s

There is error in every observation. Error arises due to limitations in the measuring device (ruler, pH meter, balance, etc.) and problems with equipment or methodology. The former are 'indeterminate' or 'random' errors and cannot be eliminated. Random errors limit the precision with which the final value can be reported. The latter are 'determinant' or 'systematic' errors and affect the accuracy of the final value. Analytical chemists continuously monitor for systematic errors in procedures.

Significant figures

'Sig-figs' are a simple, easy to apply, quick-and-dirty method of getting approximately the correct number of decimal places in a value. The correct, but more difficult, method is to *statistically* determine the uncertainty and thus the reportable number of decimal places. This approach considers the uncertainty associated with every observation and its importance in the overall uncertainty. It is possible to gain or lose decimal places compared with the sig-figs method.

Instructors may use the term 'sig-figs' when they mean 'statistically calculated number of significant digits'. This often confuses the students and instructor. Interestingly, some instructors demand the uncertainty have one sig-fig; others accept up to two; still others use a '3-30' rule.[1] Any of these methods is acceptable as long as it is consistently applied.

To report the statistical uncertainty in the final value, the text could take the form, "Sample 123A has a lead content of (9.53 ± 0.22) ppm at the 95 % confidence level." The final value has the same number of decimal places as the uncertainty. (Remember the leading zero for all numbers between -1 and 1!)

Units in calculations

Inclusion of units in calculations ensures that the final answer is not in error by a simple units conversion: joules ↔ kilojoules, grams ↔ milligrams ↔ micrograms, R = 8.314 J/(mol K) = 0.08206 L atm/(mol K), etc.

Critically evaluate every answer. If you react 5 g of A with 7 g of B, is it reasonable to expect the theoretical yield be 39 g? or 240 μg? If you repeat a titration three times, each with 5.00 mL of the unknown, is it reasonable that the required volumes of titrant are 14.27 mL, 9.54 mL, and 9.61 mL?

Rounding

Several rules for rounding are taught; you have probably met more than one in your courses. Everyone is adamant *their* rules are correct. The National Institute of Science and Technology (NIST) policy on rounding numbers is presented here.[2] (It *is* correct. ☺)

First, keep all the digits from intermediate calculations. Round the final value as follows:

If the digits to be discarded are	**Round the last digit to be kept**	**Example**
less than 5	down	3.7249999 rounded to two decimal places is 3.72.
greater than 5	up	3.7250001 rounded to two decimal places is 3.73.
exactly 5 (followed only by zeros)	even	3.72500... rounded to two decimal places is 3.72.

When manipulating data, keep all digits through intermediate calculation. Round the final value to the appropriate number of significant digits. *Don't round until the end.*

Accuracy, Precision, and Tolerance

There is no relationship between ***accuracy, precision,*** *and* ***tolerance.***

Accuracy

Accuracy is a measure of the difference between an experimental value and the true value. Any difference is due to systematic error(s). For example, a systematic error exists if a volumetric pipet is blown out or if the edge of a ruler is used instead of the zero graduation.

Accuracy can only be determined where the 'true' value of a sample is known, i.e., a reference. Certified reference materials (CRMs) are substances that contain one or more analytes in a given matrix. They have been exhaustively characterized by several laboratories using a number of analytical techniques to provide bias-free results. CRMs are expensive! Would you pay 241$ US for 55 g of soil containing 432 ppm ± 17 ppm lead at the 95 % confidence level? How about 6088$ US for a single platinum thermocouple capable of measuring absolute temperatures to within 0.2 mK? It comes in a nice wooden box...[3] If no suitable CRM is available, or is too expensive, and that level of precision is not needed, an alternative is to prepare an in-house reference.

The CRM or in-house reference is used to make quality control (QC) samples. The QCs are run at the same time as the unknowns. Since their concentration is known, systematic errors can be detected by comparing the experimental value with the true value.

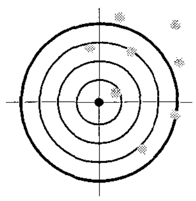

POOR accuracy
POOR precision

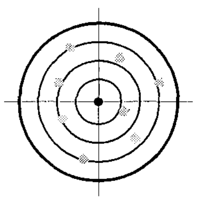

GOOD accuracy
POOR precision

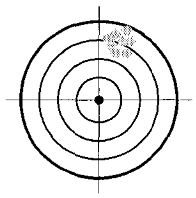

POOR accuracy
GOOD precision

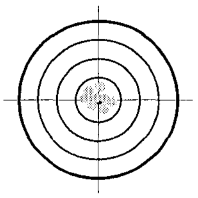

GOOD accuracy
GOOD precision

Chemists who master both accuracy and precision are deadly!

Precision

Every experimentally measured value has an associated uncertainty.

Precision is characterized as the distribution of random fluctuations about the 'true' value. Statistics assumes that the distribution is gaussian (a.k.a. 'normal').[4] A gaussian distributions' width is defined by a single parameter, the standard deviation, σ. Figure 1 illustrates the dependence on σ: 68.3 % of the gaussian's area is contained between $-\sigma$ and σ, 95.4 % between -2σ and 2σ, and 99.7 % between -3σ and 3σ. We will see that the standard deviation of a series of observations is used to determine the certainty with which we can report a value. It is *impossible* to reduce the standard deviation to zero, even with an infinite number of observations. To encompass the true value with a desired confidence, the standard deviation is multiplied by a factor, t, dependent on the number of observations and required confidence level (see ***Encompassing the true value***, below).

A multitude of factors affect precision:

- instrument noise (detector sensitivity, noise, etc.)
- experimental technique (pipetting, weighing, filling, etc.)
- sample inhomogeneity

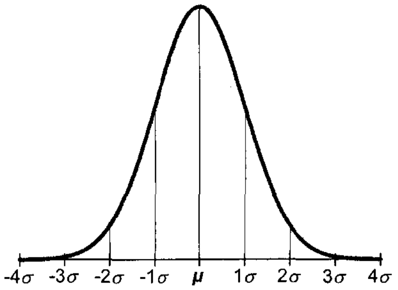

Figure 1. Gaussian distribution showing the true value, μ, and standard deviations, σ.

Tolerance

Tolerance is not a statistical parameter. For example, the tolerance of a 10.00 mL class A volumetric pipet is ± 0.02 mL. This means that the pipet is guaranteed to deliver between 9.98 mL and 10.02 mL. It *does not* mean that the pipet will deliver an average of 10.00 mL. A given pipet might routinely deliver 9.997 mL or 10.015 mL or 9.981 mL. Unlike precision, tolerance does not have a gaussian distribution. Practicing analytical chemists calibrate their pipets. Analytical chemists can repeatably deliver within ± 0.002 mL with a 10.00 mL pipet. They gain an extra decimal place and reduce the associated uncertainty by a factor of 10!

It is a systematic error if you report the volume delivered by a 10 mL pipet as (10.00 ± 0.02) mL, which is the tolerance, when the pipet actually delivers (10.011 ± 0.004) mL. The uncertainty in the final value will also be proportionately larger.

Formulae and Examples

Rejecting data (Q-test)

It is good practice to check outliers in a data set to see if they can statistically be rejected. This is done using the Q-test.

$$Q \quad \begin{matrix} \mathit{gap} \\ \mathit{range} \end{matrix} \quad \begin{matrix} \mathit{suspect} & \\ \mathit{largest} & \mathit{smallest} \end{matrix}$$

Q_{tab} is looked up in a table and compared with Q_{calc}. If $Q_{\mathrm{calc}} > Q_{\mathrm{tab}}$, the outlier data point can be rejected at the specified confidence level. (Note: this table uses n, the number of observations; all other statistical tables use degrees of freedom.)

$$_{\text{calc}} = \frac{\quad}{\quad} = \frac{\left| \quad - nearest \right|}{-}$$

Average

The average, $\bar{x}$, can be calculated as the mean, median, and mode for *n* observations of a sample.

The *mean* is calculated from the formula: $\bar{x} = \frac{1}{n}\sum_i x_i$

The *median* is the middle data point after the data are sorted in ascending or descending order. If there are an even number of data points, the median is the mean of the center two data points. The *mode* is the most frequently observed value. It can only be used with large data sets — not common in analytical labs!

If the number of observations is very large (i.e., the entire population) and if no systematic errors exist, the average value becomes the true value, μ.

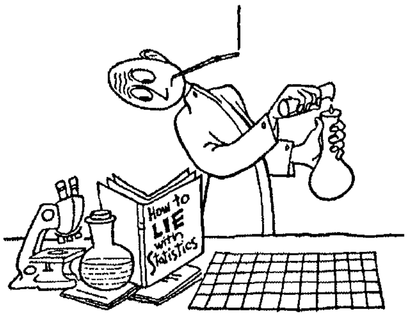

(From the book of the same title.)

Often, raw data is mathematically transformed to obtain information. It is important to convert each observation to the final value before averaging. Why? Because non-linear mathematical transformations (square root, power, logarithm, etc.) skew the distribution of observations. *There is a difference* if each observation is transformed to the final value and then averaged *or* averaged and then transformed to the final value. For example, consider reading two values versus their average from a non-linear calibration curve.

Standard deviation

The sample standard deviation, *s*, is a measure of the precision of a *single observation* in a series of observations. If the number of observations is very large (i.e., the entire population), the sample standard deviation becomes the population standard deviation, σ. Note the difference in formulae.

$$s = \sqrt{\frac{\sum_i (x_i - \bar{x})^2}{n-1}} \qquad \sigma = \sqrt{\frac{\sum_i (x_i - \mu)^2}{n}}$$

The standard deviation can also be viewed as the range in which we expect the next observation to be found with a certain confidence. We are often interested in the standard deviation of a value obtained from the original data, such as the *standard deviation of the average* ($s_{\bar{x}}$), *slope* (s_m), *intercept* (s_b), etc. These are calculable from the sample standard deviation.

$$s_i = \frac{s}{\sqrt{n}}$$

The relative uncertainty (*uncertainty/average*) can be used to evaluate the precision at various points in a process or to evaluate the precision between different methods. One common calculation is percent relative standard deviation (*%RSD*). However, similar calculations are valid for any confidence level.

$$\%RSD = \frac{\textit{standard deviation}}{\textit{average}} 100\,\% = \frac{s}{\bar{x}} 100\,\%$$

Encompassing the true value: confidence intervals

The average and standard deviation can be calculated when more than one observation of a sample is made. It is not possible to determine the true value by replicate observations, but the probability of the true value being within a calculable range can be determined. Multiplying the standard deviation by a factor t (often called Student's t's) determines the *confidence interval* (a.k.a. uncertainty and Δx) of the observation at the stated confidence level. t values for different confidence levels and degrees of freedom are tabulated. Unless there is a reason to believe otherwise, the two-tailed t-value is used, which indicates that the true value could be either above or below the calculated average.

$$\mu = \bar{x} \pm \Delta x \qquad \Delta x = t s_i = \frac{ts}{\sqrt{n}}$$

Statistics in the real world: polls and surveys often contain a statement, "The poll/survey is accurate to within (for example) three percentage points 19 times out of 20." Statistically, this statement states that the uncertainty is ± 3 % at the 95 % confidence level. (19/20 · 100 % = 95 %)

Example: A common analytical experiment is the gravimetric analysis of copper in brass. Five samples were analyzed and the percentage of copper in each determined to be 93.42 %, 93.86 %, 92.78 %, 93.14 %, and 93.60 % by mass. The mean is 93.36 % and the standard deviation is 0.417 %. For five samples (four degrees of freedom) at the 95 % confidence level, $t_{(95\ \%,\ 4)} = 2.776$. The uncertainty, $ts/\sqrt{n}$, is 0.52 %.

The report would contain the statement, "The concentration of copper in the brass was determined to be (93.4 ± 0.5) % by mass at the 95 % confidence level."

If a QC sample with known value (μ^*) is also analyzed, a t-test can be used to determine if there is a statistical difference between the experimental value and the known value. Failure of this test indicates that systematic errors may exist in the experimental method.

$$t_{\text{calc}} = \left| \frac{\sqrt{n}}{s} \left(\mu^* - \bar{x} \right) \right|$$

If $t_{\text{calc}} < t_{\text{tab}}$, there is no statistical difference between $\bar{x}$ and μ^* and no systematic errors are observed at the specified confidence level. Equivalently, if μ^* is encompassed in the confidence interval of $\bar{x}$, there is no statistical difference at the specified confidence level.

(cont.) A brass QC with a known copper content of (91.75 ± 0.11) % was analyzed and found to contain (92.2 ± 0.5) % copper, both at the 95 % confidence level.

Ignoring the uncertainty in the QC, t_{calc} is determined to be 2.413. t_{calc} is lower than t_{tab}, 2.776, so there is no statistical difference at the 95 % confidence level. No systematic errors were observed at the specified confidence level. Equivalently, the known QC value is encompassed within the confidence interval of the QC: 91.7 % to 92.7 %. Again, there is no statistical difference.

A statistical difference is found at the 90 % confidence level.

Calculations involving uncertainty in both the experimental and known value is discussed in ***Comparing multiple data sets***, below.

Percent error is another common, but not statistical, calculation that measures deviation from the true value. Unlike the t-test, percent error provides information regarding the direction of a systematic error.

$$\%\ error = \left(\frac{experimental - actual}{actual} \right) 100\ \% = \left(\frac{\bar{x} - \mu}{\mu} \right) 100\ \%$$

Sources of uncertainty (ANOVA)

The square of the standard deviation is the variance. Variance is additive for normal distributions, making it possible to determine the magnitude of various sources of uncertainty. This analysis is often called ANalysis Of VAriance (ANOVA).

$$V = s^2$$

Figure 2 shows how a sample can be analyzed to determine the contributions from sampling, preparation, and analysis to the total uncertainty. The variance in **A** is due to the analysis only; the variance in **B** is due to analysis and preparation; the variance in **C** is the total variance of all processes. Because of the additive nature of variance,

$$V_{\text{total}} = V_{\text{sampling}} + V_{\text{preparation}} + V_{\text{measurement}}$$

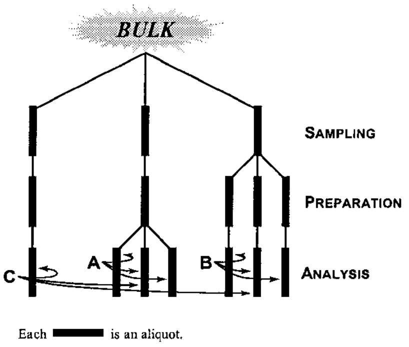

Figure 2. Sample flow-chart for an ANOVA analysis of a process.

Propagation of uncertainty

Propagation of uncertainty is additive for variance but we more commonly work with standard deviation. The formula for propagating uncertainty through an arbitrary function, $z = f(x, y, \ldots)$, is given by

$$s_z = \sqrt{\left(\frac{\partial z}{\partial x}\right)^2 s_x^2 + \left(\frac{\partial z}{\partial y}\right)^2 s_y^2 + \ldots + \left(\frac{\partial z}{\partial x}\right)\left(\frac{\partial z}{\partial y}\right) s_{xy}^2 + \ldots} \approx \sqrt{\left(\frac{\partial z}{\partial x}\right)^2 s_x^2 + \left(\frac{\partial z}{\partial y}\right)^2 s_y^2 + \ldots}$$

The covariance, s_{ij}, is dependent on two variables and therefore more difficult to determine. All too often, covariance is not calculated (ignored). Note the likely confusion between s_i, V_i, and s_{ij}: s_i is the standard deviation , V_i is the variance ($V_i = s_i^2$), and s_{ij} is the covariance. Propagation of uncertainty functions for common mathematical operations are given below. Those where covariance is ignored have '≈'.

Operation	Uncertainty	Operation	Uncertainty	
$z = x + y$ $z = x - y$	$s_z^2 = s_x^2 + s_y^2$	$z = \ln(x)$ $z = \log(x)$	$s_z = \frac{s_x}{x}$	$s_z = \frac{1}{\ln(10)}\frac{s_x}{x}$
$z = x \cdot y$ $z = x/y$	$\left(\frac{s_z}{z}\right)^2 \approx \left(\frac{s_x}{x}\right)^2 + \left(\frac{s_y}{y}\right)^2$	$z = e^x$ $z = 10^x$	$\frac{s_z}{z} = s_x$	$\frac{s_z}{z} = \ln(10) s_x$
$z = x^a = x \cdot x \cdot \ldots$	$\frac{s_z}{z} = a\frac{s_x}{x}$		↑ base e	↑ base 10

Comparing multiple data sets

The F-test determines if the *variances* of two data sets (a and b) are the same. Based on the results of the F-test, the t-test can be used to determine if the *means* of two data sets are the same. Alternatively, the F-test can be used to determine the significance of individual parameters in a model (non-linear curve fitting, for example.)

$$F_{\text{calc}} = \frac{V_a}{V_b} = \frac{s_a^2}{s_b^2} \qquad a \text{ and } b \text{ are chosen so that } F_{\text{calc}} > 1.$$

F_{tab} is then looked up for a specified confidence level. Unless there is a reason to believe otherwise, the two-tailed tabulated value is used. If $F_{\text{calc}} < F_{\text{tab}}$, we can say, “There is no statistical difference between the distributions at the specified confidence level.”, and use a pooled standard deviation, s_{pooled}, in further calculations. Otherwise, individual standard deviations must be used and the degrees of freedom of t_{tab} must be calculated separately.

Passed F-test

$$s_{\text{pooled}} = \sqrt{\frac{(n_a - 1)s_a^2 + (n_b - 1)s_b^2}{n_a + n_b - 2}}$$

$$t_{\text{calc}} = \frac{|\bar{x}_a - \bar{x}_b|}{s_{\text{pooled}}\sqrt{\frac{1}{n_a} + \frac{1}{n_b}}}$$

Failed F-test

$$t_{\text{calc}} = \frac{|\bar{x}_a - \bar{x}_b|}{\sqrt{\frac{s_a^2}{n_a} + \frac{s_b^2}{n_b}}}$$

$$d.f. = \left[\frac{\left(\frac{s_a^2}{n_a} + \frac{s_b^2}{n_b}\right)^2}{\frac{\left(\frac{s_a^2}{n_a}\right)^2}{n_a + 1} + \frac{\left(\frac{s_b^2}{n_b}\right)^2}{n_b + 1}}\right] - 2$$

(cont.) To account for the uncertainty in the QC, $F_{\text{calc}} = 0.417^2/0.056^2 = 55.4$. (The quoted uncertainty is at the 95 % confidence level; assuming that an infinite number of analyses were conducted, the standard deviation was obtained by dividing by $t(95\ \%, \infty) = 1.960$.) F_{calc} is greater than F_{tab} at the 95 % confidence level ($F_{\text{tab}}(4,\infty) = 2.786$); the two samples are not from the same population.

$t_{\text{calc}} = 2.413$, which is lower than t_{tab}, 2.776, so there is no statistical difference at the 95 % confidence level.

NB: Both calculations for t_{calc} return the same value. If the number of replicates used to determine the QC is known, t_{calc} will differ.

The examples on the next few pages illustrate how statistics is applied to more complicated systems. The examples can be omitted if desired. Beyond the examples are tabulated Q, t, and F values. These tables and this complete document are also available from www.consol.ca (Teaching *link).*

Additional Examples

Linear regression

The formulae required to conduct a linear regression analysis are beyond the scope of this summary. Furthermore, they are not needed: calculators, spreadsheets, and scientific software packages have these functions built-in. Not all programs determine the uncertainty associated with values read from a linear regression. I make an Excel spreadsheet available to assist with this calculation: www.consol.ca (Teaching link). The spreadsheet also contains the statistical tables for the tests discussed *supra.*

Linear regression analysis assumes that there is no uncertainty in the x-coordinate of each data point and that the uncertainty in the y-coordinate is constant for all data points. Figure 3 shows a typical linear calibration curve, the uncertainty in the regression, and the uncertainty in a single observation of a sample, all at the 95 % confidence level. The regression uncertainty is non-linear, being smaller near the center of the data set and larger towards the extrema. The uncertainty for a single observation of a sample is the same as the regression uncertainty; It is less for multiple measurements on the sample. The correlation coefficient, R^2, is a measure of the 'goodness of fit' of the fitting function to the experimental data points.

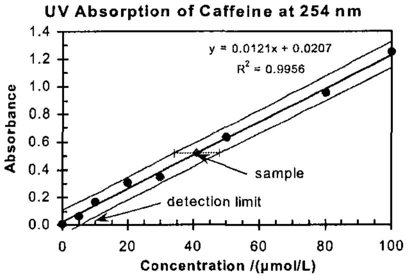

Figure 3. Caffeine calibration curve (solid line), linear regression uncertainty (light line), and single observation of a sample. All uncertainties at the 95 % confidence level.

Non-linear mathematical transformations also skew the uncertainty distribution. To obtain statistically significant results, the data must be weighted with the relative uncertainty or the uncertainty determined from a non-linear calibration curve of the original data. Uncertainty analysis from non-linear calibration curves is beyond the scope of this summary.[5]

Detection limits

The detection limit (DL) is defined as "the minimum single result [that], with a stated probability, can be distinguished from a suitable blank value."[6] In other words, the signal cannot be within the confidence interval of the blank, or a t-test between the blank and the sample must fail. In this case, a one-tailed t-value is used since the blank theoretically represents a minimum signal.

$$y_{\mathrm{DL}} = y_{\mathrm{blank}} + t s_b$$

In Figure 3, the minimum signal distinguishable from the blank is 0.072, which corresponds to a detection limit of 4.2 μmol/L.

Simplified uncertainty for linear regression analyses

> *I include this section with mixed feelings. Mostly, it is included to correct a commonly taught method that is grossly inaccurate.*

The formulae for statistically determining the uncertainty of a data point read from a linear regression analysis are complicated. Often, an estimate of the uncertainty is satisfactory and ideally, should be calculable from the uncertainty in the slope and intercept, which are provided by most programs.

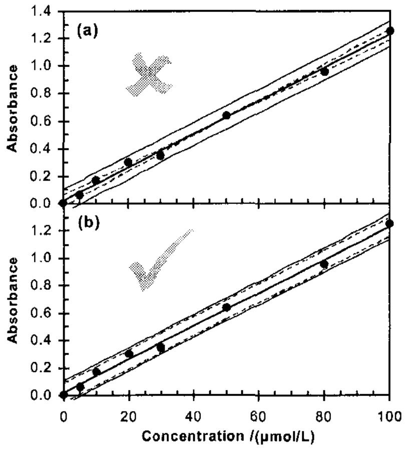

Figure 4. Simplified methods of estimating the linear regression uncertainty. Best fit (solid line), correct uncertainty (light line), and estimated uncertainty (dashed line). All uncertainties at the 95 % confidence level.

A POOR METHOD (*which is all too commonly used*) involves plotting the minimum and maximum lines from

$$y_{\substack{\max\\\min}} = (m \pm s_m)x + (b \pm s_b) \text{ or}$$

$$y_{\substack{\max\\\min}} = (m \pm s_m)x + (b \mp s_b)$$

Although seemingly intuitive, the results differs significantly from the correct uncertainty as shown in Figure 4a. Contrary to the correct uncertainty, there exists a point where the uncertainty is supposedly zero and the uncertainty increases linearly in both directions from this point. Changing the ± to ∓ only changes the location of the 'zero-uncertainty' point.

A BETTER METHOD is obtained by simplifying the correct uncertainty formula. The resulting formula is a vertical shift of the best fit line and is in good agreement with the correct uncertainty formula (Figure 4b). The equations for the minimum and maximum uncertainty are

$$y_{\substack{\max\\\min}} = mx + (b \pm 1.5s_b)$$

The factor of 1.5 scales the uncertainty to minimize the errors of the approximations.[7] The resulting unknown uncertainty is calculable from

$$s_X = \frac{1.5s_b}{m}$$

t can be included, $t(1.5s_b)$, to determine the uncertainty at a desired confidence level.

Spectral data

We are often interested in the peaks in spectra: spectroscopy, mass spectrometry, chromatography, nmr, polarography, etc. These peaks often have a gaussian or near-gaussian (lorentzian, voigt) profiles. A convenient measure of the uncertainty is the full-width at half-maximum (FWHM). For a gaussian distribution, $\text{FWHM} = 2\sqrt{2\ln(2)}\sigma \approx 2.36\sigma$. Half this value, 1.18σ, is the half-width at half-maximum (HWHM). Reporting the uncertainty as ±HWHM corresponds to, at most, the 76 % confidence level ($t(76\ \%, \infty) \approx 1.18$). (±FWHM corresponds to the 98 % confidence level.) Most peaks are comprised of fewer than an infinite number of observations, which is considered in the example below. By determining the standard deviation from the FWHM, the uncertainty at any confidence level can be determined. Alternatively, the centroid and standard deviation (x_0, s) can be determined explicitly by fitting a gaussian function to the data

Example: High-resolution spectroscopy results in many peaks. Figure 5 shows a peak that is comprised of seven statistically significant data points (i.e., above the statistical uncertainty of the baseline). The FWHM is estimated as 0.008 nm and, assuming a gaussian like distribution, the standard deviation determined. $t(98\ \%, 5) \approx 3.365$

$$\pm\,\text{FWHM} = 0.008\text{ nm} = 3.365s$$

$$s = 0.0024\text{ nm}$$

Calculation of the centroid and standard deviation (x_0, s) use two degrees of freedom. The uncertainty of the centroid at the 95 % confidence level is found to be

$$\Delta x_0 = t s_{x_0} = \frac{ts}{\sqrt{n}}$$

$$= \frac{2.571 \cdot 0.0024\text{ nm}}{\sqrt{7}} = 0.0020\text{ nm}$$

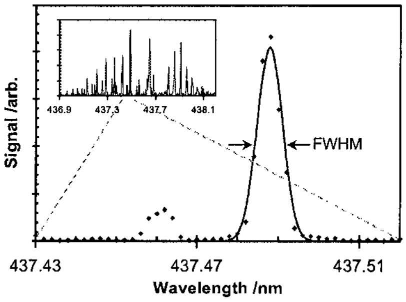

Figure 5. Gaussian distribution (solid line) fit to a single rovibronic transition in the C_2 transition (points) near 437.6 nm. (from our laboratory)

General reading

Harris D.C. *Quantitative Chemical Analysis*, 6th ed., W. H. Freeman and Company, New York, **2002**.

Harvey, D. *Modern Analytical Chemistry*, McGraw-Hill, New York, **2000**.

References

1. Shoemaker, D. P.; Garland, C. W.; Nibler, J. W. *Experiments in Physical Chemistry*, 6th ed., McGraw-Hill, New York, **1996**.
2. Taylor, B., *NIST Special Publication 811: Guidelines for the use of the International System of Units*, National Institute of Standards and Technology, **1995**.
3. *NIST Standard Reference Materials*, www.nist.gov/srm/, January **2002**.
4. The Central Limit Theorem states that the distribution resulting from an infinite number of small independent influences (of any form) on a system will be gaussian.
5. See, for example, de Levie, R., *J. Chem. Ed.*,**1999** ,*76* , 1594.
6. International Union of Pure and Applied Chemistry (IUPAC) Goldbook, www.iupac.org/publications/compendium/index.html, March **2002**.
7. Jensen, R.H., unpublished results.

Statistical Tables

Table 1. Tabulated values for the *Q*-test.

n	68%	90%	95%	98%	99%
3	0.822	0.941	0.970	0.988	0.994
4	0.603	0.765	0.829	0.889	0.926
5	0.488	0.642	0.710	0.780	0.821
6	0.421	0.560	0.625	0.698	0.740
7	0.375	0.507	0.568	0.637	0.680
8	0.343	0.468	0.526	0.590	0.634
9	0.319	0.437	0.493	0.555	0.598
10	0.299	0.412	0.466	0.527	0.568
12	0.271	0.375	0.425	0.480	0.518
14	0.250	0.350	0.397	0.447	0.483
16	0.234	0.329	0.376	0.422	0.460
18	0.223	0.314	0.358	0.408	0.438
20	0.213	0.300	0.343	0.392	0.420

Table 2. Tabulated values for the one and two-tailed *t*-tests.

D.F.	One-Tailed *t*-Test					Two-Tailed *t*-Test				
	68%	90%	95%	98%	99%	68%	90%	95%	98%	99%
1	0.635	3.078	6.314	15.894	31.821	1.819	6.314	12.706	31.821	63.656
2	0.546	1.886	2.920	4.849	6.965	1.312	2.920	4.303	6.965	9.925
3	0.518	1.638	2.353	3.482	4.541	1.189	2.353	3.182	4.541	5.841
4	0.505	1.533	2.132	2.999	3.747	1.134	2.132	2.776	3.747	4.604
5	0.497	1.476	2.015	2.757	3.365	1.104	2.015	2.571	3.365	4.032
6	0.492	1.440	1.943	2.612	3.143	1.084	1.943	2.447	3.143	3.707
7	0.489	1.415	1.895	2.517	2.998	1.070	1.895	2.365	2.998	3.499
8	0.486	1.397	1.860	2.449	2.896	1.060	1.860	2.306	2.896	3.355
9	0.484	1.383	1.833	2.398	2.821	1.053	1.833	2.262	2.821	3.250
10	0.482	1.372	1.812	2.359	2.764	1.046	1.812	2.228	2.764	3.169
12	0.480	1.356	1.782	2.303	2.681	1.037	1.782	2.179	2.681	3.055
14	0.478	1.345	1.761	2.264	2.624	1.031	1.761	2.145	2.624	2.977
16	0.477	1.337	1.746	2.235	2.583	1.026	1.746	2.120	2.583	2.921
18	0.476	1.330	1.734	2.214	2.552	1.023	1.734	2.101	2.552	2.878
20	0.475	1.325	1.725	2.197	2.528	1.020	1.725	2.086	2.528	2.845
25	0.473	1.316	1.708	2.167	2.485	1.015	1.708	2.060	2.485	2.787
30	0.472	1.310	1.697	2.147	2.457	1.011	1.697	2.042	2.457	2.750
40	0.471	1.303	1.684	2.123	2.423	1.007	1.684	2.021	2.423	2.704
50	0.471	1.299	1.676	2.109	2.403	1.004	1.676	2.009	2.403	2.678
75	0.470	1.293	1.665	2.090	2.377	1.001	1.665	1.992	2.377	2.643
100	0.469	1.290	1.660	2.081	2.364	0.999	1.660	1.984	2.364	2.626
200	0.468	1.286	1.653	2.067	2.345	0.997	1.653	1.972	2.345	2.601
500	0.468	1.283	1.648	2.059	2.334	0.995	1.648	1.965	2.334	2.586
∞	0.468	1.282	1.645	2.054	2.326	0.994	1.645	1.960	2.326	2.576

Table 3. Tabulated values for the two-tailed *F*-test.

95%		Degrees of Freedom: Numerator																									
		1	2	3	4	5	6	7	8	9	10	12	14	16	18	20	25	30	40	50	75	100	200	500	∞
Degrees of Freedom: Denominator	1	647.8	799.5	864.2	899.6	921.8	937.1	948.2	956.6	963.3	968.6	976.7	982.5	986.9	990.3	993.1	998.1	1001	1006	1008	1011	1013	1016	1017	1018
	2	38.51	39	39.17	39.25	39.3	39.33	39.36	39.37	39.39	39.4	39.41	39.43	39.44	39.44	39.45	39.46	39.46	39.47	39.48	39.48	39.49	39.49	39.5	39.5
	3	17.44	16.04	15.44	15.1	14.88	14.73	14.62	14.54	14.47	14.42	14.34	14.28	14.23	14.2	14.17	14.12	14.08	14.04	14.01	13.97	13.96	13.93	13.91	13.9
	4	12.22	10.65	9.979	9.604	9.364	9.197	9.074	8.98	8.905	8.844	8.751	8.684	8.633	8.592	8.56	8.501	8.461	8.411	8.381	8.34	8.319	8.288	8.27	8.257
	5	10.01	8.434	7.764	7.388	7.146	6.978	6.853	6.757	6.681	6.619	6.525	6.456	6.403	6.362	6.329	6.268	6.227	6.175	6.144	6.101	6.08	6.048	6.028	6.015
	6	8.813	7.26	6.599	6.227	5.988	5.82	5.695	5.6	5.523	5.461	5.366	5.297	5.244	5.202	5.168	5.107	5.065	5.012	4.98	4.937	4.915	4.882	4.862	4.849
	7	8.073	6.542	5.89	5.523	5.285	5.119	4.995	4.899	4.823	4.761	4.666	4.596	4.543	4.501	4.467	4.405	4.362	4.309	4.276	4.232	4.21	4.176	4.156	4.142
	8	7.571	6.059	5.416	5.053	4.817	4.652	4.529	4.433	4.357	4.295	4.2	4.13	4.076	4.034	3.999	3.937	3.894	3.84	3.807	3.762	3.739	3.705	3.684	3.67
	9	7.209	5.715	5.078	4.718	4.484	4.32	4.197	4.102	4.026	3.964	3.868	3.798	3.744	3.701	3.667	3.604	3.56	3.505	3.472	3.426	3.403	3.368	3.347	3.333
	10	6.937	5.456	4.826	4.468	4.236	4.072	3.95	3.855	3.779	3.717	3.621	3.55	3.496	3.453	3.419	3.355	3.311	3.255	3.221	3.175	3.152	3.116	3.094	3.08
	12	6.554	5.096	4.474	4.121	3.891	3.728	3.607	3.512	3.436	3.374	3.277	3.206	3.152	3.108	3.073	3.008	2.963	2.906	2.871	2.824	2.8	2.763	2.74	2.725
	14	6.298	4.857	4.242	3.892	3.663	3.501	3.38	3.285	3.209	3.147	3.05	2.979	2.923	2.879	2.844	2.778	2.732	2.674	2.638	2.59	2.565	2.526	2.503	2.487
	16	6.115	4.687	4.077	3.729	3.502	3.341	3.219	3.125	3.049	2.986	2.889	2.817	2.761	2.717	2.681	2.614	2.568	2.509	2.472	2.422	2.396	2.357	2.333	2.316
	18	5.978	4.56	3.954	3.608	3.382	3.221	3.1	3.005	2.929	2.866	2.769	2.696	2.64	2.596	2.559	2.491	2.445	2.384	2.347	2.296	2.269	2.229	2.204	2.187
	20	5.871	4.461	3.859	3.515	3.289	3.128	3.007	2.913	2.837	2.774	2.676	2.603	2.547	2.501	2.464	2.396	2.349	2.287	2.249	2.197	2.17	2.128	2.103	2.085
	25	5.686	4.291	3.694	3.353	3.129	2.969	2.848	2.753	2.677	2.613	2.515	2.441	2.384	2.338	2.3	2.23	2.182	2.118	2.079	2.024	1.996	1.952	1.924	1.906
	30	5.568	4.182	3.589	3.25	3.026	2.867	2.746	2.651	2.575	2.511	2.412	2.338	2.28	2.233	2.195	2.124	2.074	2.009	1.968	1.911	1.882	1.835	1.806	1.787
	40	5.424	4.051	3.463	3.126	2.904	2.744	2.624	2.529	2.452	2.388	2.288	2.213	2.154	2.107	2.068	1.994	1.943	1.875	1.832	1.772	1.741	1.691	1.659	1.637
	50	5.34	3.975	3.39	3.054	2.833	2.674	2.553	2.458	2.381	2.317	2.216	2.14	2.081	2.033	1.993	1.919	1.866	1.796	1.752	1.689	1.656	1.603	1.569	1.545
	75	5.232	3.876	3.296	2.962	2.741	2.582	2.461	2.366	2.289	2.224	2.123	2.046	1.986	1.937	1.896	1.819	1.765	1.692	1.645	1.578	1.542	1.483	1.444	1.417
	100	5.179	3.828	3.25	2.917	2.696	2.537	2.417	2.321	2.244	2.179	2.077	2	1.939	1.89	1.849	1.77	1.715	1.64	1.592	1.522	1.483	1.42	1.378	1.347
	200	5.1	3.758	3.182	2.85	2.63	2.472	2.351	2.256	2.178	2.113	2.01	1.932	1.87	1.82	1.778	1.698	1.64	1.562	1.511	1.435	1.393	1.32	1.269	1.229
	500	5.054	3.716	3.142	2.811	2.592	2.434	2.313	2.217	2.139	2.074	1.971	1.892	1.83	1.779	1.736	1.655	1.596	1.515	1.462	1.381	1.336	1.254	1.192	1.137
	∞	5.024	3.689	3.116	2.786	2.567	2.408	2.288	2.192	2.114	2.048	1.945	1.866	1.803	1.752	1.709	1.626	1.566	1.484	1.429	1.345	1.296	1.206	1.128	1

Units of Measure and Conversions

Quantity	Base SI Unit	Abbreviation	Often used as
mass	kilogram	kg	g; mg; µg; ng
volume	liter	L	mL; µL
distance	meter	m	cm; mm
time	second	s	s; ms

SI Prefix	Symbol	Value		Common Name
		Exponential	Full	
yotta	Y	10^{24}	1 000 000 000 000 000 000 000 000	
zetta	Z	10^{21}	1 000 000 000 000 000 000 000	
exa	E	10^{18}	1 000 000 000 000 000 000	
peta	P	10^{15}	1 000 000 000 000 000	
tera	T	10^{12}	1 000 000 000 000	trillion
giga	G	10^{9}	1 000 000 000	billion
mega	M	10^{6}	1 000 000	million
kilo	k	10^{3}	1 000	thousand
——		1	1	
deci	d	10^{-1}	0.1	
centi	c	10^{-2}	0.01	parts per hundred; %
milli	m	10^{-3}	0.001	parts per thousand (ppt)
micro	µ	10^{-6}	0.000 001	parts per million (ppm)
nano	n	10^{-9}	0.000 000 001	parts per billion (ppb)
pico	p	10^{-12}	0.000 000 000 001	parts per trillion (ppt; pptr)
femto	f	10^{-15}	0.000 000 000 000 001	
atto	a	10^{-18}	0.000 000 000 000 000 001	
zepto	z	10^{-21}	0.000 000 000 000 000 000 001	
yocto	y	10^{-24}	0.000 000 000 000 000 000 000 001	

Because the density of water is approximately 1 g/mL and the majority of analytical chemistry deals with aqueous solutions, the following approximate equivalents are found. They are exact when the density is exactly 1.000 g/mL.

ppm ≈ mg/L; µg/mL; mg/kg; µg/g
ppb ≈ µg/L; ng/mL; µg/kg; ng/g
pptr ≈ ng/L; pg/mL; ng/kg; pg/g

4. TRANSITION METAL-CHLORINE ANIONS AND CATIONS: MONOMERS, CLUSTERS, AND PERIODIC TRENDS

ELSEVIER

1 December 2000

Chemical Physics Letters 331 (2000) 163–169

CHEMICAL
PHYSICS
LETTERS

www.elsevier.nl/locate/cplett

Transition metal-chlorine anions and cations: monomers, clusters, and periodic trends

Chuan-Fan Ding, Yongzhi Yu, Roy H. Jensen, Walter J. Balfour, Charles X.W. Qian *

Department of Chemistry, University of Victoria, Victoria, BC, Canada V8W 3V6

Received 17 July 2000; in final form 26 September 2000

Abstract

Laser ablation and time-of-flight mass spectrometry have been used to generate and characterize aluminum-chlorine and transition metal-chlorine ionic species. Many new complexes have been observed. The structures of the monometal-chlorine species are discussed. © 2000 Elsevier Science B.V. All rights reserved.

1. Introduction

Material science has been an important branch of science in the past millennium and will be more critical in the new millennium. Generally speaking, there are three main building blocks of solid materials, i.e., cations/anions, neutral atoms and individual molecules, and correspondingly three main types of materials, ionic crystals, network solids and molecular solids [1]. In the past several decades, we have witnessed a tremendous growth in both pure and applied research in material science that challenges and changes our vision about materials. One of the most significant developments in recent years is the discovery of new carbon related materials, from fullerenes to nanotubes [2]. These new carbon compounds lie between the traditional network solids and molecular solids. Another important type of material is organic polymers [3], also in between the old classifications of network and molecular solids. Metal clusters can also be viewed as new materials and, due to their important role in heterogeneous catalysis, have attracted significant attention. In contrast to well studied simple neutral clusters, binary neutral clusters, ionic clusters, and radical clusters (ionic or neutral) have received much less attention. In the material world, however, they are the building blocks of a majority of solids. Several recent studies indicate an increasing interest in this field (see, for example, [4–8]).

Many monometal–metal chloride species have been characterized in solution and solid phase inorganic chemistry [9]. However, no ionic clusters composed only of a transition metal and chlorine seem to have been reported in the gas phase. Binary aluminum-chlorine clusters, neutral and ionic, have received considerable attention [10–12]. On the other hand, transition metal-chlorine clusters have not received as much attention, possibly due to difficulties in preparation, separation, and isolation. Only recently have iron-chlorine neutral and ionic clusters been observed in

---

* Corresponding author. Fax: +1-250-721-7147.
E-mail addresses: royj@uvic.ca (R.H. Jensen), laser@uvvm.uvic.ca (C.X.W. Qian).

PII: S0009-2614(00)01155-6

Reprinted with permission from Elsevier (see page 180)

5. ENERGY TRANSFER FROM $N_2(v)$ TO ClN_3 AND A KINETIC MODEL FOR THE CHAIN DECOMPOSITION OF CHLORINE AZIDE

J. Phys. Chem. A **2000,** *104,* 6573−6579 **6573**

Energy Transfer from $N_2(v)$ to ClN_3 and a Kinetic Model for the Chain Decomposition of Chlorine Azide

R. H. Jensen, A. Mann, and R. D. Coombe*

Department of Chemistry and Biochemistry, University of Denver, Denver, Colorado 80208

Received: June 30, 1999; In Final Form: March 27, 2000

A number of experiments have been performed in an effort to better understand the photoinitiated chain decomposition of ClN_3. Discharge-flow methods were used to determine the rate of energy exchange between vibrationally excited N_2 (a likely chain carrier) and ClN_3. The rate constant for energy transfer from $N_2(v=1)$ to ClN_3 was found to be $(2.0 \pm 1.0) \times 10^{-13}$ cm^3 s^{-1} at 300 K. This process is thought to excite the ν_2 mode in ClN_3 with the release of 281 cm^{-1} of excess energy. Experiments were also performed in which the decomposition of ClN_3 was initiated by photolysis with a pulsed KrF laser at 249 nm, with subsequent observation of the time dependence of the densities of ClN_3, electronically excited $NCl(a^1\Delta)$, and vibrationally excited $ClN_3(\nu_2)$. A kinetic model for the ClN_3 decomposition was assembled based on reactions with $NCl(a^1\Delta)$ and $N_2(v)$.

Introduction

Although azides (RN_3) are well-known energetic species prone to explosive decomposition, the energy stored by these molecules has been used for many applications other than explosives. In particular, azides have recently been used as energetic precursors for the low-temperature deposition of thin films[1,2] and as energy storage agents for the pumping of new laser systems.[3] In our laboratory, chlorine azide (ClN_3) has been used as a source of electronically excited $NCl(a^1\Delta)$, a metastable species which can collisionally excite iodine atoms to the $5^2P_{1/2}$ state.[4] Under appropriate circumstances, a population inversion can be achieved among the $5^2P_{1/2}$ and $5^2P_{3/2}$ levels in this system and lasing is observed[3] at 1.315 μm. The operation of the laser requires that the ClN_3 initially present be removed since it is an efficient quencher of excited $I^*(5^2P_{1/2})$. This removal is thought to occur by chain decomposition processes.

It has been speculated[5,6] that the chain decomposition of azides is driven by energy transfer processes involving excited dissociation fragments, in particular vibrationally excited N_2. The vibrational frequency in N_2 (2331 cm^{-1}) is near-resonant with the ν_2 vibration in azides, which typically is found in the range from 2000 to 2150 cm^{-1}. This vibration is an asymmetric stretch along the N_3 chain and is well mapped onto the dissociation coordinate leading to the nitrene NR and N_2, such that sequential excitation by collisions with $N_2(v>0)$ might well lead to dissociation. Benard and co-workers[6] have speculated that this mechanism is responsible for the chain decomposition of FN_3 observed in high-temperature shock tube studies. Also, flowing streams of $N_2(v)$ have been used to dissociate gas phase NCN_3 for the deposition of C_3N_4 thin films.[2] In the case of ClN_3, the ν_2 frequency is 2050 cm^{-1} and excitation of this vibration by collisions with $N_2(v)$ is exothermic by 281 cm^{-1}. Since the binding energy of $ClN_3(^1A')$ along the coordinate leading to $NCl(a^1\Delta) + N_2(X^1\Sigma_g^+)$ has been calculated[7] to be just 5700 cm^{-1}, sequential excitation of ClN_3 by as few as three collisions with $N_2(v)$ might dissociate the molecule. Further, since considerable energy is released when this dissociation occurs, it seems quite likely that $N_2(v)$ would be regenerated to continue the chain.

Because of the weakness of the $ClN-N_2$ bond, ClN_3 can also be dissociated by collisions with species in low-energy excited electronic states. It has been shown,[5] for example, that ClN_3 is dissociated by collisions with $O_2(a^1\Delta_g)$ to produce N_2 and $NCl(a^1\Delta)$. This process occurs with a room temperature rate constant near 10^{-11} cm^3 s^{-1}. Similarly, it has been suggested[4,5] that ClN_3 can be dissociated by collisions with $NCl(a^1\Delta)$ or with $I^*(5^2P_{1/2})$. I* quenching by ClN_3 has a rate constant[4] $k = 2.0 \times 10^{-11}$ cm^3 s^{-1}, and it is thought that this process also dissociates the azide to N_2 and $NCl(a^1\Delta)$. In our previous work[3] on the $ClN_3/NCl(a^1\Delta)/I^*$ laser system, a kinetic model was assembled which included ClN_3 chain decomposition carried by $N_2(v)$, $NCl(a^1\Delta)$, and I*. Although the model was largely speculative (rate constants for energy exchange between $N_2(v)$ and ClN_3 were unknown, as was the time dependence of ClN_3 in the system), it gave fair agreement with the $NCl(a^1\Delta)$ time profile observed in the experiments and predicted laser threshold times within a factor of 2 of the observed values.

We have continued to explore these issues by using discharge-flow methods to determine the rate constant for energy transfer from $N_2(v)$ to ClN_3, and by using pulsed laser photolysis methods to perform additional measurements of the decomposition of this azide. In the latter case, measurements of the time decay of ClN_3 in the system were performed and vibrational excitation in the ν_2 mode of the azide was detected. Time profiles for ClN_3, $NCl(a^1\Delta)$, and $ClN_3(\nu_2)$ were measured for a variety of initial conditions. The data from both the discharge-flow and laser photolysis experiments were used to assemble a new kinetic model for the decomposition.

Experimental Details

Gaseous ClN_3 was synthesized by the passage of a stream of Cl_2 diluted in He (5% Cl_2) and saturated with H_2O over NaN_3 suspended on glass wool. The azide generator was derived from a design developed by Schlie and co-workers and has been described elsewhere.[8] The efficiency with which Cl_2 was converted to ClN_3 in the reactor was greater than 90%, as determined by IR and UV spectra of the effluent. The principal impurity present is expected to be Cl_2; in fact, no Cl_2 was

10.1021/jp992253o CCC: $19.00